Universidad del País Vasco
Euskal Herriko Unibertsitatea

DEPARTAMENTO DE INGENIERÍA QUÍMICA
CHEMICAL ENGINEERING DEPARTMENT

Co_3O_4-based catalysts for methane emission control in natural gas engines: from bulk catalysts to open cell foam structured catalysts

Catalizadores basados en Co_3O_4 para el control de emisiones de metano en motores de gas natural: de catalizadores másicos a catalizadores estructurados en espumas de celda abierta

MEMORIA

para optar al Grado de
Doctor Internacional en Ingeniería Química
presentada por

Andoni Choya Atencia

Directores: Rubén López Fonseca
Beatriz de Rivas Martín

Leioa, noviembre de 2020

(c) 2021 Andoni Choya Atencia

Escuché una vez a un sabio decir que todos deberíamos saber lo que nos debemos a nosotros y lo mucho, o casi todo que debemos a los demás. Por eso esta página es tan larga, porque el haber llegado hasta aquí se lo tengo que agradecer a mucha gente.

En primer lugar, a mis directores de tesis, el doctor Rubén López Fonseca y la doctora Beatriz de Rivas Martín, por depositar su confianza en mi y darme la oportunidad de realizar esta Tesis junto a ellos, asi como por su dedicación, esfuerzo y apoyo constante durante toda la tesis. Asimismo, al doctor Jose Ignacio Gutiérrez Ortiz, por su inestimable ayuda y consejo, y por ayudarnos a mantener los laboratorios funcionando, se rompa lo que se rompa. A los tres, mi enorme agradecimiento también por permitirme compartir con vosotros la experiencia de la docencia. Muchas gracias.

A los Servicios Generales de Investigación (SGIker) de la UPV/EHU, y en especial a los técnicos Aitor Larrañaga, Francisco Javier Sangüesa, Alfredo Sarmiento, Luis Bartolomé y María Belén Sánchez, por realizar siempre el mejor trabajo posible. Sois los mejores.

A todos los miembros del grupo TQSA, por hacerme sentir uno más desde el primer día y por acompañarme en este largo camino. A todos los compañeros que siguen o han pasado durante estos años: Unai, Jonathan, Ainara, Miren, Maitane, Zouhair, Jon Ander, Adriana, Alberto, Adrián, Juan Alberto, Alejandro, Asier y Guillermo. Y en especial, a Cristina, por ayudarme y guiarme en los primeros meses; a Miryam y Amaya por aguantarme como compañero de laboratorio; y a Mónica Lanchas por sus ánimos y sabios consejos. También, a los cuatro proyectistas con los que he tenido el placer de trabajar: Fernando, Amaia, Claudia y Olatz. Gracias por vuestras ganas y vuestro esfuerzo.

Big thanks to the Materials and Surface Chemistry group of the Faculty of Chemistry of the Jagiellonian University in Kraków. Thank you, prof. Kotarba, for giving me the opportunity to work with you, and thank you to all the members of the group for making me feel at home since the very first day: Gabriela, Monika, Pawel, Paulina, Klaudia, Joanna, and specially Sylwia, for all your help, support and guidance, and Wojciech (and Ilona and Anna) for all the wonderful hours in the office, and for the Polish lessons. Dziekuje bardzo!

A mis amigos, sin los que no habría mantenido mi salud mental todo este tiempo. A todos los miembros del equipo Diskolaris Ultimate Bizkaia, por todos estos años en los que me he sentido feliz luchando junto a vosotros. A mis amigos Endika y Unai (y Jonathan y Rubén), por estar siempre ahí y no dejarme nunca en paz. Y a Ainhoa, por iluminarme cada día en el periodo más difícil y oscuro, y también después. Gracias de corazón.

Y, por último, pero no menos importante, a mi familia: a mis padres y mi hermana, sin los que no sería quien soy. Gracias por creer en mi hasta cuando yo ya no podía, por vuestro apoyo, vuestra compresión y vuestros ánimos. Gracias.

INDEX

Chapter 1

INTRODUCTION AND OBJECTIVES

ABSTRACT

Atmospheric pollution and climate change are amongst the most important challenges that society is facing nowadays. In this sense, the commercialisation of vehicles driven by natural gas engines constitutes an advanced strategy to mitigate the emissions associated with automotive, which is one of the largest emitting sectors of greenhouse effect gases, due to their reduced CO_2, NO_x, particles and hydrocarbons emissions. However, the consolidation of this type of vehicles in the automotive fleet requires the control of the residual (around 1%) unburned methane (main component of natural gas) emissions from the engine, since this gas possesses a powerful greenhouse effect potential. As a result of the high chemical stability of this compound and its low concentration in the flue gases, the low-temperature catalytic oxidation appears as an attractive solution for this purpose. In order for this treatment technology not to significantly increase the cost of the engine, the selected catalyst must present a high activity with a reasonable economic investment. Traditionally, the most commonly applied catalysts have been based on noble metals such as palladium. However, this type of catalysts is generally expensive and prone to deactivation. For this reason, spinel oxides based on transition metals can be a promising alternative for this purpose, owing to their lower cost, higher availability and relatively good activity for oxidation reactions. In the final part of this chapter, the main objective and layout of this thesis work are defined.

1. INTRODUCTION AND OBJECTIVES

1.1. INTRODUCTION

Atmospheric pollution has been a public health and social problem since centuries. As early as in the year 61 BC, philosopher Seneca complained about the heavy air in Rome, and already then, there were laws limiting the loading and unloading of animal carts for environmental reasons. Since then, several different laws and regulations have tried to limit the environmental impact of human activity throughout the history, especially in city centres, with limited to no result.

The origin of our modern problems regarding environmental pollution dates from the XVIII century with the first industrial revolution and the population growth. Industrialisation started to substitute the agricultural work and cities started to receive inhabitants from the countryside, increasing the population density. Later, in the XIX century, the inventions of the internal combustion engine and the electric energy substantially increased the consumption of fossil fuels such as coal and petroleum. Lastly, the invention and development of the motorcar did nothing but exacerbate the situation, and from the start of the XX century on, several extreme episodes of air pollution started affecting the public health. Some examples of these incidents are the one lived in Donora (USA) in 1948 when around 6,500 people suffered breathing difficulties and 17 died, or those occurred in London between 1956 and 1962 that caused the death of around 2,300 people [1].

In the last years, the public conscience and concern about the environment and its protection has risen drastically, and people have started to become aware of the impact that their day-to-day activity gives rise to and have adapted their habits and behaviour to minimise it. At the same time, society has demanded that the industry also works towards this objective, since its environmental impact is regarded to be much more important.

This has forced governments and institutions all around the globe to define and implement increasingly stricter regulations regarding pollutant emissions and resource and energy consumption, and to develope cleaner and more sustainable ways of carrying out the activities that give shape to our modern society. Nevertheless, modern society is still highly dependent of fossil fuels and follows a resource consumption trend that is far from sustainable.

Hence, in the short- and medium-term future, humankind must face a series of environmental challenges if it wants to keep living and developing in a non-hostile planet. Among the 17 Sustainable Development Goals described by the United Nations in 2015 as part of the 2030 Agenda for Sustainable Development, the necessity of producing affordable and clean energy, achieving a responsible resource consumption and production and combating desertification of land and pollution of the oceans [2], are prioritised. However, the most important challenge, regarding short-term urgency is fighting climate change.

1.2. CLIMATE CHANGE

Climate change is considered as the most important environmental challenge that society is facing nowadays, with surveys indicating that, around 70% of the people worldwide regards it to be a major threat to their country [3]. The 28th of November of 2019, the European Parliament officially declared the climate and environmental emergency, and urged all member states to take action and work harder in order to fight and contain the threat of climate change [4].

The Intergovernmental Panel on Climate Change (IPCC) defines climate change as the "changes in the state of the climate that can be identified by changes in the mean and/or the variability of its properties, and that persists or an extended period". The effects of climate change are already noticeable and tangible: extreme weather episodes, extinction of animal species or the disappearance of the arctic ice are some examples.

1.2.1. Drivers of climate change

The factors that drive this change in the climate are called "forcing mechanisms" and can be classified into internal and external. Internal forcings occur naturally in the planet and contribute to the natural variability of climate, while external forcings occur outside of the climate system itself [5]. Although the most known external forcing is human activity, orbital and solar variations and volcanism are also considered external forcing mechanisms.

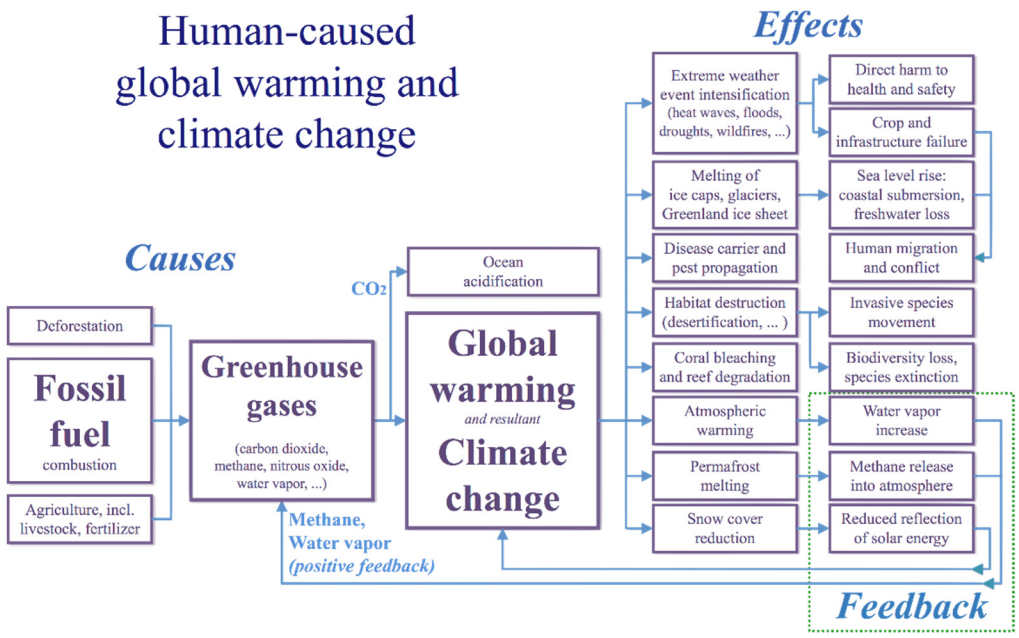

Figure 1.1. Causes and effects of global warming and climate change.

Internal forcing mechanisms are present in all time scales. Some atmospheric processes, for instance condensation of water vapour in clouds, have an almost instantaneous effect, while some others such as inter-hemispheric or inter-layer atmospheric exchanges take years. Other components such as ice sheets or the oceans take even longer time scales, and some of them are coupled to each other, for example the ocean-atmosphere coupling that generates the El Niño-Southern Oscillation.

External forcing mechanisms also have a high variability in time scales and effect. Some of them, namely the orbital and solar variations, can be evaluated with well-defined models that correlate fairly well to some observed changes in the climate. Among them, the Milankovitch cycles, associated with changes in the rotation and translation movements of the Earth with periods around 400,000 years, and the solar activity cycles (the shortest have a period of 11 years) are the ones that produce the stronger impact. On the other hand, volcanic activity can also have an important effect, but its inherently episodic nature limits the time scale of its affectation to a year or less. Tectonic movements, by contrast, are considered continuous in time but extremely slow, so their effects are only noticeable after

millions of years. Overall, the most important external forcing occurring nowadays is the human activity, in the form of global warming.

1.2.2. Global warming

Global warming is defined as the long-term rise of the average temperature of the Earth. The IPCC Fifth Assessment Report has concluded that "warming of the climate system is unequivocal, and since the 1950s the atmosphere and oceans have warmed, the amounts of snow and ice have diminished, and sea level has risen". Investigation of ice cores in Antarctica and other geological evidences have proved that there have been several prehistoric periods where natural global warming has occurred [6]. However, the rate of warming in all of them has been much slower than in the modern era, and the observed changes since the mid-XX century have been unprecedented over the past millennia.

The effects of global warming reach much farther than just increasing the temperature of the planet. The temperature increase entails a rise in the sea level, due to the melting of the arctic ice and the retreat of the non-polar glaciers [7]. Furthermore, the shrinking of the arctic ice promotes the ice-albedo feedback, that is, the lost ice cover is replaced by water or land, which reduces the albedo (a measure of reflectivity of the surface of the Earth), thus increasing the amount of solar energy absorbed by the surface leading to further warming [8]. Additionally, oxygen levels of water masses decrease because oxygen is less soluble in warm water, leading to oceans deoxygenation that damages the oceanic fauna and flora. In land, effects of global warming are translating not only into an increased frequency and duration of droughts and heat waves, but also into an increase in the occurrences of hurricanes, typhoons and flooding episodes as a result of the enhanced water evaporation with increasing temperature [9,10].

1.2.3. Radiative forcing

The main driver behind global warming is called "radiative forcing", which is the difference between the sunlight energy absorbed by the Earth and the energy radiated back to space. When the Earth's surface receives more incoming energy from sunlight than what it radiates into space, a positive radiative forcing occurs, causing warming. Radiative forcing varies with insolation (power of solar energy per unit area of the atmosphere), but is mainly regulated by three key factors:

- The land use, which causes a small negative forcing.

- The concentration of atmospheric aerosols that cause a negative forcing.
- The atmospheric concentration of radiatively active gases, also known as greenhouse gases that cause a positive forcing.

The negative forcing created by land use is generally small and normally close to zero. Land use by humans is progressively evolving towards the creation of more agricultural land through deforestation, which is also amplified by the wood production industries and wildfires [11]. This generates an equilibrium between several different effects. On one hand, a negative forcing created by the change from dark dense forests to light uncovered agricultural lands, which increases the albedo of the surface. On the other hand, the emission of greenhouse gases due to deforestation and specific uses of the land. In the overall, the increase in surface albedo dominates the equilibrium and the result is a small negative forcing, although this presents an important geographical variation [12].

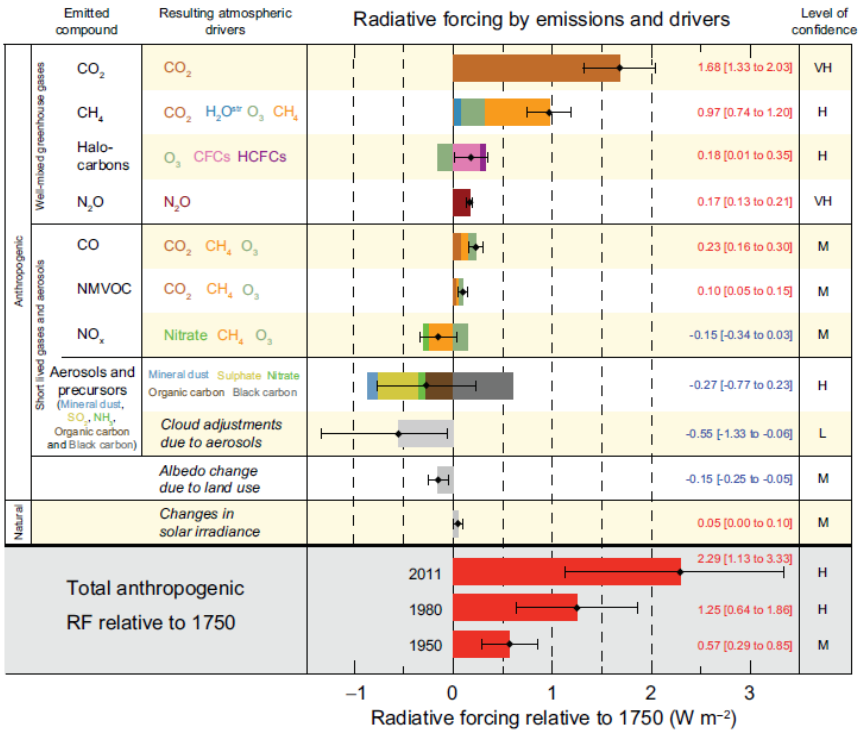

Figure 1.2. Radiative forcing by emissions and drivers [5].

The presence of aerosols in the atmosphere, such as particles from volcanoes, plankton or particulate matter, originates a negative forcing by the absorption and scattering of some of the incoming sunlight before it reaches the surface of the Earth, phenomenon known as "global dimming". Additionally, some suspended particles, such as sulphate aerosols, act like cloud seeds, generating clouds with smaller droplets that reflect sunlight more efficiently than clouds with fewer and bigger droplets [13,14]. However, concentration of aerosols in the atmosphere has been globally decreasing in the last decades, effectively reducing the cooling effect with time. Despite the large contribution of aerosols and land use, the most important factor that regulates global warming is the greenhouse gases.

1.3. GREENHOUSE GASES

The atmosphere of the Earth is composed of a 78% of nitrogen, a 21% of oxygen and a 0.9% of argon. The remaining 0.1% are trace gases, and among them, the greenhouse gases are found. The greenhouse gases are those gases that absorb and emit radiant energy in the thermal infrared range (wavelengths of 8-15 μm), and those that produce the greenhouse effect in our planet. The greenhouse gases in Earth's atmosphere are water vapour, carbon dioxide, methane, nitrous oxide, tropospheric ozone and the families of the chlorofluorocarbons (CFCs) and hydrofluorocarbons (HFCs). Other atmospheric pollutants, namely nitrogen oxides (NOx), volatile organic compounds (VOCs) and ammonia, are not considered direct greenhouse gases, but also contribute to the greenhouse effect by producing ozone and nitrous oxide by chemical reactions in the atmosphere.

Despite their low concentration in the atmosphere, greenhouse gases are crucial for the development of life in our planet, since without them the average temperature on the surface of the Earth would be around -18 °C, instead of 15 °C that we actually enjoy. However, since the beginning of the industrial revolution, human activity has progressively increased the concentration of greenhouses gases in the atmosphere, which has led to an enhanced radiative forcing that has notably boosted global warming (Table 1.1). At the current rate of emission of greenhouse gases, the increase in the average temperature of the Earth could reach 2 °C by the year 2036 [15].

Table 1.1. Current greenhouse gases concentrations.

Greenhouse gas	Pre-1750 tropospheric concentration	Recent tropospheric concentration	Increase since 1750, %	Radiative forcing increase, $W\ m^{-2}$
Carbon dioxide	280 ppm	400 ppm	42.9	1.94
Methane	722 ppb	1834 ppb	154.0	0.50
Nitrous oxide	270 ppb	328 ppb	21.5	0.20
Ozone	237 ppb	337 ppb	42.2	0.40

The contribution of each of the aforementioned greenhouse gases to the overall greenhouse effect mainly depends on the nature of the gas itself and its abundance in the atmosphere. However, since each greenhouse gas also possesses a completely different atmospheric residence time, the evaluation of that contribution is significantly imprecise. For this reason, a Global Warming Potential (GWP) value, which is calculated based on the efficiency of the gas as a greenhouse gas and its atmospheric lifetime, is assigned to each greenhouse gas. The GWP value is always calculated taking the greenhouse effect of carbon dioxide as the reference, and changes depending on the time scale taken for its determination. Thus, if a gas has a residence time longer than CO_2, its GWP will increase with time scale. The calculated GWP values of the most abundant greenhouse gases are shown in Table 1.2.

Table 1.2. Atmospheric lifetime and GWP values of the most abundant greenhouse gases.

Gas	Lifetime, years	Global Warming Potential for given time period	
		20 years	100 years
Carbon dioxide	30-95	1	1
Methane	12	84	28
Nitrous oxide	121	264	265
CFC-12 (CCl_2F_2)	100	10,800	10,200
Tetrafluoromethane	50,000	4,880	6,630
Hexafluoroethane	10,000	8,210	11,100
Sulphur hexafluoride	3,200	17,500	23,500
Nitrogen trifluoride	500	12,800	16,100

The atmospheric lifetime of water vapour is around 9 days. For this reason, atmospheric concentrations of this greenhouse gas are highly variable and largely depend on the temperature. That is the reason why water vapour is the only greenhouse gas that does not have GWP values assigned. Despite that, it is estimated that water vapour accounts for at least the 36% of the overall greenhouse effect in clear days and up to the 85% when clouds are taken into account [16]. In addition, due to its extremely short lifetime, anthropogenic emissions of water vapour have almost no effect on the overall greenhouse effect. However, human activity does have an indirect effect on this greenhouse gas, since the increase in the average temperature of the Earth increases water vapour concentrations, a process known as water vapour feedback [17].

1.3.1. Natural sources of greenhouse gases

Among all the greenhouse gases that exist, only water vapour, carbon dioxide, methane, nitrous oxide and ozone possess natural sources in our planet. The CFC and HFC families have an entirely anthropogenic origin. It is estimated that the global natural emissions of greenhouse gases sum up to 750,000 million tons of equivalent CO_2. However, most natural sources of emission are naturally balanced by sinks like photosynthesis in plants or incorporation into soil and oceans via the carbon cycle [18].

Carbon dioxide is the main by-product of animal and plants respiration. Besides, it is also released during the natural decay of organic matter and by the ocean-atmosphere exchange. Lastly, volcanic eruptions and wildfires also contribute to the natural emissions of carbon dioxide. The main natural sources of methane are the methanogenic Archaea found in wetlands, landfills and inside ruminants. Also, oceans are a great source of methane that is produced in deep sediment layers, where oxygen concentrations are low. Additionally, significant amounts of methane have been found trapped in the arctic permafrost, but due to the increase in the average temperature this methane is starting to release at a progressively increasing rate [19].

Bacteria in oceans and soils under vegetation produce most of the nitrous oxide emitted to the atmosphere, with a small amount being due to chemical reactions in the atmosphere, mainly the oxidation of ammonia. Finally, ozone is formed naturally by reaction of the oxygen with ultraviolet radiation from the sun in a specific part of the stratosphere called the ozone layer. Some of that ozone is regularly transported down to the stratosphere, where it can contribute to the concentrations of tropospheric ozone.

1.3.2. Anthropogenic sources of greenhouse gases

Only in the year 2017, the global anthropogenic emissions of greenhouse effect gases were 45261 million tons of equivalent CO_2, from which the 28% was emitted in China, the 15% in the United States and the 10% was emitted in the European Union [20]. These values are noticeably lower than the estimated emissions from natural sources, but unlike those, only a 40% of the total anthropogenic emissions are absorbed by the land and oceans and, therefore, the rest accumulates in the atmosphere.

According to the European Environment Agency, the sectors with the greatest contributions to the anthropogenic emissions of greenhouse gases in 2017 were the transportation (29%), the production of electric energy (27%), industry (20%) and agriculture (10%). From the total emissions of that year, 81% were direct CO_2 emissions, whose main emitting sectors were transport (35%), energy (33%) and industry (21%). Land use, however, acted as a CO_2 sink and, therefore, produced overall negative emissions accounting for around 8% of the total CO_2 emissions.

The main anthropogenic sources of methane emissions were biodegradation of organic matter from agriculture and enteric fermentation in livestock, which accounted for 53% of the total emissions. Besides, biogas from organic wastes (28%) and fugitive emissions from natural gas and coal mining (14%) significantly contributed to the total methane emissions. Agriculture was also the main emitting sector of nitrous oxide, accounting for 79% of the total emissions. Finally, emissions of F-compounds were almost exclusively due to industrial and manufacturing processes [21].

Since 2014, greenhouse emissions in the European Union from transport have been increasing. In comparison with 2016, emissions in 2017 increased by 2.2%, mainly due to increase in road transport and aviation. In 2017, road transport was responsible for 72% of the total greenhouse gas emissions from the sector, while 14% was due to aviation and 13% due to maritime transport. From the road transport emissions, 61% was due to passenger cars, 26% from heavy-duty vehicles (heavy trucks and buses) and 13% from light commercial vehicles [22]. Fuel combustion in the transport sector is also one of the main emitting sources of nitrogen oxides (NO_x) and volatile organic compounds (VOCs).

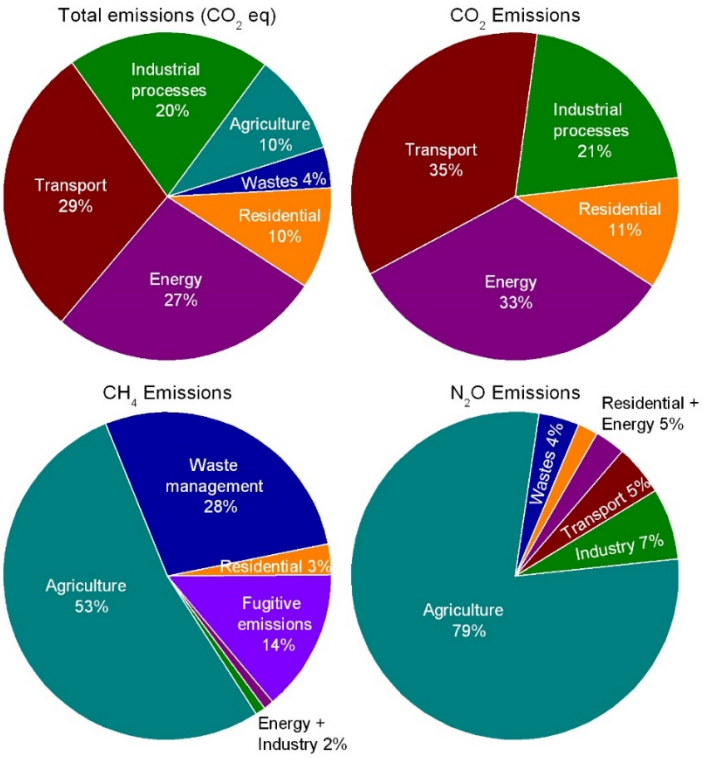

Figure 1.3. Anthropogenic emissions of greenhouse gases by sector.

1.4. MITIGATION OF EMISSIONS FROM TRANSPORT

It is estimated that there are more than 1,300 million vehicles in the world, and production rate has already reached the milestone of the 100 million units per year. In light of that situation, mitigation of emissions from transport seems a good working point for reducing the overall greenhouse effect gases in the overall.

In the European Union, air pollution from industry, road transport, domestic combustion and agriculture is legislated by the National Emission Ceilings Directive (2016/2284/EU). However, this directive only controls the emissions of atmospheric pollutants such as SO_2, NO_x, VOCs, CO, NH_3 or particulate matter. The goals for reduction of emissions of greenhouse gases were set out in 2011 by the White Paper for Transport, in the framework of the Effort Sharing Decision (406/2009/EU), which was later extended by the Effort Sharing Regulation (2018/842/EU).

The main goal contemplated in the White Paper was to reduce emissions of greenhouse gases from transport to a level that is below 60% that of 1990, which corresponds approximately to a level below 70% of the emissions of 2008. It also included an intermediate goal for 2030 of reducing greenhouse gases emissions from transport by 20% with respect of 2008 emission level.

Emissions of CO_2 from transport were in 2017 still 28% above the 1990 levels. This means that emissions will need to decrease by 66% by the year 2050 in order to meet the emissions reduction target set out by the White Paper [23]. For this purpose, several strategies for reduction of emissions are being developed, both in the EU and in the rest of the world. In general, three main strategic routes are being followed [24]:

1. **Traffic demand management**: These measures are aimed at decreasing traffic flow and reduce congestions. Promoting the use of public transport and healthy habits such as walking or biking for short journeys are also part of this strategy.
2. **Improvement of fuel efficiency**: These measures take the form of technological advances and mechanical improvement of the vehicles fleet, in order to minimise their fuel consumption.
3. **Alternative fuels and technologies:** A number of alternative fuels with lower emissions of CO_2 and other atmospheric pollutants are already available and under development.

Fuel diversification strategies have a huge potential for emission reduction in transport and indirectly contribute to solve some associated environmental problems such as oil dependence and urban air quality issues. Vehicles operating on gasoline and diesel have historically accounted for up to 99% of the total cars and trucks sales. However, sales of vehicles operated with alternative fuels, particularly electricity, are steadily growing each year. Other alternatives, already in the market are those that run on autogas (LPG), biodiesel, natural gas or hydrogen.

Each of the aforementioned alternative fuels has their own advantages and disadvantages, as shown in Table 1.3. Therefore, selecting an optimal choice can be a difficult task, since all of them offer different extents of emission reduction and entail challenges of various degrees of difficulty. However, if we pay attention solely to current availability and implementation capacity, then natural gas has to be the best option for low and medium-

term application since it is already widely available and the necessary technology for its use has already been proven and established.

Table 1.3. Advantages and disadvantages of alternative fuels.

Fuel	Advantages	Disadvantages
Electricity	Zero direct emissions	Low recharge point availability Renewability depends on electric mix
Hydrogen	Zero direct emissions Zero indirect emissions with renewable H_2	Low fuel availability Transport and storage still under development
Natural Gas	Lower emissions than traditional fuels High fuel availability	Low number of refuelling stations Control of emissions is costly
Autogas	Lower emissions than traditional fuels	Low number of refuelling stations Important safety issues in refuelling and in case of accident
Bioethanol and Biodiesel	Carbon neutral Renewable	Increases land use for crops Increases food prices

1.5. NATURAL GAS FOR VEHICLES

Natural Gas for Vehicles (NGV), also known as vehicular natural gas, is the denomination given to the natural gas applied as fuel for automotive. The use of natural gas as engine fuel dates back to 1930, but only started to be considered as a promising alternative fuel in the 1970s, due to the ongoing energetic crisis and the increase in oil prices. Since the increase in the oil price has continued in the 2000s, natural gas has progressively gained more and more popularity, especially for heavy-duty applications such as buses and trucks. Nowadays, there are approximately 28 million vehicles fuelled by natural gas and around 32,000 refuelling stations worldwide. In some countries, mainly Peru, Pakistan, Iran or Argentina, natural gas vehicles represent up to 25% of their total automotive fleet [25].

Natural gas for vehicles possesses the same composition as for domestic use, which means it is composed almost entirely by methane (up to 97%) mixed with small amounts of

ethane, propane, carbon dioxide and nitrogen. Natural gas engines for light-duty vehicles and passenger cars work following the Otto cycle, in a similar fashion as gasoline engines. The ignition of the air-fuel mixture can be provoked by spark plug, since the RON (Research Octane Number) of natural gas is around 120 [26]. For these reasons, gasoline engines can be retrofitted to work with natural gas, and dual-fuel (gasoline-NGV and diesel-NGV) applications are also possible. The only significant differences with gasoline engines are the way natural gas is stored and fed to the ignition chamber. In this sense, NGV is generally classified into two types, depending on the aggregation state in which natural gas is stored.

- **Compressed Natural Gas** (CNG) is stored in gas phase at ambient temperature and high pressure (200-250 bar) in a reinforced gas cylinder, and is directly fed to the ignition system controlled by a gas valve. It is more commonly applied for light-duty vehicles.
- **Liquefied Natural Gas** (LNG) is stored in liquid phase at low temperature (approximately -162 °C) and ambient pressure in an insulated storage tank, and has to be regasified before feeding it to the ignition chamber. Since it involves a higher structural complexity, it is frequently limited to heavy-duty vehicles and trucks.

1.5.1. Advantages and drawbacks

Natural gas presents numerous environmental and economic advantages in comparison with traditional liquid fuels (gasoline and diesel), even though it is also a fossil fuel. Firstly, natural gas is relatively abundant. Some estimations value the world reserves of natural gas to be enough for more than 200 years at least, at current production and consumption rate [27]. Therefore, short and medium-term availability is not an issue.

Natural gas is also considered the cleanest available fossil fuel. Methane, the main component of natural gas, possesses the lowest C/H ratio (0.25) among all the hydrocarbons, including those composing gasoline and diesel. For this reason, vehicles fuelled with NGV produce between 20 and 30% less CO_2 emissions per kilometre than traditional fuels. In addition, natural gas has a lower adiabatic flame temperature than gasoline or diesel, and thus, inherently emits less NO_x than these fuels, achieving reductions of up to 50-80% with respect to conventional fuels. Finally, since natural gas contains very little amount of sulphur, it emits almost no sulphur oxide, and being a gaseous fuel, it mixes more easily with air. As a result, it burns more cleanly, leading to

virtually no emissions of particulate matter and very low emissions of unburned non-methane hydrocarbons [28-30].

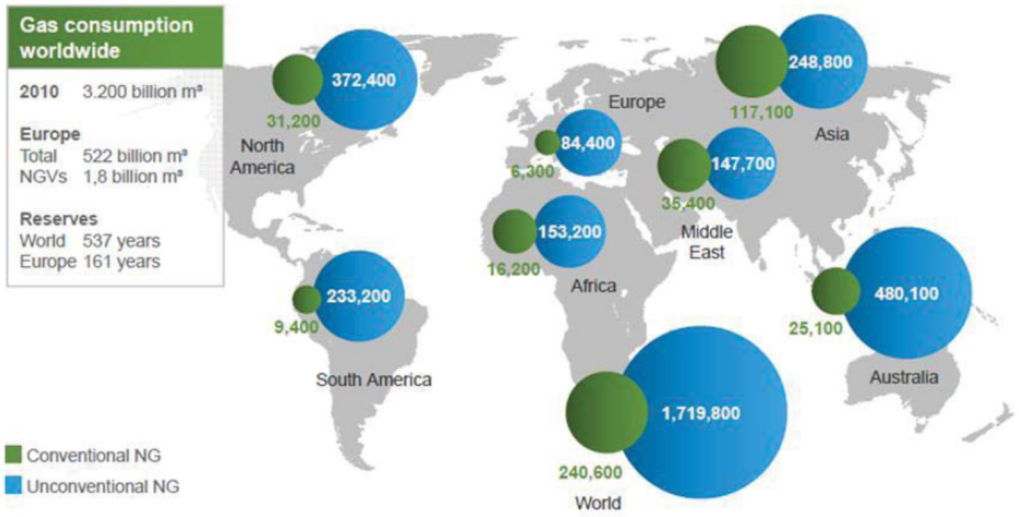

Figure 1.4. Worldwide natural gas reserves at 2010 [27].

At an economic level, engines fuelled by natural gas are only slightly more expensive than those fuelled by liquid fuels, mainly due to the need of making the engine block airtight and the structural requirements of the fuel storage systems. Nevertheless, this higher cost is usually offset by the lower cost of natural gas. Furthermore, owing to the lower combustion temperatures, the absence of soot formation and contamination of the lubricating oil, maintenance costs of natural gas engines are significantly lower than those of gasoline and diesel engines [31].

The general public perception of NGV, especially in its compressed form, is that it is more unsafe than the traditional fuels, when in reality natural gas vehicles are actually much safer than those powered by liquid fuels in the case of an accident. In its natural form, natural gas is odourless, so as a safety measure the gas is odorised prior to distribution to allow for its easy detection in the case of a leak, at concentrations as low as 0.3%. Natural gas requires a concentration between 5 and 15% in air for combustion to occur, meaning that the gas can be detected well before combustion conditions are reached.

Moreover, natural gas has a higher autoignition temperature (around 600 °C) than gasoline (around 320 °C), and the fact that is lighter than air enhances its safety. This means that, while making a lot of noise when escaping, the high pressure forces the gas to escape very quickly causing high concentrations of gas to build up. This and the natural tendency to dissipate upwards make it very unlikely that the gas will ignite before completely dissipating in the atmosphere.

However, despite all the clear advantages over traditional fuels, implementation of natural gas as an alternative fuel is still limited. This limitation responds mainly to three factors. Firstly, the aforementioned public perception of unsafety of natural gas, even when it has been demonstrated to be safer than liquid fuels. This sense of unsafety makes drivers reluctant to consider natural gas vehicles as an option when buying a new car. Secondly, the relatively low amount of refuelling stations in place nowadays increases the need for more route planning when driving a natural gas vehicle. That also adds to the reticence caused by the first factor. The last factor, which slows down the production and availability of natural gas vehicles, is the fact that burning of natural gas is not complete in an internal combustion engine owing to the fact that it is a slow process. For this reason, there is a certain amount of unburned methane in the exhaust gases from the engine that needs to be removed before venting them to the atmosphere, due to the high global warming potential of methane. Euro VI emission standards for heavy-duty vehicles fuelled with natural gas impose an emission limit of 0.5 $g\,kW^{-1}\,h^{-1}$ of methane [32]. This makes necessary the addition of an aftertreatment system to the exhaust pipeline, to allow for removal of this unburned methane.

1.5.2. Technologies for methane removal

There are a number of different strategies available for reducing methane emissions in various industrial and transport applications. Usually, emission-reducing measures can be classified into primary and secondary, similarly to those technologies that are used for volatile organic compounds. Following this classification, primary measures are those that are applied to the equipment, raw materials or process that generates the emissions, with the aim of improving them and reducing their associated emissions. When applied to natural gas engines, these measures take the form of mechanical improvements on the engine such as the optimisation of the crevice volume and the minimisation of the scavenging flows, improvements in the fuel storage and injection systems to prevent or

minimise leaking, as well as optimisation of the ignition timing and the exhaust gas recirculation (EGR) [33].

On the other hand, secondary measures are focused on removal of the residual methane that remains after the combustion of natural gas in the engine. These measures are normally divided into two types of technologies, namely, recovering technologies and destructive technologies. Recovering technologies are those that retain or accumulate the methane from the flue gas in order to obtain a methane-rich stream that can be reutilised as a fuel, while destructive technologies convert methane into other compounds with less global warming potential, generally CO_2.

Among the recovering technologies, there are some that are also used for VOCs removal, such as adsorption, condensation or membrane separation. However, taking into account that typical concentrations of methane in the exhaust of NGV engines do not exceed 1% in volume, this type of techniques are deemed not suitable for natural gas engines. Destructive technologies, on the contrary, are generally well suited for this application.

Mainly, three technologies can effectively remove methane and VOCs from gaseous streams at low concentrations: biofiltration, thermal oxidation and catalytic oxidation. However, biofiltration is only effective for very low concentrations of methane, around 2 ppm, although it has been tested with concentrations up to 300 ppm [34], due to the low water solubility and biodegradability of methane. Besides, it requires excessively large reactor volumes to treat high gas flows.

Thermal oxidation, on the other hand, is a proven technology, already in use for removal of methane and VOCs in various applications such as biogas from landfills, ventilation air methane and coal mine methane from coal mines, or deodorisation in various different industries. Thermal oxidation can treat streams with methane concentrations as low as 0.5% in volume and can be coupled with an energy recovery system whose efficiency mainly depends on the concentration of methane in the feedstream [35]. However, the temperature required to achieve complete thermal oxidation of methane is normally around 1,000 °C. This means that thermal oxidation systems treating low concentrations of methane require either compression or the addition of a secondary fuel to operate. This generally advises against this technique for application in mobile sources [36].

Finally, catalytic oxidation is essentially an upgrade of thermal oxidation, where a suitable catalyst is added to lower the temperature required for complete oxidation of methane. Since the addition of the catalyst can take the reaction temperature down to the thermal level of the exhaust gases, this technique can be implemented in vehicles and other mobile sources without the need of compression or a secondary fuel. For this reason, catalytic oxidation is considered the most suitable technology to control the methane emissions of natural gas engines.

1.6. CATALYTIC OXIDATION OF METHANE

Catalytic oxidation is the most commonly used technique to control methane emissions in mobile sources. This aftertreatment is considerably more difficult than that of other light hydrocarbons such as propane or butane. Consequently, methane is considered a model molecule, since its complete elimination also ensures the removal of many other organic compounds. The reason for this lies in the high stability of the methane molecule due to the strong covalent C-H bonds of the methane molecule (bond energy is around 450 kJ mol^{-1}).

The combustion of methane requires the activation of the C-H bonds in the methane molecule, which in turn require high reaction temperatures. However, the thermal level of the exhaust from a natural gas engine during normal operation does not exceed 500-550 °C, well below the range for the purely thermal activation of C-H bonds. Therefore, the selected catalysts are required to exhibit very high activity at relatively low temperatures, while also maintaining an excellent selectivity towards CO_2. In addition to that, the severe conditions under which the reaction must occur (Table 1.4) only add to the complexity of the challenge. The low concentrations of methane in the reaction stream (below 1%) limit the acceleration of the reaction provoked by the heat release of the exothermic combustion, which is an important factor when working with more concentrated streams. Further, the presence of concentrations of up to 10% of water vapour and CO_2 (and other pollutants in smaller concentrations) may induce an important deactivation effect on the chosen catalyst, limiting both its activity and lifetime [37-39].

Table 1.4. Parameters of a reaction unit for lean methane oxidation.

Compound	Concentration
CH_4	0.1 – 1%
CO	2,000 – 8,000 ppm
H_2O	8 – 10%
CO_2	8 – 10%
O_2	10 – 12%
N_2	Balance
GHSV	30,000 – 50,000 h^{-1}
Temperature	250-550 °C

The combustion of methane can produce CO_2 and/or CO, depending on the air/methane ratio. The complete combustion (Eq. 1.1) is favoured in the presence of excess oxygen and thus, working with high O_2/CH_4 ratios increases selectivity towards CO_2 formation.

$$CH_4 + 2O_2 \longrightarrow CO_2 + 2H_2O \quad (1.1)$$

$$CH_4 + \frac{3}{2}O_2 \longrightarrow CO + 2H_2O \quad (1.2)$$

Despite being simple, the specific mechanisms that these reactions follow are relatively complex, and strongly dependent both on the nature of the catalyst and the reaction temperatures. Other side reactions may also be involved to a greater or lesser extent. These may include steam reforming (Eq. 1.3), hydrogen combustion (Eq. 1.4) or the water-gas shift reaction (Eq. 1.5).

$$CH_4 + H_2O \longrightarrow CO + 3H_2 \quad (1.3)$$

$$2H_2 + O_2 \longrightarrow H_2O \quad (1.4)$$

$$CO + H_2O \longrightarrow CO_2 + H_2 \quad (1.5)$$

The extent of these reactions is usually small, on account of the high temperatures required for them to occur. For instance, steam reforming is only relevant at temperatures exceeding 550 °C, while water-gas shift reaction temperature greatly varies with the chosen catalyst. In general, it is accepted that carbon monoxide formation is more favoured at higher temperatures [40,41].

Overall, the main operational parameter defining the efficiency of the catalytic combustion of methane is the design of a suitable active catalyst. This catalyst must be able to operate

at relatively low temperatures and resist deactivation by sintering and the aforementioned presence of water vapour and other pollutants in the stream, while also maintaining its activity over prolonged combined operation periods and the cyclic start-stop nature of automotive catalysts.

Catalytic combustion of methane and other hydrocarbons has been extensively investigated in view of its evident environmental and economic benefits. Research on catalytic combustion has been mainly focused on the design and development of materials with higher activity for the oxidation reaction, but research work on the kinetics and mechanistic aspects of the reaction itself has been also made. A significant number of different materials have been proven active for oxidation of hydrocarbons at relatively low temperatures. However, for methane oxidation, research has traditionally focused on noble metals.

1.6.1. Noble metal-based catalysts

Noble metals, namely platinum, palladium, gold, rhodium and iridium, were the first materials considered as suitable catalysts for methane oxidation, because of their high activity for the oxidation of other hydrocarbons. In the case of complete oxidation of methane, palladium and platinum have been the most investigated precious metals. With time, research has found out that palladium is significantly more active than platinum [42,43]. Since then, research has concentrated on Pd as the active phase, with the Pd/Al_2O_3 catalytic system being the most studied among all [44,45].

The Pd/Al_2O_3 samples, with Pd loadings between 1 and 10%wt., have been widely reported to show measurable methane conversions at temperatures as low as 300 °C, with complete conversions below 480 °C and full selectivity towards CO_2 formation [46]. Regarding prolonged time operations, however, results have showed a much greater variability. Some studies have evidenced steady increases in activity with time on stream [47], while others have revealed the occurrence of both reversible and irreversible deactivation processes affecting this type of catalyst [48,49].

The activity of supported palladium-based catalyst depends on many factors such as the Pd loading, the nature of the support, the calcination temperature, the metallic precursor used, the morphology of the Pd crystallites or the catalyst pretreatment, among others. Despite the extensive research carried out on this topic, there is still some divergence

regarding the exact identity of the active phase for methane oxidation. So far, both Pd [50], PdO [51] and a mixture of Pd/PdO_x [52] have been regarded as the most active phases, and debate on this question continues today. Also, numerous works have identified a strong correlation of the activity with the Pd crystallite size, which seems to affect the mobility of their oxygen species and the oxidability of the Pd crystallites [53,54]. Again, the exact nature of this dependence is still under discussion.

Finally, the kinetic mechanism followed by the methane oxidation reaction also is controlled by the specific nature of the active phase, and the O_2/CH_4 ratio to some extent. When Pd is considered the active phase, both Langmuir-Hinshelwood [55] and Eley-Rideal [56] mechanisms have been proposed to explain the behaviour of the catalyst. When oxidised phases (PdO and PdO_x) have been taken as active, the Mars-van Krevelen mechanism [57] has also been considered as an appropriate mechanistic model. Given that all different phases of palladium seem to be active for methane oxidation, although at different temperatures and with varying efficiency, it is possible that the real mechanism is a complex conglomerate of the aforementioned three pathways, which explains the contradictory results obtained by some studies.

Despite the remarkable results shown by noble metals and specifically palladium-based catalysts, a number of drawbacks reduce their potential for extensive implementation. Firstly, commercial palladium-based catalysts for methane oxidation require metallic loadings around 2-4 %wt. to achieve proper removal of methane from the exhaust of NGV engines. Comparatively three-way catalysts for gasoline engines require metallic loadings of around 0.1-0.5%wt. [58,59]. This, coupled with the high price (around 70,000 € per kg) and low availability of palladium, drastically increases the cost of these catalytic systems.

Moreover, palladium-based catalysts are sensitive to deactivation by sintering, due to the strong dependency of activity on the palladium crystallite size, and by the presence of sulphur and water vapour in the reaction stream [60,61]. Sulphur poisoning is generally not a problem in the exhaust of natural gas engines, due to the low sulphur content of natural gas. However, the presence of water vapour is unavoidable, and thus, if the catalytic performance is inhibited by this compound, the corresponding activity can be severely penalised upon operation under real conditions. Regarding this, some studies have revealed that palladium-based catalyst suffer two different deactivation processes: a fast reversible inhibition due to adsorption of water molecules onto of the active sites, and a

slow irreversible deactivation due to hydroxylation of the surface of palladium nanoparticles to form a stable phase of PdOH [62,63].

As a consequence of all this, the lifetime of palladium-based catalysts operating with the exhaust of natural gas engines is rather limited. This increases the frequency of required maintenance and substitution operations, further increasing the cost of these systems. For this reason, the development of alternative, cheaper materials that can also act as active catalysts for methane oxidation has been an important subject in the last years, due to the potential for reduction of costs in aftertreatment systems and, hence, increasing the attractiveness of the NGV engines. Among all the alternative catalysts investigated, those based on transition metal oxides are the most promising.

1.6.2. Transition metal oxides

Metal oxides have many important applications in oxidation catalysis, mainly because metals, and more specifically transition metal elements, generally possess multiple oxidation states and the capacity to switch between them with relative ease. This allows them to take part in redox cycles between their low and high oxidation states and, at the same time, confers the oxygen ions in the lattice with mobility, allowing them to be released and restored [64]. In addition, compared with noble metals, transition metals are much more abundant, which makes them remarkably cheaper as well.

Generally, oxides of transition metals exhibit a lower intrinsic activity than noble metals, although they also tend to present a higher resistance to thermal deactivation and poisoning. Moreover, the specific properties of transition metals-based catalysts can be tuned by changing their formulation, to adapt to different reactions, further closing their activity gap with the catalysts derived from noble metals. In this sense, transition metals can be used in the form of single oxides or as mixed oxides with different crystalline structures, which normally depend on the metallic formulation and the synthesis route. Regarding catalytic oxidation of methane, materials such as perovskites, hexaaluminates and spinels have been proven active to variable extent.

- Single oxides:

The oxides of transition metals such as copper, manganese, nickel, chromium or cerium have been extensively investigated as oxidation catalysts for methane, due to their low cost and simplicity, both in their bulk form and supported over some other materials. Among the single oxides, copper oxide seems to be one of the most active for both carbon monoxide and methane combustion, especially when supported over porous materials such as alumina or zirconia, since its bulk form possesses extremely poor structural properties [65]. It is widely accepted that, despite being mainly in its oxidised form, the most active phase of supported CuO catalysts are the isolated metallic Cu species of the surface [66,67].

Manganese oxides (MnO_x) also show a good behaviour in oxidation reactions, owing to the highly variable electronic structure of manganese giving it a notable oxygen storage capacity. Moreover, due to their easy phase-transformation capabilities, multivalent manganese oxides (MnO_2, Mn_2O_3) with high oxygen contents are formed when synthesising catalysts based on manganese [68,69]. On the other hand, cerium oxide, also known as ceria, has attracted extensive attention due to its high reducibility and oxygen storage capacity. However, as a consequence of the significant selectivity towards CO formation showed by bulk ceria catalysts, this material is normally not used as single oxide, and is more commonly doped with other metals, such as nickel, or used as a dopant for other catalysts [70,71].

Finally, nickel and chromium-based catalysts have also been examined, but their respective activities for complete methane oxidation have been regarded as inferior compared with the rest of the previously described metals, and also present some additional drawbacks [72]. In particular, nickel-based catalysts tend to show CO formation via reforming reactions, and chromium oxides tend to be difficult to handle due to the threat of hexavalent chromium.

- Perovskites:

A perovskite is any material with a similar crystal structure as calcium titanate ($CaTiO_3$), which is the mineral known by that name. Usually, a perovskite is any mixed oxide that follows the general formula ABO_3, where A is a large cation with a dodecahedral coordination and B is a smaller cation with a six-fold coordination. The large amount of

different elements that can be chosen as A and B make perovskites very versatile materials, which can be used as catalyst for many different reactions besides methane oxidation [73]. Perovskite mixed oxides can be synthesised by various methods, with the most commonly used being the citrate method, sol-gel complexation and co-precipitation [74]. However, these methods always involve high temperature solid-state reactions, and as a result, the textural properties of the resulting materials are generally poor.

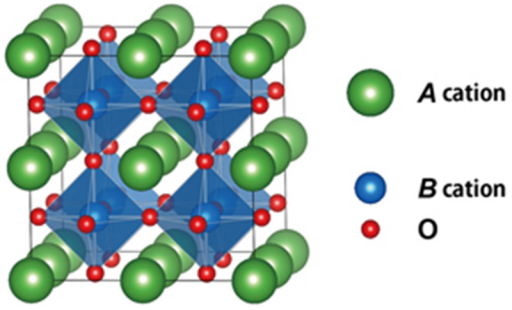

Figure 1.5. Crystal structure of a generic perovskite.

For the ideal structure ABO_3, methane combustion activity is mainly influenced by the B cation. Most studies have investigated combustion of methane over perovskites with manganese, cobalt and iron in the B site, whereas for the A site, which is normally occupied by a lanthanide metal, lanthanum has been the most frequently utilised metal. Accordingly, the most studied perovskite structures has been $LaMnO_3$, $LaFeO_3$ and $LaCoO_3$, all of which have been found to be active for methane oxidation with different degrees of efficiency [75-77].

Furthermore, the perovskite structure can be also partially substituted with other elements to improve its catalytic performance. Substitution of cations from the perovskite lattice can occur on A sites, B sites, or both simultaneously and can lead to drastic modifications of the properties with respect to the unsubstituted counterpart. Substitution of perovskite structures can be made with other non-noble metals, such as strontium or calcium [78,79], or can be made by doping with small amounts of noble metals such as palladium or silver [80,81].

- Hexaaluminates:

Hexaaluminate mixed oxides are a family of hexagonal aluminate compounds with a peculiar structure that gives them some interesting properties, the main one being their exceptional resistance to sintering. Hexaaluminates present the general formula $AAl_{12}O_{19}$ where A can be a cation of an alkali or an alkaline earth element. The extraordinary thermal resistance of these materials arises from their unique layered structure, consisting of alternate alumina blocks in mirror planes where the A cations are located [82]. Despite their lower performance compared with noble metals or perovskites for low temperature catalytic oxidation, hexaaluminates have gained increased attention for high temperature applications because of their resistance to sintering [83].

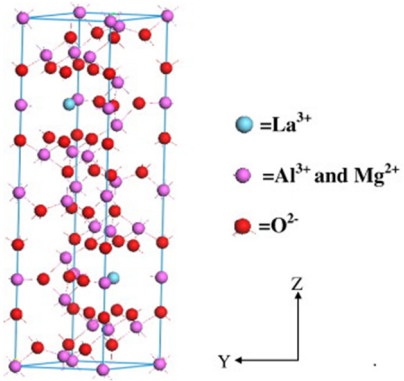

Figure 1.6. Crystal structure of a lanthanum hexaaluminate.

Most works so far have focused on methane combustion over lanthanum and barium hexaaluminates, with the latter being the most studied one, since it can retain relatively high specific surface areas (around 20 $m^2 g^{-1}$) at temperatures as high as 1200 °C [84]. In view of this relevant property, hexaaluminates are regarded as a promising catalytic material for high-temperature applications such as catalytic combustion, partial oxidation, dry reforming or N_2O abatement [85,86].

Furthermore, the catalytic activity of hexaaluminates can be improved by partially substituting Al^{3+} cations with a transition metal, hence obtaining $AB_xAl_{12-x}O_{19}$-like structures with an additional active phase [87]. However, hexaaluminates are generally less tolerant for partial substitution than perovskites, and tend to lose surface area in the process due to the destabilisation of the hexaaluminate lattice [88].

- Spinels:

Spinel oxides are a class of complex oxides with a crystal structure similar to the one possessed by the mineral "spinel", which is composed of magnesium aluminate ($MgAl_2O_4$). Hence, a spinel oxide is any mixed oxide that follows the general formula AB_2O_4, where A is a divalent cation and B is a trivalent cation. Spinels crystallise in a cubic structure with oxide anions arranged in a cubic closed-packed lattice (fcc) [89].

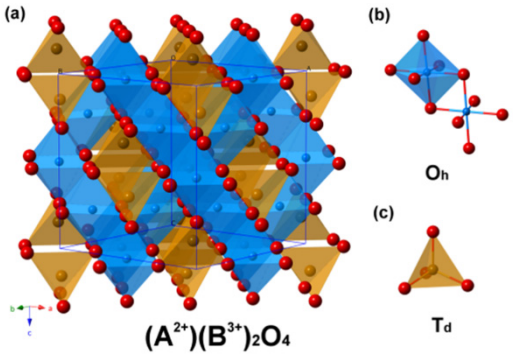

Figure 1.7. Crystal structure of a generic spinel.

One of the most interesting properties of spinel oxides is the wide range of cation distributions that this system can accommodate. In the ideal spinel structure, also known as "normal" spinel, the divalent A cations occupy one-eight of the tetrahedral sites, while trivalent B cations occupy half of the octahedral sites [90]. However, some spinels can exhibit an "inverse" spinel distribution, where the tetrahedral voids are occupied by B cations, while both A and B cations occupy octahedral voids. Also, intermediate structures with formula $(A_{1-x}B_x)[A_xB_{2-x}]O_4$ can exist. In these cases, cations in parenthesis occupy tetrahedral sites, while cations in square brackets occupy octahedral sites. The value x is known as the "inversion degree", and can range from 0 for a normal spinel to 1 for an inverse spinel [91]. The inversion degree of a particular spinel mainly depends on the synthesis method and varies with the calcination temperature used to obtain the spinel [92].

Compared with the rest of the previously described mixed oxides, spinel oxides possess a substantially higher degree of structural flexibility, allowing cations in them to participate in redox cycles with relative ease. The spinel structure can accommodate almost any metal

capable of existing in the +2 or +3 oxidation states. Thus, the alkali and alkaline earths and a major part of the transition metals can form spinel oxides. Moreover, the same element can occupy both A and B sites in the general formula. Hence, single oxides such as Fe_3O_4, Mn_3O_4 or Co_3O_4 are also spinel oxides. The easiness that cations in spinel structures show for switching between oxidation states, gives oxygen species within the crystal lattice an extraordinary mobility, which enables them to react at low temperatures [93]. Therefore, this results in lower light-off temperatures for oxidation reactions with respect to perovskites and hexaaluminates. For these reasons, spinel oxides are the most studied among the mixed oxides for oxidation of CO, methane and other hydrocarbons.

1.6.3. Cobalt spinel oxide

Among the enormous variety of spinel oxides, those based on cobalt are regarded as the most active for oxidation reactions. Specifically, the spinel type cobalt oxide (Co_3O_4) is considered the most versatile, and has been extensively investigated for various applications such as CO oxidation below and above room temperature [94], N_2O decomposition [95], oxidation of VOCs and chlorinated VOCs [96,97], gas sensing [98], pigments for ceramics [99], or solar energy absorbers [100], among others.

The main reason behind the increasing attention on Co_3O_4 is its strong Co^{3+}/Co^{2+} redox system that gives oxygen ions in its lattice an extreme mobility, allowing for a relatively easy reduction of Co_3O_4 to CoO and subsequently to metallic Co, as well as an easy reoxidation back to its initial form. According to the available bibliography, methane oxidation over Co_3O_4 follows the Mars-van Krevelen mechanism. This means that methane is actually oxidised by the oxygen species from the cobalt oxide lattice, generating oxygen vacancies and consequently reducing the Co^{3+} ions to Co^{2+}. Then, the oxygen from the gas phase refills the oxygen vacancies provoking the subsequent reoxidation of the Co^{2+} back to Co^{3+} [101]. The structural flexibility of Co_3O_4 entails a good functioning of this redox cycle, which is the key property for the remarkable activity of this material for methane oxidation.

Table 1.5. Recent research studies on methane combustion over noble metal-free Co_3O_4-based catalysts.

Catalyst	Synthesis method	Space velocity	T_{50}, °C	Reference
Mn_xCo_y	Hydrothermal	30,000 h^{-1}	326	[104]
Co_3O_4	Hydrothermal	21,000 $cm^3 g^{-1} h^{-1}$	500	[105]
Co_3O_4/SiO_2	Hydrothermal	30,000 $cm^3 g^{-1} h^{-1}$	400	[106]
Co_3O_4	Precipitation	18,000 $cm^3 g^{-1} h^{-1}$	345	[107]
$Co_3O_4/SmMn_2O_5$	Deposition-precipitation	60,000 $cm^3 g^{-1} h^{-1}$	390	[108]
Co_3O_4-Mn_x	Hydrothermal	30,000 $cm^3 g^{-1} h^{-1}$	360	[109]
Co_3O_4	Hydrothermal	30,000 $cm^3 g^{-1} h^{-1}$	350	[110]
Co_3O_4	Precipitation	12,000 $cm^3 g^{-1} h^{-1}$	292	[111]
$CoFe_x$	Solution combustion synthesis	6,000 $cm^3 g^{-1} h^{-1}$	525	[112]
Co_3O_4/HZSM-5	Incipient wetness impregnation	36,000 $cm^3 g^{-1} h^{-1}$	525	[113]
Co_3O_4	Hydrothermal	18,000 $cm^3 g^{-1} h^{-1}$	300	[114]
Co_3O_4	Hydrothermal	110,000 h^{-1}	350	[115]
Co_3O_4/CeO_2	Ultrasound Impregnation	18,000 $cm^3 g^{-1} h^{-1}$	260	[116]
Co_3O_4/γ-Al_2O_3	Incipient wetness impregnation	36,000 $cm^3 g^{-1} h^{-1}$	600	[117]
Co_3O_4/CeO_2	Citrate sol-gel	30,000 $cm^3 g^{-1} h^{-1}$	400	[118]
Co_3O_4-SnO_2	Co-precipitation	18,000 $cm^3 g^{-1} h^{-1}$	420	[119]
Co_3O_4/SBA-15	Impregnation	20,000 $cm^3 g^{-1} h^{-1}$	506	[120]
Co_3O_4-CeO_2	Co-precipitation	60,000 $cm^3 g^{-1} h^{-1}$	455	[121]
Co_3O_4/γ-Al_2O_3	Solution combustion synthesis	15,000 h^{-1}	325	[122]
Co_3O_4/Ce-Zr	Incipient wetness impregnation	12,000 h^{-1}	480	[123]
Co_3O_4/γ-Al_2O_3	Impregnation	6,600 $cm^3 g^{-1} h^{-1}$	›500	[124]
Co_3O_4/CeO_2			340	
Co_3O_4/ZrO_2			495	

Nevertheless, catalytic activity of Co_3O_4 for methane oxidation is relatively reduced at low temperatures, and is profoundly affected by various parameters, such as the synthesis method, the calcination temperature, the nanomorphology and exposed crystal facets or the presence of moisture or other impurities on its surface, among many others [102,103].

Spinel type cobalt oxide can be synthesised by a wide number of both dry and wet synthetic routes, such as basic precipitation [125], sol-gel complexation [126], freeze-drying [127], spray pyrolysis [128], solution combustion synthesis [129], reactive grinding [130], or simple calcination of a cobalt salt [131]. At temperatures higher than 300 °C, any cobalt precursor will partially oxidise and convert into cobalt oxide, although if the temperature exceeds 900 °C, Co_3O_4 reduces back to cobalt (II) oxide (CoO). The selection of the most appropriate synthesis route and calcination temperature can produce a cobalt oxide catalyst with optimal structural and textural properties, which can help promoting its performance at low temperatures.

Besides, nowadays many studies have evidenced a clear morphology effect for the combustion of methane over Co_3O_4 nanostructures. Moreover, some specific crystal planes have been shown to be much more active than others, mainly due to their different content of Co^{3+} and Co^{2+} ions [132,133]. Cobalt oxide catalysts with controlled nanomorphology are some of the most active catalysts ever found for methane oxidation, but present two major drawbacks. Their synthesis routes are generally complex and very difficult to upscale for industrial production. Additionally, the complex nanomorphologies that give them their extremely high activity are also very sensitive to high temperatures. Thus, these catalysts tend to exhibit a very low thermal resistance.

1.7. OBJECTIVES AND LAYOUT

The ongoing climate change has forced European and international institutions to develop treaties and policies that demand more control over the emissions of greenhouse effect gases. The transport sector, being the one with the largest emissions of greenhouse gases and other atmospheric pollutants, provides some very good opportunities for the reduction of the overall emissions. In this sense, fuel diversification strategies are starting to promote the use of alternative fuels, as a way to move away from the traditional fuels and start the transition to a future zero-emissions mobility.

One of the most promising of these transition technologies is natural gas, due to its lower CO_2 and NO_x emissions, higher availability and lower cost, compared with gasoline and diesel. However, natural gas engines also require a strict control of the unburned methane emissions, owing to its high greenhouse effect potential. For this purpose, catalytic oxidation is the most suitable available technology. Traditionally, catalysts for methane oxidation have been based on supported noble metals, mainly palladium, since they exhibit a high activity at low temperatures. However, these catalysts that can contain up to 4%wt. of palladium, are remarkaly expensive and their activity decreases with time due to sintering and the presence of water vapour. Consequently, the development of alternative catalysts based on transition metal oxides, which are much cheaper, is an interesting challenge.

This thesis proposes the development of noble metal-free cobalt oxide-based catalysts with improved properties that can serve as an alternative to precious metal-based catalysts for the control of methane emissions in natural gas engines. The starting hypothesis of this research work is that spinel-type cobalt oxide is active for the oxidation of residual methane from compressed natural gas engines. However, the catalytic activity of this material at low temperatures is not enough to substitute noble metals, and it requires more research efforts to optimise catalyst formulations for real applications.

Accordingly, three main objectives have been defined in this thesis. First, defining the optimal synthesis methods for cobalt oxide catalysts. This initial study has been carried out for bulk pure and doped (manganese, iron, nickel, copper, zinc and cerium) Co_3O_4 catalysts. The examined preparation routes have been chosen among those that can be more easily upscaled and applied industrially. Second, intensive efforts have been made in indentifying, on one hand, the most suitable porous support for Co_3O_4 catalysts, and on the other hand, in improving the catalytic behaviour of the supported samples by analysing the influence of various promoters, namely magnesium, nickel and cerium. Third, optimising the formulation by incorporating the optimal catalytic system onto an open cell foam leading to an efficient structured catalyst that can be easily implemented in a NGV-based engine.

The research methodology followed for each of the previous milestones has been based on three main experimental tasks: first, the synthesis of the different formulations of cobalt-based catalysts including bulk, powdered and open cell foam structured samples.

Secondly, the extensive characterisation of the resulting materials by a wide number of analytical techniques (WDXRF, ICP-AES, N_2 physisorption, XRD, UV-vis-NIR DRS, Raman spectroscopy, XPS, H_2-TPR, O_2-TPO, CH_4-TPRe, SEM, HAADF-STEM coupled to EDX and/or EELS and (HR)TEM) in order to thoroughly determine their structural, textural, chemical and redox properties; and finally, the analysis of the behaviour of the synthesised catalysts in terms of their activity, selectivity and stability under dry and humid conditions. The comparison between the characterisation and kinetic results will allow for the determination of the key parameters defining the catalytic performance of the synthesised materials. It should be pointed out that a part of the experimental work was carried out by the candidate in the laboratories of Prof. Andrzej Kotarba's research group (Materials and Surface Chemistry Group) at the Faculty of Chemistry, Jagiellonian University, Kraków, Poland.

The proposed optimal catalyst should show a good performance for methane oxidation under similar conditions as those found in the exhaust of a natural gas engine. The catalyst should be active at moderate temperatures (around 500 °C) with complete selectivity towards CO_2 formation and its activity should not be significantly affected by the presence of important amounts of "spectators" such as water vapour. The global objective of this work is that the behaviour of the proposed optimised catalysts justifies the substitution of noble metal catalysts in real applications, taking into account their respective performances and costs.

This thesis work has been structured in nine chapters. An overview of the content of the chapters, excluding those related to the nomenclature and cited literature, is shown in the following concept map (Figure 1.8).

Chapter 1 discusses the causes and effects of the ongoing climate change, as well as the sectors of human activity that are responsible for the largest contribution to the emissions of greenhouse effect gases. Likewise, the current European directives and emission reduction strategies for transport are reviewed, and the most common available technologies for controlling emissions from mobile sources are described. The chapter ends with the analysis of the state of the art of catalytic oxidation of methane, as the most suitable technique for the control of emissions of unburned methane from natural gas engines, and a review of the most promising alternatives to noble metal catalysts, including Co_3O_4-based catalysts.

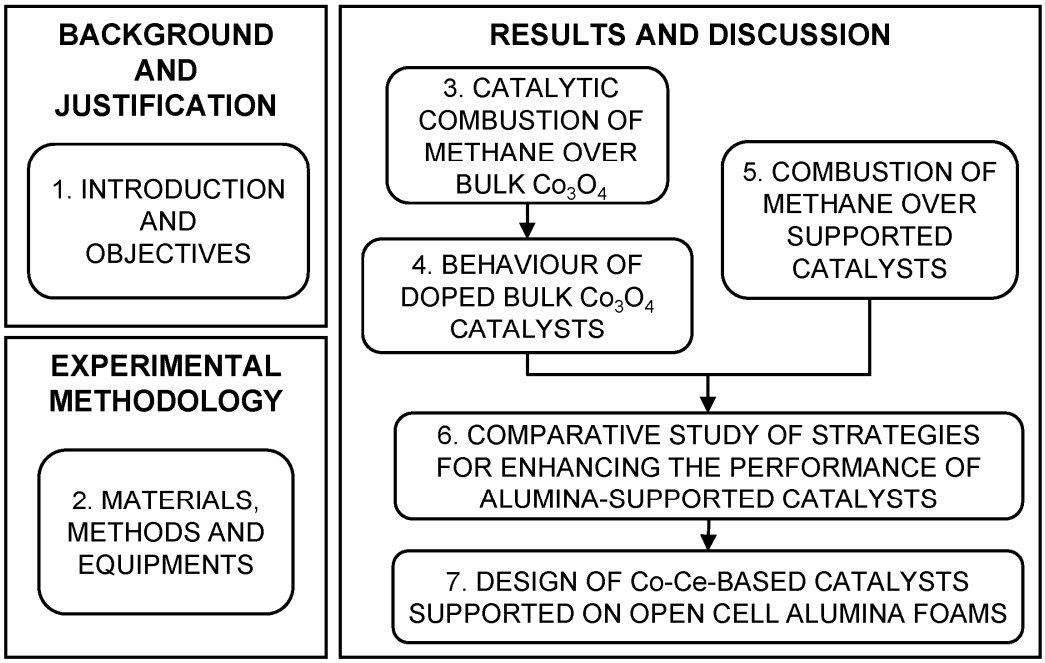

Figure 1.8. Concept map of the chapters of the thesis work.

Chapter 2 describes the materials and reagents used in the different synthetic routes used during the thesis work. In addition, this chapter presents the theoretical basis of each of the employed characterisation techniques and a brief description of the equipments used to examine the main physico-chemical properties of the synthesised catalysts. Finally, the reaction unit used for the examination of the catalytic behaviour is thoroughly detailed.

Chapters 3 and 4 focus on the design of highly efficient bulk Co_3O_4 catalysts. Thus, in Chapter 3 main efforts are devoted to the analysis of the effect of the synthesis route. In addition, the influence of the calcination temperature on the catalytic performance is evaluated. Chapter 4 deals with the promotion of the catalytic efficiency by doping with other metal (Mn, Fe, Ni, Cu and Ce) and the determination of the optimal loading of the promoter.

In Chapter 5, the most suitable material for supporting the cobalt oxide is determined, among a selection of the most commonly available supports (gamma alumina, magnesia and ceria). Then, the cobalt loading is optimised, and the key parameters that control the

performance of this type of catalysts are identified, to serve as a guideline for the proposal of the different formulations investigated in the following chapter.

Chapter 6 describes the main results obtained by different proposed strategies related to the addition of oxide promoters for the improvement of alumina-supported cobalt oxide catalysts. Overall, three strategies were examined: surface protection of the alumina with a non-promoting agent (MgO), redox promotion of the active phase with nickel, and surface protection of alumina with a redox-promoting agent (CeO_2). The results in this chapter allowed for the identification of the optimal formulation that would be used in the next chapter.

Chapter 7 deals with the incorporation of the optimal catalyst identified in Chapter 6 onto open cell alumina foams as an alternative to conventional monolithic substrates. First, the optimal formulation was adapted for its application over powdered alpha-alumina. Then the optimisation of the properties of the structured catalysts prepared by solution combustion synthesis was carried out, along with the analysis of its kinetic behaviour.

Finally, the nomenclature and the bibliography employed throughout this work are included in Chapters 8 and 9, respectively.

Chapter 2

MATERIALS, METHODS AND EQUIPMENTS

ABSTRACT

This chapter deals with the materials, methods and equipments employed for the synthesis, characterisation and catalytic testing of all the materials developed throughout this thesis work. Firstly, the materials and reagents used in the preparation of the catalysts are defined. Then, the analytical techniques used in the characterisation of the properties of the samples, including WDXRF, ICP-AES, N_2 physisorption, XRD, UV-vis-NIR DRS, Raman spectroscopy, XPS, temperature-programmed techniques, SEM and TEM, are detailed. Finally, the reaction unit and protocols applied for the catalytic testing are described, as well as the criteria used to check the absence of diffusional limitations in the reaction system.

2. MATERIALS, METHODS AND EQUIPMENTS

In this chapter the materials, methods and equipments used throughout the development of this thesis work are described. Firstly, the used reagents in the synthesis of the catalysts are detailed. Then, the theoretical fundamentals of each of the characterisation techniques applied to the synthesised catalysts are explained, as well as their corresponding experimental methods and equipments. Finally, the facility for the reaction experiments is described. In particular, the reaction conditions and the experimental protocols for the analysis of the reaction streams are detailed.

2.1. MATERIALS AND REAGENTS

2.1.1. Description of the synthesis apparatus

All the synthesis routes described in this thesis work were carried out in the homemade set-up depicted in Figure 2.1.

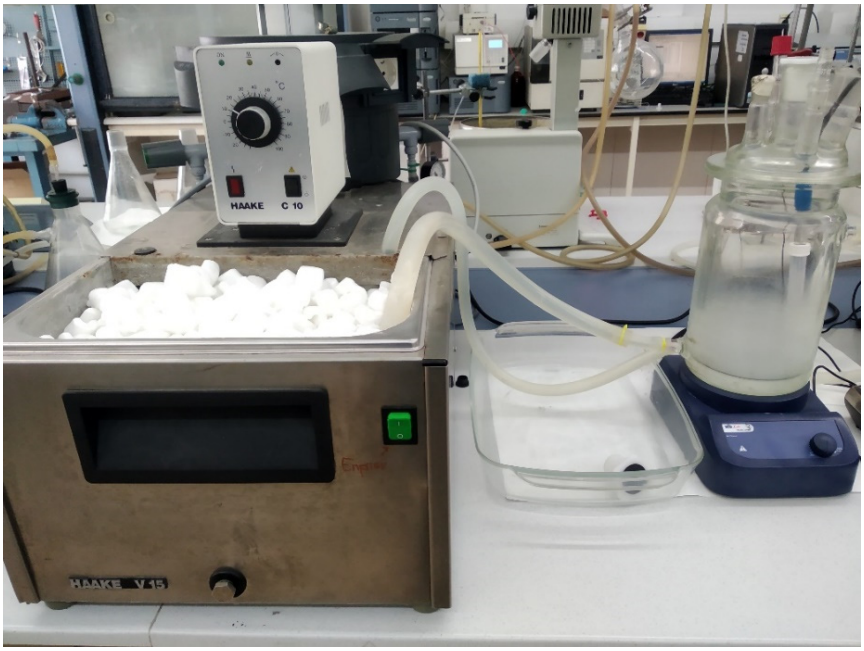

Figure 2.1. Experimental set-up for catalyst synthesis.

The catalytic precursors were prepared in a 1.5 L jacketed glass reactor connected to a *Haake V-15* 15 L water bath and a *Haake C-10* heating pump to allow for heating of the reactor. A *Testo 735* multichannel thermometer equipped with a type K thermocouple monitored the temperature inside the reaction liquor during the synthesis process. The pH of the reaction mixture was controlled by a *Crison GLP22 pHISE* pH-meter running in continuous mode fitted with a *Hach 50 14* pH electrode. The dropwise addition of reagents was performed by a *MasterFlex Easy-Load 7518-00* peristaltic pump operating at 4 cm^3 min^{-1}.

2.1.2. Reagents

Throughout this thesis work, a wide number of catalysts have been prepared with various formulations and synthesis methodologies. The specifications of each of the utilised reagents are summarised in Table 2.1

Table 2.1. Specifications of the used reagents.

Name	Chemical Formula	CAS Number	Supplier	Assay
Aluminium (III) nitrate nonahydrate	$Al(NO_3)_3 \cdot 9H_2O$	7784-27-2	Merck	≥98.5%
Cerium (III) nitrate hexahydrate	$Ce(NO_3)_3 \cdot 6H_2O$	10294-41-4	Sigma Aldrich	99%
Cobalt (II) nitrate hexahydrate	$Co(NO_3)_2 \cdot 6H_2O$	10026-22-9	Fluka	≥98%
Copper (II) nitrate trihydrate	$Cu(NO_3)_2 \cdot 3H_2O$	10031-43-3	Panreac	≥98%
Glycine	$C_2H_5NO_2$	54-40-6	Sigma Aldrich	≥99%
Iron (III) nitrate nonahydrate	$Fe(NO_3)_3 \cdot 9H_2O$	7782-61-8	Alfa Aesar	≥98%
Magnesium (II) nitrate hexahydrate	$Mg(NO_3)_2 \cdot 6H_2O$	13446-18-9	Merck	≥98%

Table 2.1 (cont.). Specifications of the used reagents.

Manganese (II) nitrate tetrahydrate	$Mn(NO_3)_2 \cdot 4H_2O$	20694-39-7	Merck	≥98.5%
Nickel (II) nitrate hexahydrate	$Ni(NO_3)_2 \cdot 6H_2O$	13478-00-7	Merck	≥98%
Sodium carbonate	Na_2CO_3	497-19-8	Fluka	≥99.8%
Urea	$CO(NH_2)_2$	57-13-6	Sigma Aldrich	≥99%
Zinc (II) nitrate hexahydrate	$Zn(NO_3)_2 \cdot 6H_2O$	10196-18-6	Sigma Aldrich	≥99%

The gamma-alumina (γ-Al_2O_3) used as a support was supplied by Saint Gobain in the form of pellets of around 3 mm with the commercial designation of SA6173. According to the specifications detailed by the supplier, this alumina possessed a specific surface area of 212 $m^2 g^{-1}$ with a mean pore diameter of 80 Å. Before its utilisation, the commercial alumina was subjected to a thermal stabilisation process consisting of a calcination step in static air at 850 °C for 4 hours. After that, the pellets were crushed and sieved to a particle size of 0.25-0.30 mm. On the other hand, the α-Al_2O_3 was obtained by calcination of powdered boehmite (*Versal*) at 1300 °C for 6 hours.

All the gases utilised in the experimental reaction unit for catalytic runs, namely methane, nitrogen and synthetic air were supplied by *Air Liquide* at a 99.999% purity. In addition, for the chromatographic analysis of the reaction stream, helium, supplied by the same company with a similar purity, was used as the carrier gas. Finally, the pure gases helium, argon, nitrogen or methane, and the gaseous mixtures 5%H_2/Ar and 5%O_2/He employed for the various characterisation techniques were supplied by *Praxair* with a 3X quality.

2.2. CHARACTERISATION TECHNIQUES

The determination of the physico-chemical properties of the prepared catalysts is of vital importance to establish the main parameters that govern their behaviour in a particular reaction. The knowledge obtained from the characterisation techniques also allows for the adaptation of the synthesis methodologies towards the improvement of the catalytic efficiency of the investigated samples. On the other hand, the analysis of the used catalysts

after reaction contributes to the identification of the deactivation processes that may affect the behaviour of the catalysts.

2.2.1. Wavelength Dispersive X-Ray Fluorescence (WDXRF)

Wavelength Dispersive X-Ray Fluorescence (WDXRF) spectrometry is an analytical technique mainly employed for the determination and quantification of the elements present in solid samples [134,135]. This technique uses the X-Ray fluorescence generated by a sample after it is irradiated with X-Ray to identify the elements present in the sample and establish their concentration.

The X-Ray fluorescence is generated due to the ionisation of the atoms in the material. X-Ray can be energetic enough to expel an electron from an inner orbital of an atom. The removal of that electron makes the electronic structure of the atom unstable, and thus, another electron in a higher orbital can fall into the lower orbital to fill the hole left behind. When falling, the electron releases a photon with an energy that equals the energy difference of the two orbitals, and consequently, the material emits radiation with specific energies that are characteristic of the present elements.

Figure 2.2 shows a schematic diagram with the main components of a WDXRF spectrometer. The source of the X-Ray radiation that induces the fluorescence is normally an X-Ray tube, which consists of a vacuum tube with an anode and a cathode. The cathode consists of a wolfram coil wire that releases electrons when heated, while the anode, which can be made from various different metals, is the component that produces the X-Ray when the electrons released by the cathode collide with it.

Wavelength dispersive spectrometers carry out the selection of the characteristic wavelengths by diffraction in a monochromator crystal. By varying the angle of incidence of the radiation on the crystal, a small X-Ray wavelength can be selected. Then, the diffracted radiation is detected in an X-Ray counter. Two main types of detectors can be used in WDXRF. Sealed or flow gas detectors, which contain a gas that is ionised by X-Ray photon, are best for measuring low energies, while scintillation detectors, which work based on the property of luminescence, are more suitable for measuring higher energies.

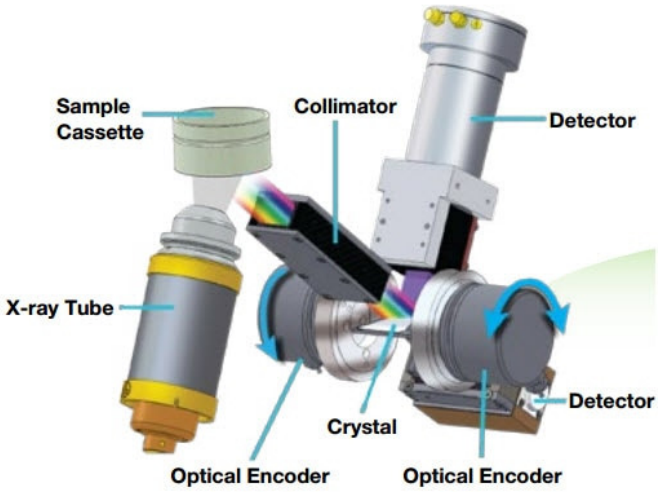

Figure 2.2. Schematic diagram of a WDXRF instrument.

Experimental protocol

The WDXRF analysis was performed in a *PANalytical AXIOS* sequential wavelength dispersive X-Ray fluorescence spectrometer, equipped with an Rh tube and three different detectors (gas flow, scintillation and Xe sealed) and a maximum power of 4 kW. The analysis of the samples was performed over a boron glass pearl. The glass pearl was prepared by fusion at around 1200 °C in a microfurnace. The sample was mixed with the flux material Spectromelt A12 (66% lithium tetraborate/34% lithium metaborate, Merck) in a 1:20 mass ratio to facilitate the fusion process.

The intensity of the X-Ray detected was converted into metal concentration by using calibration curves. For the generation of these calibration curves, international standards of rocks and minerals (such as MgO and NiO) were used. Additionally, physical mixtures of γ-Al_2O_3, Co_3O_4 were used as standards for the preparation of a calibration curve adapted to the Co loading range (up to 40%wt.Co) used throughout the thesis. On the other hand, a semi-quantitative analysis programme determined the Ce loading of the samples analysed by WDXRF. The measurements were performed by the Analysis of Rocks and Minerals Unit of the General X-Ray Service (SGIker) of the University of the Basque Country UPV/EHU.

In addition to that, the composition of the catalysts supported over alpha-alumina (Chapter 7) was determined by Energy Dispersive X-Ray Fluorescence (EDXRF), using a *Thermo Scientific ARL QUANT'X* spectrometer. The X-ray radiation was generated with a Rh anode (at 4–50 kV with 1 kV step), a 1 mm size beam and a 3.5 mm Si(Li) drifted-crystal detector with Peltier cooling was used. For the quantitative analysis, *UniQuant* software was employed.

2.2.2. Inductively Coupled Plasma Atomic Emission Spectroscopy (ICP-AES)

Atomic emission spectroscopy studies the emission of radiation by free atoms or ions in an excited state. The wavelength of the emitted radiation is characteristic of each element, which allows for its determination. On the other hand, the intensity of the specific radiation is directly proportional to the amount of element present in the sample, and thus, quantification of the radiation allows for quantification of the elements. The atomic emission spectroscopy technique is based on the generation of radiation from the atoms of a material that is subjected to a series of consecutive processes of dissolution, nebulisation and bond rupturing leading to single atoms in an excited state. When an atom in an excited state spontaneously returns to the fundamental state, it emits radiation that can be quantified. To obtain an atom in an excited state it is necessary to apply an energetic input by means of a flame or a plasma. Plasma is an aggregation state of matter composed of a mixture of neutral particles (atoms and molecules) and charged particles (ions and electrons). Therefore, plasma is a highly ionised gas, yet globally neutral, that emits radiation. The most commonly used gas for generation of plasma is argon since it is a monoatomic gas with a very simple emission spectrum, low reactivity and high ionisation energy [136,137].

Experimental protocol

The equipment employed for ICP-AES analysis was a *Thermo Elemental Iris Intrepid* apparatus, using Ar to generate the inductively coupled plasma. From all of the possible emission lines for the analysed elements, only those originating an intensity of 10 times that of the background for a concentration of 10 ppm were selected. Therefore, the selected lines were those located at 229.888 nm for cobalt, at 167.079 nm for aluminium and 240.272 nm for cerium.

The preparation of the solid samples prior to the analysis involved the acid digestion of a small mass (5-10 mg) of the powdered samples with *aqua regia* (mixture of HCl and HNO_3 in a 3:1 molar ratio) in a microwave digester, followed by redissolution in *MilliQ* water and adjustment of the total volume to 100 cm^3. The analysis was carried out by the Spectroscopy Division of the Central Research Service for Science and Technology of the University of Cádiz.

2.2.3. Physical adsorption of gases

The physical adsorption or physisorption of gases is the most commonly applied technique to investigate the textural properties of solid materials. This method provides information about the specific surface area and the pore structure (pore volume and size distribution) of the investigated materials [138]. Physisorption of gases is based on weak interactions between an adsorbing gas and the surface of the solid under study. This phenomenon is characterised by low energy forces such as *Van der Waals* forces, independently of the type of solid material investigated [139].

At low temperatures the molecules of the adsorbing gas tend to form a monolayer on the surface of the solid, whose shape only depends on the size of the molecules of the adsorbing gas. The molecules tend to group together as closely as their size allows. The most frequently used adsorbing gas for determination of textural properties by the physisorption technique is nitrogen at its boiling point (-196 °C). The transversal area of the nitrogen molecules can be calculated from the density of liquid nitrogen assuming a close-pack sphere model. The commonly accepted value for the nitrogen molecules in the operation conditions of the analysis is 0.162 nm^2. Therefore, knowing the surface occupied by a single molecule of nitrogen, the surface of the solid can be calculated based on the number of nitrogen molecules needed to form a complete monolayer over its surface. This measurement is usually performed by volumetric or gravimetric methods.

The adsorption of a gas on a solid surface is generally characterised by an isotherm curve representing the amount of gas adsorbed on the solid at a constant given temperature with respect to the pressure. Representing the total adsorbed and desorbed volumes with respect to the equilibrium pressures, the corresponding adsorption and desorption isotherms are defined.

Depending on the properties of the solid material under study, Brunauer, Emmet and Teller [140] proposed five different isotherm models, corresponding to different type of materials. In this way, type I isotherms are characteristic of microporous materials, while type II isotherms are typical of macroporous or non-porous solids. Type III and type V isotherms generally occur when the interaction between the solid adsorbent and the adsorbing gas are weak. However, type V isotherms present pore filling after the formation of the monolayer, while type III isotherms do not. An additional type VI isotherm was added by Sing [141] to model the layer-by-layer adsorption on highly uniform non-porous surfaces. Finally, type IV isotherms are characteristic of mesoporous solids. This type of isotherm also presents a hysteresis cycle between the adsorption and desorption curves, due to the capillary condensation inside the pores generating a surface tension that opposes to the desorption of the gas molecules. According to IUPAC [142], there are also for different types of hysteresis loops depending on the predominant pore shape, that is, if the majority of the pores have a cylindrical shape (H1), a bottle-neck shape (H2) or a uniform (H4) and non-uniform (H3) narrow slit-like shape.

The linearization and fit of the Brunauer, Emmett and Teller equation, also known as the BET equation is the most commonly applied method for the calculation of the specific surface area. In its linearised and simplified form, the BET equation is expressed as:

$$\frac{P}{V_{ads}(P_0 - P)} = \frac{1}{V_m C} + \frac{C-1}{V_m C}\frac{P}{P_0} \tag{2.1}$$

where V_{ads} ($cm^3\ g^{-1}$) is the volume of adsorbed gas per unit mass of solid in equilibrium at a given pressure P (kPa); V_m ($cm^3\ g^{-1}$) is the volume of adsorbing gas required to form a complete monolayer; P_0 (kPa) is the saturation pressure of the adsorbing gas in the analysis conditions and C is a parameter associated with the adsorption and desorption enthalpies [143].

Taking the results from the adsorption isotherm for relative pressures in the 0.05-0.25 range and fitting them to Equation 2.1 allows for the calculation of the V_m and C parameters from the slope and the intercept of the resulting straight line, respectively. Once the value of the V_m parameter has been determined, the calculation of the specific surface area S_{BET} ($m^2\ g^{-1}$) of the investigated solid material can be made by the expression:

$$S_{BET} = \frac{V_m N_A}{m V_{mol}} A_m \cdot 10^{-18} \quad (2.2)$$

where N_A is the Avogadro number, V_{mol} is the molar volume of the adsorbing gas ($cm^3\ mol^{-1}$) under the conditions of the analysis, A_m is the transversal surface of a molecule of the adsorbing gas (nm^2) and m is the mass of solid (g) used in the analysis.

The total pore volume of the samples can be estimated from the total adsorbed volume at a relative pressure of 0.99, which represents the total gas volume that the sample is capable of adsorbing on its pores. On the other hand, for the determination of the pore size distribution, the generally accepted methodology is that proposed by Barrett, Joyle and Halenda, also known as the BJH method [144]. This model, which is based on the Kelvin equation that describes capillary condensation, is applied to the desorption isotherm to evaluate the pore radius for different values of the relative pressure, as follows:

$$r_p = \frac{2\sigma V_{ads} \cos \upsilon}{RT \ln\left(P/P_0\right)} 10^3 + t \quad (2.3)$$

where r_p is the pore radius (nm), σ is the surface tension of the adsorbing gas ($N\ m^{-1}$), υ is the contact angle between the condensed phase and the surface of the solid (rad), T is the temperature (K) and t is the thickness of the adsorbed layer (nm). This parameter can be estimated by many different correlations depending on the relative pressure (P/P_0). Among them, the Halsey correlation gives reasonably good results for mesoporous materials and is defined as follows:

$$t = 3.54 \left[\frac{-5}{\ln\left(P/P_0\right)}\right]^{\frac{1}{3}} \quad (2.4)$$

Experimental protocol

The nitrogen physisorption analysis was performed in a *Micromeritics TriStar II* apparatus at the normal boiling point of nitrogen (-196 °C). The objective of the analysis was to define the main textural properties of the synthesised catalysts, namely their specific surface area, pore volume and pore size distribution. All samples were subjected to a degassing step prior to the analysis in a *Micromeritics SmartPrep* portable degasser at 300 °C for 10 hours

with a N_2 flow, to remove the moisture and other molecules that could be initially adsorbed in the samples and interfere with the analysis.

The sampling process to obtain the isotherms was automatic and controlled by a computer. The adsorption isotherms were obtained by adding successive volumes of N_2 to the samples and recording the equilibrium pressures from the lowest value (‹1 Pa) to almost saturation pressure (≈ 101.3 kPa). Then, the desorption isotherm was obtained by removing volumes of N_2 from the samples and registering the equilibrium pressures until the hysteresis loop is closed.

For the calculation of the S_{BET} the relative pressures in the range 0.05-0.25 from the adsorption isotherm were selected. For the determination of the pore size distribution, however, the whole desorption isotherm (0.04-0.99 range of relative pressure) was considered when applying the BJH method.

2.2.4. X-Ray Diffraction (XRD)

Crystals are regular arrays of atoms. Atoms can scatter X-Ray waves, mainly through their electrons. When the scattered X-Ray possess the same wavelength as the incident radiation, this phenomenon is known as "elastic scattering", and the electrons in the atoms are called the "scatterers". A regular array of scatterers produces a regular array of spherical scattered waves. Although these waves cancel each other in most directions by destructive interference, there are certain directions where they add constructively [145]. The Bragg's law determines these directions, as follows:

$$n\lambda = 2d \sin\theta \tag{2.5}$$

where d is the spacing between different crystal planes. The usual spacing value for crystalline materials turns out to be the same order of magnitude as the wavelength of the X-Ray radiation (0.1-10 Å). For this reason, X-Ray waves can diffract in a crystalline lattice. For a given monochromatic (constant λ) X-Ray radiation, a wave is diffracted in a certain direction (θ) if the difference in the path-length of the wave train is an integer (n) multiple of the wavelength.

The technique of X-Ray Diffraction or XRD allows for the investigation of the internal structure of crystalline solids. The most widespread analysis method is the one performed over powdered samples, also known as polycrystalline samples. Since this type of particles

are made of very fine particles oriented towards all random directions, all the possible crystal orientations are exposed to the X-Ray beam, and therefore represented in the results.

In the typical configuration (known as Bragg-Brentano geometry), the sample is loaded into a disc that can rotate around its normal axis to provide an extra randomisation of the crystal orientation. The X-Ray emission source and the detector are mounted in a goniometer, in order to control their angle with respect to the plane of the sample (θ). During the analysis, the θ angle of both the X-Ray source and the detector is varied in a way such that the angle between them is always 2θ, while the radiation intensity in the detector is registered. As a result, a certain type of spectrum called a "diffractogram" is obtained.

In a diffractogram, the radiation intensity detected is plotted against the 2θ position, and the position of the peaks indicates the Bragg's positions characteristic of the crystal structure of the sample. The comparison of the experimental diffractograms with those characteristic of each crystalline phase, which are gathered in the ICDD (*International Centre for Diffraction Data*) database in the form of PDF (*Powder Diffraction File*) cards, allows for the identification of the crystalline phases present in each sample. In each PDF card, the Bragg's positions, relative intensities and Miller indexes of the corresponding planes are summarised, along with other properties of the standard sample and the methodology used to obtain the diffraction pattern.

On the other hand, from the signals in the patterns, the crystal size of the phase that generated the diffraction signals can be estimated based on the intensity and the width of the signals. The simplest equation to perform this estimation is the Scherrer equation [146]:

$$D = \frac{K\lambda}{\beta \cos\theta} \tag{2.6}$$

where λ is the wavelength of the X-Ray radiation, θ is the position angle of the specific signal considered, K is a shape factor (usually taken as 0.9 for sphere-like particles) and β is a parameter related the width of the specific signal. The value of this parameter is normally corrected to account for the fraction of peak widening that occurs due to the analysis instrument. The correction is made as follows:

$$\beta^2 = B^2 - b^2 \tag{2.7}$$

where B is the experimental FWHM (Full Width at Half Maximum) or width of the signal at half of its maximum intensity, and b is a specific parameter of the instrument employed for the analysis, usually taken to be 0.1 if no other data is available.

Experimental protocol

The X-Ray diffraction measurements in polycrystalline samples were carried out in a PANalytical *X'Pert PRO* automated diffractometer with Bragg-Brentano geometry. This instrument was equipped with a secondary graphite monochromator adjusted for Cu K_α radiation (λ = 1.5406 Å). The X-Ray source was operated at 40 kV and 40 mA and the PIXcel solid-state detector was fixed at an active length of 3.347°. Two different measurement conditions were established for the analysis of the samples. The conditions for low resolution measurements were optimised for a 2θ angle range of 10-80° with a step size of 0.026° and a counting time of 2.0 s for each step. On the other hand, high resolution analysis was carried out in the same angle range, with the same step size, but with a higher counting time (26.8 s) for each step. The diffractometer was controlled by the *X'Pert Data Collector* software. All the XRD measurements were performed by the Analysis of Rocks and Minerals Unit of the General X-Ray Service (SGIker) of the University of the Basque Country UPV/EHU.

The processing of the results was carried out with specific software for XRD analysis. In particular, *WinPLOTR* software was used to aid in the phase identification and estimation of the crystal sizes. On the other hand, the high resolution patterns were used to carry out full profile matchings without structural model with the aim of calculating the cell parameters of the crystal phases. This task was completed using the *FullProf.2k* software.

2.2.5. Ultraviolet-visible-Near Infrared Diffuse Reflectance Spectroscopy (UV-vis-NIR DRS)

Diffuse reflection is the reflection of light from a surface such that the incident radiation is scattered at many angles, rather than in a single direction. Diffuse reflection in solids is generally not due to surface roughness, because most of the reflected light comes from scattering centres (atoms) below the solid surface. When the material is light-absorbent, diffused light can lose some wavelengths during its walk into the material, and the reflected light will emerge coloured. Similarly, if such material is irradiated with monochromatic light, the absorption capacity of the solid for the specific wavelength of the

light will determine the amount of light that the solid will reflect. This is the foundation of the Diffuse Reflectance Spectroscopy technique.

This technique is useful for qualitative and structural characterisation of solid materials. DRS measurements allow for the determination of the coordination state of the ionic species in the material under study [147]. In this analysis, the sample is irradiated with a monochromatic light that is diffusively reflected. The reflected radiation is then detected by a photosensitive cell.

The intensity of the diffusely reflected light is independent of the angle of the incident light, and only depends on the absorption and scattering coefficients of the material. For the analysis of the reflected light obtained in a DRS experiment, a phenomenological theory is required to allow for the separation of the absorption and scattering coefficients. The most commonly applied theory is the Schuster-Kubelka-Munk or SKM model. This model can obtain the absorption spectrum of a solid material from the diffuse reflectance spectrum provided that some conditions are fulfilled, mainly, that the scattering coefficient is independent of the wavelength of the incident light [148].

In the SKM model the diffuse reflectance of a layer with infinite thickness R_∞ is linked with the absorption coefficient K and the scattering coefficient S by the Schuster-Kubelka-Munk remission function:

$$F(R_\infty) = \frac{(1 - R_\infty)^2}{2R_\infty} = \frac{K}{S} \tag{2.8}$$

With this equation, the measured reflectance spectrum R(λ) can be converted into an absorption spectrum S(λ). This can be used to identify the main species present in the sample and their coordination environment based on the different absorption bands observed in the spectrum.

Experimental protocol

The DRS experiments were carried out in a *Jasco V-570* diffuse reflectance spectrometer in the 200-2300 nm wavelength range. The spectra were registered in reflectance mode and subsequently transformed into absorbance spectra via the SKM function.

The analysis was performed by the Bizkaia Central Analysis Service (SCAB) of the Advanced Research Facilities (SGIker) of the University of the Basque Country UPV/EHU.

2.2.6. Raman Spectroscopy

Raman spectroscopy is a photonic high-resolution technique that can provide information about the chemical and structural properties of a wide range of organic and inorganic materials, also allowing for their identification [149].

The analysis by Raman spectroscopy works by irradiating a sample with a monochromatic with frequency ν_0 and examining the light dispersed by the sample. The majority of the dispersed light presents the same frequency as the incident light, but a small fraction presents a frequency shift due to its interaction with matter. The light that maintains the same frequency ν_0 as the incident light is known as "Rayleigh scattering" and does not give any information about the analysed sample. On the other hand, the dispersed light that presents a different frequency with respect to the incident radiation is the one that reveals information about the structure of the sample, and is known as "Raman scattering".

The frequency difference ν_r between the incident radiation and the Raman scattering is called the "Raman shift", and is dependent on the chemical nature and aggregation state of the sample, and independent of the frequency of the incident radiation. Each material possesses a group of Raman shift values characteristic of their polyatomic structure and the nature of the present atomic bonds [150]. A Raman spectrum represents the optical intensity of the scattered light as a function of its Raman shift, normally expressed as wavenumber in cm^{-1}.

Experimental protocol

The analysis by Raman spectroscopy were carried out in a *Renishaw In Via Raman* confocal microscope composed of a spectrometer and two different lasers, coupled to a *Leica DMLM* microscope. The excitation wavelength of the lasers were 514 nm (green) and 785 nm (NIR), which allows for carrying out the analysis with two different energies, effectively duplicating the chances of success of the analysis and avoiding possible fluorescence phenomena. The spectrometer was equipped with different modular optics for each of the lasers, in order to achieve a spectral resolution of 1 cm^{-1} with a good signal/noise ratio in both cases.

On the other hand, the *Leica* microscope incorporated 5x20x50 objectives with the aim of obtaining an optimal yield of the laser photons, thereby increasing the Raman effect. This confocality also allowed to obtain the maximum lateral resolution from the microscope. The analysis was performed at the Coupled Multispectroscopy Singular Laboratory (Raman-LASPEA) of the Advanced Research Facilities (SGIker) of the University of the Basque Country UPV/EHU.

2.2.7. X-Ray Photoelectronic Spectroscopy (XPS)

X-Ray Photoelectronic Spectroscopy (XPS) is a surface-sensitive analytical technique that uses diagnostic information encoded in the kinetic energy of low-energy electrons, which are emitted due to the photoelectric effect. In XPS, the absorption of an X-Ray by the sample drives the emission of a photoelectron. The kinetic energy (KE) of the emitted electron is the difference between the energy of the absorbed photon ($\hbar\nu$) and the binding energy of the electron in the atom (BE) [151]. For solid samples, the contact between the sample and the spectrometer causes a contact potential difference that induces a work function of the spectrometer in the sample (ϕ). Hence, the energy balance of the emitted electron can be considered as follows:

$$KE = \hbar\nu - BE - \phi \tag{2.9}$$

Therefore, by measuring the kinetic energy of the emitted electron, its binding energy in the atom can be calculated. The binding energy is characteristic for the atomic or molecular orbital from which the electron was ejected. Frequently, "chemical shifts" are discussed, which are differences between the binding energy of an element in an unknown sample and that in a reference state, often the elemental or metallic state. These chemical shifts can provide information regarding the oxidation state of the elements in the investigated sample.

The XPS technique works by detecting the photoelectrons that can escape from the sample into the vacuum and reach the detector. In order to escape from the sample, photoelectrons must travel through the sample, where they can suffer inelastic collisions, recombination or trapping in other atoms, which effectively reduces their free path and leads to an exponential attenuation function as the depth increases. This makes the signals detected from the surface of the sample notably stronger than that from deeper below the surface, which gives this technique its surface sensitivity.

Figure 2.3 shows the schematic diagram of a conventional XPS spectrometer, which is made up of an ultra-high vacuum (UHV) chamber, with a pre-chamber for sample introduction and handling, a X-Ray source, electron lenses to direct the emitted electrons into the detector, a hemispherical electron analyser and a detector. In addition, a "flood gun" is normally added when analysing non-conducting samples that require charge neutralisation during the analysis.

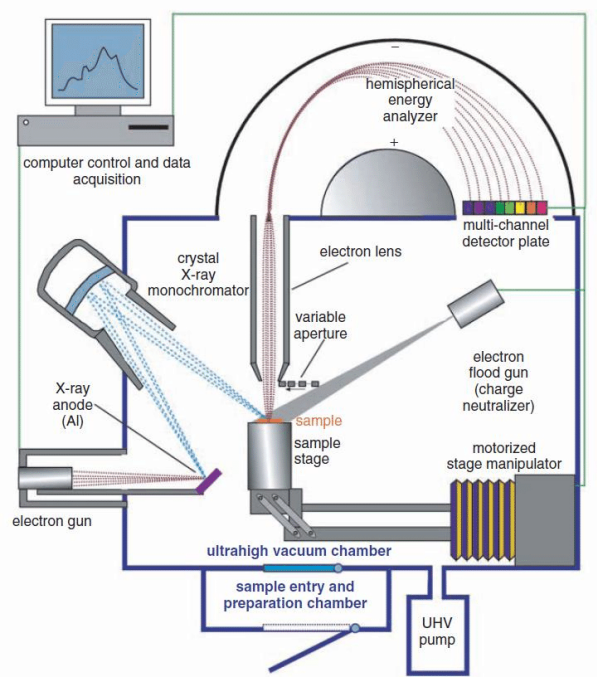

Figure 2.3. Schematic diagram of a conventional XPS apparatus.

Experimental protocol

The XPS measurements described in this thesis work were carried out with two different apparatus. Firstly, a *SPECS Phoibos 150 1D* analyser coupled with a *DLD* monochromatic Al K_α (1486.6 eV) radiation source, and a flood gun for charge neutralisation. An initial survey scan was performed with a pass energy of 40 eV, and after that, detailed spectra of specific regions were obtained with a pass energy of 20 eV. These measurements were performed by the X-Ray Photoelectron Spectroscopy Unit of the Advanced Research Facilities (SGIker) of the University of the Basque Country UPV/EHU.

Secondly, a *Kratos AXIS Supra* spectrometer was used with a 225 W AlK_α radiation source. The general survey scans were carried out with a pass energy of 160 eV, while the detailed scans were performed with a pass energy of 20 eV. These measurements were carried out in the Advanced Microscopy Laboratory (LMA) of the University of Zaragoza.

The analysis of the obtained results was performed by means of the *CasaXPS* software. All spectra were corrected by fixing the signal of adventitious carbon at a binding energy of 284.6 eV. The adjustment of the spectra was made by using pseudo-Voight distributions and *Shirley*-type background subtraction [152].

2.2.8. Temperature-programmed techniques

Temperature-programmed techniques, usually denoted as TPX where X stands for the specific process studied, are in common use in the field of heterogeneous catalysis. In these techniques, the evolution of the sample is monitored via a specific detector, while a temperature programme T(t) is run. A wide range of such techniques exists, depending on the gases that the sample is put in contact with, and the specific parameters that are monitored.

All the temperature-programmed experiments performed in this thesis work were carried out in a *Micromeritics Autochem 2920* apparatus equipped with a thermal conductivity detector (TCD) or a mass spectrometer (MS). A scheme of this apparatus is depicted in Figure 2.4.

2.2.8.1. Temperature-Programmed Reduction with Hydrogen (H_2-TPR)

Temperature-Programmed Reduction (TPR) is a technique widely used in catalysis when the materials under study are metallic oxides susceptible to reduction. By using this technique, the reducibility of the samples can be determined as well as the temperature required to achieve a certain reduction degree [153,154].

In a typical TPR run, the solid sample is reduced by the action of a gaseous mixture, generally H_2 diluted in an inert gas, while its temperature is increased at a constant rate. The reduction process can be followed by measuring the concentration of the reducing agent in the gaseous phase by a suitable detector.

While the reduction process progresses, one or more hydrogen consumption events can be observed at specific temperatures, which are usually characteristic of the different species present in the sample.

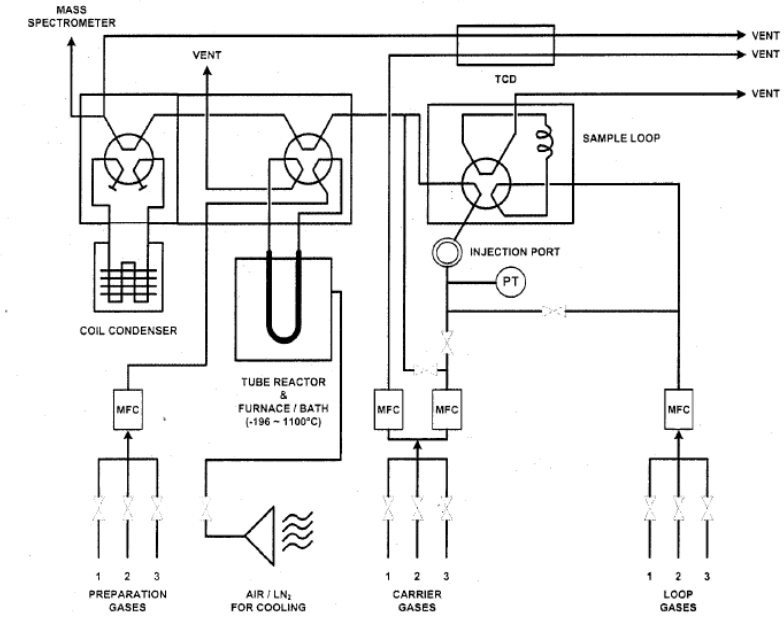

Figure 2.4. Schematic diagram of the TPX apparatus.

The complexity of reduction process normally does not allow simple models to be applied for the analysis of the reduction profiles. For this reason, this technique is used as a qualitative way, and normally combined with other techniques to correctly identify the species present in the sample. Additionally, the analysis of reference samples with known composition and stoichiometry and the subsequent comparison of their TPR profiles with the studied sample can allow for the estimation of the relative abundance of the identified species.

Experimental protocol

The H_2-TPR analysis was conducted in the previously described instrument, using a 50 cm^3 min^{-1} flow of a 5%H_2/Ar mixture as the reducing gas. In each experiment, 30-100 mg of the sample was placed in a U-shape quartz reactor between two layers of quartz wool, which served as the support. The reactor was then loaded into the oven of the apparatus,

and subjected to a heating programme from ambient temperature to a final temperature in the 600-950 °C range, depending on the specific nature of the analysed sample, with a heating rate of 10 °C min^{-1}.

Prior to the analysis, each sample was subjected to a pretreatment process with a 5%O_2/He mixture consisting of a heating program from ambient temperature to 300 °C at a heating rate of 10 °C min^{-1} with a 30-minute isotherm at 300 °C. The aim of the pretreatment process was to remove the impurities that could possibly be adsorbed on the surface of the samples, and to ensure they started the TPR analysis in the most oxidised form.

During the reduction process, the oxygen species of the sample react with the hydrogen gas to form water vapour. To avoid that water vapour would reach the TCD and interfere the measurement, the gases passed through a "cold trap" before reaching the TCD. The cold trap was kept at a temperature below -10 °C by immersing it in an isopropanol slurry, which was cooled down with liquid nitrogen.

2.2.8.2. Temperature-Programmed Oxidation with Oxygen (O_2-TPO)

Temperature-Programmed Oxidation is a very useful technique to evaluate the oxidability of catalytic materials, which can provide information regarding the mobility of its oxygen species and their easiness for recovery, and also to characterise the coke deposits on the surface of a used catalyst. The basis of this technique is very similar to that of the H_2-TPR technique, although it can only be applied to oxidisable metallic materials. In the case of characterisation of coke deposits, the process can also be performed in a thermogravimetry apparatus, where the removal of coke can be followed by mass difference.

Experimental protocol

The O_2-TPO analysis were carried out in the aforementioned apparatus, using a 50 cm^3 min^{-1} flow of a 5%O_2/He mixture as the reducing gas. In each experiment, 30-100 mg of the sample was placed in a U-shape quartz reactor between two layers of quartz wool, which served as the support.

The reactor was then loaded into the oven of the apparatus, and subjected to a heating programme from ambient temperature to a final temperature in the 600-950 °C range, depending on the specific nature of the analysed sample, with heating rate of 10 °C min^{-1}.

Prior to the analysis, each sample was subjected to a pretreatment process with a 5%H_2/Ar mixture consisting of a heating program from ambient temperature to 600 °C at a heating rate of 10 °C min^{-1} with a 10-minute isotherm at 600 °C. The aim of the pretreatment process was to completely reduce all the metal oxide species in the sample to their respective metallic forms.

2.2.8.3. Temperature-Programmed Reaction with Methane (CH_4-TPRe)

This technique belongs to a family of temperature-programmed techniques known as Temperature-Programmed Surface Reactions (TPSR or TPRe). In this type of technique, the sample is put in contact with a gaseous mixture with which it can react in a certain way. The main difference between the TPRe and the TPR/TPO techniques is that simple detectors such as a TCD cannot be utilised, since the reaction that takes place generates several different products. For this reason, to carry out a TPRe experiment, the TPX instrument is usually coupled to a mass spectrometer or some other class of gas analyser.

Temperature-Programmed Reaction techniques can be helpful in identifying the active phases or sites for a specific reaction, and estimating their relative presence in the studied catalysts. If the composition of the reacting gas is chosen appropriately, the varying reactivity of the active phases of the samples can be ascertained by the difference in temperature needed to detect the desired products in the gas analyser. In addition, this technique can also reveal the presence of unwanted phases that may produce secondary reactions and affect the selectivity of the studied catalyst towards the desired reaction.

Experimental protocol

In this thesis work, TPRe experiments were carried out using a gaseous mixture of 5%CH_4/He, in order to carry out the reduction reaction between the prepared catalysts and methane. Contrary to activity tests conducted in the reaction unit, the TPRe experiments were performed in the absence of molecular oxygen in the reacting stream, so that the only oxygen atoms that could react with methane were the oxygen species present in the catalytic sample.

The CH_4-TPRe analysis were also carried out in the same apparatus as the other TPX experiments, using a 100 cm^3 min^{-1} flow of a 5%CH_4/He mixture as the reacting gas. In each experiment, 50 mg of sample were placed in a U-shape quartz reactor between two layers of quartz wool, which served as the support. The reactor was then loaded into the oven of the device, and subjected to a heating programme from room temperature to a final temperature in the 600-950 °C range, depending on the specific nature of the analysed sample, with a heating rate of 10 °C min^{-1}.

Prior to the analysis, each sample was submitted to a pretreatment process with a helium flow consisting of a heating program from ambient temperature to 300 °C at a heating rate of 10 °C min^{-1} with a 30-minute isotherm at 300 °C. The goal of this step was to remove the impurities that could possibly be adsorbed on the surface of the samples.

The evolution of the reaction process was monitored by a *Pffeifer Vacuum DUO 2.5* portable mass spectrometer connected to the TPX apparatus. The mass spectrometer was operated in Secondary Electron Multiplier mode, in order to monitor the evolution of the m/z signals corresponding to H_2 (m/z = 2), He (m/z = 4), CH_4 (m/z = 16), H_2O (m/z = 18), CO (m/z = 28) and CO_2 (m/z = 44).

2.2.9. Scanning Electron Microscopy (SEM)

Scanning Electron Microscopy (SEM) is a microscopy technique that produced images of a sample by scanning its surface with a focused electron beam. The electrons interact with the surface of the sample and produce signals that contain information about the topography of the surface. The electron beam is normally scanned in a raster pattern, and the intensity of the secondary electrons detected is combined with the position of the beam to form an image. The signal intensity of the secondary electrons detected depends, among other factors, on the topography of the sample [155].

Secondary electrons have usually very low energies (around 50 eV), which limits their free path when travelling in solid matter. For this reason, secondary electrons can only escape from the first few nanometres of a solid surface. The signal from secondary electrons tends to be highly focused at the point of impact of the primary electron beam, thus allowing this technique to collect images with a resolution below 1 nm. Due to the very narrow beam, SEM micrographs have a lager depth of field, which gives them a characteristic three-

dimensional appearance, thus making them very useful for understanding the surface structure of a sample [156].

In a typical SEM, an electron beam is emitted from an electron gun (usually fitted with a wolfram or LaB_6 cathode). One or two condenser lenses focus the electron beam, which normally possesses an energy between 0.2 and 40 keV, into a spot of around 0.4 to 5 nm in diameter. In the final lens, pairs of scanning coils (or deflector plates) deflect the beam in the x and y axis in order to scan in a raster pattern. The interaction between the electron beam and the sample surface results in the reflection of high-energy electrons by elastic scattering, the emission of secondary electrons by inelastic scattering and the emission of electromagnetic radiation, each of which can be measured with a suitable detector. Each detection event is synchronised with the position of the beam in the sample to create a distribution map of the intensity of the signal from each scanned position on the sample.

Experimental protocol

Prior to the analysis, all solid samples were placed in an aluminium sample holder and fixed in placed with carbon adhesive tape. SEM images were obtained in a *JEOL JSM-6400* scanning electron microscope with a W filament and in a *JEOL JSM-7000F* scanning electron microscope with Schottky-type field emission. The analysis was performed by the Electronic Microscopy and Material Microanalysis Service of the Advanced Research Facilities (SGIker) of the University of the Basque Country UPV/EHU.

2.2.10. Transmission Electron Microscopy (TEM)

Transmission Electron Microscopy (TEM) is a technique that can provide information regarding the textural and structural properties of a material, as well as about its elemental composition, making it an important and useful characterisation technique [157].

TEM is based on irradiating a sample with a highly focused electron beam, similarly to SEM. The electron beam is emitted by a filament, accelerated by a potential difference and focused by a series of condensing lenses to create a beam that reaches the sample perpendicularly. The electrons that go through the sample are scattered as a consequence of their interaction with the sample while travelling through it.

The scattered electrons are refocused and sent to a detector to form an image, in a similar way as it happens in SEM [158]. The main advantage of this technique lies in the possibility of focusing the electron beam on extremely reduced spots of the sample.

The images obtained by TEM allow direct visualisation of the metallic crystallites present in a catalyst sample. Thus, this technique is very useful for the structural characterisation of supported metal catalysts, and more specifically provides information about the morphology and size distribution of metallic crystallites, as well as the dispersion and distribution of the different metals present in a sample. In its high-resolution version (HRTEM), this technique also allows the resolution of the lattice fringes of individual crystals, which can provide information about their preferential orientation and morphology.

A TEM apparatus can be also equipped with additional scanning coils and detectors to form a STEM (Scanning Transmission Electronic Microscopy) apparatus. In STEM the electron beam is focused on a fine spot (as in TEM), which is then scanned over the sample (as in SEM). The rastering of the beam across the sample allows STEM to be coupled with analytical techniques such as High-Angle Annular Dark Field imaging (HAADF), Energy Dispersive X-Ray spectroscopy (EDX) or Electron Energy Loss Spectroscopy (EELS).

In HAADF, an annular detector is used to collect only the scattered electrons instead of those from the main beam. For elements with higher Z, the number of scattered electrons is higher due to the increased electrostatic interactions between the nucleus and the electron beam. For this reason, in HAADF, the atoms with higher Z appear brighter, allowing for the identification of metal particles and determination of their distribution. On the other hand, EDX operates by detecting the X-Ray released by the atoms in the sample when the incident beam excite electrons in their inner shells, similarly as what happens in XPS. Thus, EDX allows the elemental composition of the sample to be measured. Finally, in EELS the amount of energy lost by the electrons in the beam due to inelastic scattering is measured via an electron spectrometer and interpreted in terms of what caused said energy loss. Since the energy loss due to inner shell ionizations is specific of the element that caused it, EELS can determine the type and number of atoms of each type being struck by the beam, allowing for determination of the elemental composition of the sample.

Experimental protocol

Prior to the analysis, the solid samples were crushed in a pestle mortar and a small amount of the resulting powder was suspended in ethanol with an ultrasonic bath for at least 1 hour. After that, two drops of the resulting suspension were placed in a specimen rack, a circular copper grid covered with amorphous carbon, and left to dry in air.

The TEM images were obtained by a *Philips CM200* transmission electron microscope equipped with a LaB_6 filament operating at 200 kV as the electron source. Bright field images were acquired by a *Gatan 696* high-resolution CCD camera. High Resolution Transmission Electron Microscopy (HRTEM) measurements were performed in a *FEI Titan Cubed G2 60-300* electron microscope equipped with a high-brightness X-FEG Schottky-type field emission electron gun operating at 300 kV, a monochromator and a *CEOS* CETCOR spherical aberration corrector on the image side. The images were recorded on a *Gatan UltraScan 1000 2kx2k* CCD camera.

On the other hand, Scanning Transmission Electron Microscopy - High Angle Annular Dark Field (STEM-HAADF) images were obtained in a Cs-probe-corrected *ThermoFisher Scientific/FEI Titan* electron microscope at a working voltage of 300 kV, coupled with *CEOS* CESCOR corrector and a *Fischione* HAADF detector. The STEM apparatus was also equipped for EDX and EELS experiments. Both spectroscopic techniques, when combined with the imaging technique, were able to provide spatially resolved elemental analysis of the samples. X-ray Energy Dispersive Spectroscopy (EDX) elemental maps were obtained with an *Oxford Intruments Ultim Max* detector. For EELS analysis the microscope was fitted with the *Tridiem Gatan* Energy Filter. The acquisition time was 50 ms per spectrum. For every map, a spectrum was acquired every 1-3 nm, depending on the area and the size of the spectrum-image. The energy dispersion used for the analysis was 0.2 eV per pixel. The collected maps were presented in the form of a matrix of coloured pixels with the intensity corresponding to the amount of the element.

The analysis was performed by the Electronic Microscopy and Material Microanalysis Service of the Advanced Research Facilities (SGIker) of the University of the Basque Country UPV/EHU, and in the Advanced Microscopy Laboratory of the University of Zaragoza.

2.3. REACTION SYSTEM

2.3.1. Reaction equipment

The performance of the synthesised powdered catalysts was examined in a bench-scale fixed-bed tubular reactor. The reactor was located inside a *PID Eng & Tech Microactivity-Reference* modular reaction system. This equipment was design to allow the simulation of the reaction conditions of the real effluents from a natural gas engine exhaust, while at the same time minimising mass and heat transfer limitations. As a result, the reaction equipment worked with a relatively low reagents and catalyst consumption, and reduced operation time intervals to reach steady state conditions. The reaction equipment was divided into three main zones, as shown in Figure 2.5: reagents feeding zone, reaction zone and analysis zone.

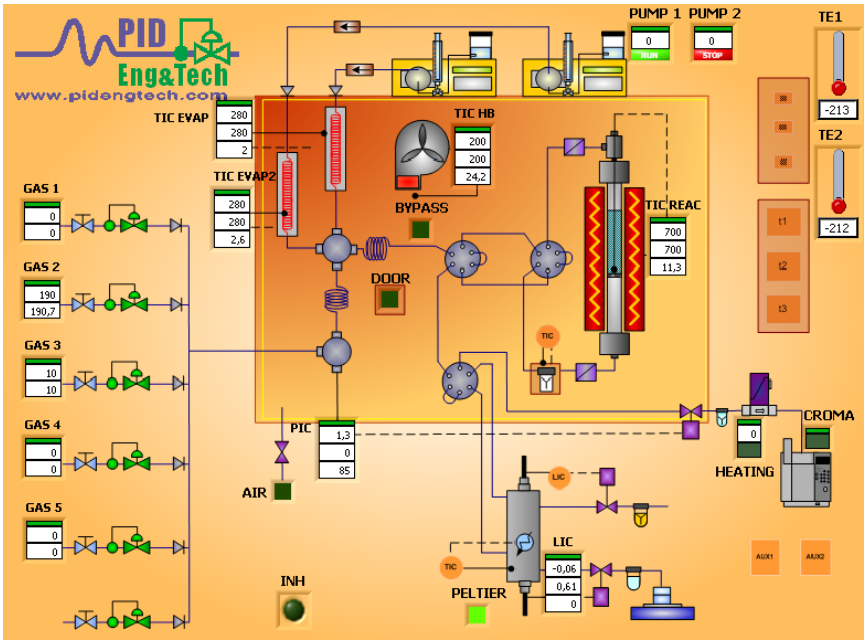

Figure 2.5. Schematic diagram of the reaction set-up.

On the other hand, the performance of the structured catalysts was analysed out in a straight quartz tubular reactor. The quartz tube was placed inside a cylindrical horizontal oven equipped with a PID controller for temperature control. Simultaneously, the flow and composition of the gaseous feedstream was determined with flow mass controllers.

2.3.1.1. Reagents feeding zone

The reagents feeding zone comprises the gases feeding system and the liquids feeding system. The gases feeding system was composed of three gas lines ultimately connected to compressed gas bottles of synthetic air, nitrogen and methane. Each line was fitted with a cut valve and a *Bronkhorst High-Tech EL FLOW* flow mass controller for the regulation of the flow rate.

On the other hand, the liquid feeding system consisted of a *GILSON 307* piston pump with a 1000 cm^3 liquid reservoir. The piston pump was connected to an evaporator located inside the reaction zone that was kept at a temperature of 180 °C to avoid condensation of the liquid. The evaporator was fitted with a *Toho TTM-005* PID controller and a type K thermocouple for temperature control. Before being fed into the reactor, both gases and liquid were circulated into a 300 cm^3 dead volume to allow a complete homogenisation of the reaction mixture. Finally, the feedstream was sent into a *Vici Valco* 6-way valve that allowed directing it into the reactor or bypassing it.

2.3.1.2. Reaction zone

The fixed-bed tubular reactor was made of *Hastelloy X* stainless steel produced by *Autoclave Engineers*. The dimensions of the tube were 9 mm of internal diameter, 14 mm of external diameter and 305 mm of length. At 138 mm from the base, the tube possessed a small notch that was used to support a small quartz wool ball, which in turn served to hold the catalytic bed.

The reactor tube was placed inside a cylindrical oven fitted with a heating resistance. The temperature inside the reactor was controlled by a type K thermocouple inserted from the upper part of the tube into the catalytic bed. The thermocouple and the heating resistance were connected to a *Toho TTM-005* PID controller to regulate the temperature inside the reactor. The whole ensemble was located inside a stainless steel prismatic box known as the "hot box". The hot box was kept at a temperature of 150 °C to minimise heat loss in the reactor and thermal stress in the components that were in contact with it. Once outside of the hot box, the gas line that connected the reactor exit with the analysis system was run through a Peltier cooling system with the aim of condensing and separating the water vapour produced in the reaction and avoiding it interfering with the analysis system.

2.3.1.3. Analysis zone

A suitable on-line analysis system was designed to allow for reliable and quick acquisition of experimental data to monitor the course of the reaction, in order to make the determination of activity and performance parameters of the different tested catalysts possible. The chosen method to screen the concentrations of the various reaction products was gas chromatography.

Gas chromatography is a technique capable of separating the different compounds of a gaseous mixture based on their relative speed when moving across a stationary solid phase transported by a mobile gas phase. This technique is suitable for separation of gaseous or easily vaporisable components. A small volume of the gaseous mixture is injected in a stream of inert gas (mobile phase) that flows through a column (a capillary tube filled with a solid phase) that is capable of separating the components of the mixture on account of their relative interaction with the solid phase. The chemical species of the mixture then emerge from the column at different times and can be detected separately [159]. Once the components of the mixture are separated, they flow through the detector. The most common detector for gaseous mixtures is the thermal conductivity detector. The different components of the sample are separately fed into the TCD, where they are exposed to a hot filament. The different thermal conductivity of each component of the sample induces a change in the temperature of the filament that is translated into an electric signal.

In this thesis work, the gas chromatograph connected to the reaction apparatus was an *Agilent 490 microGC*. This apparatus was composed of two separation channels (A and B), each of them fitted with a column and an individual TCD, suitable for separation and analysis of different components. Thus, channel A was fitted with a 10 m 5A molecular sieve column with a 3 m PBQ pre-column, suitable for separation and analysis of permanent gases such as H_2, N_2, O_2 and CO. This channel worked in "backflush" mode in order to trap the CO_2 and any other "heavy" component in the pre-column and preventing them from reaching the column. On the other hand, channel B was equipped with a 10 m PPQ column suitable for the analysis of CH_4 and CO_2. Table 2.2. summarises the operation conditions of the various components of both channels.

Table 2.2. Operation conditions of the gas chromatograph.

Parameter	Channel A	Channel B
Inlet temperature, °C	100	
Injector temperature, °C	70	70
Column temperature, °C	50	50
Sampling time, s	10	
Injection time, ms	100	100
Backflush time, s	15	20
Run time, s	120	
Column pressure, psi	22	22

The operation of the gas chromatograph, as well as the analysis and quantification of the chromatographic results, was carried out by the *Soprane II* software. The software was capable of identifying and integrating the signals of the different components (provided that their respective residence time was known), thus producing a results report where the integrated areas were summarised. The integrated areas were converted into concentration measurements of each component by means of calibration curves generated by analysis of standard gas mixtures of $CO/CO_2/CH_4/N_2$ and O_2/N_2.

In addition to that, the analysis of the reaction products in the tubulat reactor used for structured catalysts was carried out by mass spectrometry. In this case a *SRS RGA200* quadrupole mass spectrometre was used to monitor the evolution of the masses m/z = 16 for CH_4, 18 for H_2O, 28 for CO, 32 for O_2 and 44 for CO_2.

2.3.2. Reaction protocols

Two main reaction protocols were defined and conducted during the course of this thesis work, one with the aim of measuring the activity and kinetic parameters of the catalysts and the other one with the objective of determining their thermal and hydrothermal stability. In all reaction experiments, 1 g of catalyst granulated to a particle size of 0.25 – 0.30 mm was mixed with 1 g of inert quartz granulated to a particle size of 0.5 – 0.8 mm and placed in the reactor tube. The thermocouple was inserted into the tube up to the point where it was in contact with the catalytic bed, and then locked in place and closed with a steel nut, to minimise gas leaks. The catalytic experiments were carried out with a total

flow of 500 $cm^3\ min^{-1}$ in all cases. Since the bed volume was around 1 cm^3, the corresponding space velocity was 30,000 h^{-1}.

The reaction program for the catalytic determination protocol consisted of an initial pre-heating of the reactor to 200 °C with a N_2 flow until reactor temperature was stable. Then, the reaction mixture, composed of 1%CH_4/10%O_2/89%N_2, was admitted into the reactor. When the feedstream flow was stabilised, the bypass valve was activated and the exit stream was analysed in order to determine its composition without the influence of the catalytic bed. Then, the bypass valve was deactivated, and the heating program was initiated. The heating program involved a stepwise progression, with heating ramps of 1 °C min^{-1} followed by 15-minute isotherm periods each 25 °C, where the analysis of the exit stream was performed. Each chromatographic analysis was run in triplicate, and the methane conversion was calculated based on the difference of the inlet and outlet methane concentrations, as described in Equation 2.10:

$$X_{CH_4} = \frac{[CH_4]_{in} - [CH_4]_{out}}{[CH_4]_{in}} \cdot 100 \tag{2.10}$$

On the other hand, the reaction program for the stability determination included the same initial pre-heating procedure as for the catalytic activity protocol. However, the final temperature value was chosen to be such that methane conversion was around 75%, in any case well below 100%. Once the composition of the feedstream was defined via the bypass valve, the reaction mixture was readmitted into the reactor. After that, the exit stream was analysed every 20 minutes at constant temperature for a period of 25 hours. Then, the water-feeding pump was activated to provide a constant liquid flow of 0.04 $cm^3\ min^{-1}$, which resulted in a feedstream composition of 1%CH_4/10%O_2/10%H_2O/79%N_2. These conditions were maintained for another 25 hours, when the water pump was then deactivated. The complete reaction program consisted of three such cycles, accounting for a total time on stream of 150 hours.

In all cases, to ensure that the obtained kinetic results with powdered catalysts were not affected by mass or heat transfer limitations, the criteria for intra- and extra-particle heat and mass transfer, and temperature gradients were checked, according to the *Eurokin* procedure [160,161]. According to this procedure, nine different criteria must be met in

order to consider the kinetic data representative of the activity of the tested catalysts. The nine considered criteria are the following:

1. Minimum bed length

For the axial dispersion effects in the reactor to be considered negligible, the catalytic bed must have a minimum length such that Equation 2.11 holds as follows:

$$\frac{L_b}{d_p} > \frac{20n}{Bo} \ln\left(\frac{1}{1-X}\right) \tag{2.11}$$

where L_b is the bed length, d_p is the particle diameter, n is the considered reaction order and Bo is the Bodenstein number.

2. Minimum reactor diameter

In order to be able to disregard the wall effects in solid-gas systems, the reactor tube must have a minimum diameter such that Equation 2.12 holds as follows:

$$\frac{d_t}{d_p} > 10 \tag{2.12}$$

3. Extra-particle mass transfer

In order to be able to consider negligible the resistance to the mass transfer outside the catalytic particles, the Carberry number must follow Equation 2.13 as follows:

$$Ca = \frac{r_{v,obs}}{a' k_f C_b} < \frac{0.05}{|n|} \tag{2.13}$$

where a' is the external surface of the catalytic particles ($a' = 6/d_p$ for spherical particles), k_f is the mass transfer coefficient for the fluid phase and $r_{v,obs}$ is the reaction rate per unit volume of catalytic particles.

4. Extra-particle heat transfer

Similarly, for the resistance to the heat transfer outside the catalytic particles to be considered negligible, the Mears criterion (Equation 2.14) for the heat transfer must be met as follows:

$$\gamma\beta_e Ca = \left(\frac{E_a}{RT}\right)\left|\frac{(-\Delta H_r)k_f C_b}{hT}\right|\left(\frac{r_{v,obs}}{a' k_f C_b}\right) < 0.05 \quad (2.14)$$

where the dimensionless temperature (γ) depends on the activation energy of the reaction (E_a), while the heat generation coefficient (β_e) depends on the reaction enthalpy and the heat transfer coefficient (h).

5. Intra-particle mass transfer

In order to be able the disregard the mass transfer resistance inside the pores of the catalytic particles, the Weisz-Prater criterion (Equation 2.15) must be met as follows:

$$\eta\phi^2 = \left(\frac{r_{v,obs}L^2}{D_e C_i}\right)\left(\frac{n+1}{2}\right) < 0.15 \quad (2.15)$$

where L is characteristic dimension of the catalytic particles ($L = d_p/6$ for spherical particles) and D_e is the effective diffusion coefficient of the gas phase.

6. Intra-particle heat transfer

Similarly, to be able to disregard the heat transfer resistance inside the pores of the catalytic particles, Equation 2.16, which is based on the Weisz-Prater criterion, must hold as follows:

$$\gamma\beta_i(\eta\phi^2) = \left(\frac{E_a}{RT}\right)\left|\frac{(-\Delta H_r)D_e C_i}{\lambda_e T}\right|\left(\frac{r_{v,obs}L^2}{D_e C_i}\right) < 0.1 \quad (2.16)$$

where λ_e is the effective thermal conductivity of the catalytic particles.

7. Radial temperature gradient

In order to consider negligible the temperature gradient in the radial direction of the reactor tube, Equation 2.17 should hold as follows:

$$\frac{E_a}{RT}\left|\frac{(-\Delta H_r)r_{v,obs}(1-\varepsilon)(1-b)r_t^2}{\lambda_e T}\right|\left(\frac{1}{8}+\frac{1}{Bi}\frac{d_p}{d_t}\right) < 0.05 \quad (2.17)$$

where (1-b) is the volumetric fraction of catalyst in the bed and Bi is the Biot number.

8. Bed dilution

In order to be able to disregard the effect of the catalytic bed dilution over the conversion achieved by the catalyst, Equation 2.18 must hold as follows:

$$\frac{2.5bd_p}{(1-b)L_p} < 0.05 \tag{2.18}$$

where b is the volumetric fraction of inert diluent, so (1-b) is the volumetric fraction of the catalyst.

9. Intra-particle temperature gradient

The temperature gradient inside the catalytic particle should be, at most, of 0.3 °C to be considered negligible. This temperature gradient can be calculated by Equation 2.19 as follows:

$$\Delta T_{max} = \frac{\Delta H_r D_e C_i}{\lambda_e} < 0.3 \tag{2.19}$$

Prior to performing the aforementioned calculations, several parameters needed to be measured and/or calculated following various equations and correlations. A summary of these parameters and their respective method of determination can be found in Table 2.3.

Table 2.3. Summary of the parameters used in the calculations of the thermo-diffusional limitations.

Parameter	Method of determination	Value
Axial diffusivity (D_{ax}), $m^2\ s^{-1}$	Wakao Equation [162]	$2.1 \cdot 10^{-5}$-$6.2 \cdot 10^{-5}$
Bed length (L_b), m	Direct measurement	0.022
Bed porosity (ε_b)	Direct measurement	0.567
Bed tortuosity (τ_b)	Puncochar-Drahos correlation [163]	1.328
Bodenstein number (Bo)	$Bo = u \cdot d_p / D_{ax}$	0.65-1.89
Density of species i (ρ_i), $kg\ m^{-3}$	Ideal gas law	0.21-0.41 (CH_4) 0.42-0.83 (O_2) 0.37-0.72 (N_2)

Table 2.3 (cont.). Summary of the parameters used in the calculations of the thermo-diffusional limitations.

Diffusivity coefficients of species i in the gaseous mixture ($D_{i,MIX}$), $m^2\ s^{-1}$	Fuller-Schettler-Giddings correlation [164]	0.49-1.44 (CH_4)
Dynamic viscosity of species i (μ_I), $kg\ m^{-1}\ s^{-1}$	Sutherland equation [165]	$1.9\cdot10^{-5}$-$3.1\cdot10^{-5}$ (CH_4) $2.9\cdot10^{-5}$-$4.5\cdot10^{-5}$ (O_2) $2.5\cdot10^{-5}$-3.8 (N_2)
Effective diffusivity of species i to the catalytic particles ($D_{e,i}$), $m^2\ s^{-1}$	$1/D_{e,i} = 1/D_{bulk} + 1/D_{knudsen}$	$9.3\cdot10^{-6}$-$1.3\cdot10^{-5}$ (CH_4)
Heat transfer coefficient (h), $W\ m^{-2}\ K^{-1}$	$Nu = h\cdot d_p/\lambda_{MIX}$	396-554
Mass transfer coefficient (k_f), $m\ s^{-1}$	Chilton-Colburn analogy [166]	0.042
Particle diameter (d_p), m	Direct measurement	$2.74\cdot10^{-4}$
Reaction enthalpy (ΔH_r), $kJ\ mol^{-1}$	From database	-801
Specific heat capacity of species i ($C_{p,I}$), $J\ mol^{-1}\ K^{-1}$	Shomate equation	45-69 (CH_4) 31-35 (O_2) 29-32 (N_2)
Thermal conductivity of gaseous mixture (λ_{MIX}), $W\ m^{-1}\ K^{-1}$	Modified Eucken model [167]	0.037-0.061
Thermal conductivity of catalytic particles (λ_e), $W\ m^{-1}\ K^{-1}$	From database	15
Tube diameter (d_t), m	Direct measurement	$8.55\cdot10^{-3}$

Chapter 3

CATALYTIC COMBUSTION OF METHANE OVER BULK Co_3O_4

ABSTRACT

This chapter deals with the optimisation of the synthesis methodology to prepare bulk pure Co_3O_4 catalysts that are active for the complete oxidation of methane under lean conditions. The examined routes were selected due to their relatively low complexity and their easiness for scale-up, and involved direct calcination, reactive grinding, precipitation, precipitation-oxidation, solution combustion synthesis and sol-gel complexation. The synthesised catalysts were characterised and kinetically investigated to identify the most suitable synthesis route, which was precipitation with sodium carbonate. In addition, attention was paid to analysing the effect of the calcination temperature of the catalytic precursor obtained by the aforementioned precipitation route. Again, the characterisation and catalytic testing were combined to evidence that the most suitable calcination temperature for the catalytic precursor was 600 °C. Finally, the influence of the residual sodium that could be present in the catalytic precursor on the activity of the final catalyst was determined. Thus, the sodium ions were found to have a detrimental effect on the surface properties of the resulting Co_3O_4 catalyst, thereby revealing their removal during the synthesis was deemed essential.

3. CATALYTIC COMBUSTION OF METHANE OVER BULK Co_3O_4

Spinel-type cobalt oxide (Co_3O_4) is a highly active catalyst for oxidation of CO and light hydrocarbons as mentioned in Chapter 1. The properties that make this material efficient for these reactions can be also adequate for oxidation of methane, although with a more limited efficiency owing to the high stability of this molecule. Bulk Co_3O_4 catalysts can be synthesised by a vast amount of methodologies with several degrees of complexity. The physico-chemical properties of the resulting catalysts usually vary from one to the other. Despite the wide range of synthesis parameters, almost all routes share a common final step where a given catalytic precursor is subjected to a controlled calcination process to form the final catalyst. The specific temperature of this thermal step also possesses a strong influence on the characteristics of the obtained catalyst.

For these reasons, the objective of this chapter is to determine the most suitable synthesis methodology for the production of bulk Co_3O_4 catalysts for methane combustion. The examined synthesis routes were chosen among those with lower complexity in order to facilitate a posterior scale-up to industrial level. Also, for the methodology that produced the catalyst with the best performance, a study of the effect of the calcination temperature and the washing step of the catalytic precursor was performed.

3.1. SELECTION OF THE SYNTHESIS METHOD

For the selection of the optimal synthesis route to obtain a bulk Co_3O_4 catalyst for methane oxidation, eight Co_3O_4 samples were prepared with various methodologies. The investigated methodologies were direct calcination of cobalt nitrate (DC) and cobalt hydroxycarbonate (HC), basic reactive grinding with ammonium hydrogen carbonate (GB), precipitation with ammonium carbonate (CN) and sodium carbonate (CC), wet precipitation-oxidation with sodium hydroxide (OW), solution combustion synthesis with glycine (SCS) and sol-gel complexation with citric acid (SG). Except for the HC sample, the used cobalt precursor was cobalt (II) nitrate hexahydrate. Additionally, a commercial Co_3O_4 sample was purchased from *Alfa Aesar* (COM), to serve as a reference. Note that the specific synthesis route of this sample was unknown.

3.1.1. Description of the synthesis methodologies

Firstly, both methodologies based on direct calcination implied a simple thermal activation in static air in a muffle oven of a given cobalt salt. Particularly, certain amounts of cobalt (II) nitrate hexahydrate (around 18 g, $Co(NO_3)_2 \cdot 6H_2O$, *Fluka*) and cobalt hydroxycarbonate (about 6.5 g, $Co_2CO_3(OH)_2$, *Panreac*) were calcined, leading to the so-called DC and HC samples, respectively.

The reactive basic grinding (GB) synthesis route involved grinding a mixture of 9 g of cobalt (II) nitrate hexahydrate and 6.1 g of ammonium hydrogen carbonate ($(NH_4)HCO_3$, *Fluka*) in an agate mortar for 30 minutes. The mixture behaved like a heterogeneous physical mixture for the first minutes of grinding. Afterwards, the two components started reacting between themselves to produce a homogeneous paste that was later dried and subjected to calcination.

Regarding the precipitation methodologies, three different approaches were investigated, although the common experimental protocol was fairly similar. In the three cases, a 100 cm^3 aqueous solution of cobalt nitrate (II) hexahydrate was placed in the synthesis reactor and heated to 80 °C. Then, the precipitation of a cobalt precursor was induced by the dropwise addition of a precipitating agent, until the pH reached 8.5. After their respective precipitation processes, each solid was filtered and thoroughly washed with, at least, 8 L of deionised hot water. The precipitates were then dried in static air at 110 °C for 16 hours and submitted to calcination to form the final catalysts.

As for the CN catalyst, the precipitating agent was a solution of ammonium carbonate 1M, while a solution of sodium carbonate 1.2M was used for the CC sample. Finally, in the case of the OW sample the precipitating agent was an aqueous solution of NaOH 3.2M. Once the precipitation was complete, 100 cm^3 of 50%H_2O_2/50%H_2O (*Sigma Aldrich*) were added dropwise to the reaction mixture.

The solution combustion synthesis (SCS) route involved the flameless combustion of an organic fuel (glycine) with an oxidiser (cobalt (II) nitrate hexahydrate), which generated the energy necessary to transform the cobalt species into cobalt oxide. The synthesis methodology consisted of preparing a solution (50 cm^3) of the cobalt salt and glycine. A small volume of this solution (around 2 cm^3) was placed inside a muffle oven, where it was first heated at 250 °C for 30 minutes and then subjected to calcination.

The stoichiometric concentrations of glycine and cobalt nitrate were chosen for the complete combustion of the fuel and nitrates into CO_2, H_2O and N_2, as shown in Equation 3.1:

$$3Co(NO_3)_2 + \frac{28}{9}C_2H_5O_2N \longrightarrow Co_3O_4 + \frac{14}{9}CO_2 + \frac{70}{9}H_2O + \frac{41}{9}N_2 \qquad (3.1)$$

Finally, the sol-gel (SG) approach was based on the complexation of cobalt (II) nitrate hexahydrate with citric acid. Thus, 3.5 g of citric acid were added to 250 cm^3 of a solution of the cobalt salt 0.1M. The solution was heated to 40 °C to progressively evaporate the water until the formation of a viscous gel. The gel was subsequently introduced in a drier at 70 °C to further evaporate the remaining water during 16 hours. The result was a spongy, highly hygroscopic material that was crushed and calcined in a muffle oven.

All cobalt catalytic precursors, including the commercial sample (COM), were calcined in static air as the last step of each specific synthesis route. The calcination protocol was defined based on the results obtained from a previous thermogravimetric analysis performed over cobalt hydroxycarbonate selected as a reference precursor. This experiment involved three heating steps separated by 30-minute isotherms as described in Table 3.1:

Table 3.1. Parameters of the calcination process.

Initial temp., °C	Final temp., °C	Heating ramp, °C min^{-1}	Isothermal time, min
Ambient	125	5	30
125	300	1	30
300	600	5	240

3.1.2. Physico-chemical characterisation of the catalysts

The described synthesis methodologies produced a family of eight bulk Co_3O_4 catalysts along with a commercial sample. The textural properties of these oxides in terms of specific surface area, pore volume and pore size distribution were determined by N_2 physisorption. The results are summarised in Table 3.2. All samples presented type IV isotherms (see Figure 3.1) with H2 hysteresis cycles, although some of the hysteresis cycles were difficult to note due to the low adsorbed volume of some of the oxides. The specific surface area varied from 5 to 16 $m^2 g^{-1}$. The pore volume followed a relatively consistent trend with respect to the surface area. Thus, the samples with lowest specific surface area (DC and SG samples) also showed the lowest pore volume values (0.02 and 0.01 $cm^3 g^{-1}$, respectively), while the sample with the highest specific surface area (GB sample) also presented the largest pore volume (0.10 $cm^3 g^{-1}$). Nevertheless, some discrepancies to this trend were also found that could be attributed to the differences in the mean pore diameter. For instance, despite the fact that both CC and SCS samples exhibited a specific surface area of 14 $m^2 g^{-1}$, the former presented a pore volume twice as large as the latter. This was because the pores in the CC sample were significantly larger than in the SCS sample, thereby occupying a larger volume for the same specific surface area.

Table 3.2. Textural and structural properties of the bulk Co_3O_4 catalysts.

Catalyst	BET surface, $m^2 g^{-1}$	Pore volume, $cm^3 g^{-1}$	Mean pore diameter, Å	Crystallite size, nm
DC	5	0.02	355	84
HC	12	0.06	350	64
GB	16	0.10	275	58
CN	6	0.02	460	92
CC	14	0.09	255	63
OW	9	0.02	170	86
SCS	14	0.04	170	89
SG	5	0.01	370	102
COM	8	0.03	410	75

On the other hand, the average pore diameter of the samples varied from 170 Å for the OW and SCS samples to 460 Å for the CN sample. However, a detailed inspection of the pore size distributions, included in Figure 3.2, revealed some differences between the prevalent pore diameter and the mean pore diameter of various samples.

Firstly, although both OW and SCS samples exhibited a mean pore size of 170 Å, however, their respective pore size distributions were notably different. The SCS sample presented a bimodal distribution with maxima around 90 and 700 Å, while the OW sample was characterised by a relatively homogeneous distribution with an extremely small maximum at around 800 Å. In addition, the SG sample displayed a pore size distribution very similar to that of the OW sample, with a small maximum at around 1090 Å. Nevertheless, their respective mean pore sizes were notably different (370 and 170 Å, respectively).

Several samples exhibited pore size distributions with marked maxima in somewhat comparable values. In particular, the CC, GB, HC and DC oxides showed unimodal distributions centred in the mesopore region. The CC and GB samples presented very similar distributions centred around 335 Å, in agreement with their akin mean pore diameter (255-275 Å). In this sense, the HC and DC samples also presented almost equivalent mean pore sizes (350 Å) in line with their comparable size distributions, although the former exhibited a larger pore volume.

The structural properties of the bulk catalysts were investigated by XRD. Figure 3.3 shows the diffraction patterns of the nine samples. All catalysts exhibited diffraction signals located at 2θ positions of 19.0, 31.3, 36.8, 44.8, 59.3 and 65.2°, assignable to a cubic phase with spinel structure that can only be attributed to the presence of spinel type cobalt oxide (Co_3O_4), as specified in its corresponding ICDD card (00-042-1467). No diffraction signals from other cobalt phases such as CoO or metallic Co were detected, although the SCS sample presented some additional signals that were identified to be due to the presence of traces of the refractory material from the oven where it was prepared.

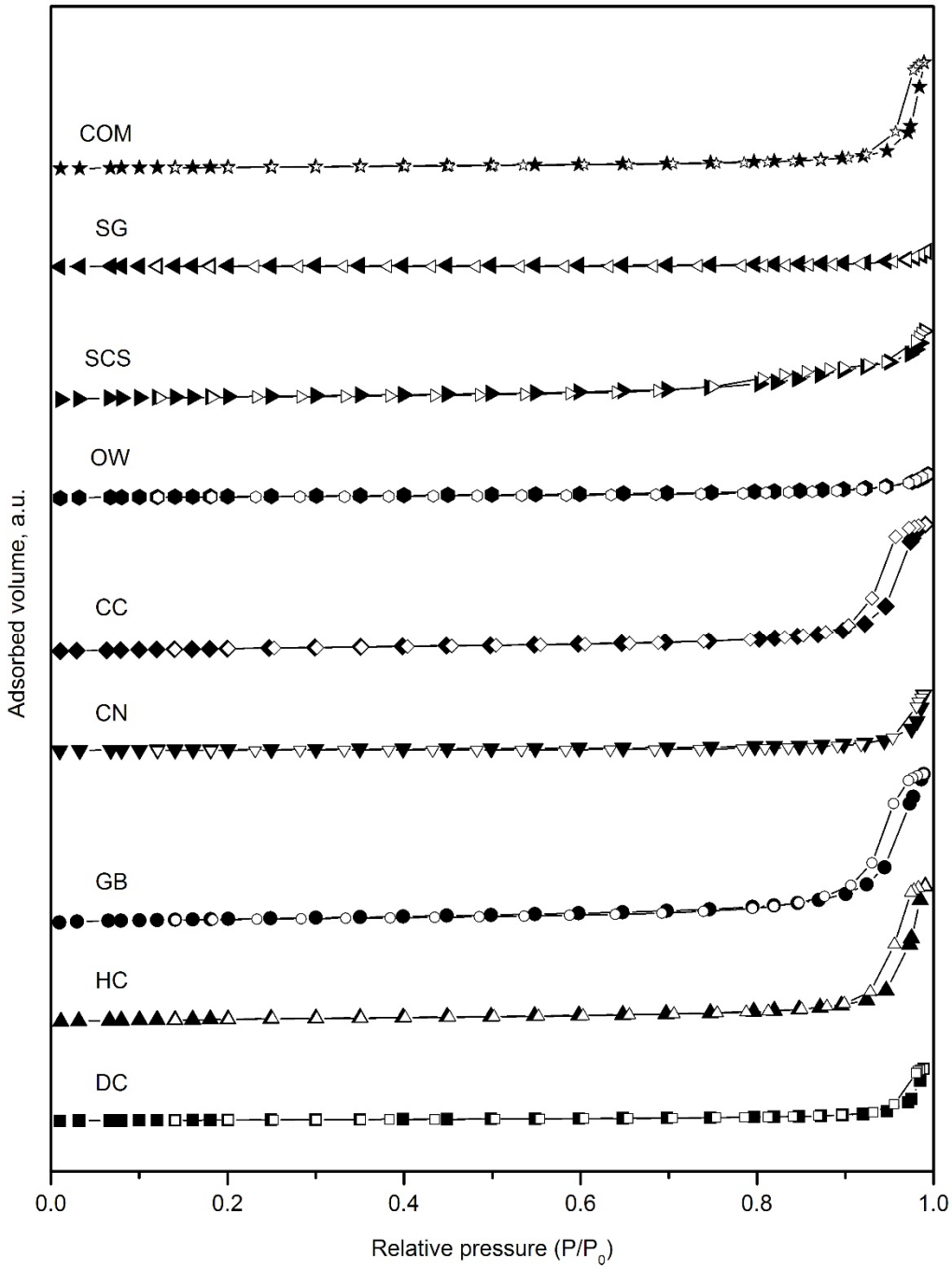

Figure 3.1. N_2 physisorption isotherms of the bulk Co_3O_4 catalysts.

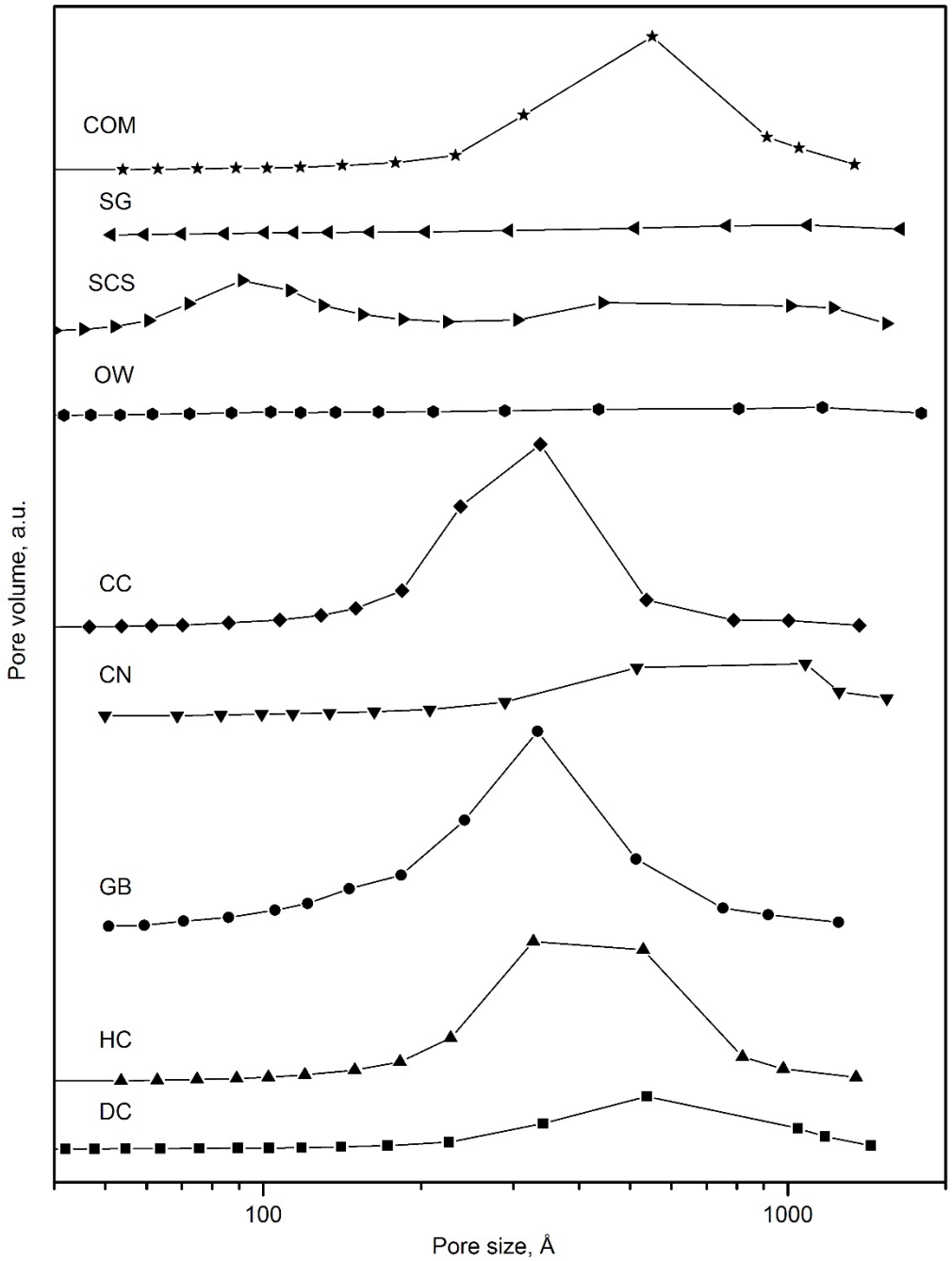

Figure 3.2. Pore size distributions of the bulk Co_3O_4 catalysts.

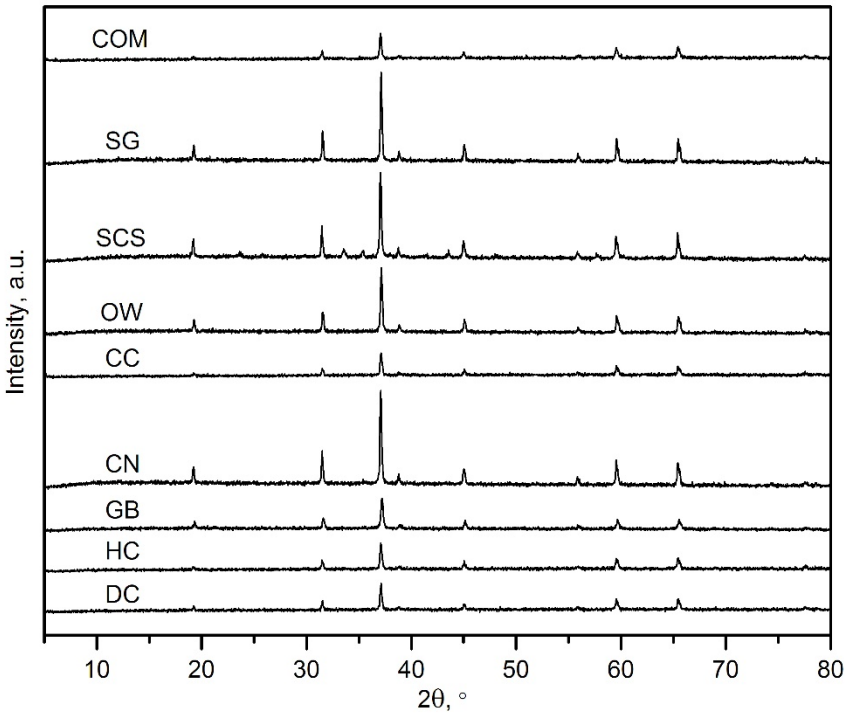

Figure 3.3. XRD patterns of the bulk Co_3O_4 catalysts.

The average Co_3O_4 crystallite size (Table 3.2) was estimated by the application of the Scherrer equation with the Full Width Half Maximum (FWHM) of the most intense signal of the spinel, located at $2\theta = 36.8°$ and corresponding to the (3 1 1) plane. The crystallite size varied from 58-64 nm for the GB, CC and HC samples to 102 nm for the SG sample. A relatively clear inverse relationship was found between the textural properties in terms of specific surface area and pore volume and the structural properties in terms of crystallite size. This was expected since smaller crystallites tend to exhibit larger available surface areas [168,169].

The reducibility of the synthesised oxides was investigated by means of the H_2-TPR technique. The corresponding reduction profiles are depicted in Figure 3.4. All reduction profiles presented a two-step reduction process, although their relative position and shape varied significantly.

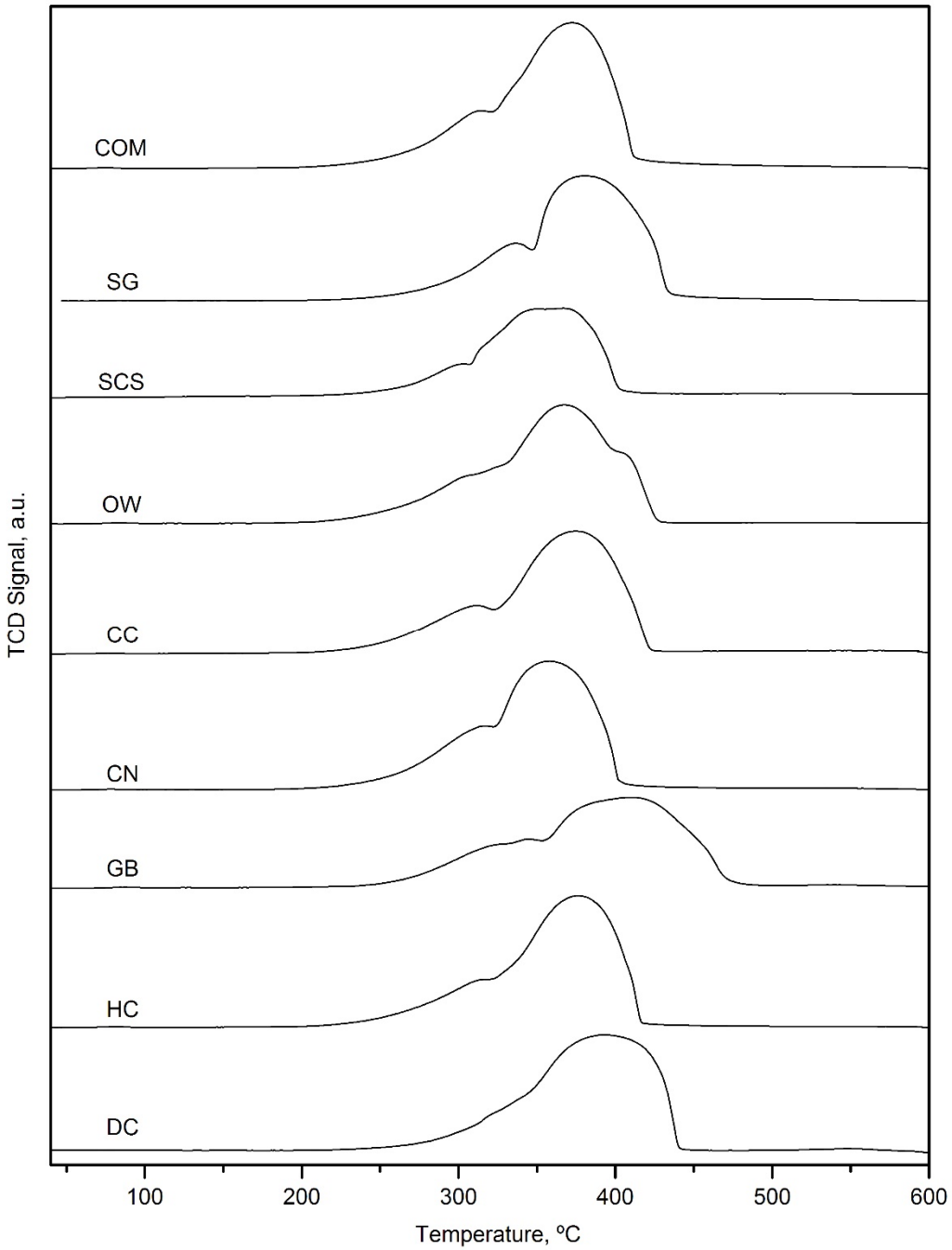

Figure 3.4. H_2-TPR profiles of the bulk Co_3O_4 catalysts.

The first reduction event, centred between 300 and 330 °C, corresponded to the reduction of Co^{3+} cations into Co^{2+} (Eq. 3.2), while the second one, located at around 350-400 °C, was attributed to the reduction of the Co^{2+} cations to metallic cobalt Co^0 (Eq. 3.3) [170,171]. This second reduction process is often not homogeneous, and several different contributions can be identified, thus suggesting the presence of various types of Co^{2+} species with different degrees of reducibility. No other hydrogen uptakes were detected above 500 °C. It was therefore concluded that the only reducible phase in the samples was Co_3O_4.

$$Co_3O_4 + H_2 \longrightarrow 3CoO + H_2O \quad (3.2)$$

$$3CoO + 3H_2 \longrightarrow 3Co + 3H_2O \quad (3.3)$$

After integration and quantitative evaluation of the TPR profiles, the specific hydrogen uptake of each reduction step and their corresponding ratio were computed, as shown in Table 3.3. In all cases, the total amount of hydrogen consumed during the reduction process was close to 16.6 mmol g^{-1}, which coincided with the stoichiometric amount required for the complete reduction of Co_3O_4. Ideally, the relative H_2 uptake between the low-temperature and high-temperature contributions would be 0.33. However, this ratio varied between 0.19 for the DC sample to 0.38 for the CC sample. This revealed marked differences in reducibility and relative distribution of the reducible species (Co^{3+} and Co^{2+} species) with the synthesis methodology.

Moreover, the temperature for the onset of reduction, defined as the temperature at which 5% of the total H_2 uptake was consumed, also evidenced important variations. Hence, the onset temperature shifted from 265 °C for the CC catalyst, to 300 °C for the DC sample. The onset temperature was roughly correlated with the aforementioned ratio between low- and high-temperature uptakes, where the samples that started to be reduced at lower temperatures also tended to consume larger H_2 amounts at low temperatures. However, this trend was not fully consistent for all the samples, since the onset temperature was also influenced by the textural and structural properties of the samples.

Table 3.3. Results of the H_2-TPR analysis of the bulk Co_3O_4 catalysts.

Catalyst	Low-temperature H_2 uptake, mmol g^{-1}	High-temperature H_2 uptake, mmol g^{-1}	Relative H_2 uptake at low and high temperature	Reduction onset temperature, °C
DC	2.6	13.9	0.19	300
HC	3.3	13.4	0.25	270
GB	4.3	12.4	0.34	285
CN	4.1	12.6	0.32	270
CC	4.6	12.0	0.38	265
OW	3.4	12.3	0.25	270
SCS	3.9	12.7	0.30	280
SG	4.0	12.7	0.32	290
COM	4.2	12.4	0.34	275

The analysis by H_2-TPR allowed the degree of reducibility of the samples to be estimated, which was presumed a key catalytic property as also reported elsewhere [172-174]. On one hand, some samples, namely CC, GB, CN and COM oxides, revealed relatively high H_2 uptakes at low temperatures (4.1-4.5 mmol H_2 g^{-1}) with low onset temperatures (265-285 °C), thus showing a high reducibility. On the other hand, the DC, OW and HC samples were characterised by ratios between the low- and high-temperature uptakes (0.19-0.25) below the stoichiometric value (0.33), and relatively high onset temperatures (270-300 °C), thereby exhibiting a poorer reducibility.

3.1.3. Catalytic performance of the synthesised catalysts

The catalytic efficiency of each bulk Co_3O_4 catalyst for the complete oxidation of lean methane was assessed by defining their respective light-off curves (GHSV = 30,000 h^{-1}). Since the calcination process would stabilise the catalysts up to the calcination temperature (600 °C), light-off curves were taken between 200 and 600 °C. For each sample, three consecutive tests were performed. In all cases, the second and third cycles were characterised by an identical light-off curve. Thus, data from the third cycle are shown in Figure 3.5. This revealed that the first cycle worked as a "conditioning" cycle and, after that, the catalysts became stable under the studied reaction conditions.

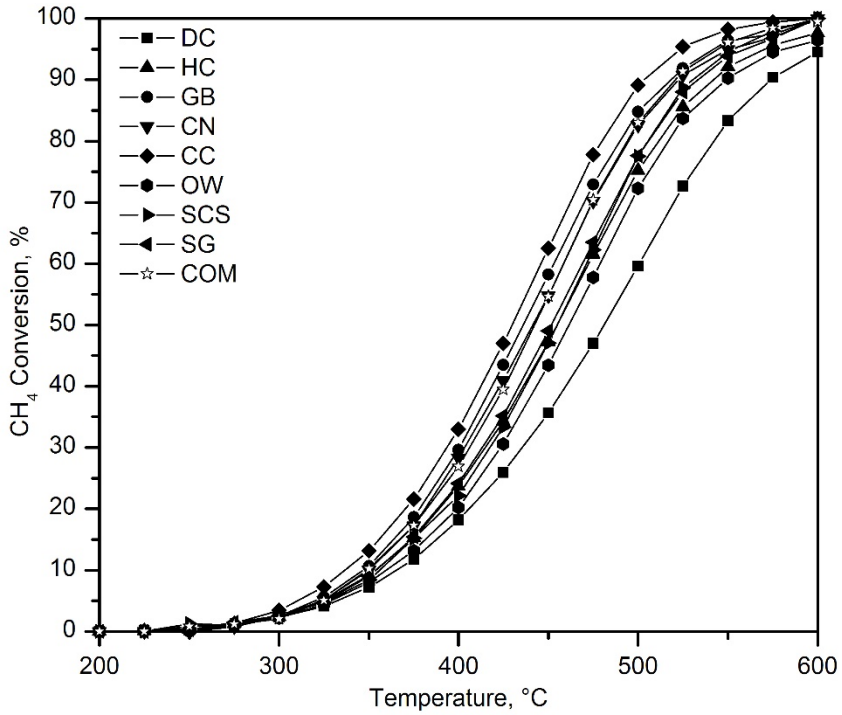

Figure 3.5. Light-off curves of the bulk Co_3O_4 catalysts.

As explained in Chapter 2, the criteria for intra-particle and extra-particle mass and energy diffusion, as well as the temperature gradients were checked to be above the limit, to ensure that any diffusional effects did not affect the kinetic results. In this sense, Table 3.4 shows the calculated values for the various evaluated criteria over the CC catalyst.

All synthesised catalysts exhibited a 100% selectivity towards CO_2 formation. Based on the T_{50} values (temperature required to achieve 50% CH_4 conversion), the following trend was noticed: CC › GB › CN › COM › SG › SCS › HC › OW › DC. Interestingly, the bulk oxides that achieved the lowest T_{50} values were those that presented a promoted reducibility, according to the H_2-TPR results.

The reaction rate of the catalysts was calculated at 375 °C using the differential method, that is, for methane conversions lower than 20%. The estimated values were in the 1.06-1.83 mmol CH_4 g_{Co}^{-1} h^{-1} range (Table 3.5). The CC catalyst exhibited the highest specific activity, followed by the COM (1.68 mmol CH_4 g_{Co}^{-1} h^{-1}) and the GB (1.60 mmol CH_4 g_{Co}^{-1} h^{-1})

catalysts. In contrast, the DC (1.06 mmol CH_4 g_{Co}^{-1} h^{-1}) and OW (1.11 mmol CH_4 g_{Co}^{-1} h^{-1}) samples achieved the slowest reaction rates.

Table 3.4. Criteria for accurate analysis of intrinsic reaction rates (as evaluated for the CC catalyst at 375 °C).

Criterion number	Recommendation	At 375 °C	Least favourable conditions
1.	Bodenstein parameter $< L_{bed}/d_{particle}$	4.5 < 79.5	55.6 < 79.5[a]
2.	$d_{tube}/d_{particle} > 10$	31.2	31.2
3.	Carberry number < 0.05/n	0.0042	0.046[a]
4.	$\gamma\beta_e Ca < 0.05$	0.0017	0.028[b]
5.	Wheeler-Weisz modulus < 0.15	$4.3 \cdot 10^{-4}$	$8.0 \cdot 10^{-4}$[c]
6.	Mears parameter < 0.1	$2.0 \cdot 10^{-6}$	$4.2 \cdot 10^{-6}$[c]
7.	Radial gradient < 0.05	0.004	0.0057[c]
8.	Bed dilution parameter < 0.05	0.047	0.047
9.	Temperature gradient < 0.3	0.15	0.175[b]

[a]Determined at 500 °C; [b]Determined at 600 °C; [c]Determined at 450 °C.

Table 3.5. Kinetic results of the bulk Co_3O_4 catalysts.

Catalyst	T_{50}, °C	Reaction rate at 375 °C, mmol CH_4 g_{Co}^{-1} h^{-1}	E_a, kJ mol^{-1}
DC	480	1.06	71 ± 2
HC	455	1.44	74 ± 2
GB	435	1.60	74± 1
CN	440	1.43	74 ± 2
CC	430	1.83	74 ± 2
OW	460	1.11	73 ± 2
SCS	455	1.21	75 ± 1
SG	450	1.19	73 ± 2
COM	440	1.68	74 ± 1

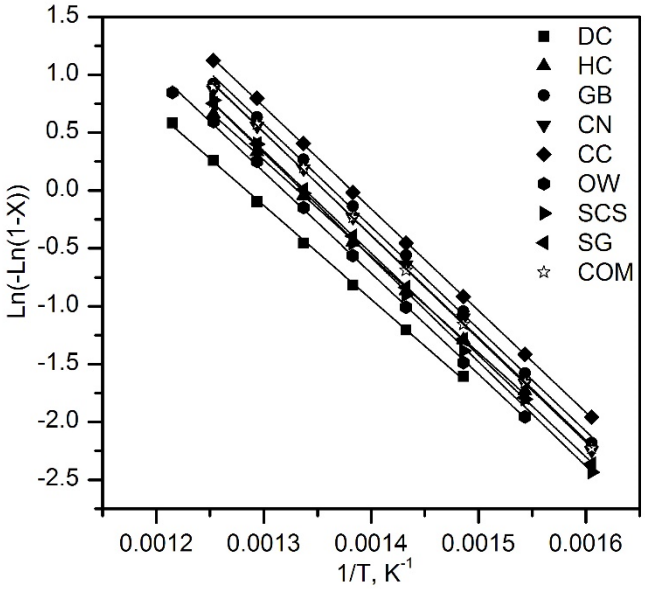

Figure 3.6. Pseudo-first order fit for the experimental data obtained over the various bulk Co_3O_4 catalysts.

The activation energy of all synthesised samples were quite similar (71–75 kJ mol^{-1}) and comparable with the values reported in the literature for methane oxidation over cobalt oxide catalysts [175-178]. Therefore, it could be concluded that Co_3O_4 was the only active phase in the synthesised catalysts.

3.2. EFFECT OF THE CALCINATION TEMPERATURE

From the eight methodologies studied, the catalyst prepared by precipitation with sodium carbonate (CC) exhibited the best behaviour owing to its promoted reducibility. Although the textural and structural properties of this catalyst were slightly superior to the other investigated oxides, even so they were relatively poor, as expected for a bulk sample. These properties are, however, notably sensitive to the chosen calcination temperature to form the final catalyst. Therefore, optimising the thermal activation is of notable importance.

With the aim of determining the influence of calcination temperature on the properties of the CC oxide, the catalytic precursor prepared by precipitation with sodium carbonate was calcined between 400 and 800 °C. Particularly, the selected temperatures were 400, 500, 600, 700 and 800 °C. The calcination protocol was identical to the one described in Table 3.1, with the final calcination temperature being the one selected for each particular precursor. The corresponding samples were characterised and catalytically evaluated.

3.2.1. Physico-chemical characterisation of the catalysts

The characterisation of these catalysts was similar to that followed in the previous section devoted to the determination of the most efficient synthesis route. Thus, the textural and structural properties were initially investigated by N_2 physisorption and XRD, respectively. The results are summarised in Table 3.6. All samples exhibited type IV isotherms with H2 hysteresis cycles. The specific surface area of the oxides was in the 2-37 $m^2\ g^{-1}$ range whereas the pore volumes were between 0.01 and 0.13 $cm^3\ g^{-1}$.

Table 3.6. Textural and structural properties of the bulk Co_3O_4 (CC) catalysts submitted to varying calcination temperature.

Calcination temperature, °C	BET surface, $m^2\ g^{-1}$	Pore volume, $cm^3\ g^{-1}$	Crystallite size, nm
400	37	0.11	29
500	27	0.13	38
600	14	0.09	63
700	9	0.03	78
800	2	0.01	132

The pore size distribution of the synthesised catalysts was clearly negatively affected by the calcination temperature, as shown in Figure 3.7. All catalysts exhibited a unimodal distribution with a maximum that was located at around 200 Å for the sample treated at 500 °C, and progressively shifted towards larger pore sizes up to 600 Å for the oxide calcined at 800 °C, although the pore volume of this sample was extremely low (0.01 $cm^3\ g^{-1}$). The catalyst treated at 400 °C did not seem to follow this trend, and instead presented a bimodal distribution with a large maximum at around 600 Å, and an additional small peak in the micropore range (around 20 Å). This suggested that the calcination process at this low

temperature was either not complete, or it did not proceed through the same thermal phenomena as the rest of the samples.

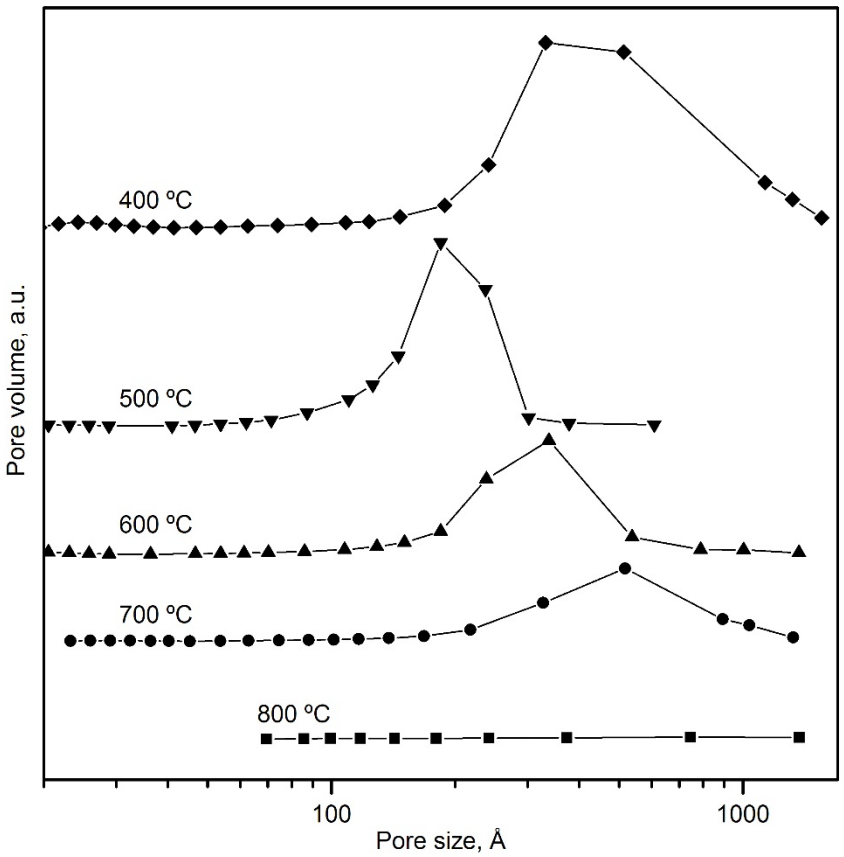

Figure 3.7. Pore size distributions of the bulk Co_3O_4 (CC) catalysts submitted to varying calcination temperatures.

The XRD analysis of the samples visibly evidenced the significant effect that the calcination temperature had on the structural properties. The diffractograms of the oxides (Figure 3.8) revealed a notable increase in their crystallinity with the calcination temperature, with the diffraction signals becoming more intense and sharp as the temperature increased. None of the samples evidenced the presence of any other phase than Co_3O_4.

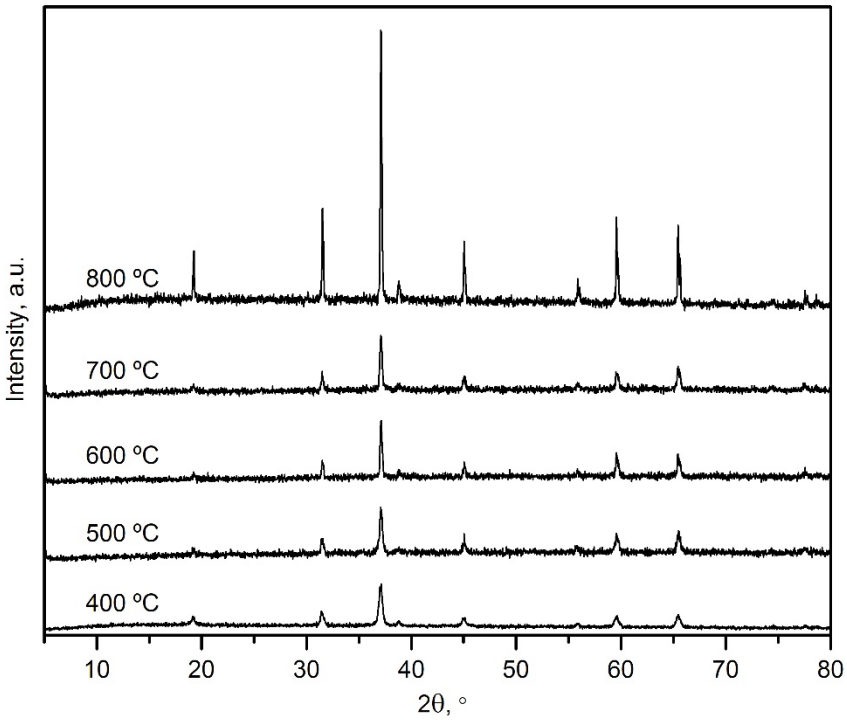

Figure 3.8. XRD patterns of the bulk Co_3O_4 (CC) catalysts submitted to varying calcination temperatures.

The application of the Scherrer equation to the main signal at $2\theta = 36.8°$ allowed for the estimation of the crystallite size (Table 3.5). It varied from 29 nm for a calcination temperature of 400 °C, to 132 nm for a calcination temperature of 800 °C. The increasing trend clearly pointed out the crystallite sintering at high temperatures. Moreover, when compared with the results obtained from the textural characterisation, a clear correlation between the specific surface area and the calcination temperature was found, as demonstrated in Figure 3.9.

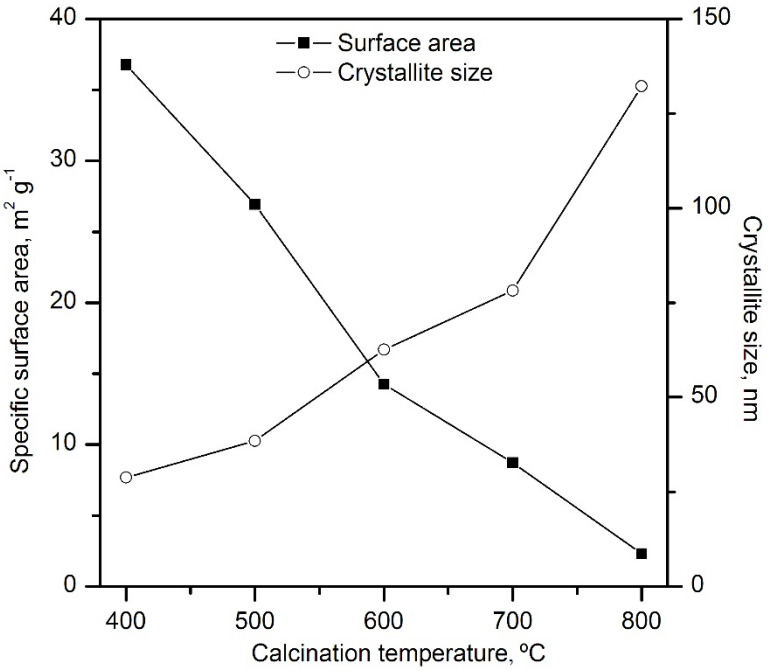

Figure 3.9. Evolution of the textural and structural properties of the bulk Co_3O_4 (CC) catalysts with varying calcination temperatures.

The calcination temperature also had a strong detrimental effect on the reducibility of the prepared catalysts, as shown by the H_2-TPR profiles included in Figure 3.10. All samples showed the expected two-step reduction process for the complete reduction of Co_3O_4. However, the calcination temperature greatly influenced the position of the peak reduction temperatures and the ratio between the low- and high-temperature H_2 uptakes.

On one hand, elevated calcination temperatures provoked a shift of both reduction events towards higher temperatures, probably due to the sintering effect that worsened the textural and structural properties of the resultant oxides. Thus, the low-temperature reduction step was centred at 275 °C for the sample calcined at 400 °C, whereas it was located at around 335 °C for the oxide calcined at 800 °C. Analogously, the high-temperature contribution shifted from 340 °C up to 390 °C.

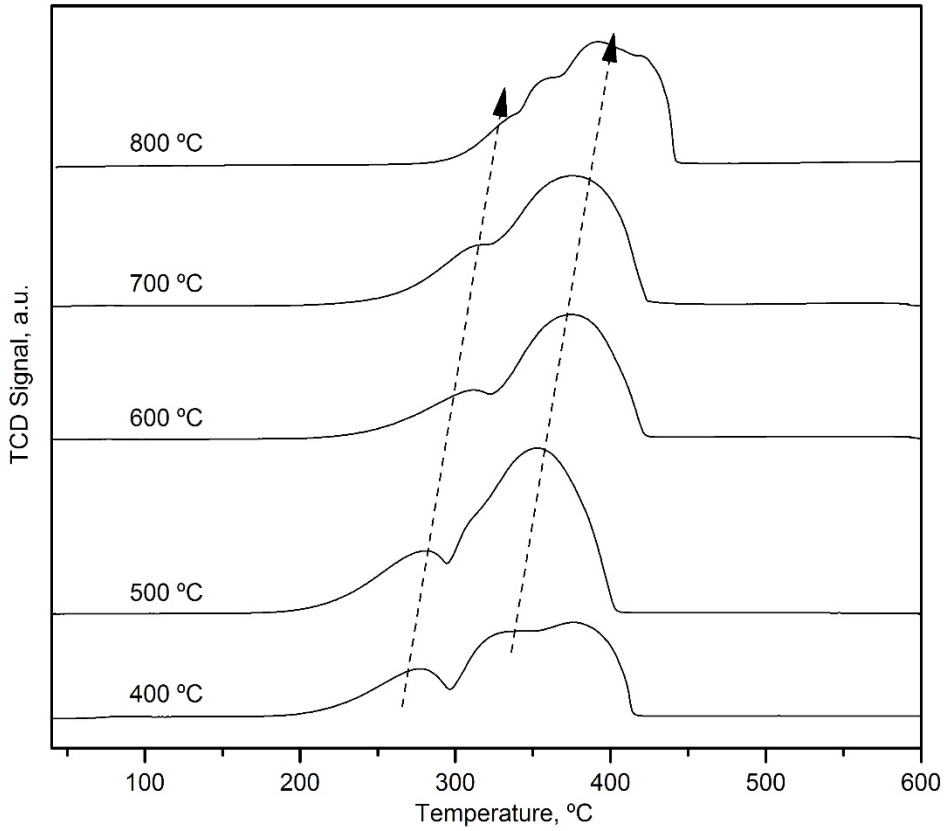

Figure 3.10. H_2-TPR profiles of the bulk Co_3O_4 (CC) catalysts submitted to varying calcination temperatures.

On the other hand, the ratio between the low- and high-temperature contributions (Table 3.7), related to the relative presence of Co^{3+} and Co^{2+} species, presented an optimal value for the sample calcined at 600 °C. For lower calcination temperatures, the lower ratio could be attributed to an incomplete formation of Co_3O_4 due to insufficient temperature during the calcination process, as the pore size distribution of the sample calcined at 400 °C already suggested. However, the amount of not converted precursor could not be large, since no other phase than Co_3O_4 was apparently detected in the XRD analysis. Similarly, for higher calcination temperatures (800 °C), the observed lower ratio (0.14) could be assigned to the partial reduction of the Co_3O_4 to CoO [179]. The formation of this cobalt oxide could also be evidenced by the slightly lower total H_2 uptake of the sample calcined at 800 °C (16.2 mmol g^{-1}) with respect to the rest of the samples.

Table 3.7. Results of the H_2-TPR analysis of the bulk Co_3O_4 (CC) catalysts submitted to varying calcination temperatures.

Calcination temperature, °C	Low-temperature H_2 uptake, mmol g^{-1}	High-temperature H_2 uptake, mmol g^{-1}	Relative H_2 uptake at low and high temperature	Reduction onset temperature,°C
400	3.7	12.9	0.29	245
500	3.9	12.7	0.31	250
600	4.6	12.0	0.38	265
700	3.8	12.8	0.30	280
800	2.0	14.2	0.14	325

3.2.2. Catalytic performance of the synthesised catalysts

The light-off curves of the catalysts calcined at varying temperatures are shown in Figure 3.11 (GHSV = 30,000 h^{-1}). As previously explained, the calcination process stabilises the catalysts up to the selected temperature. For this reason, the light-off curve of each catalyst was only monitored up to its respective calcination temperature. Note that if the catalyst were allowed to operate at a temperature higher than their calcination temperature, their physico-chemical properties would be altered and no correlation with the catalytic activity could be reliably established. The reaction runs were conducted at 30,000 $cm^3\ g^{-1}\ h^{-1}$.

The T_{50} values of the catalysts monotonously increased with the calcination temperature from 360 °C for the oxide calcined at 400 °C, up to 590 °C for the sample calcined at 800 °C. However, due to the different temperature domains, this parameter could not be used to discern the most suitable catalyst. Instead, the optimal calcination temperature was taken as the lowest that would allow the corresponding catalyst to achieve complete methane conversion. Hence, the calcination temperature of 600 °C was identified as the most appropriate.

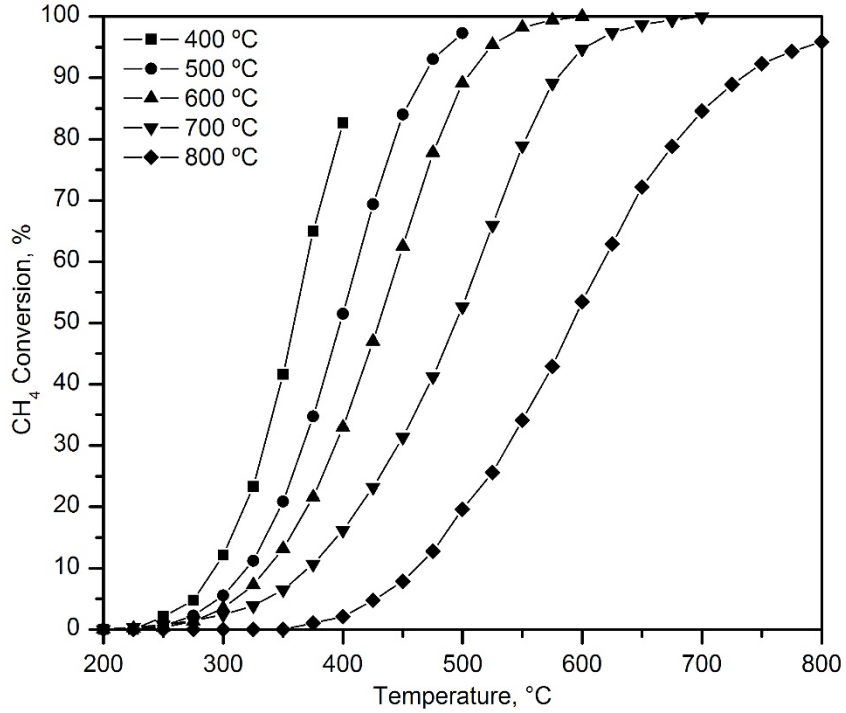

Figure 3.11. Light-off curves of the bulk Co_3O_4 (CC) catalysts submitted to varying calcination temperatures.

Finally, the apparent activation energies were estimated from the Arrhenius plots, in a similar way as it was conducted for the catalysts prepared by different routes. However, contrary to what was noticed for those samples, the CC oxides calcined at increasing temperatures exhibited different values of the apparent activation energy. More specifically, the activation energies of the catalysts calcined at 400 and 500 °C were 88 and 79 kJ mol^{-1}, respectively. These values contrasted with those achieved by the oxides calcined at temperatures higher than 600 °C (71-74 kJ mol^{-1}). This deviation further evidenced the presence of non-converted cobalt precursors due to the insufficient calcination temperature. On the other hand, it is noteworthy that the sample calcined at the most elevated temperature presented a relatively low apparent activation energy despite its poor specific activity. As aforementioned, this sample contains inactive CoO but that would not affect the value of the activation energy, since the only active species in this sample was still Co_3O_4.

3.3. EFFECT OF THE PRESENCE OF RESIDUAL SODIUM

Despite being the optimal methodology, the synthesis by precipitation with sodium carbonate (CC) could be affected by a critical issue that is not present in any other of the investigated synthesis methodologies. The sodium ions from the sodium carbonate used for precipitation remain in the reaction liquor after the precipitation process. As a result, these may end up deposited on the dried catalytic precursor, and therefore on the final catalyst after calcination, if they are not properly washed in the filtration step. The effect of the presence of these residual sodium ions (and other alkali metals) in Co_3O_4 catalysts have been thoroughly investigated for some other reactions, especially for the abatement of acid gases such as N_2O or NO, where they were shown to have a promotional effect on the catalytic activity [180-182].

In these studies, the promoting effect of the presence of the alkaline metals was deemed to be due to a larger presence of Co^{2+} cations within the catalyst surface, an increased electron density in the surface and an enhanced oxygen desorption from Co_3O_4. Considering this, it is not clear whether the residual alkaline metals would have a beneficial effect on the catalytic performance of Co_3O_4, since methane oxidation over Co_3O_4 seems to be controlled by the population of highly reducible Co^{3+} species.

For this reason, an additional CC Co_3O_4 catalyst was prepared by a basic precipitation method with sodium carbonate 1.2M, while intentionally leaving some residual sodium (this sample was denoted as CC-Na), in order to examine the influence of the presence of this cation on the catalytic activity for the complete oxidation of methane. The obtained catalysts were thoroughly characterised, including Raman spectroscopy and XPS, and the role of the surface sodium, cobalt and oxygen species on the oxidation process was ascertained.

3.3.1. Synthesis of the Co_3O_4 precursors

When preparing the bulk Co_3O_4 samples by precipitation with sodium carbonate, the catalytic precursors were filtrated and washed with varying amounts of deionised hot water between 1-8 L. The filtrates extracted from the filtration step were recovered and their pH was measured to qualitatively estimate the extent of removal of residual sodium from the precursor with varying amounts of water. The evolution of pH value as a function of the volume of water used for washing is shown in Figure 3.12.

It was found that the pH of the filtrates remained almost constant (pH = 7.8) after washing the precipitate with 4 L of water, which would suggest that all residual sodium from the synthesis process was removed with this amount of water. This residual pH was somewhat above 7 due to the basicity and slight solubility of the cobalt precipitate. The CC-Na sample was obtained after using 2 L of water in the washing step, while the CC oxide was washed with 8 L. The solid was dried in static air at 110 °C for 16 hours and subsequently subjected to calcination at 600 °C for 4 hours.

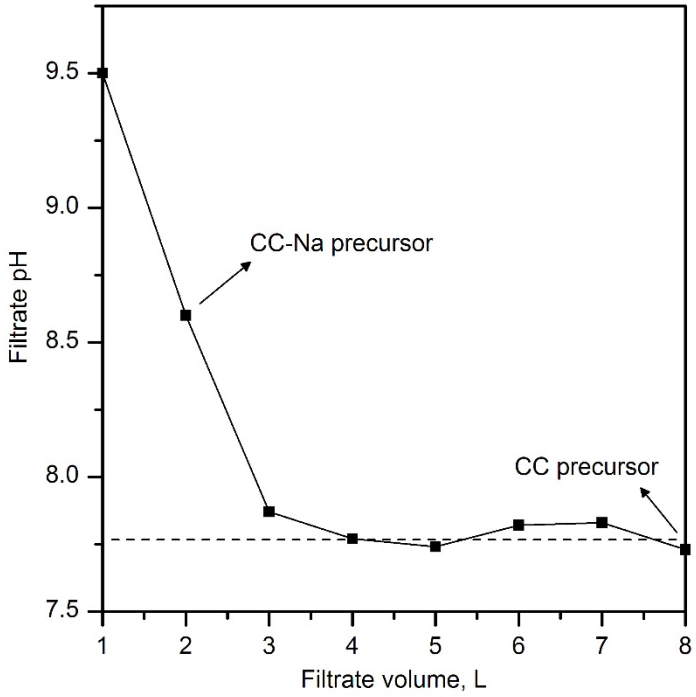

Figure 3.12. pH of the filtrate from the washing step of the CC catalytic precursors.

3.3.2. Physico-chemical characterisation of the catalysts

The structural characterisation of these two samples was performed by XRD. The diffractograms in Figure 3.13 only revealed signals attributable to a pure phase of spinel-type Co_3O_4. No signals attributable to Na_2O or any other Co-Na mixed oxides were detected in the catalyst with residual sodium (CC-Na). However, the diffraction peaks displayed by the CC-Na sample were markedly wider than those displayed by the Na-free counterpart

and shifted towards lower diffraction angles, as can be seen in Figure 3.13 Inset. This revealed that the presence of trace amounts of sodium (0.4%wt. as determined by WDXRF) induced a slight distortion of the spinel lattice of Co_3O_4.

The crystallite size of Co_3O_4 was estimated from the Full Width Half Maximum (FWHM) of the characteristic peak located at 36.8°, by applying the Scherrer equation. Besides, the cell size could be calculated by performing a profile matching of the patterns. It was found that the crystallite size of the CC-Na catalyst was almost half of that of the CC catalyst, while its cell size was notably larger, which was in agreement with the aforementioned distortion caused by the inclusion of sodium into the spinel lattice. This distortion can be explained in terms of the difference in ionic radius between Co^{2+} and Co^{3+} ions (72 and 69 pm, respectively) and Na^{+} ions (113 pm).

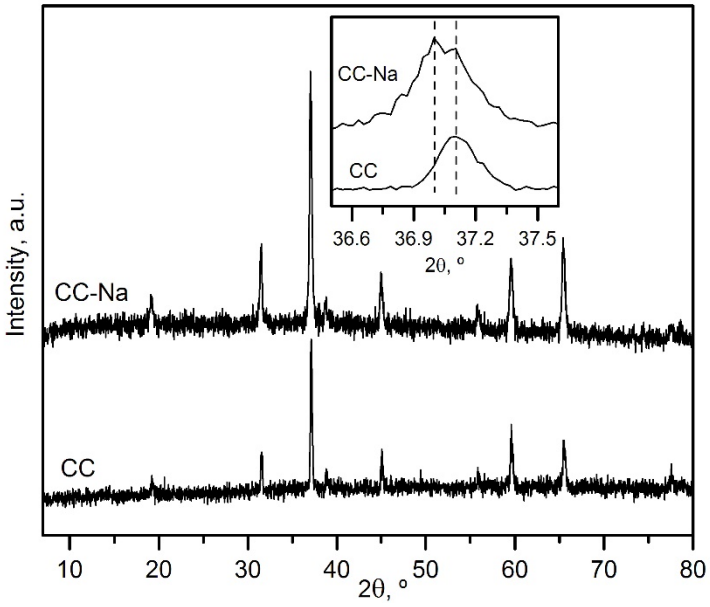

Figure 3.13. XRD diffractograms of the bulk Co_3O_4 (CC and CC-Na) catalysts. Inset: detail of the most intense diffraction signal.

Table 3.8. Results from the physico-chemical characterisation of the bulk Co_3O_4 (CC and CC-Na) catalysts.

Catalyst	BET surface, $m^2\ g^{-1}$	Pore volume, $cm^3\ g^{-1}$	Mean pore diameter, Å	Crystallite size, nm	Cell size, Å	Na content, %wt.
CC	14	0.09	148	63	8.096	0.0
CC-Na	26	0.12	257	34	8.108	0.4

The results from the textural characterisation listed in Table 3.8 evidenced that the catalyst with residual sodium exhibited almost twice as much surface area (26 $m^2\ g^{-1}$) as the Na-free sample (14 $m^2\ g^{-1}$), and a pore volume a 25% larger. This suggested that the distortion caused in the spinel lattice caused an enhancement of the textural properties of the Co_3O_4. The pore size distributions also revealed a shrinking effect on the mean pore diameter when cobalt oxide is contaminated with residual sodium. These observations have already been reported in other studies regarding doping of Co_3O_4 catalysts with other metallic elements [183,184]. It must be noticed that all those variations observed in our CC-Na sample were originated by a relatively low bulk concentration of sodium (0.4%wt.).

The structure of the samples was additionally studied by Raman spectroscopy and XPS. The results from Raman spectroscopy, depicted in Figure 3.14, also pointed out the aforementioned lattice distortion. The resulting spectra for both samples showed five Raman bands. The bands located at 194, 519 and 617 cm^{-1} could be attributed to the F_{2g} mode, while the bands located at 479 and 687 cm^{-1} could be assigned to the E_g and A_{1g} modes, respectively [185,186]. However, the bands of the CC-Na sample slightly shifted (for instance, the position of the A_{1g} moved from 687 to 684 cm^{-1}) and were wider with respect to those of the CC sample (the FWHM value accordingly increased from 11 to 16 cm^{-1}). Besides, the band attributed to the A_{1g} mode also displayed a marked asymmetry, which is was a clear sign of lattice distortion according to the bibliography [187,188].

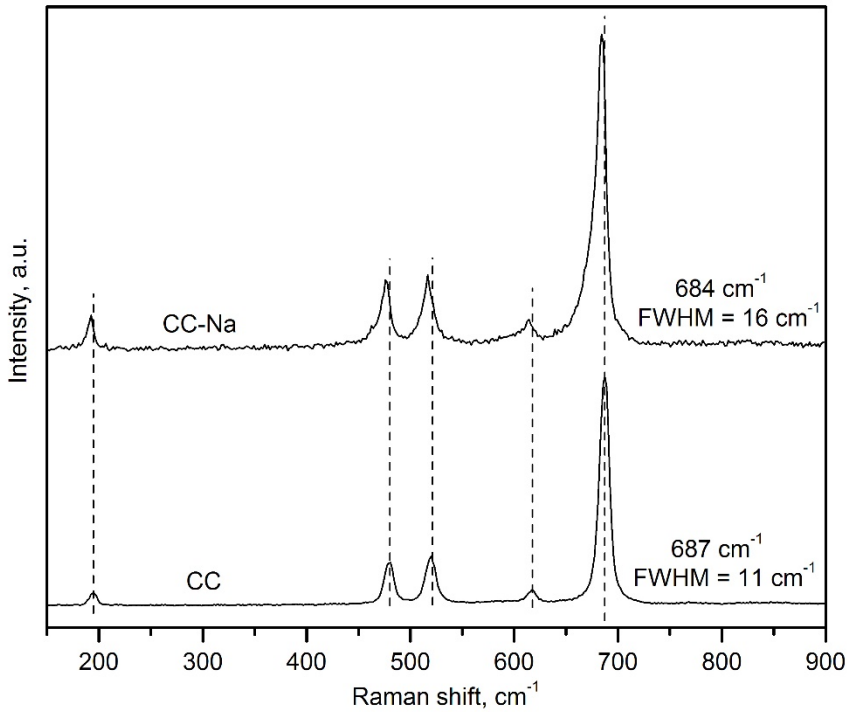

Figure 3.14. Raman spectra of the bulk Co_3O_4 (CC and CC-Na) catalysts.

Figures 3.15 shows the Co 2p and O 1s XPS spectra of the samples, respectively. The Co $2p_{3/2}$ spectra of both oxides were composed of 5 different signals. The two features with the lowest binding energies, located at 779.5 and 780.7 eV, were assigned to Co^{3+} and Co^{2+} ions, respectively, while the signal centred at 782.2 eV was attributed to the presence of CoO in the surface of the samples [189]. The abundance of this species was appreciably higher for the CC-Na sample (14%) than for the CC sample (8%). The two signals with the highest binding energies (785.7 and 789.3 eV) were identified as the satellite signals from Co^{3+} and Co^{2+} ions, respectively. The comparable intensity of both satellite signals pointed out that the surface of the catalysts was mainly composed of Co_3O_4 [190].

On the other hand, the O 1s spectra exhibited two signals for both samples, located at 529.9 and 531.3 eV, respectively. The low binding energy signal was attributed to lattice oxygen species (O_{latt}), while the high binding energy signal was assigned to weakly adsorbed oxygen species (O_{ads}) [191]. Finally, for the CC-Na catalyst an extra peak at a binding energy of 1071.8 eV was attributed to the presence of Na^+ ions.

The deconvolution and integration of the XPS spectra allowed for a quantitative analysis of the composition of the surface, as shown in Table 3.9. It must be noticed that the concentration of sodium on the surface of the CC-Na sample was several times higher (5.1%wt.) than in the bulk (0.4%wt.). This evidenced that the majority of the sodium atoms present in this sample were located on its surface. Nevertheless, a certain amount probably migrated and diffused into the spinel lattice during the calcination process. On the other hand, the Co^{3+}/Co^{2+} molar ratio of the oxide with sodium was notably lower than for its clean counterpart, while the O_{ads}/O_{latt} molar ratio was higher. This was explained as a consequence of sodium atoms donating electrons to oxygen ions within the spinel lattice. The resulting increase in electronic density transformed Na sites into strong Lewis sites that were able to donate electrons to cobalt cations with a concomitant effective decrease in their overall oxidation state [192,193]. This effect was further confirmed by the slight shift (0.4 eV) of the O 1s spectra of the CC-Na towards lower binding energy values, which indicated an increase in the electron density of oxygen anions and also caused a weakening of Co-O bonds, which was coherent with the observed increase in the O_{ads}/O_{latt} molar ratio.

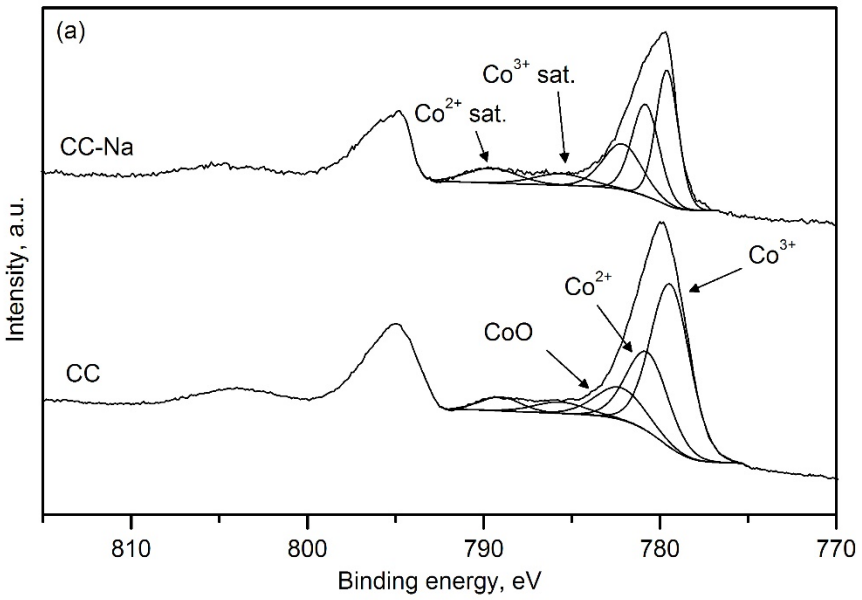

Figure 3.15. XPS spectra of the bulk Co_3O_4 (CC and CC-Na) catalysts (a) Co 2p, (b) O 1s and (c) Na 1s.

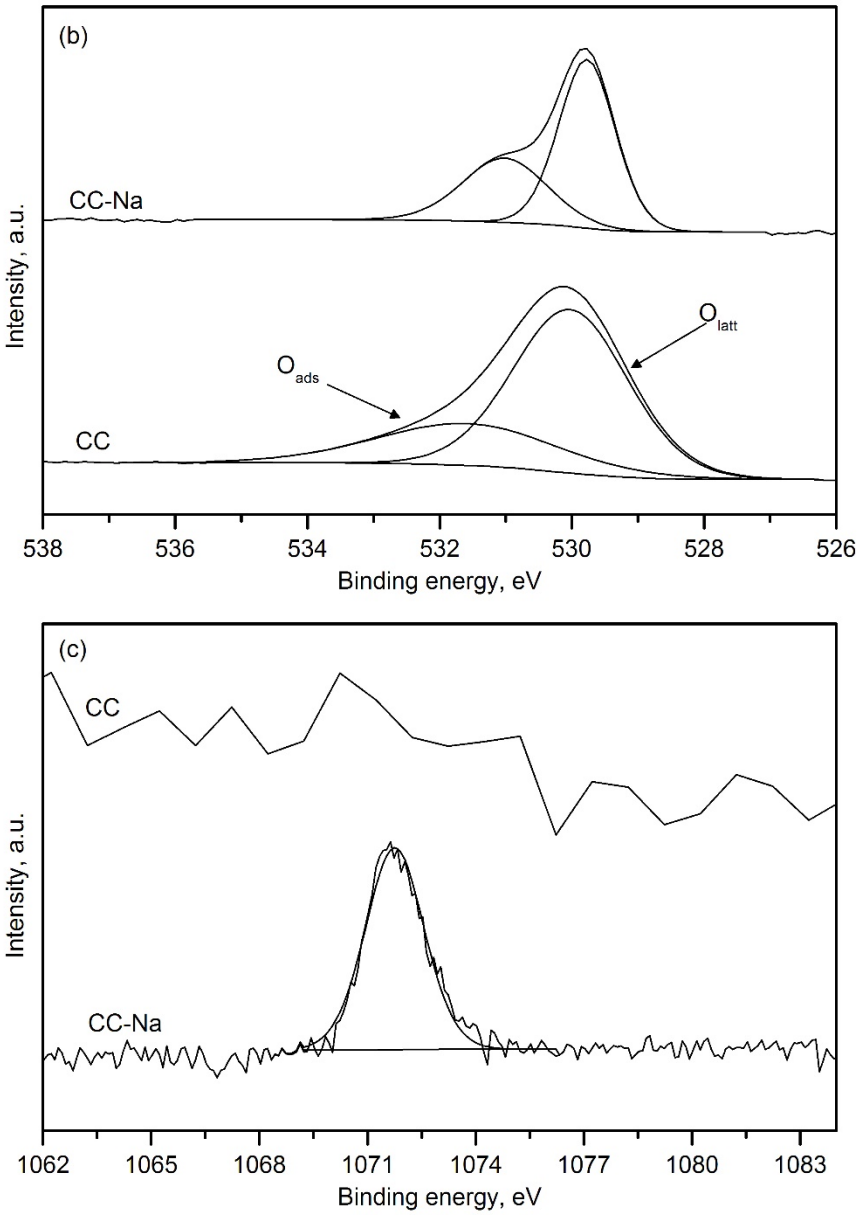

Figure 3.15 (cont.). XPS spectra of the bulk Co_3O_4 (CC and CC-Na) catalysts (a) Co 2p, (b) O 1s and (c) Na 1s.

Table 3.9. Surface composition of the bulk Co_3O_4 (CC and CC-Na) catalysts.

Catalyst	O, %at.	Co, %at.	Na, %at.	Co^{3+}/Co^{2+} molar ratio	O_{ads}/O_{latt} molar ratio
CC	66.5	33.5	0.0	1.96	0.40
CC-Na	57.6	35.4	7.0	1.20	0.57

Figure 3.16 includes the H_2-TPR profiles of both CC samples. As already described previously, the TPR profile of a bulk Co_3O_4 catalyst consisted of two H_2 uptakes. The trace of the sample with residual sodium also exhibited these two contributions, but their shape was notably different, probably as a consequence of the distortion of the spinel lattice caused by Na species. Furthermore, the second H_2 uptake did not take the shape of a single peak, but instead was formed of at least two different contributions. This pointed out the presence of Co^{2+} species with different reducibilities, namely free CoO that was detected by XPS analysis along with Co^{2+} from the spinel lattice.

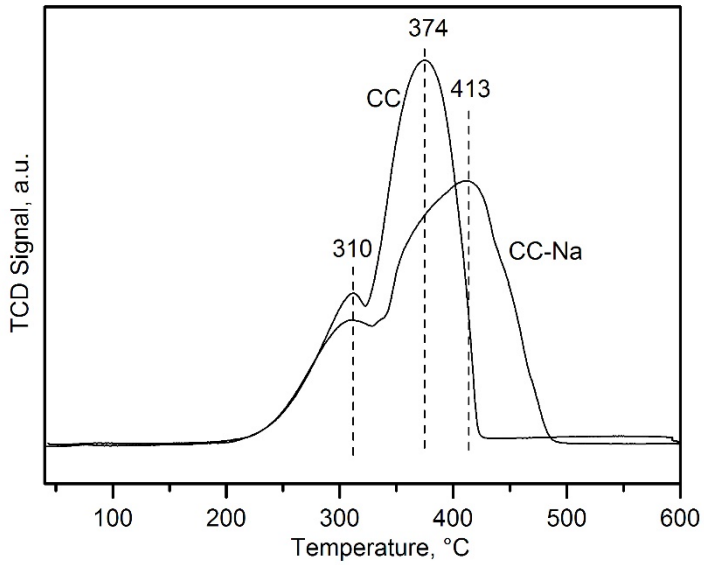

Figure 3.16. H_2-TPR profiles of the bulk Co_3O_4 (CC and CC-Na) catalysts.

Immediately after the H_2-TPR analysis, an O_2-TPO run was carried out in order to check the capacity of reoxidation of the catalysts after their complete reduction to metallic cobalt. The corresponding profiles, shown in Figure 3.17, clearly evidenced the influence of sodium on the reoxidability of the Co_3O_4 catalysts. The CC sample displayed a high intensity

oxidation peak centred at 330 °C with a tail starting around 200 °C, while the sample with sodium exhibited a considerably lower intensity peak located at about 360 °C, with a tail starting around 250 °C. Furthermore, the total O_2 uptake of the Na-containing sample was only 51% of that consumed by the Na-free oxide. These results revealed that not only the sample with sodium was more difficult to reoxidise, but also that it could not be completely reoxidised, after complete reduction, below 600 °C. This was probably due to the reducing effect of sodium ions over cobalt species and subsequent weakening of Co-O bonds, which in turn made the reincorporation of oxygen into the spinel lattice more difficult.

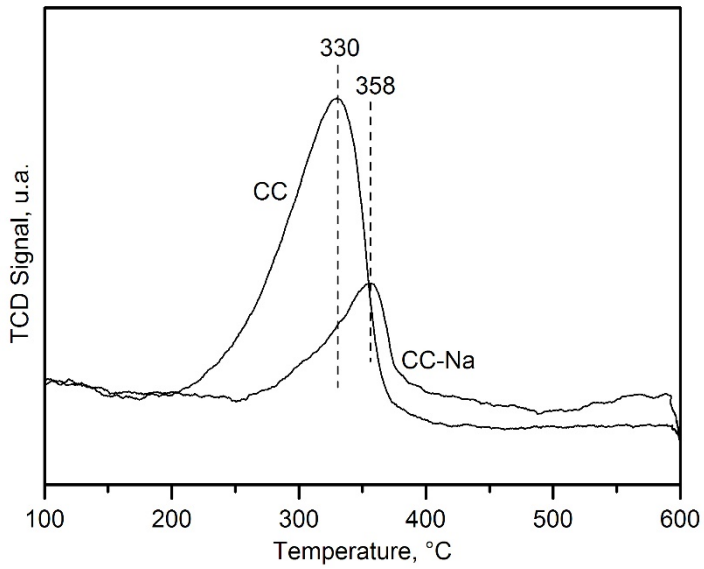

Figure 3.17. O_2-TPO profiles of the bulk Co_3O_4 (CC and CC-Na) catalysts after H_2-TPR analysis.

3.3.3. Catalytic performance of the synthesised catalysts

Three consecutive light-off tests were carried out with each catalyst (GHSV = 30,000 h^{-1}). Over both samples, and line with the previous results reported in section 3.1.3, the second and third cycles were characterised by an identical conversion profile. The light-off curves corresponding to the third cycle are shown in Figure 3.18. It was clear that the catalyst without sodium was far more active than the sample with sodium, thus evidencing the inhibiting effect caused by this alkali metal. Taking into account that the primary mechanism of methane oxidation over metallic oxides is the Mars-van Krevelen mechanism, the negative effect of sodium on the behaviour of the CC-Na catalyst could be

explained as a consequence of the reduced oxygen mobility, which was demonstrated by the H_2-TPR and O_2-TPO experiments, and the decrease in the amount of Co^{3+} on the surface and the subsequent decrease in population of the active lattice oxygen species, as shown by the XPS results. However, it must be noticed that both samples were able to achieve a 100% methane conversion at 600 °C. This pointed out that the aforementioned inhibition effect was only apparent at low temperatures, as can be observed from the marked differences between the T_{10} (temperature at which 10% conversion was attained) and T_{50} values (Table 3.10).

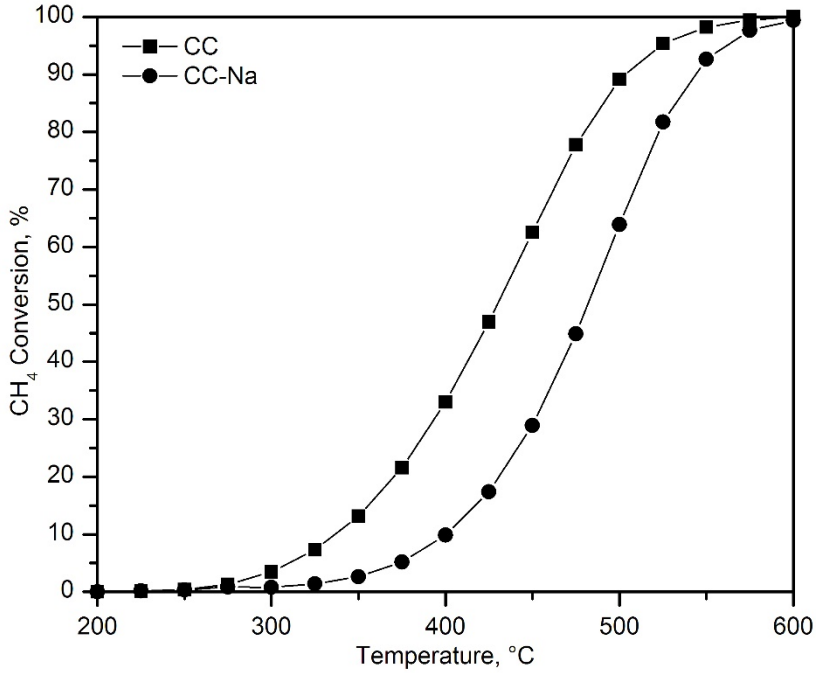

Figure 3.18. Light-off curves of the bulk Co_3O_4 (CC and CC-Na) catalysts.

A differential kinetic analysis was performed for conversion values below 15%. The results included in Table 3.10 further confirmed the negative influence of residual sodium over the CC-Na catalyst. The activation energy of this sample was noticeably higher (99 kJ mol^{-1}) with respect to the CC sample (74 kJ mol^{-1}). In addition, the pre-exponential factor of the CC-Na sample was about 4 times higher than that of the CC sample, which could be a consequence of the beneficial effect of residual sodium on the structural properties of this catalyst.

Table 3.10. Kinetic results of the bulk Co_3O_4 (CC and CC-Na) catalysts.

Catalyst	T_{10}, °C	T_{50}, °C	T_{90}, °C	Initial reaction rate at 350 °C, mmol CH_4 g_{Co}^{-1} h^{-1}	E_a,kJ mol^{-1}	$k_0 \cdot 10^{-5}$, s^{-1}
CC	335	430	500	1.2	74 ± 2	1.1
CC-Na	400	480	545	0.3	99 ± 2	25

3.4. GLOBAL VIEW AND CONCLUSIONS

The synthesis of bulk pure Co_3O_4 catalysts by different routes has been examined in order to obtain highly active catalysts for lean methane combustion. The optimisation of the catalyst preparation involved two main steps. First, the most suitable methodology for obtaining the catalytic precursor was identified. For this, eight synthesis routes were evaluated, which were selected based on their relatively low complexity and easiness for scale-up. The second step dealt with the determination of the optimal calcination temperature for the catalytic precursor and the effect of the presence of sodium traces.

The investigated procedures were direct calcination of two different cobalt precursors (cobalt nitrate and cobalt hydroxycarbonate), basic grinding route, two basic precipitation routes with various precipitating agents (ammonium carbonate and sodium carbonate), precipitation-oxidation, solution combustion synthesis and sol-gel complexation. A commercial Co_3O_4 was also used as a reference. Among the several examined procedures, direct calcination of cobalt hydroxycarbonate (HC sample), basic grinding (GB sample) and basic precipitation employing sodium carbonate as the precipitating agent (CC sample), produced bulk catalysts with fairly good textural and structural properties, and remarkable redox properties, which were found to be crucial for their good performance. All catalysts exhibited complete methane conversion at a temperature of 600 °C and 100% selectivity towards CO_2 formation while operating at 30,000 h^{-1}. Among these, the CC catalyst was the only one that achieved a specific reaction rate higher than that of the reference commercial Co_3O_4 catalyst.

After defining the most suitable synthesis route, a further attempt was made to control the textural and structural properties of this selected bulk oxide by optimising the calcination temperature employed for its activation. Several calcination temperatures were evaluated in the 400-800 °C range. The results revealed that using calcination temperatures lower than 600 °C was appropriate to obtain catalysts with improved properties, namely higher specific surface areas and lower crystallite sizes. However, an insufficient calcination temperature also led to the partial conversion of the catalytic precursors to Co_3O_4, which in turn resulted in samples that could not achieve complete methane conversion. On the other hand, calcination temperatures above 600 °C produced catalysts with even poorer structural properties that contained inactive CoO formed by Co_3O_4 reduction. Consequently, the optimal calcination temperature was fixed at 600 °C.

Finally, the effect of the residual sodium from the precipitation process on the resulting catalyst was analysed. The characterisation of the two catalysts (CC and CC-Na) evidenced that the presence of the residual sodium ions with a concentration as low as 0.4%wt. had a great impact on the properties of the catalyst. Firstly, the insertion of the sodium atoms into the spinel lattice induced a distortion that improved the structural properties of the Co_3O_4, thereby inhibiting crystallisation and increasing the specific surface area. However, this distortion was also responsible for a decrease in the reducibility of the cobalt oxide.

On the other hand, the accumulation of Na^+ ions on the surface of the catalyst induced a reduction of the Co^{3+} ions into Co^{2+}, due to their high Lewis acidic properties, thus increasing the electron density within the lattice oxygen ions and weakening the Co-O bonds, making it more difficult for the catalyst to reoxidise. These changes provoked a decrease in the abundance of lattice oxygen species that were catalytically active for the methane oxidation reaction. The overall effect of the presence of residual sodium in the Co_3O_4 was a notable decrease in the catalytic activity, especially at low temperatures. These results pointed out the importance of properly washing the catalytic precursors after the synthesis process, particularly when the precipitating agent is a sodium base.

The results presented in this chapter extensively defined the synthesis methodology that would be followed for the synthesis of all the cobalt catalysts evaluated throughout the subsequent chapters. Hence, the metal precursors would be precipitated with sodium carbonate and then thoroughly washed with hot water (1-8 L) to eliminate the residual sodium ions. After drying, the corresponding catalytic precursor would be calcined at

600 °C for 4 hours to obtaine the final catalyst. This procedure was simple enough to allow for a relatively easy scale-up, and could also be adapted for the production of supported catalysts, as will be shown in the following chapters.

Although many more parameters associated with the synthesis methodology, such as the addition rate of the precipitating agent, or the concentration of metallic solutions, could be optimised, it is unlikely that these would have a significant effect on the physico-chemical properties or kinetic behaviour of the resulting catalyst. For this reason, the next step for the enhancement of the performance of the as-prepared Co_3O_4 bulk catalyst would be the addition of a second metal to the catalytic formulation, in order to further improve thetextural, structural and redox properties of the active phase.

Chapter 4

BEHAVIOUR OF DOPED BULK Co_3O_4 CATALYSTS

ABSTRACT

The number of operational parameters of the synthesis methodology, whose optimisation would have a significant effect on the activity of the resulting bulk Co_3O_4 catalyst, is relatively limited. For this reason, a further improvement of a cobalt oxide bulk catalyst prepared by precipitation with sodium carbonate would require the addition of a second active or promoting metallic phase. This will be the main objective of this chapter, which will be essentially focused on the viability of doping the previously optimised Co_3O_4 sample with a promoting metal. First, the most suitable doping additive, chosen amongst those more typically applied for redox promotion, was determined. The resulting catalyst were thoroughly characterised to define the improvement in the textural, structural and redox properties associated with each of the selected promoters. The results pointed out that cerium was the doping metal with the largest redox promotion effect over Co_3O_4. Once the optimal dopant was identified, the effect of the dopant loading was also determined, in order to find the optimal composition for the modified catalyst. The content was limited to a maximum of 20%wt. to avoid segregation. The characterisation and catalytic testing of the resulting catalysts revealed that the suitable cerium loading was 10%wt. Ce.

4. BEHAVIOUR OF DOPED BULK Co_3O_4 CATALYSTS

In the previous chapter, the attractive performance of bulk Co_3O_4 catalysts for methane combustion was demonstrated. The best behaviour was found for oxides prepared by precipitation with sodium carbonate (the so-called CC sample). Moreover, the calcination temperature was optimised and the need for an appropriate removal of traces of sodium on the surface was ascertained. However, for pure bulk catalysts the number of variables that have a marked effect on the activity are relatively limited. Hence, once the synthesis methodology has been properly designed, any further tuning of the preparation conditions rarely leads to a significant enhancement of the activity. For this reason, an alternative promoting strategy can be adding a second metal to the cobalt oxide with the aim of improving its properties.

Nevertheless, since Co_3O_4 must be the predominant active phase in these catalysts as well, the content of the promoting metal should be limited to a relatively small amount. Under these conditions, the second metal is normally expected to insert into the cobalt spinel lattice, acting as a dopant of the cobalt oxide instead of working as a separate active phase. When dealing with the synthesis of doped catalysts, two main parameters need to be taken into consideration. Firstly, the most suitable doping metal for a given specific reaction must be found. In this case, the doping metals should be selected based on their redox promotional effect, since that would be the main contribution for the expected promotion in activity. Secondly, it will be necessary to control the loading of the most appropriate metal in order to achieve the most pronounced beneficial effect without the presence of segregated phases.

4.1. SELECTION OF THE OPTIMAL DOPANT

For the selection of the most suitable metallic additive for the bulk Co_3O_4 catalyst, six different samples were synthesised by co-precipitation, following the precipitation route (CC) previously described in Chapter 3, but introducing the doping metal precursor along with the cobalt nitrate into the synthesis reactor. The amount of the salt containing the dopant was adjusted in each case to obtain a 10%wt. metal loading in the final bulk catalyst. The investigated metals were manganese, iron, nickel, copper, zinc and cerium. These metals were selected based on published reports on a variety of catalysts doped with these specific promoters that were found active for oxidation of methane and other light

hydrocarbons [194-198]. All catalysts were thoroughly washed with hit water and subsequently calcined at 600 °C for 4 hours following the same calcination procedure as the bulk catalysts prepared in Chapter 3. The obtained catalysts were denoted as Me-Co, where Me corresponded to each of the doping metals.

4.1.1. Physico-chemical characterisation of the catalysts

The doped cobalt catalysts were characterised in order to determine the effect of the promoter on their properties. The characteristics of the bare Co_3O_4 catalyst were also considered to serve as a reference. The metal loading of the promoted oxides was verified to be in 10.0-10.4%wt. range, as determined by WDXRF and ICP-AES. All samples exhibited type IV isotherms with H2 type hysteresis cycles, characteristic of mesoporous materials (Figure 4.1).

The main textural properties of the modified samples are summarised in Table 4.1. The specific surface areas of the catalysts varied between 11 and 35 $m^2 g^{-1}$ while the pore volume was in the 0.02-0.14 $cm^3 g^{-1}$ range. The effect of doping on the main textural properties significantly varied depending upon the type of metal. In this sense, two groups of promoters could be differentiated. On one hand, dopants such as Ni, Cu or Zn had an overall detrimental effect on the textural properties, decreasing both surface area and pore volume of the resulting catalysts with respect to the undoped Co_3O_4. Only for the Zn-doped catalyst the surface area (19 $m^2 g^{-1}$) was slightly higher than for the pure Co_3O_4 (14 $m^2 g^{-1}$), but its pore volume was still significantly lower. On the other hand, the rest of the examined additives, namely Mn, Fe and Ce, produced catalysts with enhanced textural properties. More specifically, the resulting catalysts presented specific surface areas between 43 and 150% higher and pore volumes between 11 and 56% larger. These beneficial effects have already been observed in other studies regarding the doping of Co_3O_4 catalysts with other metallic elements [168,199].

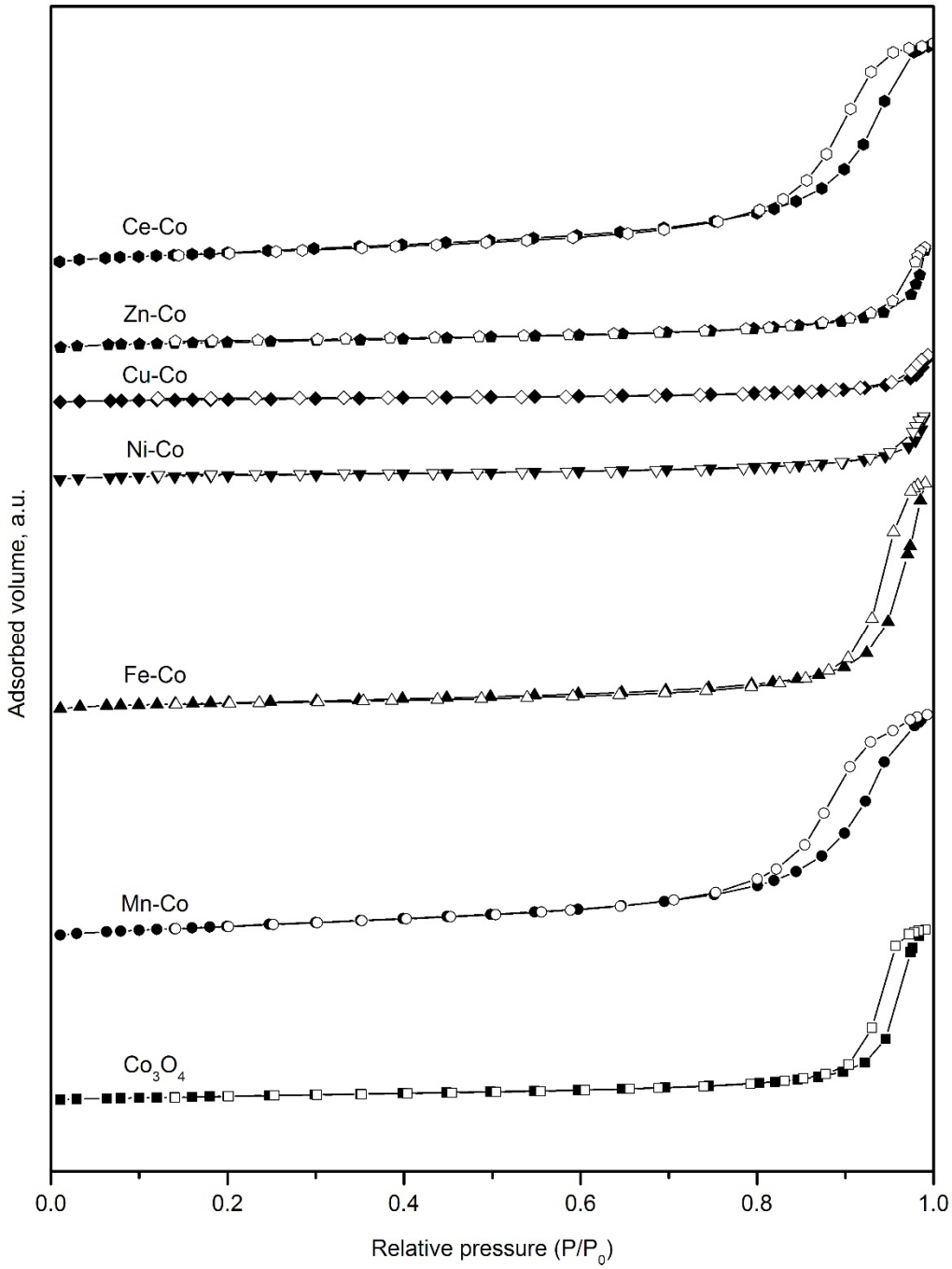

Figure 4.1. N_2 physisorption isotherms of the doped bulk Co_3O_4 catalysts.

Table 4.1. Textural and structural properties of the doped bulk Co_3O_4 catalysts.

Catalyst	Me loading, %	BET surface, m^2g^{-1}	Pore volume, cm^3g^{-1}	Mean pore diameter, Å	Crystallite size, nm
Co_3O_4	0	14	0.09	257	63
Mn-Co	10.3	33	0.13	135	27
Fe-Co	10.4	20	0.10	284	44
Ni-Co	10.0	13	0.02	234	56
Cu-Co	10.0	11	0.02	280	66
Zn-Co	10.0	19	0.04	193	51
Ce-Co	10.1	35	0.14	143	29

The influence of doping on the pore size distributions of the resulting catalysts was also noticeable, as shown in Figure 4.2. In general, two different effects were observed, coinciding with the two aforementioned groups of doping metals. Thus, for the metals that produced a detrimental effect on the textural properties (Ni, Cu and Zn), the resulting catalysts exhibited unimodal pore size distributions with maxima located at larger pore sizes (890, 850 and 1010 Å, respectively) with respect to the bare oxide (335 Å), and notably smaller pore volumes (0.02-0.04 $cm^3\ g^{-1}$).

On the other hand, the resulting catalysts with the doping metals that enhanced the textural properties of the Co_3O_4 (Mn, Fe and Ce) presented unimodal distributions as well, but with maxima located at similar or smaller pore sizes. More specifically, the catalyst modified with Fe showed an identical pore size distribution as the undoped Co_3O_4 catalyst, while the catalysts containing Mn and Ce exhibited maxima located at around 150 and 190 Å, respectively.

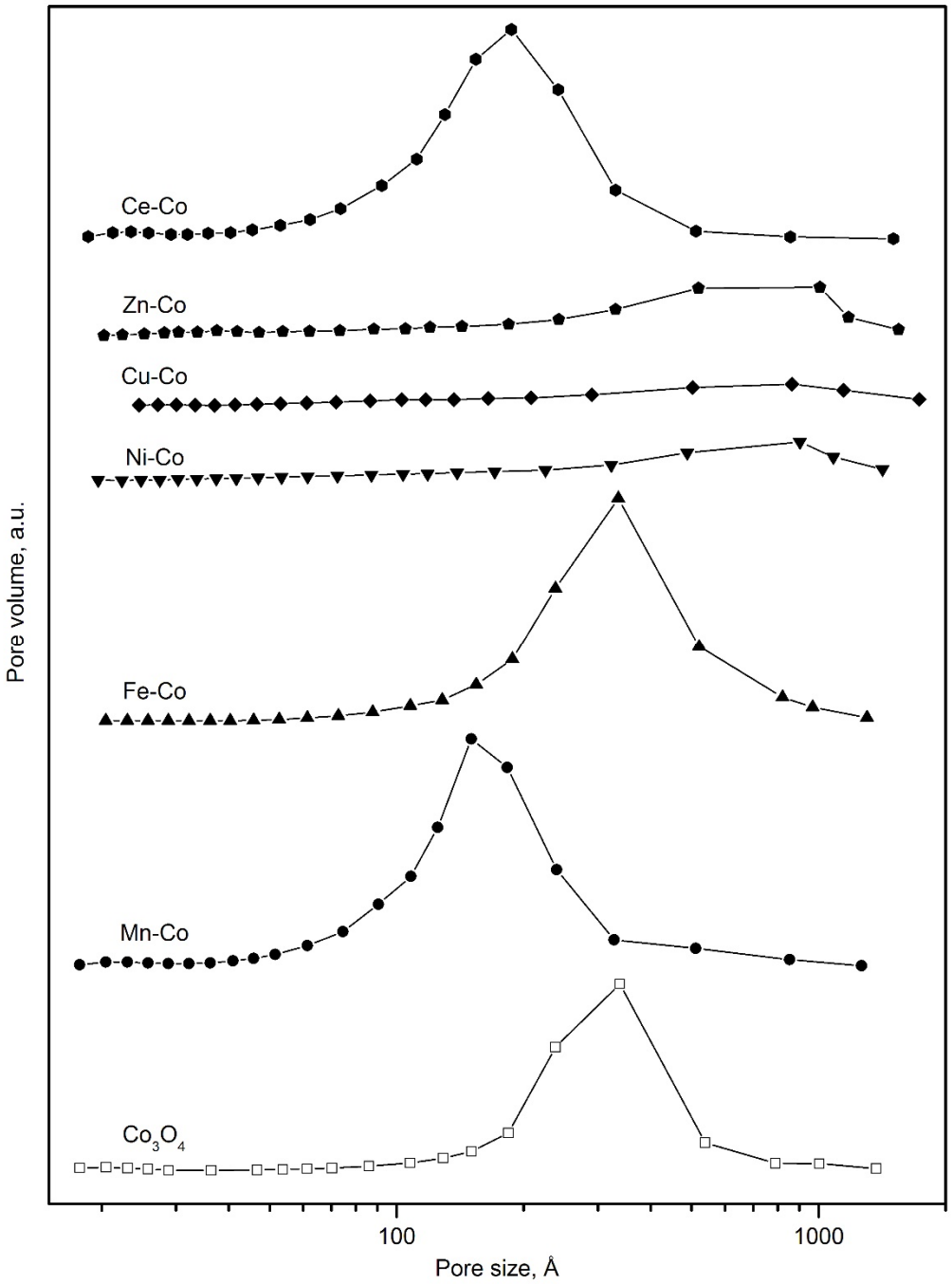

Figure 4.2. Pore size distributions of the doped bulk Co_3O_4 catalysts.

The structural properties of the promoted catalysts were determined by XRD. The resulting diffraction patterns are depicted in Figure 4.3. All catalysts exhibited diffraction signals located at 2θ positions of 19.0, 31.3, 36.8, 44.8, 59.3 and 65.2°, assignable to the spinel type cobalt oxide Co_3O_4 (ICDD 00-042-1467). No secondary phases were detected in any of the doped catalysts, which in principle suggested an efficient incorporation of all the promoters into the structure of the cobalt oxide.

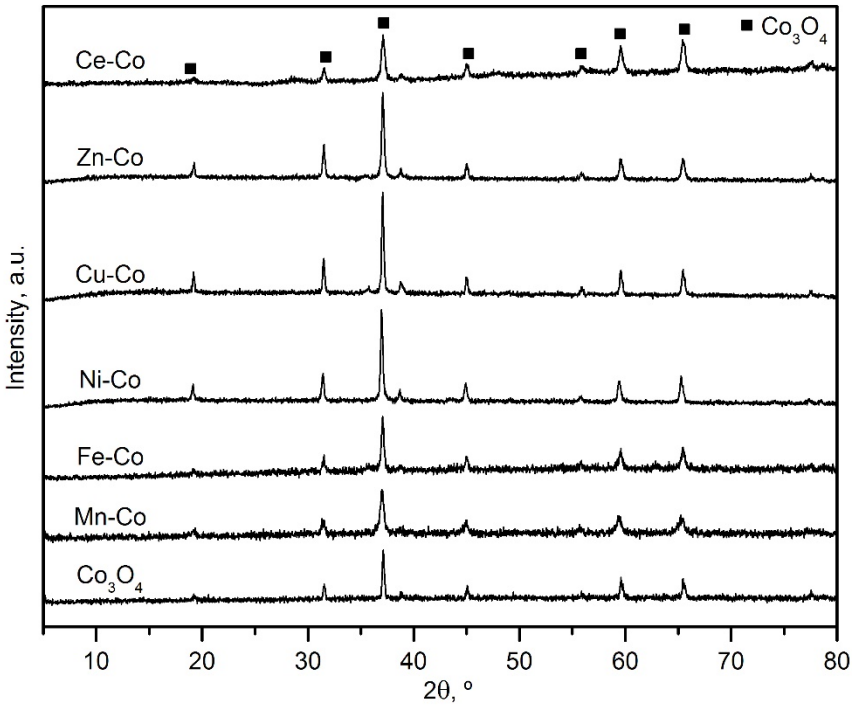

Figure 4.3. XRD patterns of the doped bulk Co_3O_4 catalysts.

The size of Co_3O_4 crystallites in the modified samples, estimated by the Scherrer equation, also evidenced the previously found two different effects of metallic doping. As expected, the catalysts that suffered a decrease in the specific surface area (those doped with Ni, Cu or Zn) also exhibited relatively large crystallite sizes (56, 66 and 51 nm, respectively). Recall that the crystallite size of the undoped catalyst was 63 nm. On the other hand, the catalysts with Mn, Fe or Ce, which showed an enhancement of their textural properties, presented smaller crystallite sizes (22, 44 and 29 nm, respectively).

The observed influence on the textural and structural properties was related to the insertion of the doping metal cations into the structure of the cobalt oxide spinel. This insertion is hinted by the lack of detection of diffraction signals associated with the doping metals or their oxides, although this observation could also be due to the relatively low metal loading of the dopants. However, a close-up observation of the most intense signal of the cobalt spinel, located at around $2\theta = 36.8°$, could also give evidences of this cation insertion. Thus, as seen in Figure 4.4, the main signal of the cobalt spinel significantly shifted towards lower angle values with respect to the bare cobalt spinel.

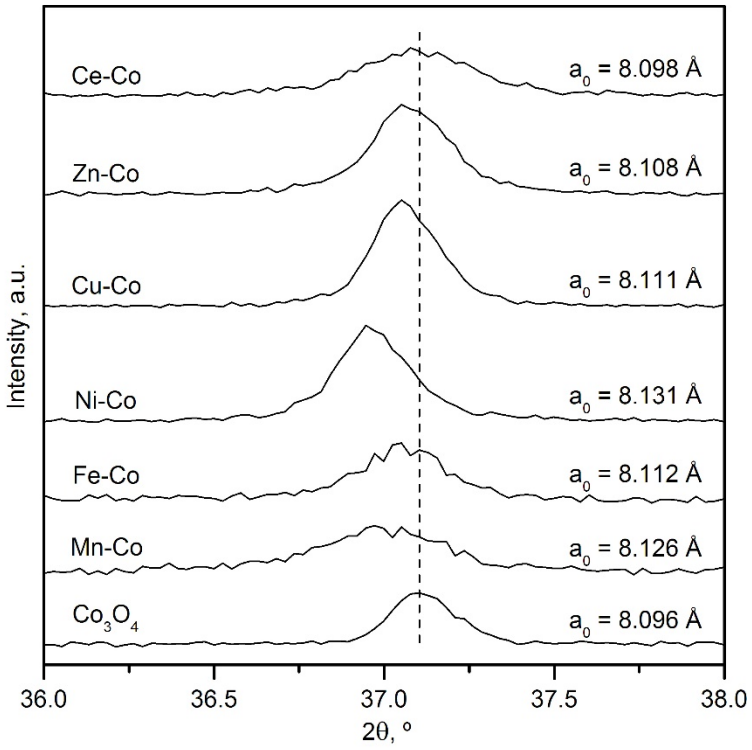

Figure 4.4. Close-up view of the XRD patterns of the doped bulk Co_3O_4 catalysts in the 2θ range of 36-38°.

The shift of the diffraction signal towards lower angles translated into a larger cell size of the cobalt spinel in the doped catalysts. Hence, the cell size varied from 8.098 Å for the Ce-doped catalyst to 8.131 Å for the Ni-doped sample. It must be noted that the cell size of the promoter-free oxide was 8.096 Å. This larger cell size of the doped catalysts further

evidenced the distortion of the spinel lattice as a consequence of the insertion of the dopant metal cations.

The reducibility of the modified cobalt oxides was analysed by H_2-TPR measurements. The corresponding reduction profiles are included in Figure 4.5. The expected two-step reduction profile, typical of Co_3O_4, was noticed for all samples, although a significant distortion and additional signals appeared in some cases. For instance, the reduction process over the Mn- and Ce-doped catalysts was significantly more extensive with temperature. In other words, a significant reduction was evident above around 425 °C, which is the limit temperature of the pure oxide. In addition, reduction started at notably higher temperatures for the former (285 °C), while it was rather the opposite for the latter (260 °C). This suggested that those metals preserved the structure of the Co_3O_4 intact, but greatly affected its overall reducibility at the same time.

On the other hand, up to four different H_2 uptakes (located around 300, 340, 390 and 450 °C) over the Fe-doped catalyst could be distinguished. The two contributions centred at 300 and 390 °C could be attributed to the reduction of the cobalt oxide, while the other two could be assigned to the two-step reduction of the iron spinel (Fe_3O_4) [200,201]. It should be pointed out that the presence of this segregated phase was not detected by XRD, probably due to its high dispersion and/or low amount.

Finally, the catalysts with Ni, Cu and Zn exhibited an appreciable distortion of their corresponding high-temperature H_2 signal, since additional peaks appeared that could be attributed to the reduction of the bivalent cations of the metal dopants (Ni^{2+}, Cu^{2+} and Zn^{2+}), less reducible than the Co^{2+} cations. These signals were located at around 445 °C for the Zn-Co sample and at about 410 °C for the Cu-Co sample, while this high-temperature uptake over the Ni-Co sample was probably the result of the simultaneous reduction of both Ni^{2+} and Co^{2+} cations. Despite the lower reducibility of these cations, the distortion of the spinel lattice that they induced led to an enhanced reducibility of the cobalt oxide, as evidenced by the shift of the low-temperature signal (250-260 °C) towards lower temperatures with respect to the undoped catalyst (265 °C). This shift was more noticeable for the Ni-doped catalyst.

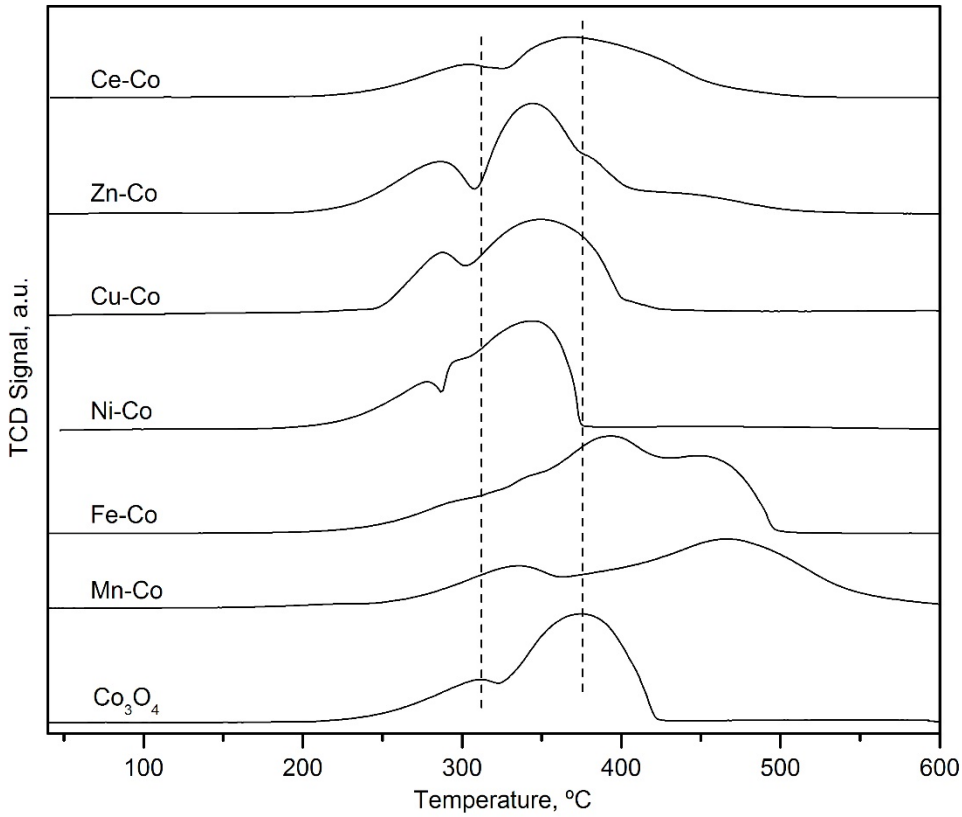

Figure 4.5. H_2-TPR profiles of the doped bulk Co_3O_4 catalysts.

The integration and quantification of the reduction profiles allowed for the estimation of the H_2 uptakes at low and high temperatures, and their relative intensity, in a similar procedure as it was made for the bulk Co_3O_4 catalysts. The corresponding results are summarised in Table 4.2. The total H_2 consumption of the doped catalysts varied between 15.2 and 16.9 mmol g^{-1}, in contrast with the theoretical value for the stoichiometric reduction of Co_3O_4 (16.6 mmol g^{-1}), thus evidencing the presence of phases with varying degrees of reducibility in the samples. Thus, the catalysts doped with Mn, Zn and Ce showed lower total uptakes than the theoretical value, which evidenced the existence of oxides with lower reducibility than Co_3O_4. More specifically, it is known that reduction of manganese oxides at low temperatures only progresses up to the formation of Mn^{2+} [202], while in the case of cerium, typically the surface Ce^{4+} cations can be only reduced to Ce^{3+}

[203]. In the case of zinc, it is possible that the cations inserted into the spinel lattice became non-reducible at low temperatures [204].

On the other hand, the catalysts modified with Fe, Ni and Cu exhibited similar overall H_2 uptakes as the undoped counterpart, which pointed out the formation of phases with a comparable reducibility to Co_3O_4. For instance, iron species could have been present in a mixed +2/+3 oxidation state as in Fe_3O_4, analogous to the one of cobalt in Co_3O_4, while nickel and copper could have been intimately combined with cobalt oxide forming mixed spinel structures such as $NiCo_2O_4$ and/or $CuCo_2O_4$ [205,206].

Table 4.2. Results of the H_2-TPR analysis of the doped bulk Co_3O_4 catalysts.

Catalyst	Low-temperature H_2 uptake, mmol g^{-1}	High-temperature H_2 uptake, mmol g^{-1}	Relative H_2 uptake at low and high temperature	Reduction onset temperature, °C
Co_3O_4	4.5	12.0	0.38	265
Mn-Co	3.7	11.5	0.32	280
Fe-Co	2.5	14.4	0.17	275
Ni-Co	4.2	12.4	0.34	250
Cu-Co	4.1	12.7	0.33	265
Zn-Co	3.9	12.2	0.32	255
Ce-Co	4.1	11.5	0.36	260

The addition of the metallic promoters to Co_3O_4 also affected the relative intensity of the low- and high-temperature H_2 uptakes. In particular, this ratio was markedly low (0.17) over the Fe-doped catalyst, which along with the lower H_2 uptake at low temperatures and higher onset temperature, suggested that iron doping was detrimental for the reducibility of Co_3O_4. The rest of the studied metals only induced a slight decrease in ratio (0.32-0.36) with respect to that of the undoped Co_3O_4 (0.38), and showed relatively lower H_2 consumption al low temperatures, although most of them (Ni-, Cu-, Zn- and Ce-doped samples) also evidenced a shift of the onset reduction temperature to lower values (250-265 °C). In view of those three parameters, it could be concluded that the best redox promoters for bulk Co_3O_4, among those studied, were nickel and cerium.

4.1.2. Catalytic performance of the synthesised catalysts

The catalytic activity of each doped Co_3O_4 sample for the complete oxidation of methane was studied by defining their respective light-off curves (GHSV = 30,000 h^{-1}) in the 200-600 °C (Figure 4.6). All tested catalysts achieved a 100% selectivity towards CO_2 formation irrespective of the doping metal.

The criteria for intra-particle and extra-particle mass and heat transport, as well as the temperature gradients were checked to be above the limit, as explained in Chapter 2, to ensure that any diffusional effects did not affect the kinetic results. In this sense, Table 4.3 lists the estimated values for the various evaluated criteria.

Table 4.3. Criteria for accurate analysis of intrinsic reaction rates (as evaluated for the Ce-Co catalyst at 375 °C).

Criterion number	Recommendation	At 375 °C	Least favourable conditions
1.	Bodenstein parameter $< L_{bed}/d_{particle}$	4.1 < 79.5	61.6 < 79.5[a]
2.	$d_{tube}/d_{particle} > 10$	31.2	31.2
3.	Carberry number $< 0.05/n$	0.0013	0.039[b]
4.	$\gamma\beta_e Ca < 0.05$	0.0018	0.030[b]
5.	Wheeler-Weisz modulus < 0.15	$1.4 \cdot 10^{-4}$	$2.5 \cdot 10^{-4}$[c]
6.	Mears parameter < 0.1	$4.7 \cdot 10^{-7}$	$7.5 \cdot 10^{-7}$[c]
7.	Radial gradient < 0.05	0.004	0.011[a]
8.	Bed dilution parameter < 0.05	0.047	0.047
9.	Temperature gradient < 0.3	0.15	0.175[b]

[a]Determined at 500 °C; [b]Determined at 600 °C; [c]Determined at 450 °C.

On the basis of the T_{50} values summarised in Table 4.3, the only catalyst that showed a slightly better performance than the reference Co_3O_4 (T_{50} = 430 °C) was the Ce-doped oxide (T_{50} = 425 °C). In the low temperature range the behaviour of both samples was comparable, although the efficiency of the Ce-Co sample was slightly better above 400 °C. Among the rest of the modified catalyst, the following trend of doping metals was observed: Ni > Cu > Zn > Fe > Mn. This trend was partially in agreement with the H_2-TPR results, and in particular, with the relative ratio between the low- and high-temperature H_2 uptakes, at least for the catalysts doped with Ni, Cu and Zn. Interestingly, despite its notably

lower reducibility, the catalyst doped with Fe performed significantly better than the one doped with Mn. This could suggest that manganese is an activity inhibitor for the oxidation of methane over Co_3O_4.

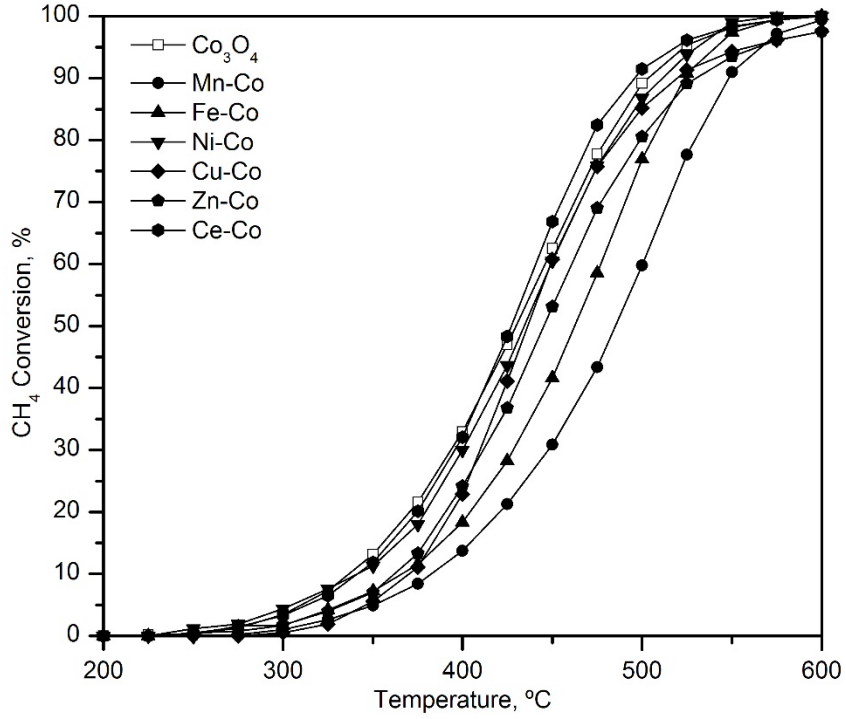

Figure 4.6. Light-off curves of the doped bulk Co_3O_4 catalysts.

The specific reaction rate per cobalt mass of the catalysts was calculated at 375 °C using the differential method, that is, for methane conversions lower than 20%. The reaction rates were normalised in order to facilitate the comparison with the undoped catalyst (Table 4.4). The reaction rate of the modified catalysts varied in the 0.79-2.02 mmol CH_4 g_{Co}^{-1} h^{-1} range, while it was 1.83 mmol CH_4 g_{Co}^{-1} h^{-1} over the undoped CC catalyst. As expected, the two doped catalysts described as the most reducible ones (Ce-Co and Ni-Co) attained the highest specific activity, although the Ce-Co oxide was the only one that achieved a higher reaction rate than the non-modified sample.

The trend pointed out by the specific activity was slightly different from that observed according to the T_{50} values. In particular, the Cu-doped catalyst showed a lower reaction rate (0.99 mmol CH_4 g_{Co}^{-1} h^{-1}) than the Fe-Co sample (1.09 mmol CH_4 g_{Co}^{-1} h^{-1}), despite achieving a T_{50} value 20 °C lower.

Table 4.4. Kinetic results of the doped bulk Co_3O_4 catalysts.

Catalyst	T_{50}, °C	Reaction rate at 375 °C, mmol CH_4 g_{Co}^{-1} h^{-1}	E_a, kJ mol^{-1}
Co_3O_4	430	1.83	74 ± 1
Mn-Co	485	0.79	83 ± 2
Fe-Co	460	1.09	79 ± 2
Ni-Co	435	1.61	77 ± 1
Cu-Co	440	0.99	88 ± 4
Zn-Co	445	1.16	79 ± 2
Ce-Co	425	2.02	79 ± 1

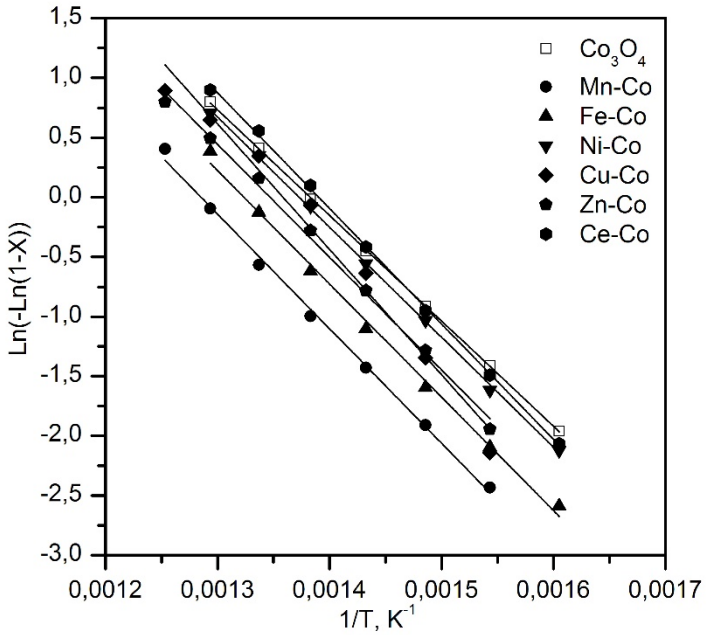

Figure 4.7. Pseudo-first order fit for the experimental data obtained over the doped bulk Co_3O_4 catalysts.

Finally, the apparent activation energies of the cobalt catalysts, estimated by the integral method, were in the 77-88 kJ mol^{-1} range, while for the undoped Co_3O_4 it was 74 kJ mol^{-1}. The corresponding Arrhenius plots are shown in Figure 4.7 while the obtained apparent activation energies for each catalyst are listed in Table 4.4. The catalysts with Fe, Ni, Zn and Ce presented an activation energy around 77-79 kJ mol^{-1}, which was relatively similar to that of the undoped counterpart, thus suggesting that the active phase in all these oxides was also Co_3O_4. However, the activation energies for the Mn- and Cu-doped catalysts were notably higher (83 and 88 kJ mol^{-1}, respectively), which was in accordance with their lower specific reaction rates. These results highlighted the unsuitability of these two metals for the activity promotion of Co_3O_4 catalysts.

4.2. OPTIMISATION OF THE DOPANT LOADING

From the six doping metals tested for activity promotion of the Co_3O_4, only the cobalt oxide modified with cerium (Ce-Co) revealed a certain potential for producing promoted Co_3O_4-based catalysts. The reason for its interesting behaviour could lie on the improvement in the textural and structural properties while at the same time maintaining the good redox properties of the active cobalt oxide. Since no signals of segregated ceria were detected in the Ce-doped catalyst, it is not clear if the Co_3O_4 lattice could accommodate a higher cerium loading, or if working with a lower loading could be even more beneficial for the resulting catalyst.

Taking these hypotheses into account, three additional catalysts with cerium loadings of 5, 15 and 20%wt. were prepared by the same methodology as the initial Ce-doped catalyst (with a 10%wt.Ce). The catalysts were denoted as xCe-Co, where x corresponded to the cerium content. In addition to that, a sample of pure CeO_2 was also synthesised by the same precipitation methodology, to serve as a reference for the characterisation results and the activity tests.

4.2.1. Physico-chemical characterisation of the catalysts

The textural and structural properties of the Ce-doped bulk Co_3O_4 (xCe-Co) samples along with the pure Co_3O_4 and CeO_2 oxides are shown in Table 4.5.

Table 4.5. Textural and structural properties of the xCe-Co catalysts.

Catalyst	BET surface, $m^2\ g^{-1}$	Pore volume, $cm^3\ g^{-1}$	Mean pore diameter, Å	Crystallite size, nm	Ce/Co molar ratio	Co_3O_4 cell size, Å
Co_3O_4	14	0.09	257	63	0	8.0958
5Ce-Co	33	0.14	155	32	0.033 (0.030)	8.0980
10Ce-Co	35	0.14	143	29	0.063 (0.064)	8.0982
15Ce-Co	30	0.11	176	38	0.100 (0.101)	8.0948
20Ce-Co	34	0.11	153	35	0.142 (0.143)	8.0940
CeO_2	12	0.05	235	-	-	-

Values in brackets correspond to the nominal Ce/Co molar ratios.

The specific surface area of Ce-modified catalysts varied between 30 and 35 $m^2\ g^{-1}$, which was more than twice that of the surface area of the undoped sample. At the same time the pore volume increased by 50% approximately and the pore diameter decreased by the same amount, thus demonstrating that the addition of Ce to the bulk Co_3O_4 could improve their textural properties irrespective of the cerium loading.

The xCe-Co samples showed the various diffraction signals of the cubic Co_3O_4 but slightly shifted from their positions with respect to the pure spinel (Figure 4.8). In addition, the crystallite size significantly decreased from 63 to 29-38 nm. On the other hand, the samples with a Ce loading of 15 and 20wt% also exhibited signals (2θ = 28.8°, 33.3°, 47.7°, 56.6°, 59.4°, 69.6°, 76.9° and 79.3°) related to segregated cubic fluorite-like CeO_2 (ICDD 00-034-0394).

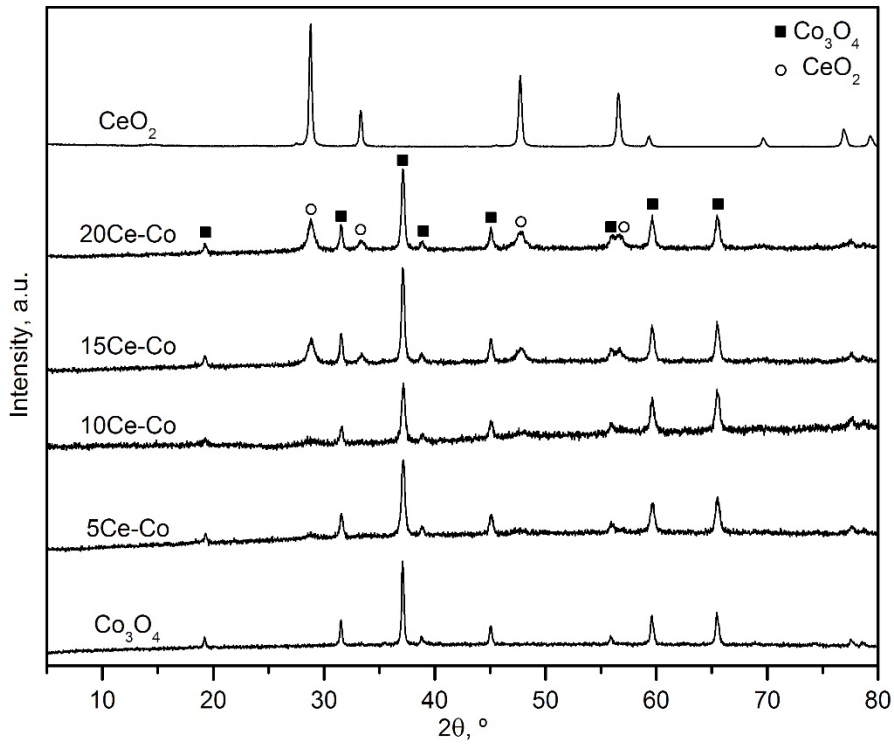

Figure 4.8. XRD patterns of the xCe-Co catalysts.

These evidences pointed out that the addition of small amounts of Ce (5 and 10%wt.) caused a distortion in the spinel structure, which in turn decreased the Co_3O_4 crystallite size and increased the unit cell size, as can be seen in Figure 4.9. This finding has also been reported by other authors [118,183], with the latter being attributed to the larger ionic radius of Ce^{4+} (101 pm) in comparison with Co^{2+} (79 pm) and Co^{3+} (69 pm). The upper limit for the amount of cerium atoms that could be incorporated into the lattice of Co_3O_4 seemed to be close to 10%wt. Above this loading, excess of cerium led to the formation of segregated CeO_2.

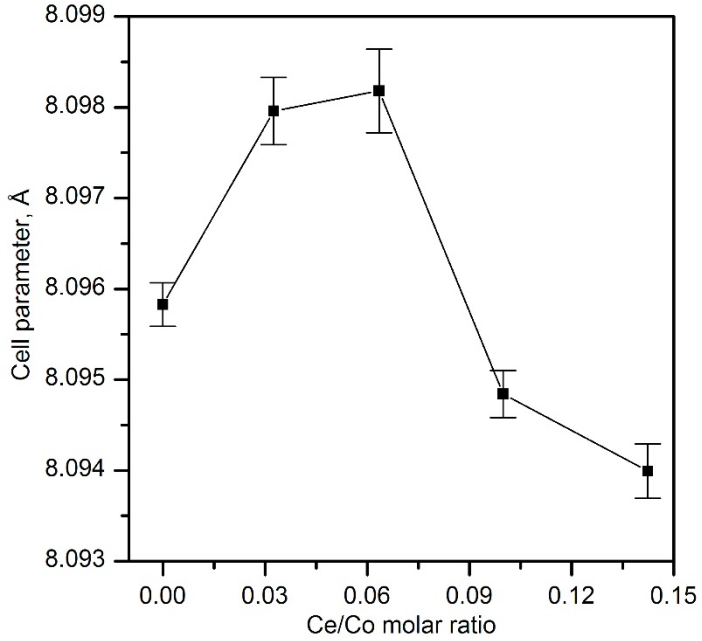

Figure 4.9. Co_3O_4 cell size of the xCe-Co catalysts.

To further assess the distortion caused by the insertion of Ce atoms into the lattice of the Co_3O_4 spinel, Raman spectrometry was applied to all Ce-doped samples. The resulting spectra are included in Figure 4.10. The xCe-Co oxides displayed the same five Raman bands of the Co_3O_4 phase, but shifted from their original positions and with broader shapes, thus suggesting the alteration of the size of the lattice. Hence, the bands located at 194, 519 and 617 cm^{-1} could be assigned to the F_{2g} mode, while the bands at 479 and 687 cm^{-1} could be assigned to the E_g and A_{1g} modes, respectively. Pure CeO_2, however, only displayed a markedly intense signal, located at 462 cm^{-1}, attributable to the symmetrical stretching of CeO_8 units [207]. The xCe-Co samples also exhibited much weaker forms of this signal, and shifted from its original position as well. This evidenced that the segregated CeO_2 in the 15Ce-Co and 20Ce-Co samples could also present some degree of distortion on its own lattice.

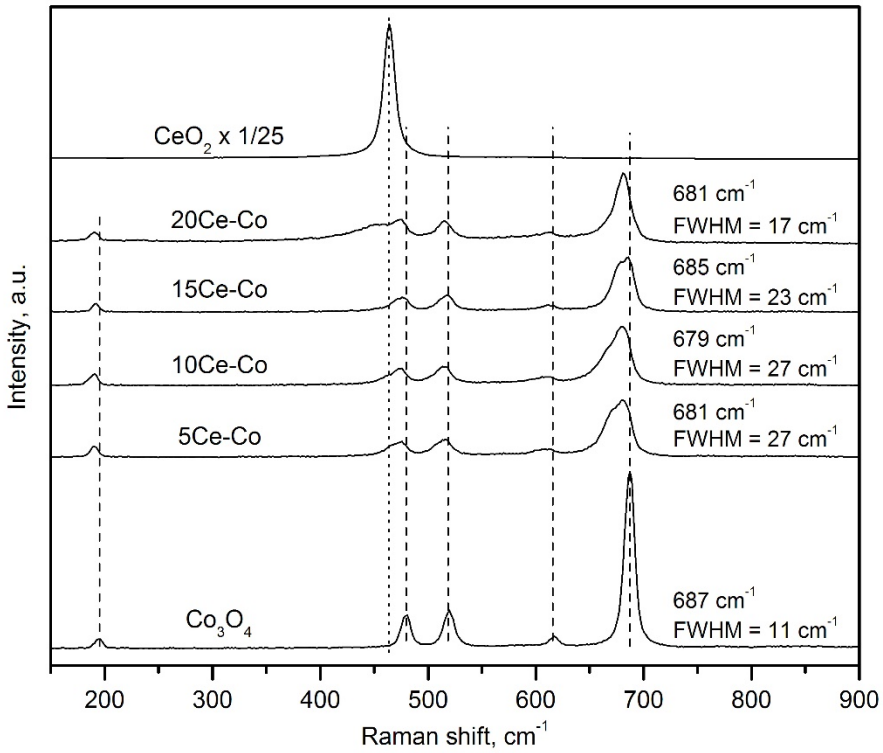

Figure 4.10. Raman spectra of the xCe-Co catalysts.

The band related to the A_{1g} mode showed a considerably broader shape for the Ce-doped samples, with substantially higher FWHM values between 17 and 27 cm^{-1} in comparison with the pure cobalt oxide (11 cm^{-1}). The highest values were noted over the 5Ce-Co and 10Ce-Co samples, thereby pointing out that the largest extent of lattice distortion occurred in these catalysts. Accordingly, these were the oxides that presented the largest cell size.

The XPS analysis of Ce-modified oxides also helped in determining the role of Ce and its eventual influence on the valence changes of cobalt species. The spectra of all xCe-Co samples were fitted with ten peaks corresponding to five pairs of spin-orbit doublets. Following the convention adopted by Romeo et al. [208], letters U and V were used to refer to the $3d_{5/2}$ and $3d_{3/2}$ spin-orbit components, respectively. From the five pairs of peaks, three of them (namely V,U; V'',U'' and V''',U''') were associated with electrons from Ce^{4+} while the remaining pairs (V_0,U_0 and V',U') were attributed to electrons from Ce^{3+} species (Figure 4.11).

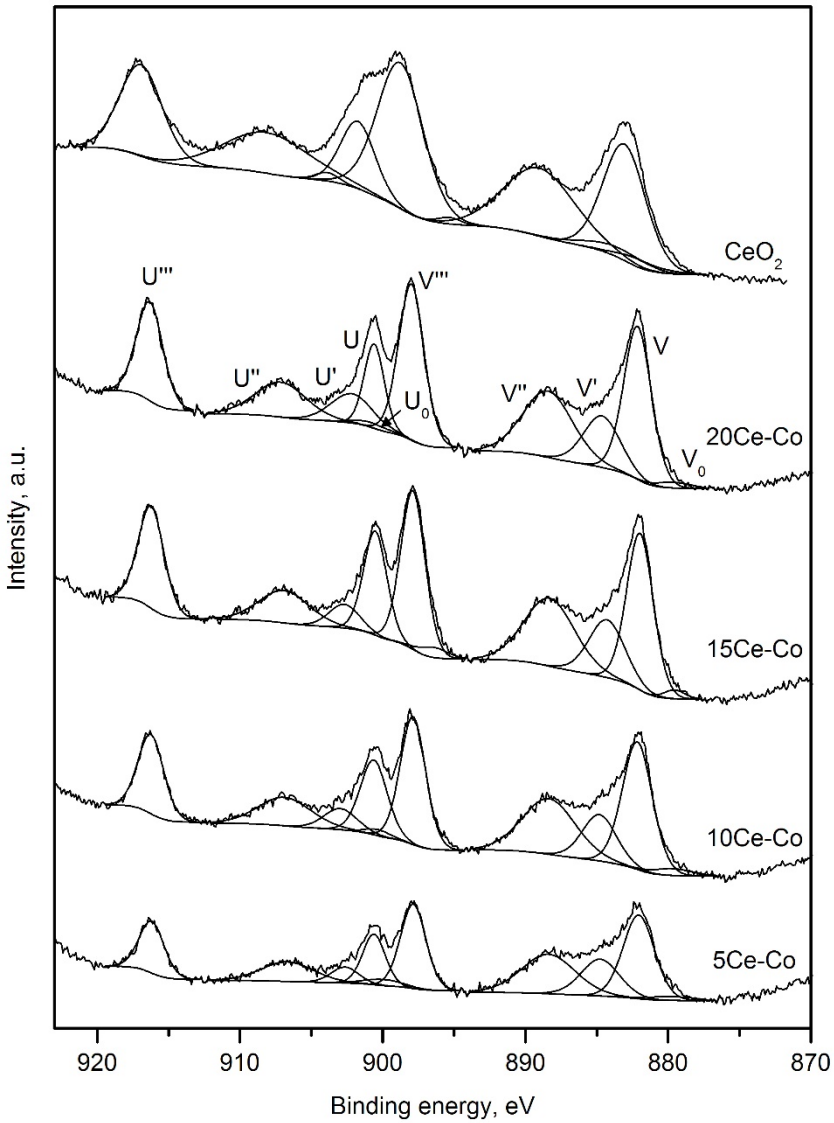

Figure 4.11. Ce 3d XPS spectra of the xCe-Co catalysts.

The Ce^{3+}/Ce^{4+} molar ratios were obtained from the areas of both $3d_{5/2}$ and $3d_{3/2}$ components for each species. These calculated ratios were correlated with the molar Co^{3+}/Co^{2+} ratios calculated from the respective Co2p spectra, as shown in Figure 4.12. An inverse relationship was found, which could be explained in terms of the equilibrium $Ce^{3+} + Co^{3+} \leftrightarrow Ce^{4+} + Co^{2+}$, established by the requirement of charge balance within the cations of

the spinel lattice [209,210]. An increase in Co^{3+} population at the cost of Co^{2+} resulted in a decrease of Ce^{3+} ions in favour of Ce^{4+}.

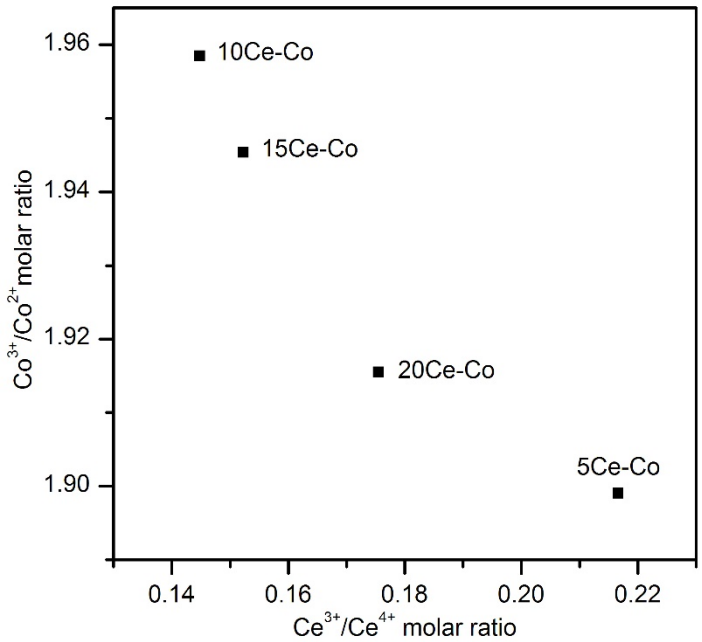

Figure 4.12. Relationship between Co^{3+}/Co^{2+} and Ce^{3+}/Ce^{4+} molar ratios of the xCe-Co catalysts.

The redox properties of the Ce-doped catalysts were investigated by temperature-programmed reduction with hydrogen (H_2-TPR) and temperature-programmed reaction with methane (CH_4-TPRe). The corresponding H_2-TPR profiles are included in Figure 4.13. The hydrogen consumption profiles of the xCe-Co catalysts were similar to those displayed by the pure Co_3O_4, showing the same two-step reduction process, with peak temperatures at 310 and 375 °C. Note that the second reduction peak, assigned to the reduction of Co^{2+} ions, was characterised by a broader temperature window with respect to the bare cobalt oxide, probably due to the distortion caused by the insertion of Ce atoms into the spinel lattice.

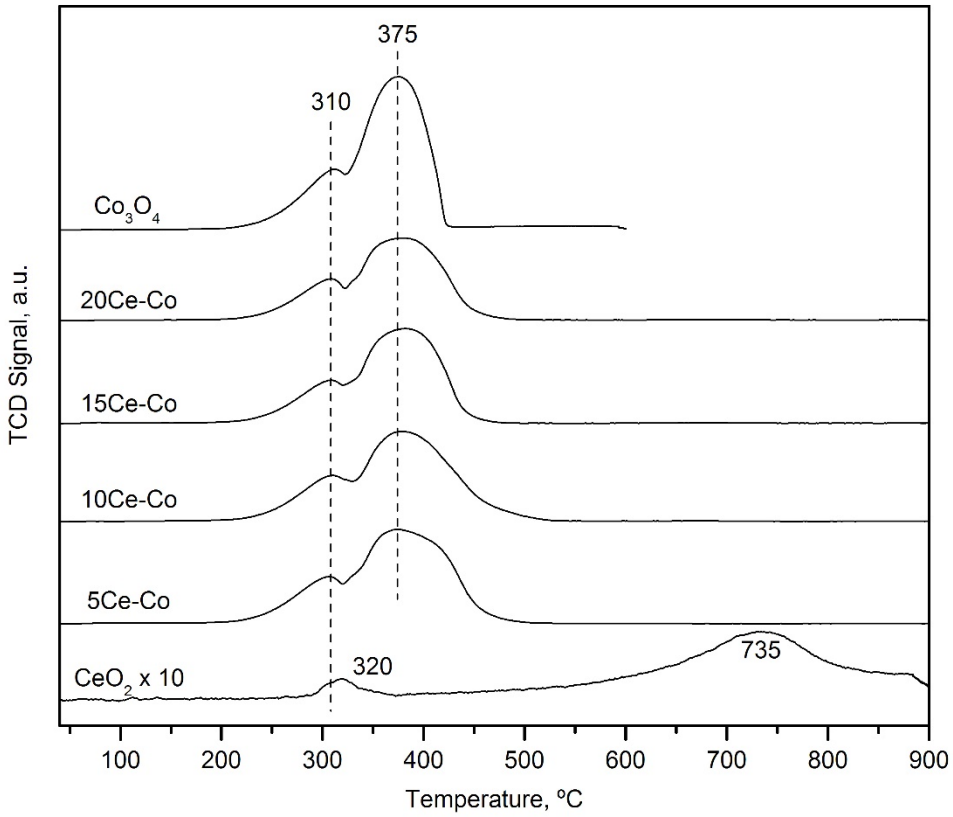

Figure 4.13. H_2-TPR profiles of the xCe-Co catalysts.

The reduction profile of CeO_2 also exhibited a two-step reduction process, where the first step, centred at about 320 °C, is usually attributed to the reduction of the surface while the second one, located at 735 °C, is assigned to the reduction of the bulk [211,212]. However, the intensity of these reduction events was substantially lower than for the reduction of Co_3O_4, and none of the Ce-doped catalysts revealed signals of CeO_2 reduction in their TPR profiles, presumably owing to the low amount of free CeO_2 present in the samples.

The results included in Table 4.6 pointed out that Ce doping did not result in a relevant variation of the relative H_2 uptake at low and high temperature corresponding to the reduction of the spinel, although the H_2 uptake of the 10Ce-Co catalyst at low temperatures was notably higher than for the rest of the Ce-doped samples.

Table 4.6. Results of H_2-TPR analysis of the xCe-Co catalysts.

Catalyst	Low-temperature H_2 uptake, mmol g^{-1}	High-temperature H_2 uptake, mmol g^{-1}	Relative H_2 uptake at low and high temperature
Co_3O_4	4.6	12.0	0.38
5Ce-Co	3.8	11.4	0.33
10Ce-Co	4.1	11.5	0.36
15Ce-Co	3.4	9.7	0.35
20Ce-Co	3.2	9.2	0.34

Since the investigation of the redox properties of the xCe-Co oxides by H_2-TPR did not evidence marked differences among the various samples, a new attempt was made by substituting H_2 with CH_4. This change of the reductant could provide more useful insights on the characterisation and identification of the available oxygen species for methane oxidation. The exit stream of the CH_4-TPRe experiment was analysed by mass spectrometry. Thus, the m/z = 44 (CO_2), the m/z = 28 (CO) and the m/z = 2 (H_2) signals were monitored. The evolution of these two carbon oxides with the temperature for all xCe-Co catalysts and the reference Co_3O_4 sample are shown in Figure 4.14.

Over all samples, the formation of CO_2 occurred at 350-550 °C and 600-700 °C. However, as opposed to the H_2-TPR profiles, the temperature windows for both reactions were clearly discernible and both CO_2 contributions took the shape of definite non-Gaussian peaks. At lower temperatures the generation was assigned to the oxidation of methane by oxygen species associated with Co^{3+} ions. Conversely, at higher temperatures the CO_2 production was attributed to the oxidation of methane by oxygen species associated with Co^{2+} ions [133].

In all cases, the formation of CO_2 at high temperatures was also accompanied by the generation of CO and H_2 to some extent. This could be due to the ability of Co^{2+} ions to catalyse the reforming of methane as well [213] and also due to the deficit of oxygen present in the catalysts after all Co^{3+} ions were reduced.

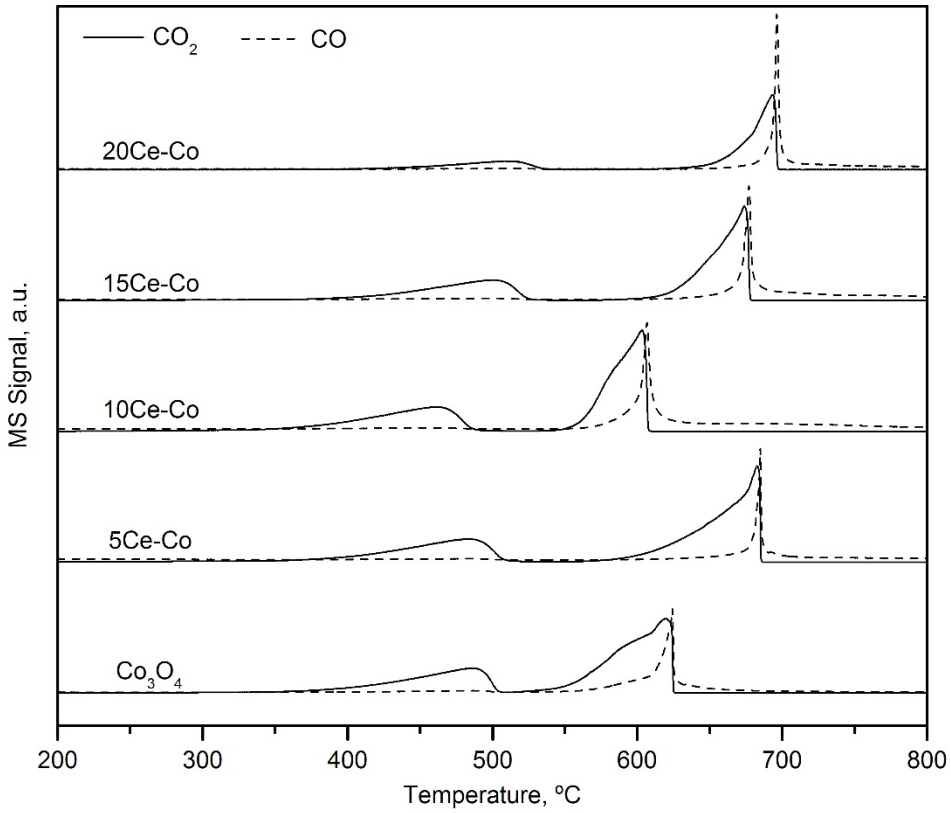

Figure 4.14. CH_4-TPRe profiles of the xCe-Co catalysts.

Interestingly, for the 10Ce-Co sample, the formation of CO_2 occurred at significantly lower temperatures (460 and 605 °C) when compared with the undoped Co_3O_4 sample (485 and 620 °C). Each CH_4-TPRe experiment was followed by a H_2-TPR analysis to check if methane could completely reduce the catalysts. No hydrogen uptake was found, thereby evidencing that all samples were completely reduced by methane. Integration and quantification of the CO_2 production at low and high temperatures (Table 4.7) revealed a better behaviour for the conversion of CH_4 at low temperatures over the 10Ce-Co sample. These results demonstrated that the addition of small amounts of Ce to bulk Co_3O_4 catalysts improved not only their textural and structural properties, but also their ability for methane oxidation.

Table 4.7. Results of CH_4-TPR analysis of the xCe-Co catalysts.

Catalyst	Low-temperature peak, °C	High-temperature peak, °C	Relative CO_2 production at low and high temperature
Co_3O_4	485	620	0.56
5Ce-Co	480	680	0.54
10Ce-Co	460	605	0.66
15Ce-Co	500	675	0.61
20Ce-Co	510	695	0.63

4.2.2. Catalytic performance of the synthesised catalysts

The corresponding light-off curves of the Ce-doped Co_3O_4 catalysts at 30,000 h^{-1} are included in Figure 4.15. All the light-off curves of the Ce-doped catalysts were relatively similar with a T_{50} in the 425-435 °C range. It must be pointed out that the pure CeO_2 was virtually inactive, with a conversion as low as 10% at 600 °C. Only the 10Ce-Co sample showed a slightly better behaviour with respect to the undoped Co_3O_4 catalyst.

More perceptible differences were noticed when the specific reaction rates at 375 °C (with methane conversions lower than 20%) were compared (Table 4.8). Thus, the reaction rate was 2.02 mmol CH_4 g_{Co}^{-1} h^{-1} over the 10Ce-Co sample and 1.83 mmol CH_4 g_{Co}^{-1} h^{-1} over the non-modified cobalt oxide, as already described in the previous section. This revealed that the introduction of cerium had a positive effect on the specific activity of bulk Co_3O_4, but also that this positive effect was limited to a relatively narrow window of cerium loadings.

The estimated apparent activation energy of the 5Ce-Co, 10Ce-Co and 15Ce-Co catalysts were 78-79 kJ mol^{-1}, close to the value determined for the Ce-free counterpart. Over the 20Ce-Co catalyst, characterised by a considerable amount of segregated ceria, the value significantly increased up to 85 kJ mol^{-1}. Note that pure CeO_2 gave an activation energy of 108 kJ mol^{-1}.

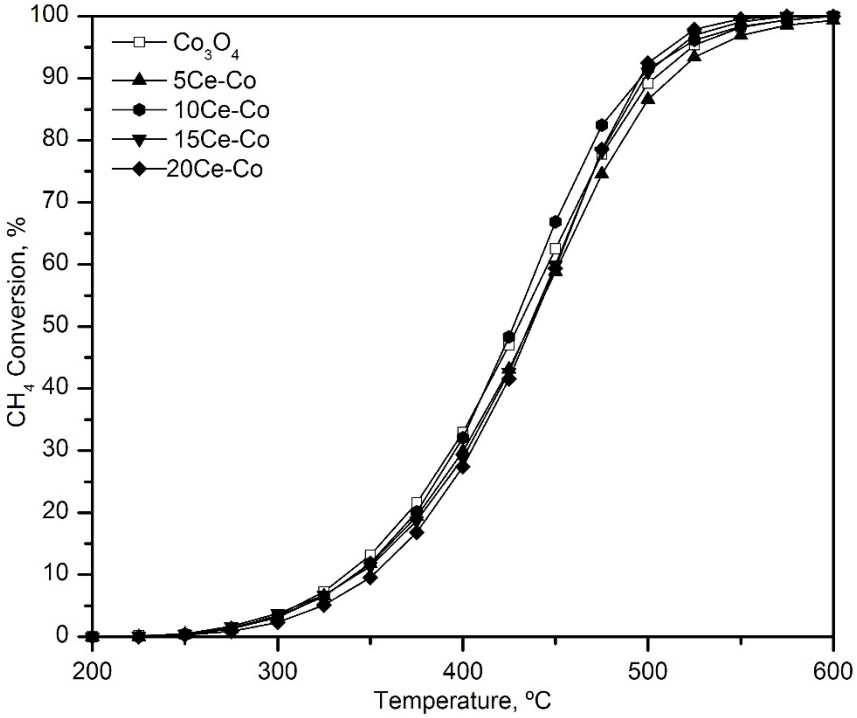

Figure 4.15. Light-off curves of the xCe-Co catalysts.

Table 4.8. Kinetic results of the xCe-Co catalysts.

Catalyst	T_{10}, °C	T_{50}, °C	T_{90}, °C	Reaction rate at 375 °C, mmol CH_4 g_{Co}^{-1} h^{-1}	E_a, kJ mol^{-1}
CC	335	430	505	1.83	74 ± 1
CeO_2	›600	›600	›600	---	108 ± 2
5Ce-Co	340	435	515	1.81	78 ± 1
10Ce-Co	340	425	495	2.02	79 ± 1
15Ce-Co	340	435	500	1.97	79 ± 2
20Ce-Co	350	435	495	1.90	85 ± 2

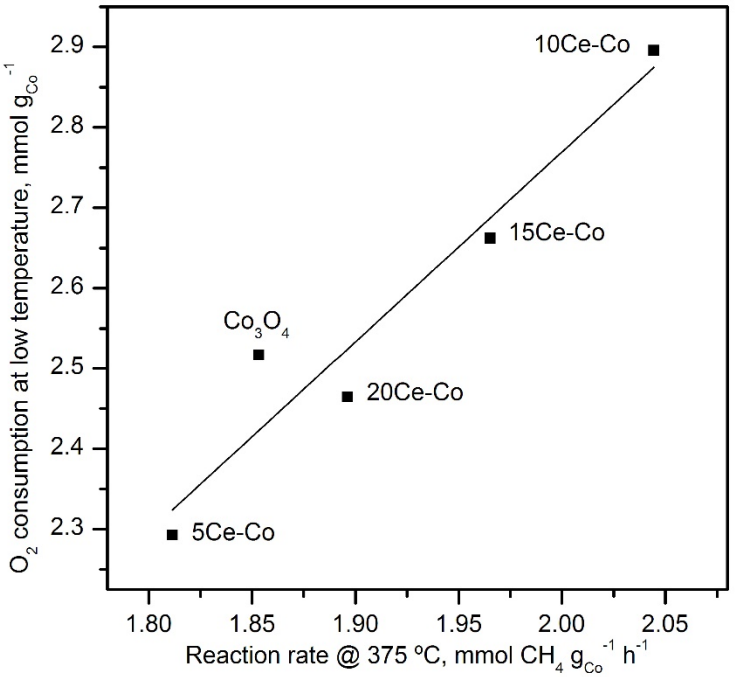

Figure 4.16. Relationship between the O_2 consumption at low temperatures (CH_4-TPRe) and the specific reaction rate over the xCe-Co catalysts.

The relationship shown in Figure 4.16 revealed that the specific reaction rate was clearly influenced by the mobility of the oxygen species, which was evaluated from the amount of oxygen reacting with methane at low temperatures, which in turn corresponded to the $Co^{3+} \rightarrow Co^{2+}$ reduction step in the CH_4-TPRe run. In sum, it could be concluded that the addition of small amounts of cerium atoms, which were introduced into the lattice of Co_3O_4, resulted in an enhancement of the intrinsic activity of the spinel. This improvement was mainly owing to the distortion of the crystalline structure, which ultimately led to an increased population of Co^{3+}, an improved reducibility and a higher mobility of the oxygen species in the spinel lattice.

Finally, attention was paid to examining the stability of the most active catalysts, namely 10Ce-Co and the bare Co_3O_4, when operating at constant temperature (450 °C) during a relatively prolonged time (150 hours). The results included in Figure 4.17 revealed that both oxides gave a relatively stable conversion close to 75%, although the cerium-free sample showed a slight instability. The characterisation of the used 10Ce-Co sample by N_2

physisorption and XRD revealed a reduced impact on its surface area (30 $m^2 g^{-1}$, 35 $m^2 g^{-1}$ for the fresh sample) and crystallite size (30 nm, 29 nm for the fresh sample).

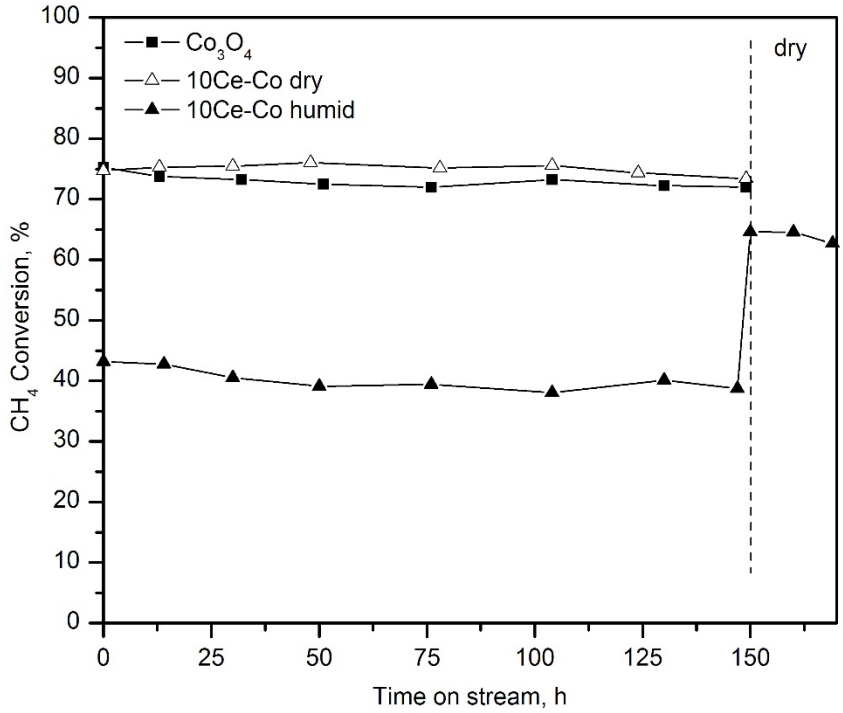

Figure 4.17. Evolution of conversion as a function of time over the Co_3O_4 and 10Ce-Co catalysts at 450 °C under dry and humid conditions.

Given the reasonably good results achieved by the 10Ce-Co catalyst its stability at 425 °C was also evaluated under humid conditions (in the presence of 10% vol. H_2O) for 150 hours. The results are also included in Figure 4.17. It was found that water noticeably decreased the catalytic performance with a reasonably constant conversion around 40%. The surface area after this run decreased to 24 $m^2 g^{-1}$ in line with the concomitant enlargement of the crystallite size (35 nm).

This used sample was further submitted to an additional stability test under dry conditions for 20 hours (Figure 4.17). It was noticed that conversion was not fully recovered, but it was still around 65%. This finding certainly evidenced that water, apart from inhibiting the catalytic activity by competitive effects, also had a significant negative effect on the physicochemical properties of the sample [174,214].

4.3. GLOBAL VIEW AND CONCLUSIONS

In this chapter, the viability of further improving the properties of the previously synthesised bulk Co_3O_4 catalyst by adding a promoting metal was evaluated. This global objective implied two different steps. First, the most suitable doping metal was selected. Then, the metal loading of this promoting metal was adjusted.

For the identification of the most suitable promoter, several Co_3O_4 oxide catalysts doped with different metallic elements were synthesised by the optimised precipitation route. From the six examined potential dopants (Mn, Fe, Ni, Cu, Zn and Ce), copper, nickel and cerium provided the the most notable redox promotional effects for the cobalt oxide. However, both copper- and nickel-doped catalysts exhibited worse textural and structural properties with respect to the undoped counterpart. On the other hand, cerium was found the most appropriate promoter due to the resulting catalyst exhibiting improved textural and structural properties while maintaining the good reducibility of the cobalt oxide spinel. The doped catalyst showed a slight reduction of the T_{50} of 5 °C with respect to the pure cobalt oxide.

Once the most suitable dopant was defined, attention was paid to optimising its metallic loading (in the 5-20%wt.Ce range) in order to ensure the maximum achievable improvement of the Co_3O_4 catalyst. The strategy led to the conclusion that a metallic loading of 10%wt. was essentially the optimal value, since lower loadings (5%wt.) did not exhibit any significant improved behaviour, and higher loadings (15-20%wt.) led to segregation of the added cerium in the form of CeO_2, with no marked beneficial effects on the activity of the resulting catalysts.

The activity of the tested catalysts was found to be controlled by the Co^{3+}/Co^{2+} surface molar ratio, which controlled the presence of surface lattice oxygen species in the catalyst and their participation in the methane oxidation reaction. The addition of a relatively small amount of cerium (10%wt.) to the Co_3O_4 lattice led to an increase in the inherent catalytic activity of the cobalt phase due to an improvement in the mobility of lattice oxygen species associated with easily reducible Co^{3+} ions, which in turn was favoured by the insertion of the Ce^{4+} cations into the spinel lattice. This optimised catalyst also exhibited a marked stability under both dry and humid conditions during a relatively prolonged reaction time.

Despite the improvement of the structural and textural properties provided by the cerium doping, these were still relatively poor over the resulting catalyst. The addition of a second promoting metal would probably not change that situation and would also increase the risk of segregated phases appearing, therefore not being a useful strategy to further improve the doped Co_3O_4 catalyst. Consequently, in the following chapter an alternative approach for enhancement of the textural and structural properties was followed. This strategy consisted of dispersing the cobalt oxide on the surface of a porous material, to obtain a high surface supported catalyst with expectedly promoted physico-chemical properties.

Chapter 5

COMBUSTION OF METHANE OVER SUPPORTED CATALYSTS

ABSTRACT

Despite the improvements achieved by the optimisation of the precipitation route of bulk Co_3O_4 catalysts, the structural and textural properties of the resulting oxide remained being rather poor, which limited the effectiveness of their excellent redox properties. The best alternative to solve this problem consists of supporting the cobalt oxide onto the surface of a porous material, in order to make use of its good textural properties. In this chapter, firstly, the most adequate support material was selected, among those most commonly applied and available. The evaluation of the various supports was made not only on the basis of the activity of the resulting catalyst, but also taking into consideration the improvement in the structural and textural properties of the resulting supported catalysts with respect to the bulk oxide. The results revealed that gamma-alumina provided the largest promotion of the morphological properties of the supported cobalt oxide, but with the drawback of a strong cobalt-alumina interaction which partially inhibited the catalytic activity. Secondly, the effect of the cobalt loading on the specific activity was evaluated. The characterisation and catalytic testing concluded that the optimal loading was close to 30%wt.Co.

5. COMBUSTION OF METHANE OVER SUPPORTED CATALYSTS

Bulk spinel cobalt oxide (Co_3O_4) catalysts have been demonstrated to exhibit a high activity for methane combustion in the previous chapters, and can be thus considered solid alternative candidates to noble metal based catalysts, owing to their relatively low cost, reasonable thermal and hydrothermal stability and high selectivity to CO_2.

As has been also verified, the origin of the notable activity of cobalt oxide catalysts in oxidation reactions lies in the excellent redox properties of this material, particularly, in its high reducibility and mobility of active oxygen species. The key physicochemical properties of these catalysts are highly dependent on the synthesis methodology, the calcination temperature, and the presence and chemical nature of doping metals. Nevertheless, irrespective of the combination of those parameters that is considered, the structural and textural properties of the resulting bulk catalyst are usually very poor when using conventional synthesis methodologies, for example precipitation, direct calcination, reactive grinding or sol-gel complexation, with relatively low specific surface areas and large crystallite sizes [215,216]. This introduces a limitation for this type of materials, since not all catalyst mass is available for reaction, and therefore they do not make the most of their superior redox properties. Also noteworthy is the weak mechanical resistance of bulk catalysts that conditions its use for real operation.

Better textural properties can be obtained with solvothermal or hard-template-based routes [130,217-219]. However, these synthesis routes are often complex, and subsequently rather difficult to scale up to industrial production. In a simpler way, an increased available metallic surface area and improved structural properties can be simply achieved by depositing the Co_3O_4 phase over the surface of a porous support. This classical strategy has been reported to enhance the inherent catalytic activity of Co_3O_4 in some cases [220,221], but, in other cases, the interactions between cobalt oxide and the support can be detrimental owing to their negative impact on the redox properties [222].

The selection of an appropriate support is not a trivial task and can have a significant effect on the properties of the final catalyst, due to the different nature of the cobalt-support interactions, to the point of even rendering the catalyst useless for the specific purpose under study. For cobalt oxide catalysts the most commonly used supports are alumina [223,224], magnesia [225,226], zirconia [129,227], silica [228,229], ceria [121,230], silicon

carbide [231,232], zeolites [120,233] or cordierite [176,234]. The decision of using one or other support for a specific cobalt-based catalyst is generally made on the basis of the specific catalytic properties that the support is required to enhance.

Regarding this, many studies have dealt with the effect of specific supports on the performance Co_3O_4 catalysts for different reactions. For instance, Grzybek et al. [235] found out that cobalt oxide showed a very different behaviour for N_2O abatement depending on which polymorph of alumina was used as the support. Their work concluded that it was better to sacrifice the textural properties of the final catalyst by using low-surface α-Al_2O_3 instead of γ-Al_2O_3 with the objective of inhibiting the occurrence of cobalt-alumina interactions.

This effect was also found by Solsona et al. [97], when studying the total oxidation of propane with cobalt oxide supported over alumina with low, medium and high surface area. On the other hand, Yung et al. [236] examined the oxidation of NO with cobalt catalysts supported over titania and zirconia, finding that the latter was a more suitable support. However, on a different study, Kim et al., [237] reported that high-surface ceria was a better support than titania or zirconia for this same reaction. Ceria was also found to be, as pointed out by Wyrwalski et al. [238], the most suitable support for cobalt oxide for the complete oxidation of propene. This type of investigations has been carried out for liquid phase reactions as well. For example, Zhang et al. [239] analysed the influence of several supports on the degradation of organic dyes in solution. They concluded that MgO was the most suitable for this purpose on account of the increase in the population of surface Co^{2+} ions induced by cobalt-magnesia interactions.

In the case of methane oxidation, it has been demonstrated that the population of Co^{3+} species in the spinel lattice is the key parameter that provides the catalyst with the good reducibility and oxygen mobility involved in the Mars – van Krevelen mechanism [240,241]. Thus, an appropriate support for this reaction should enable a high dispersion of the cobalt deposited, while simultaneously allowing the cobalt oxide species to preserve their good redox properties as intact as possible.

A wide number of works have investigated the oxidation of methane over supported cobalt catalysts, each one focusing on a specific support, under variable reaction conditions, with different degrees of success [242-244]. However, these studies have often employed

synthesis methodologies such as wet impregnation, incipient wetness impregnation or solid combustion synthesis. In this sense, to the best of our knowledge, no reports are available on the analysis of supported catalysts prepared by precipitation.

For this reason, firstly it would be necessary to define the most suitable porous material for preparing a supported cobalt oxide catalyst following the previously optimised precipitation route. Among the wide variety of existing supports, three were chosen for this investigation in view of the results reported in the available literature. The selection should be made not only on the basis of the activity of the resulting catalysts, but also by taking into account the relative improvement of the textural and structural properties that each support is capable of providing to the active phase. Once the most suitable support is determined, it would be then essential to tune the cobalt loading in order to make the most of the physicochemical properties of the chosen support. Note that in both studies regarding the support and the Co content, the analysis of cerium addition to the catalyst formulation will be postponed for the following chapter for the sake of simplifying the analysis of the characterisation results of the supported catalysts.

5.1. SELECTION OF THE MOST SUITABLE SUPPORT

With the aim of finding the most appropriate support, three Co_3O_4 catalysts supported over gamma-alumina, magnesia and ceria were synthesised by precipitation with sodium carbonate. After thermal activation at 600 °C, the resulting catalysts were extensively characterised and examined for the oxidation of methane under lean conditions. The ultimate goal was to determine the effect that the various supports have on the textural, structural and redox properties and the specific activity of the oxide phase.

To prepare the supported catalysts, the synthesis route was modified by adding the support, in powder form, to the cobalt nitrate solution before the addition of the precipitating agent, with the objective of provoking the precipitation of the cobalt precursor onto the surface of the support. As a reference, the cobalt loading of all three catalysts was fixed at 30%wt. of metallic cobalt, due to the uncertainty that all deposited cobalt would convert into Co_3O_4 after calcination. The supported catalysts were denoted Co/X, where X stands for the metal element of the support (Al, Mg and Ce). Ceria and magnesia supports were also produced by precipitation, starting from cerium nitrate hexahydrate and magnesium nitrate hexahydrate, respectively. The obtained samples

were thermally activated at 600 °C for 4 h. The gamma-alumina, however, was acquired as a commercial γ-Al_2O_3 powder (Saint Gobain Norpro SA 6173). This sample was stabilised at 850 °C for 4 hours in static air.

5.1.1. Physico-chemical characterisation of the supports

The textural properties of the commercial gamma-alumina and the as-prepared magnesia and ceria are shown in Table 5.1. Notable differences were noticed among the investigated supports. Hence, γ-Al_2O_3 showed the largest specific surface area (139 $m^2 g^{-1}$), followed by MgO (80 $m^2 g^{-1}$) and CeO_2 (8 $m^2 g^{-1}$). This decreasing trend was also consistent for the estimated pore volume. Thus, it varied from 0.56 $cm^3 g^{-1}$ (gamma-alumina) to 0.08 $cm^3 g^{-1}$ (ceria). The supports all showed type IV isotherms with H2 hysteresis loops, characteristic of mesoporous materials.

On the other hand, XRD patterns of the as-prepared supports well matched with those expected for the corresponding pure oxides (Figure 5.1). Hence, the observed diffraction signals could be indexed as gamma-alumina (2θ= 37.7, 45.8 and 67.3°, ICDD 01-074-2206), magnesium oxide (2θ= 43.0, 62.3, 74.7 and 78.6°, ICDD 00-004-0829) and cerium oxide (2θ= 28.5, 33.3, 47.5, 56.4 and 76.7°, ICDD 00-004-0593). Moreover, the crystallinity of both magnesia and ceria was higher than that of gamma alumina in view of their noticeably more intense and sharper signals.

Table 5.1. Textural and structural properties of the supports.

Support	BET surface, $m^2 g^{-1}$	Pore volume, $cm^3 g^{-1}$	Mean pore diameter, Å	Crystallite size, nm
Al_2O_3	139	0.56	123	5
MgO	80	0.19	106	21
CeO_2	8	0.03	230	32

It is worth mentioning that the formation of ceria was further corroborated by Raman spectroscopy, which revealed a strong peak assigned to the F_{2g} Raman-active mode (462 cm^{-1}) characteristic of the fluorite-like lattice of CeO_2. Note that the vibrational modes of MgO and γ-Al_2O_3 are essentially Raman inactive.

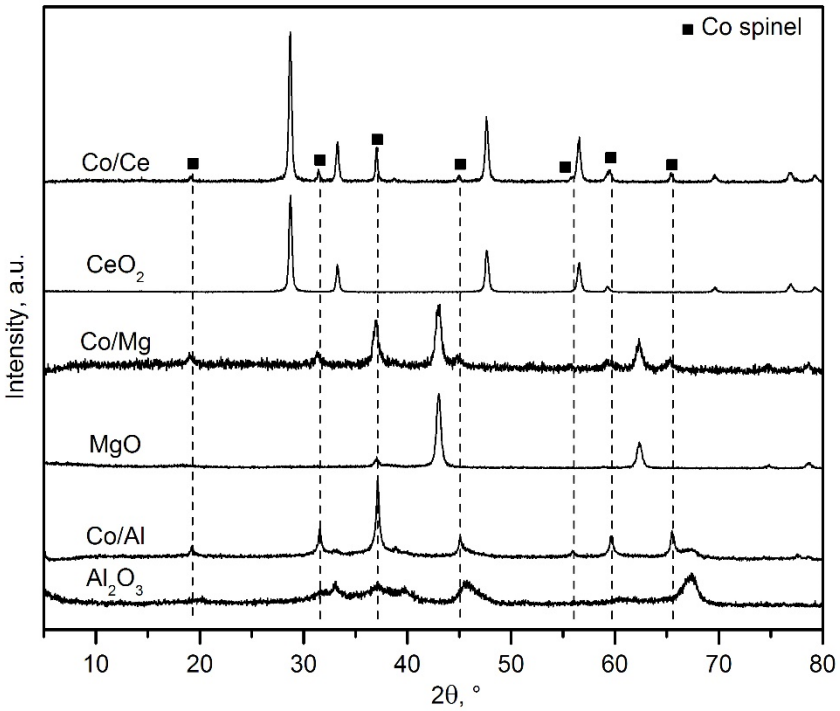

Figure 5.1. XRD patterns of the bare supports and the supported cobalt catalysts.

5.1.2. Physico-chemical characterisation of the supported cobalt catalysts

Table 5.2 specifies the cobalt loading of the synthesised cobalt catalysts as determined by WDXRF and ICP-AES (in the case of the Co/Ce sample). It was thus verified that this content was relatively close to the nominal value (30%wt. Co). N_2 physisorption measurements revealed that cobalt species markedly blocked the pores of the alumina and magnesia supports, as evidenced by the notable decrease in the surface area of the Co/Al and Co/Mg catalysts, from 136 to 108 $m^2 g^{-1}$ (26%) and 80 to 47 $m^2 g^{-1}$ (42%), respectively.

Similarly to the blank supports, the Co/Al and Co/Mg catalysts showed type IV isotherms with H2 hysteresis loops as well. Both samples presented a decreased pore volume with respect to their corresponding support (0.29 and 0.16 $cm^3 g^{-1}$, respectively). By contrast, the impact on the textural properties of the Co/Ce sample was less noticeable. In fact, a slight increase in both surface area and pore volume was found (18 $m^2 g^{-1}$ and 0.07 $cm^3 g^{-1}$, respectively).

Table 5.2. Textural properties of the supported cobalt catalysts.

Catalyst	Cobalt content, %wt.	BET surface, $m^2 g^{-1}$	Pore volume, $cm^3 g^{-1}$	Mean pore diameter, Å	Co-spinel crystallite size, nm	Support crystallite size, nm
Co/Al	27.9	108	0.29	89	29	6
Co/Mg	31.9	47	0.16	204	17	16
Co/Ce	28.9	18	0.07	225	44	33

The comparative analysis of the pore size distributions of the supports and the cobalt catalysts (Figure 5.2) evidenced that the deposition of cobalt particles was highly dependent on the pore accessibility and interconnectivity. Hence, when cobalt was deposited over gamma-alumina, which exhibited a bimodal distribution centred at 90 and 150 Å, the cobalt preferentially deposited over its largest pores. Conversely, when using magnesia as a support, characterised by pores with a markedly different size (35-50 and 325 Å), the cobalt species favourably located on the smaller pores.

Finally, in the case of ceria, both support and catalyst possessed a unimodal distribution centred around 225 Å, but with an increased width for the cobalt-containing sample. This could be due to the fact that cobalt species did not find enough space to deposit on the pores of ceria, and preferentially located on its external surface as well. Also, since the amount of pores of 335 Å (the prevalent pore size of bulk Co_3O_4) was larger in the Co/Ce catalyst than in the ceria support, it could be assumed that this catalyst contained segregated cobalt oxide to some extent.

Figure 5.1 also includes the diffractograms of the cobalt catalysts. Their patterns were characterised by the presence of Co_3O_4 (2θ = 31.3, 37.0, 45.1, 59.4 and 65.3°) along with some weak signals corresponding to the respective support (2θ = 43.0 and 62.3° for MgO, and 2θ = 28.5, 47.5 and 56.4° for CeO_2).

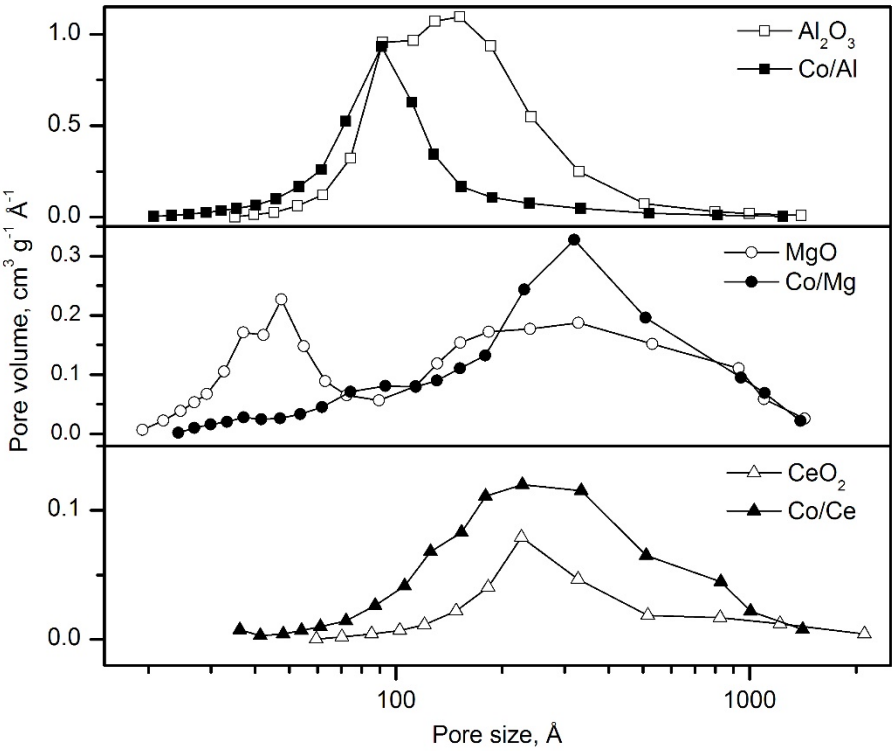

Figure 5.2. Pore size distributions of the bare supports and the supported cobalt catalysts.

However, it is widely reported in the literature that, in samples where cobalt and alumina are in contact, moderate temperatures (above 450 °C) can induce the migration of Co^{2+} ions into the structure of the alumina, which results in the formation of a mixed spinel phase known as cobalt aluminate ($CoAl_2O_4$, ICDD 00-044-0160), as follows from Equation 5.1 [222,245]. The diffraction signals of this spinel are virtually identical to those of Co_3O_4 since the cell size of cobalt aluminate is almost equal to that of cobalt oxide. For this reason, the presence of $CoAl_2O_4$ on the supported catalysts could not be ruled out by XRD.

$$CoO + Al_2O_3 \longrightarrow CoAl_2O_4 \tag{5.1}$$

On the other hand, the crystallinity of the support phases did not noticeably change since their crystallite size was similar before and after cobalt deposition (Table 5.2). However, the crystallite size of the cobalt spinel was highly dependent on the employed support. The smallest crystallite size was obtained over the magnesia (17 nm) while the largest size was found over the ceria (44 nm). This finding was consistent with the poorer textural properties of the as-prepared ceria, which led to a favoured location of Co_3O_4 on its external surface. As for the alumina-supported catalyst, the estimated crystallite size should be taken as the averaged contribution of the two possible cobalt spinels present in the sample (Co_3O_4 and $CoAl_2O_4$).

The Raman spectra in the 150-900 cm^{-1} region of the cobalt catalysts supported on alumina, magnesia and ceria are shown in Figure 5.3. As a reference, the spectrum of pure Co_3O_4 is shown as well. Apart from a relatively intense band at 462 cm^{-1} (F_{2g} mode of CeO_2) for the Co/Ce catalyst, all supported catalysts displayed the five Raman actives modes attributable to Co_3O_4, namely three F_{2g} modes located at 194, 519 and 617 cm^{-1}, and the E_g and A_{1g} modes at 479 cm^{-1} and 687 cm^{-1}, respectively.

In addition, two shoulders at 705 and 725 cm^{-1} attached to the A_{1g} vibration mode were also visible in the case of the Co/Al catalyst. These two signals evidenced the presence of cobalt aluminate in this sample [246,247]. As far as the Co/Mg catalyst was concerned, an inspection of the 1000-1500 cm^{-1} region revealed the presence of the Co-Mg solution. As shown in Figure 5.4, the spectrum of pure MgO displayed a band located at 1100 cm^{-1} that could be attributed to a two-phonon vibration induced by some disorder in the structure of magnesia [248,249]. When cobalt was deposited over the pure MgO, this disorder band was still visible, along with additional small bands at about 1250 and 1350 cm^{-1} that would imply an increase in the disorder of the structure of MgO due to the insertion of cobalt ions leading to the formation of a Co-Mg solid solution [250]. Note that the formation of this mixed oxide was difficult to verify by XRD since no significant changes in the Bragg positions of the Co/Mg catalysts were noted with respect to those of pure magnesia.

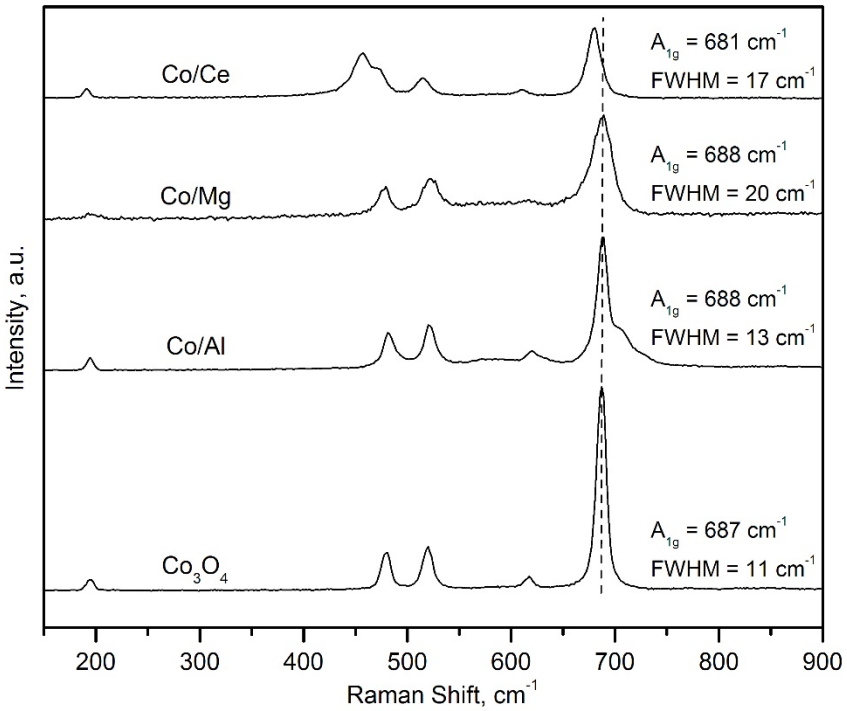

Figure 5.3. Raman spectra of the supported cobalt catalysts.

A closer inspection of the A_{1g} mode as function of the type of used support could be useful for determining the characteristics of the lattice of deposited Co_3O_4. This influence was analysed in terms of the observed shift and the full width at half maximum (FWHM) of this signal. The Raman spectra of a bulk Co_3O_4 was used as a reference. Thus, this Raman mode was located at 687 cm^{-1} and its FWHM was 11 cm^{-1}. While no significant shift in the position of the band was evident for the Co/Al (688 cm^{-1}) and Co/Mg (688 cm^{-1}) catalysts, a remarkable shift to a lower frequency (681 cm^{-1}) was noted over the Co/CeO_2 sample. This redshift of the signal could be assigned to the distortion of the spinel lattice, probably owing to insertion of Ce ions [251] that in turn also increased the FWHM value (17 cm^{-1}). On the other hand, the largest FWHM value (20 cm^{-1}) for the Co/Mg catalyst was assigned to the presence of Co-Mg mixed oxides.

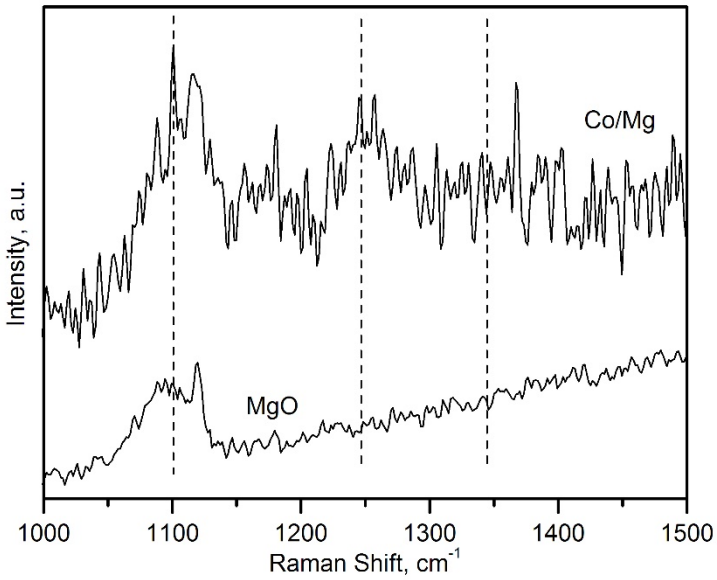

Figure 5.4. Close-up view of the distortion-induced phonon region of the Raman spectra of pure MgO and Co/Mg samples.

The lattice distortion in the cobalt spinel generated by the insertion of Ce ions and/or formation of Co-Mg mixed oxides was further evidenced by a slight increase in the cell parameter of the Co_3O_4 phase. Hence, for both Co/Mg (8.127 Å) and Co/Ce (8.126 Å) catalysts, the Co_3O_4 cell size was larger with respect to the bulk Co_3O_4 sample (8.096 Å).

The surface composition of the samples was investigated by XPS. The Co2p spectra of the supported cobalt catalysts are shown in Figure 5.5, along with the spectrum of bulk Co_3O_4 for comparison. Broad signals were noticed for all samples that suggested the presence of various different cobalt species on the surface of the catalysts. More specifically, all spectra showed the main $Co2p_{3/2}$ signal in the position range 781.4-779.9 eV, along with two satellite signals centred around 785.9-786.7 eV and 789.5-790.2 eV, that were attributed to the presence of Co^{2+} and Co^{3+} ions, respectively [190]. For the Co/Ce catalyst, the position of the main signal (779.9 eV) and the intensity of the satellite signals were comparable to that of the bulk sample. This pointed out that the nature of the cobalt oxide in this catalyst was similar to that of the bulk sample. Nevertheless, a certain shift of the main signal was noticed over the other two samples.

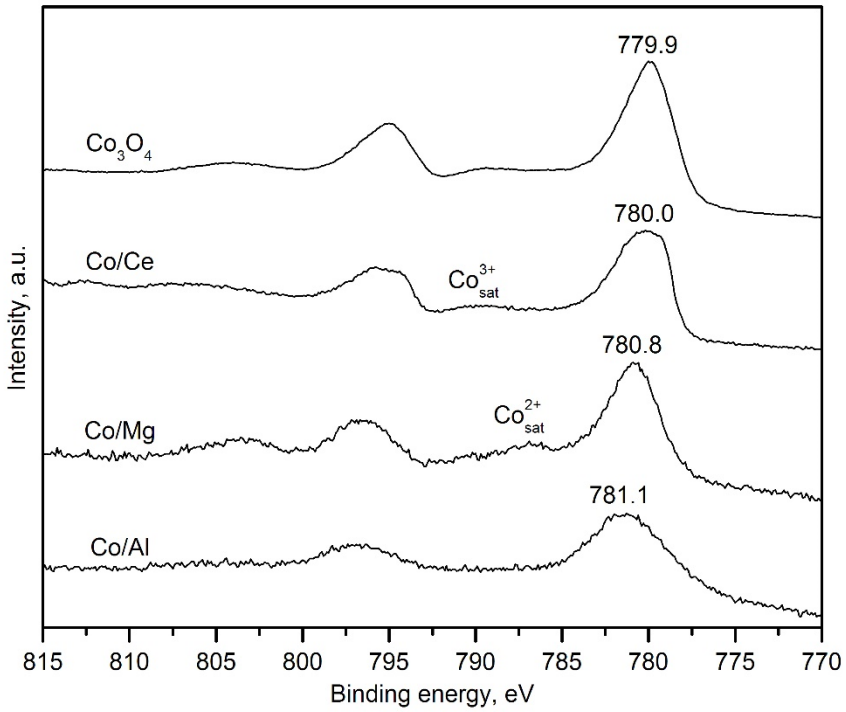

Figure 5.5. Co2p XPS spectra of the supported cobalt catalysts.

Hence, the main signal of the Co/Mg sample was shifted towards higher binding energy values while the intensity of the Co^{2+} satellite signal was notably stronger with respect to the bulk oxide. Both features were compatible with a higher presence of Co^{2+} ions in the surface of the Co/MgO catalyst [252], probably as a result of the Co-Mg interaction and the subsequent formation of the Co-Mg solid solution. Lastly, the main signal was located at 781.1 eV over the Co/Al catalyst, which was typically assigned to the presence of cobalt aluminate [253].

Besides, the surface composition was determined from the integration of the XPS spectra. The respective Co/M (M = Al, Mg and Ce) surface molar ratio could be then calculated and compared with the bulk ratio calculated by XRF analysis. The surface ratio (0.43 and 3.15, respectively) was higher than the bulk ratio (0.39 and 1.39, respectively) for both Co/Al and Co/Ce catalysts. This enrichment evidenced a more preferential presence of cobalt on the surface of these samples. Particularly, the observed pronounced increase over the Co/Ce catalyst suggested the presence of segregated Co_3O_4. Conversely, the surface ratio (0.12)

was notably lower than the bulk ratio (0.38) for the Co/Mg sample. This could be due to the strong Co-Mg interaction and the partial insertion or dissolution of Co ions in the MgO lattice to form a Co-Mg solid solution. The formation of this highly stable mixed oxide thus decreased the amount of cobalt present on the surface of this catalyst.

The redox properties of the catalysts were studied by H_2-TPR in the 50-900 °C temperature range. The corresponding profiles are displayed in Figure 5.6 while the quantitative results of the analysis are listed in Table 5.3. A noticeably different redox behaviour was found among the three cobalt catalysts. Hence, the largest H_2 uptake was exhibited by the sample supported on ceria (7.6 mmol g^{-1}) followed by the catalysts supported on alumina (5.6 mmol g^{-1}) and magnesia (4.6 mmol g^{-1}).

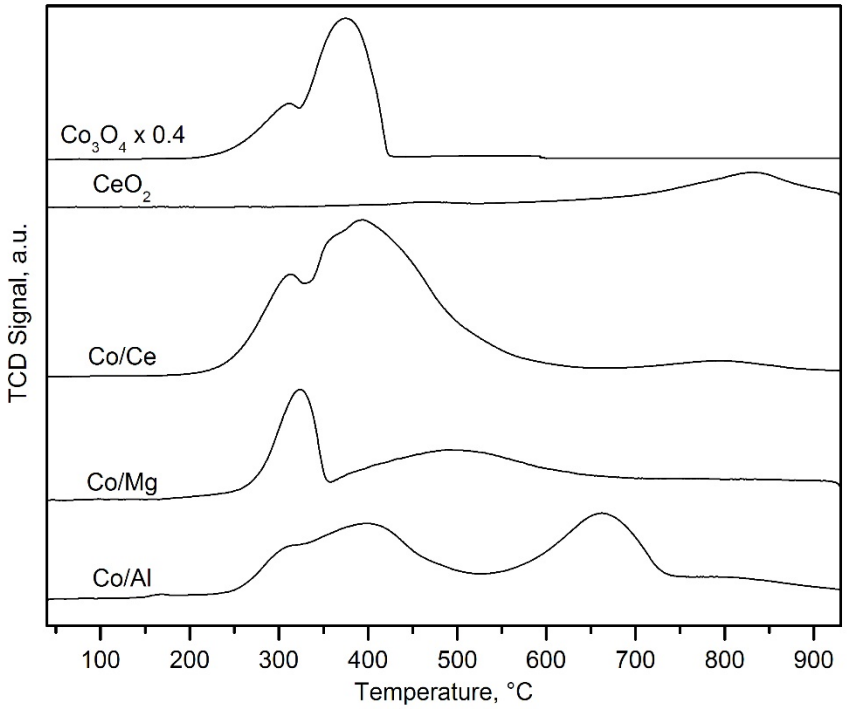

Figure 5.6. H_2-TPR profiles of the supported cobalt catalysts.

First, the redox properties of the latter two samples will be comparatively discussed since both γ-Al_2O_3 and MgO could be considered non-reducible in the studied temperature window. Hence, the observed H_2 consumption could be exclusively assigned to the

reduction of the present cobalt species. In this sense, and taking as a reference the ideal specific H_2 uptake for the reduction of Co_3O_4 as the only cobalt phase (22.6 mmol H_2 g_{Co}^{-1}), both Co/Al and Co/Mg catalysts revealed a significantly lower consumption, namely 18.7 and 14.5 mmol H_2 g_{Co}^{-1}, respectively. Therefore, the estimated degrees of Co reduction were 88 and 64%. In line with the results given by Raman spectroscopy, these findings clearly suggested that a fraction of deposited cobalt species strongly interacted with these supports, thereby negatively influencing their redox properties.

Table 5.3. Redox properties of the supported cobalt catalysts derived from TPR analysis with H_2 and CH_4.

Catalyst	Total H_2 uptake[1], mmol g_{Co}^{-1}	H_2 uptake at low temperature[1], mmol g_{Co}^{-1}	Degree of Co reduction, %	O_2 consumption at low temperature (CH_4-TPRe), mmol g_{Co}^{-1}
Co/Al	18.7 (5.6)	9.8 (2.7)	88	0.28
Co/Mg	14.5 (4.6)	9.9 (3.2)	64	0.51
Co/Ce	26.2 (7.6)	23.4 (6.8)	100	0.70
CeO_2	--- (1.5)	---	---	---

The values in brackets correspond to the H_2 uptake on a catalyst weight basis.

Two main H_2 uptakes were clearly distinguished over the Co/Al catalyst. The first contribution, located at about 250-550 °C, could be assigned to reduction of free Co_3O_4. This consumption could be in turn subdivided into other two features with peak reduction temperatures at 310 and 400 °C, following the same reduction steps revealed by the bulk Co_3O_4 catalysts. This consisted of the sequential reduction to CoO and metallic Co, respectively [254]. An additional peak between 550-750 °C was clearly ascertained. This was attributed to the presence of significant amounts of $CoAl_2O_4$ derived from the strong interaction between Co_3O_4 and Al_2O_3. It was quantitatively deduced that the total amount of cobalt of the sample was equally distributed as Co_3O_4 (49%) and $CoAl_2O_4$ (51%).

The H_2-TPR profile of the Co/Mg sample also revealed two distinct reduction regions although the temperatures windows were markedly different when compared with the alumina-supported counterpart. Hence, the observed consumption at low-temperature (200-350 °C) was ascribed to easily reducible free Co_3O_4 species as well. The band located at higher temperatures (350-650 °C) was assigned to the reduction of Co-Mg species formed during the synthesis route.

The integration of these two features gave the following cobalt distribution, 57% as Co_3O_4 and 43% as Co-Mg mixed oxides. The formation of Co-Mg mixed oxides with a superior stability, which would not be reduced even at 950 °C, could not be however ruled out, as the total H_2 uptake of this sample was rather low in view of its Co content [255]. In fact, when assuming that the uptake at low temperatures (< 350 °C) was owing to the reduction of Co_3O_4 with a stoichiometry of 4 moles of H_2:3 moles of Co, and the uptake at higher temperatures (350-650 °C) was related to the reduction of Co^{2+} species with a stoichiometry of 1 mol of H_2:1 mol of Co, the corresponding metal content of the sample, in view of its overall H_2 uptake, would be equivalent to about 25%wt. This was considerable lower than the actual Co loading as determined by WDXRF (close to 32%wt.). Anyway, the amount of free Co_3O_4, with a significantly higher oxidation activity in comparison with $CoAl_2O_4$ or Co-Mg mixed oxides, was relatively similar for both γ-Al_2O_3 and MgO supported catalysts.

While the H_2 uptake of both pure alumina and magnesia was negligible, the bare CeO_2 sample exhibited a weak signal at 450-500 °C that corresponded to the surface reduction of the oxide whereas the notable H_2 consumption peaking at about 825 °C was related to the reduction of the bulk [256,257]. The TPR profile of the Co/Ce catalyst was characterised by a remarkable uptake between 200-600 °C that was related to the reduction of precipitated Co_3O_4. Similarly to the Co/Al sample, this reduction event exhibited two fairly discernible peaks at 310 and 380 °C. A small band was noted at 800 °C as well, which corresponded to the reduction of the bulk of the support. Note that this occurred to slightly lower temperatures (around 800 °C) with respect to the bare support (about 850 °C), probably due to catalytic role played by cobalt [258].

A quantitative analysis of the amount of consumed H_2 revealed that the overall uptake (7.6 mmol H_2 g^{-1}) reasonably matched with that theoretically expected for the total reduction of Co_3O_4 along with the reduction of ceria (1.8 mmol H_2 g_{Ce}^{-1}). This corresponded to a 100% degree of Co reduction (Table 5.3). At low temperatures the amount of consumed H_2 was 23.4 mmol g_{Co}^{-1}, which was slightly larger than theoretically required for the reduction of the Co_3O_4 oxide (22.6 mmol g_{Co}^{-1}). This pointed out that deposited cobalt facilitated the reduction of the surface of the ceria in this temperature range.

An overall overview of the redox properties of the three cobalt catalysts revealed that the use of ceria was beneficial for obtaining a catalyst with a limited interaction of the active phase with the surface support, thereby not favouring the formation of hardly reducible

cobalt oxides such as cobalt aluminate or cobalt-magnesium mixed oxides. In addition, cobalt slightly helped in promoting the reducibility of the ceria. However, the similarities between the Co/Ce catalyst and the bulk Co_3O_4 sample also suggested that this behaviour could be partially caused by the presence of cobalt oxide segregated from the ceria support.

More useful insights on the influence of the catalyst composition on the reactivity of available active oxygen species for methane oxidation were obtained by CH_4-TPRe analysis coupled to mass spectrometry. The analysis was performed between 50 and 600 °C with a subsequent isothermal step at this temperature for 30 min. The evolution of CO_2 (m/z = 44) and CO (m/z = 28, not shown) was monitored (Figure 5.7).

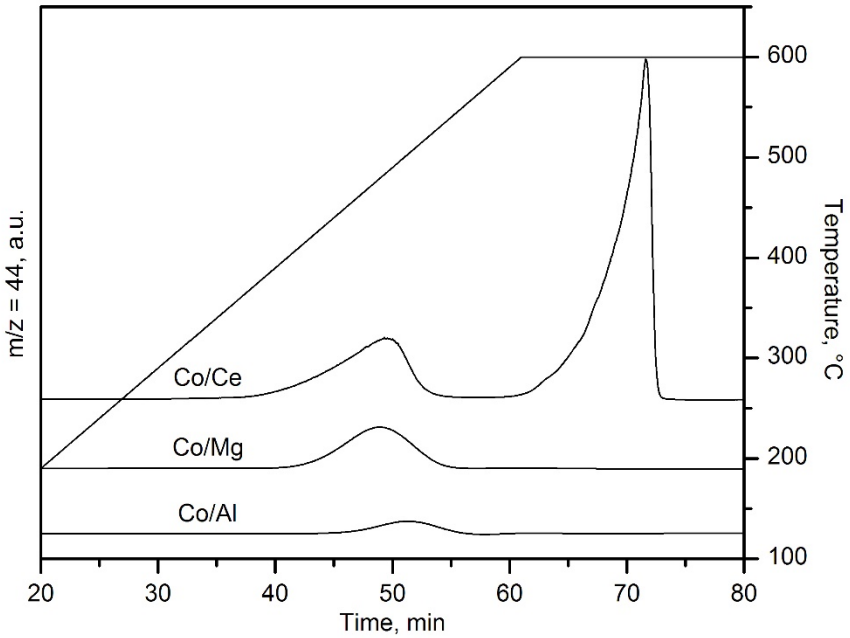

Figure 5.7. CH_4-TPRe profiles of the supported cobalt catalysts.

In the low temperature range (Figure 5.8), namely 375-525 °C, the generation of CO_2 was noticed over the three cobalt catalysts (peaking at about 485 °C). This was attributed to the oxidation of methane by oxygen species associated with Co^{3+} ions. However, the extent of this reaction was considerably different over each sample in view of the comparatively larger amount of consumed oxygen (0.70 mmol O_2 g^{-1}) or the concomitant larger yield of CO_2 over the Co/Ce sample, followed by the Co/Mg (0.51 mmol O_2 g^{-1}) and Co/Al

(0.28 mmol O_2 g^{-1}) catalysts. (Table 5.3) Moreover, the temperature for the onset of reduction (marked by arrows in Figure 5.8) was significantly lower for the Co/Ce sample (395 °C) in comparison with the other two samples, namely 415 and 425 °C over Co/Mg and Co/Al, respectively.

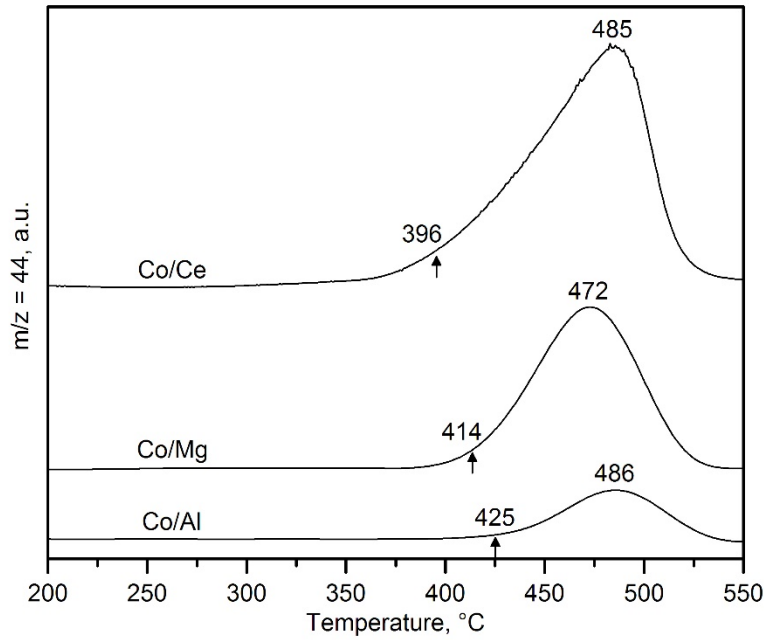

Figure 5.8. Close-up view of the 200-550 °C temperature range of the CH_4-TPRe profiles of the supported cobalt catalysts.

5.1.3. Catalytic performance of the supported catalysts

The performance of the supported cobalt catalysts was examined by their corresponding light-off curves (GHSV = 30,000 h^{-1}) in the 200-600 °C temperature range (Figure 5.9). Recall that only CO_2 was detected in the product stream in the whole temperature range.

To ensure that any diffusional effects did not affect the kinetic results, the criteria for intra-particle and extra-particle mass and energy diffusion, as well as the temperature gradients were checked to be above the limit, as explained in Chapter 2. Regarding this, Table 5.4 includes the calculated values for the various evaluated criteria.

Table 5.4. Criteria for accurate analysis of intrinsic reaction rates (as evaluated for the Co/Ce catalyst at 425 °C).

Criterion number	Recommendation	At 425 °C	Least favourable conditions
1.	Bodenstein parameter $< L_{bed}/d_{particle}$	$3.7 < 79.5$	$67.3 < 79.5^{c}$
2.	$d_{tube}/d_{particle} > 10$	31.2	31.2
3.	Carberry number $< 0.05/n$	0.0013	0.048^{c}
4.	$\gamma\beta_e Ca < 0.05$	0.0012	0.014^{b}
5.	Wheeler-Weisz modulus < 0.15	$3.3\cdot10^{-4}$	$8.0\cdot10^{-4a}$
6.	Mears parameter < 0.1	$1.0\cdot10^{-6}$	$2.1\cdot10^{-6a}$
7.	Radial gradient < 0.05	0.003	0.005^{a}
8.	Bed dilution parameter < 0.05	0.047	0.047
9.	Temperature gradient < 0.3	0.15	0.175^{b}

[a]Determined at 500 °C.
[b]Determined at 600 °C.
[c]Determined at 575 °C.

Appreciable methane conversion (>5%) was detected over 350 °C over the Co/Ce catalyst while a similar conversion level was attained at significantly higher temperatures (400 °C) over the samples supported on both magnesia and alumina.

The T_{50} value was used as criterion for the relative reactivity of each sample (Table 5.5). In a similar way to the results found in the low-conversion range, a substantially different performance was ascertained with values close to 500 °C (Co/Ce), 525 °C (Co/Mg) and 550 °C (Co/Al). Accordingly, conversion values at around 85% (Co/Al), 95% (Co/Mg) and 98% (Co/Ce) were noted at 600 °C.

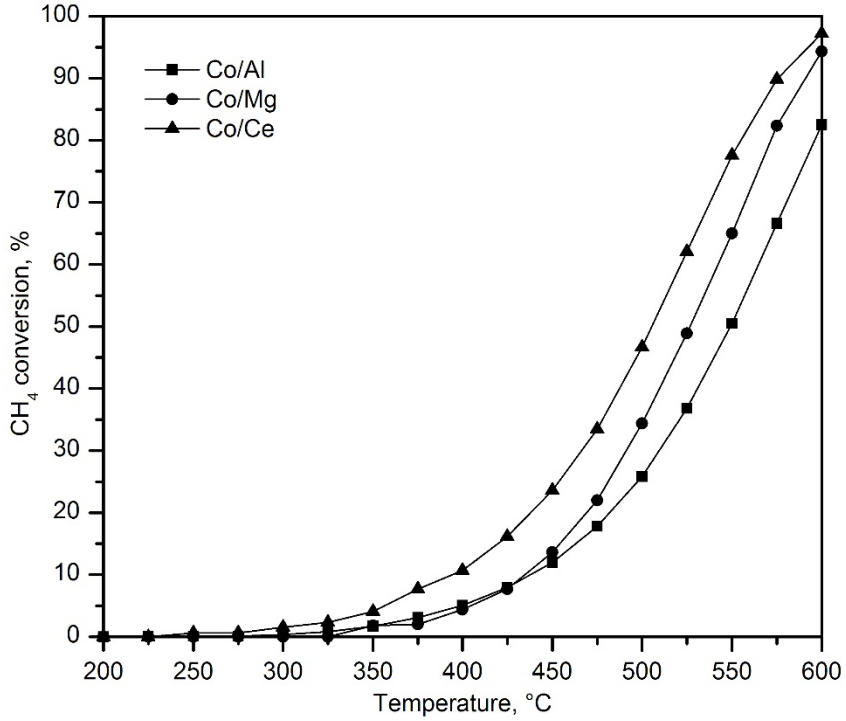

Figure 5.9. Light-off curves of the supported cobalt catalysts.

Table 5.5. Kinetic results of the oxidation of lean methane over the supported cobalt catalysts.

Catalyst	T_{50}, °C	Specific rate at 425 °C, mmol CH_4 g_{Co}^{-1} h^{-1}	E_a, kJ mol^{-1}
Co/Al	550	1.8	82 ± 2
Co/Mg	525	1.4	102 ± 2
Co/Ce	500	3.1	82 ± 2

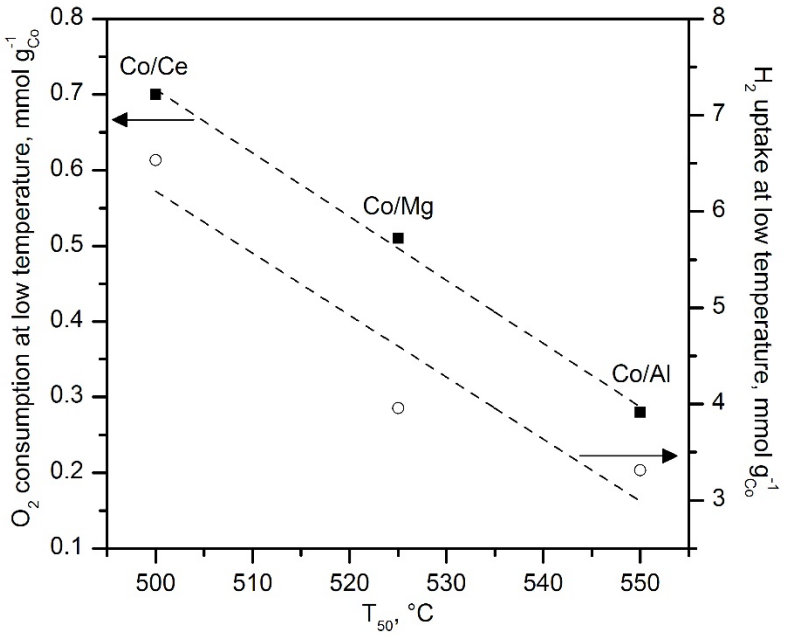

Figure 5.10. Relationship between the activity and the redox properties of the supported catalysts as determined by both H_2-TPR and CH_4-TPRe analysis.

Taking into consideration that the oxidation of methane over Co_3O_4-based catalysts involves the participation of highly active oxygen species [132,259], the observed trend in catalytic activity was proposed to be directly connected to the amount of easily reducible cobalt species in each sample as expressed by the specific oxygen consumption at low temperatures in the CH_4-TPRe profiles. In this sense, Figure 5.10 reveals that there was a reasonably good correlation between the T_{50} values and the reacted O_2 below 550 °C. Accordingly, a comparable relationship was evidenced in relation with the H_2 uptake involved in the reduction of the free Co_3O_4 present in each supported cobalt catalyst (H_2-TPR profiles).

The integral method was followed for evaluating the apparent activation energy of the reaction over the examined cobalt catalysts. The results are listed in Table 5.5 while the corresponding linearised plots are depicted in Figure 5.11.

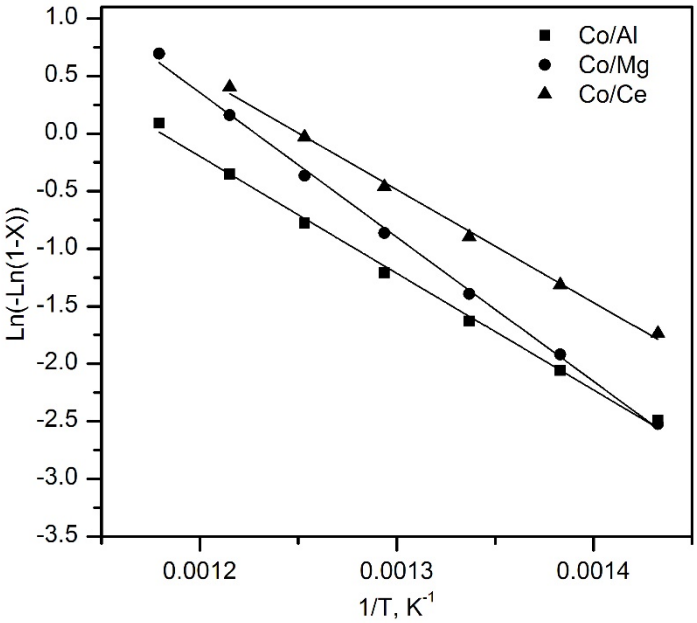

Figure 5.11. Pseudo-first order integral fit for the experimental kinetic data obtained over the supported cobalt catalysts.

The following activation energies were estimated, namely 82 kJ mol^{-1} over Co/Ce and Co/Al and 102 kJ mol^{-1} over Co/Mg. When compared with the value obtained by the bulk Co_3O_4 (74 kJ mol^{-1}) a closer similarity was found when referred to the Co/Ce and Co/Al catalysts. This finding was coherent with the fact that the nature of the active cobalt phase was the same in both cases, namely, Co_3O_4. A noticeable higher activation energy was noticed for the sample in which a mixture of cobalt phases was present such as Co_3O_4/Co-Mg mixed oxide (Co/Mg catalyst). Consequently, it could be established that the formation of a stable Co-Mg solid solution would negatively affect the kinetic behaviour of the Co/Mg catalyst.

In sum, strictly taking into account the catalytic behaviour of the resulting catalyst, ceria would be the most suitable support for cobalt oxide. However, as evidenced by the physicochemical characterisation, the synthesised ceria presented some extremely poor textural properties and most likely there was segregated cobalt oxide physically mixed with supported cobalt oxide in the formulation of the Co/Ce catalyst. On the other hand, between the Co/Al and the Co/Mg catalysts, it must be noted that the former presented a better catalytic performance at low temperatures than the latter despite exhibiting worse

redox properties. The reason for this behaviour seemed to lie in the better textural and structural properties of gamma-alumina and the fact that it did not fixed as much cobalt into an inactive phase as magnesia. For these reasons, the chosen support for the subsequent optimisation of the cobalt loading was gamma-alumina.

5.2. OPTIMISATION OF THE COBALT LOADING OVER γ-Al_2O_3

When considering the suitability of a supported catalyst for a specific material, the first and most important parameter that needs a proper adjustment is the metal loading. A too low metal content will not make full use of the good structural properties of the support. Conversely if the metal concentration is too high, it can completely block the surface of the support or even segregate from it, thus creating rather a physical mixture. Both cases normally result in catalysts with a sub-optimal activity.

For the optimisation of the cobalt loading over gamma-alumina, the selected metallic Co contents were 10, 20, 30, 35 and 40%wt. The corresponding samples were denoted as xCo/Al where x stands for the nominal cobalt loading. This set of samples was prepared by precipitation with sodium carbonate, and catalytic precursors were calcined at 600 °C for 4 h. For comparative purposes, a bulk $CoAl_2O_4$ sample was also prepared by the same co-precipitation route, where the cobalt salt ($Co(NO_3)_2{\cdot}6H_2O$) and an aluminium salt ($Al(NO_3)_3{\cdot}9H_2O$) with stoichiometric proportions were precipitated until pH 9 was achieved. The samples were thermally stabilised at 600 and 850 °C, and labelled as $CoAl_2O_4$ 600 and $CoAl_2O_4$ 850. A temperature as high as 850 °C were used in order to massively induce the formation of the aluminate.

5.2.1. Physico-chemical characterisation of the catalysts

The textural properties (specific surface area, mean pore diameter and pore volume) and the actual Co loading of the supported Co_3O_4/Al_2O_3 samples (xCo/Al) are shown in Table 5.6. The results indicated that the cobalt species deposited over the surface of the support progressively blocked its pores with increasing metallic loading, as pointed out by the observed decrease in the surface area from 139 $m^2\ g^{-1}$ for the bare γ-alumina to 84 $m^2\ g^{-1}$ for the 40Co/Al catalyst.

Table 5.6. Textural and structural properties of the supported xCo/Al catalysts.

Catalyst	Cobalt loading, %wt.	BET surface, $m^2 g^{-1}$	Pore volume, $cm^3 g^{-1}$	Pore size distribution maxima, Å	Co-spinel crystallite size, nm
γ-Al_2O_3	-	139	0.56	150, 110	-
10Co/Al	9.0	138	0.32	75	13
20Co/Al	21.7	120	0.34	90	16
30Co/Al	27.9	108	0.29	90	29
35Co/Al	33.1	95	0.23	90	35
40Co/Al	40.5	84	0.23	90	34

All samples presented a lower pore volume than the support, and this slightly decreased with Co loading. Furthermore, as can be noticed in Figure 5.12, all cobalt catalysts exhibited a unimodal distribution centred at a smaller size (75-90 Å) in comparison with the pure γ-Al_2O_3, which presented a bimodal distribution (110 and 150 Å). This suggested that the addition of cobalt to the alumina gradually blocked its largest pores.

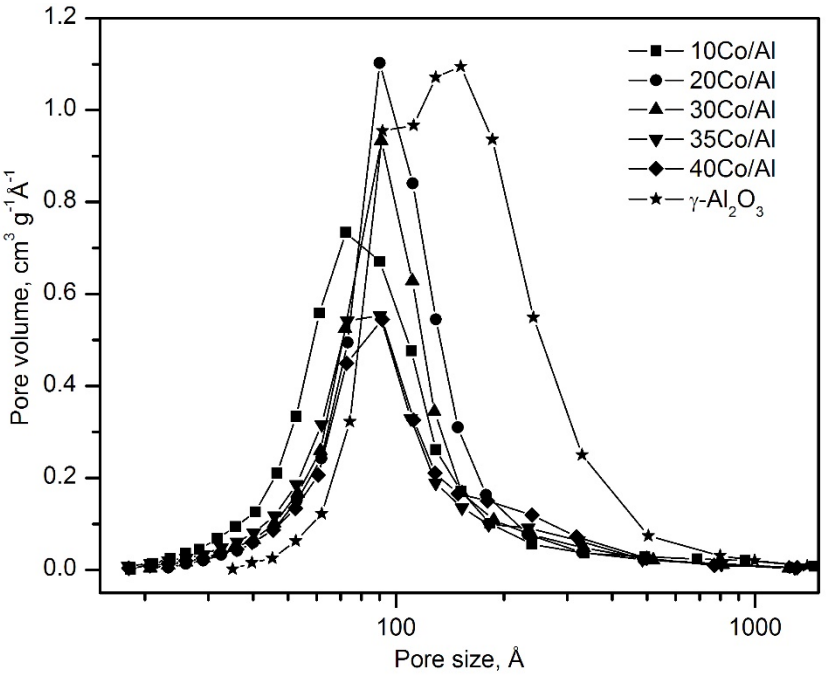

Figure 5.12. Pore size distribution of the supported xCo/Al catalysts.

The XRD patterns of the alumina supported Co_3O_4 catalysts are shown in Figure 5.13. For the sake of comparison the patterns of the bare alumina support is also included. The following signals located at 2θ = 19.0, 31.3, 36.8, 44.8, 59.4 and 65.2° were clearly visible. These could, in principle, be assigned to the Co_3O_4 phase. However, as already pointed out, the formation of $CoAl_2O_4$ is very frequent in Co/alumina systems due to the strong interaction between Co_3O_4 and the support at mild temperatures (›450 °C) [260,261]. On the other hand, the signals of the alumina support (2θ = 33.0, 37.1, 39.7, 45.6 and 67.3°) were also observed, more appreciably over the samples with a Co loading between 10 and 30%wt.

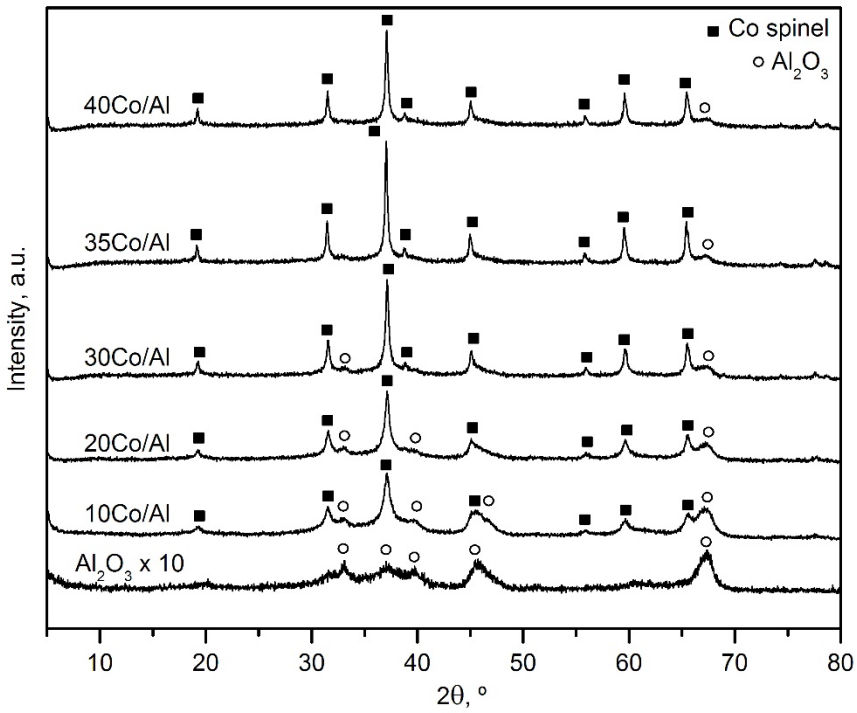

Figure 5.13. XRD patterns of the supported xCo/Al catalysts.

Additionally, it was clear that the crystallinity of the samples increased with the Co loading since the diffraction signals became sharper. This, in turn, would mean that the Co-containing crystallites became larger with Co loading. An attempt was made to calculate the average crystallite size of the Co-phases with a spinel structure (Co_3O_4 or $CoAl_2O_4$). For this calculation the most intense peak of both phases (2θ = 36.8°) was not used since it overlapped with one signal assignable to the gamma-alumina support (2θ = 37.1°).

Accordingly, the signal at 2θ = 59.4° was selected for this estimation. The calculated values (Table 5.6) evidenced that crystallite size gradually increased from 13 to 35 nm with Co loading up to 35%wt. No further increase was noticed for the sample with the highest metal loading (34 nm).

The structure of the samples was additionally investigated by UV-vis-NIR diffuse reflectance spectroscopy. For comparative purposes two bulk cobalt aluminate samples prepared by precipitation and calcined at 600 and 850 °C were analysed. The spectra of these samples along with those corresponding to the supported catalysts are shown in Figure 5.14.

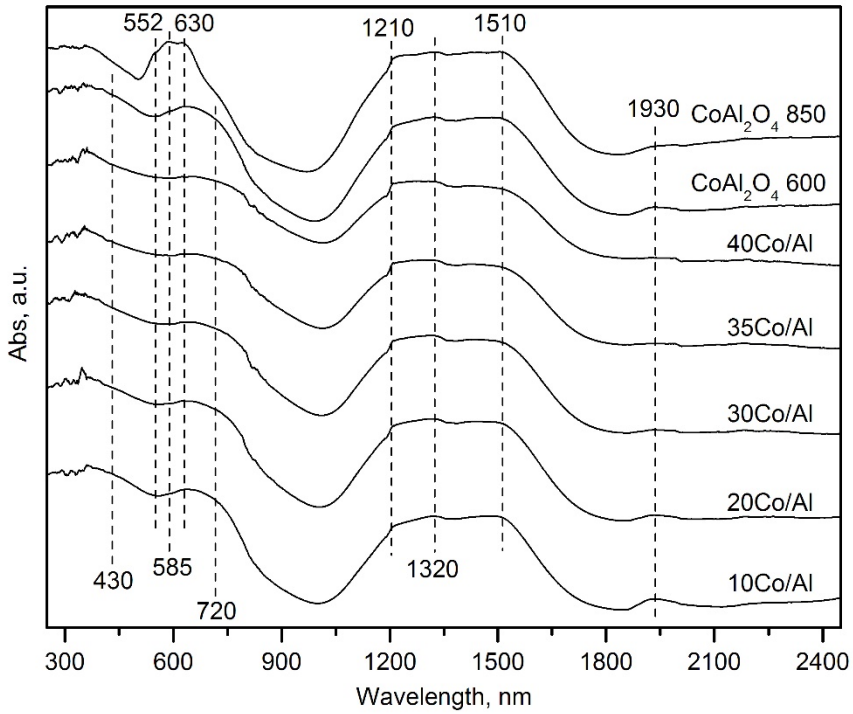

Figure 5.14. UV-vis-NIR diffuse reflectance spectra of the supported xCo/Al catalysts.

For all the samples the spectra displayed three absorption bands located at 1210, 1320 and 1510 nm, consistent with tetrahedral Co^{2+} species, along with weak bands at 430 and 720 nm consistent with octahedral Co^{3+} species, both associated with free Co_3O_4 [262,263]. In addition, a set of bands at 552, 585 and 630 nm, related to the presence of $CoAl_2O_4$, was

visible in the spectra of the 10Co/Al and 20Co/Al samples [264]. This finding suggested that both Co_3O_4 and $CoAl_2O_4$ were present in the supported catalysts. In addition, the samples with a low Co content exhibited a band at 1930 nm associated with hydrated alumina [265].

The XPS spectra of the supported samples were characterised by a lower signal/noise ratio than that exhibited by the bulk samples examined in previous chapters due to the relatively lower presence of cobalt. Hence, the deconvolution of these profiles was not possible. Nevertheless, since the two cobalt cations (Co^{3+} and Co^{2+}) tend to produce signals at specific and differentiated binding energies (779.9 and 781.1 eV, respectively), their relative presence in a sample affects the location of the main signal. Therefore, the position of that signal in the $Co2p_{3/2}$ spectra (Figure 5.15) could give some relevant information about the nature of the cobalt species on the surface.

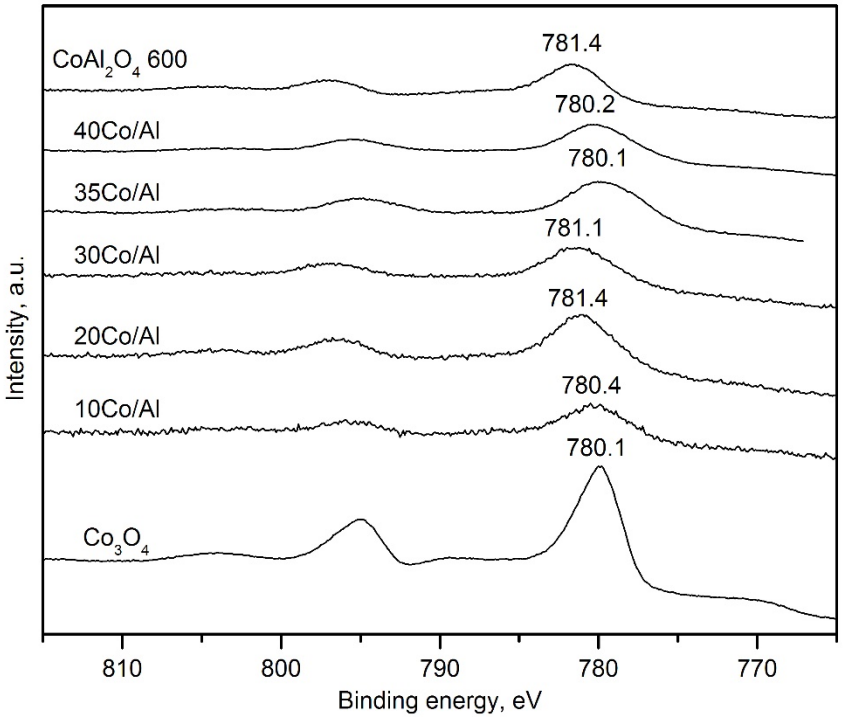

Figure 5.15. $Co2p_{3/2}$ XPS spectra of the supported xCo/Al catalysts.

The binding energy of the 10Co/Al, 20Co/Al and 30Co/Al catalysts increased from 780.4 to 781.1-781.4 eV, thereby revealing that $CoAl_2O_4$ and Co_3O_4 coexisted on the surface, in line

with the results obtained by diffuse reflectance spectroscopy. Note that the main signal of the Co2p spectra in the bulk $CoAl_2O_4$ sample calcined at 600 °C was located at 781.4 eV, in agreement with its higher Co^{2+} content. By contrast, the main signal (780.1-780.2 eV) for the catalysts with the highest cobalt loadings (35Co/Al and 40Co/Al) was closer to that of the bulk Co_3O_4 (780.1 eV). This indicated that Co_3O_4 was the most abundant phase on the surface [253], although it could also indicate that part of the deposited cobalt was segregated from the surface in the form of Co_3O_4 due to the high cobalt loading.

The redox properties were investigated by temperature-programmed reduction with hydrogen. The resulting profiles are included in Figure 5.16. It is worth pointing out that all cobalt species present in the catalysts were completely reduced to metallic Co. This was verified by XRD analysis of the samples recovered after the TPR run since only metallic Co and Al_2O_3 were detected (Figure 5.17).

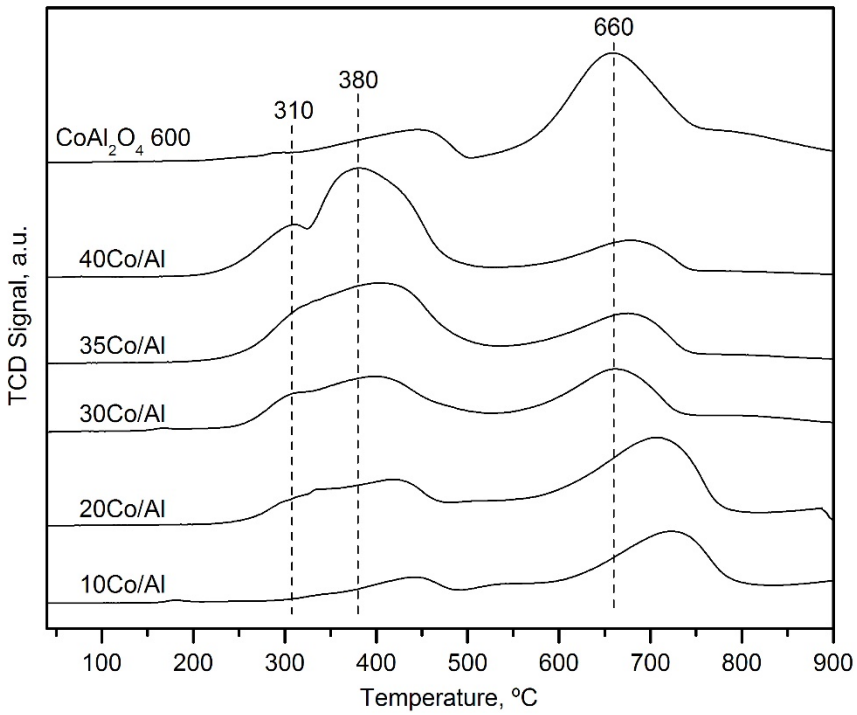

Figure 5.16. H_2-TPR profiles of the supported xCo/Al catalysts.

Two main H_2 uptakes were clearly distinguished. The first contribution, located at about 250-450 °C, could be assigned to reduction of free Co_3O_4. This consumption could be in turn subdivided into other two with peak reduction temperatures at 310 and 380-440 °C, following the same reduction steps as for the bulk Co_3O_4 catalysts. Note that, unlike the bulk samples, the sequential reduction $Co^{3+} \rightarrow Co^{2+} \rightarrow Co^0$ was less discernible, especially for the lowest cobalt loadings. However, for higher loadings (35Co/Al and 40Co/Al) the TPR profiles started to be more similar to that of the bulk catalyst, thus pointing out that Co_3O_4 was the main phase in these samples.

The second main uptake, centred at higher temperatures (660-730 °C), could be related to Co species with a substantially lower reducibility. In the literature there is still a debate on the nature of this contribution since it could be attributed to either the formation of cobalt aluminate $CoAl_2O_4$ [224], or to strong interactions between Co species and the alumina support [117].

In an attempt to shed some light on the origin of this contribution, a H_2-TPR analysis of the bulk cobalt aluminate calcined at 600 °C was performed in order to serve as a reference for comparison with the supported catalysts. Its corresponding profile included in Figure 5.16 was comparable to those of the alumina-supported catalysts. Note that cobalt species present in this sample was fully reduced into metallic cobalt (Figure 5.17). Thus, a low H_2 consumption was noticed at about 450 °C, which corresponded to the reduction of cobalt species (probably Co_3O_4) not fully incorporated into the lattice of $CoAl_2O_4$. Above 600 °C the full reduction of $CoAl_2O_4$ took place. Accordingly, the measured overall H_2 uptake (6.49 mmol H_2 g^{-1}) of this sample was slightly higher than the theoretical value for pure $CoAl_2O_4$ (5.65 mmol H_2 g^{-1}).

Therefore, the comparison between the profiles of the alumina supported catalysts and that of the bulk $CoAl_2O_4$ sample evidenced that the high-temperature H_2 consumption noticed over the supported Co_3O_4 samples could be assigned to the presence of varying amounts of cobalt aluminate. Note that the shoulder at about 900 °C observed in the profile of the 20Co/Al catalyst was due to an instrumental artefact involving the application of the heating ramp of the experiment. Occasionally, when the temperature was about 10 °C lower to the temperature limit of the run (in this case, 900 °C), the furnace would stop heating. Then the ongoing reduction process would undergo a sudden halt that resulted in that small sharp peak, which had no meaning on the redox properties of the sample.

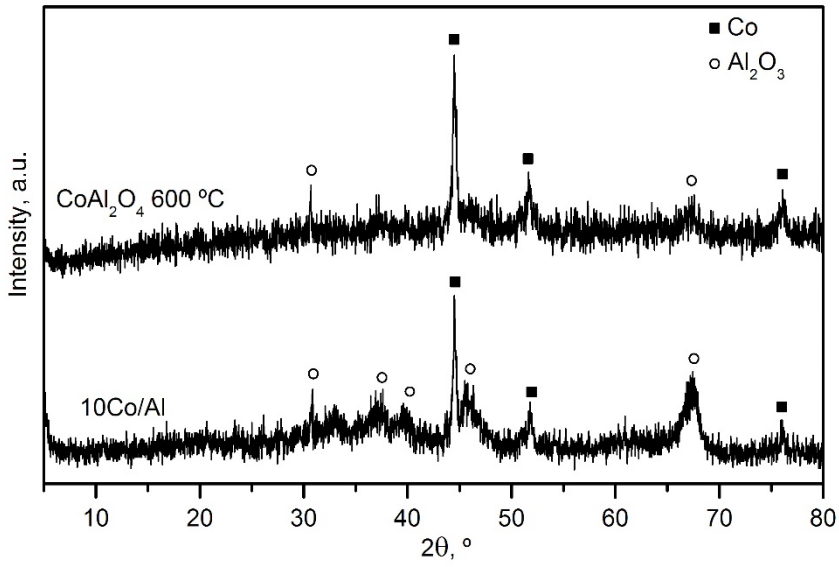

Figure 5.17. XRD patterns of the supported xCo/Al catalysts after H_2-TPR analysis.

The quantitative integration of the profiles (Table 5.7) indicated that the total H_2 uptake of the 10Co/Al and 20Co/Al catalysts was quite close to that expected when assuming that all cobalt species were present as $CoAl_2O_4$. By contrast, the observed consumption over the 35Co/Al and 40Co/Al samples was comparable with that theoretically predicted for the exclusive presence of Co_3O_4.

Table 5.7. Results of the H_2-TPR analysis of the supported xCo/Al catalysts.

Catalyst	Low-temperature H_2 uptake, mmol g^{-1}	High-temperature H_2 uptake, mmol g^{-1}	Co as Co_3O_4, %wt.	Co as $CoAl_2O_4$, %wt.
10Co/Al	0.2	1.4	1.0	8.0
20Co/Al	1.8	2.4	7.7	14.0
30Co/Al	3.1	2.4	13.7	14.2
35Co/Al	4.6	2.3	20.0	13.1
40Co/Al	6.4	2.4	27.0	13.5

Based on the corresponding H_2 consumption at 250-450 °C and 600-800 °C the relative distribution of Co species between Co_3O_4 and $CoAl_2O_4$ could be estimated for each sample. It was found that cobalt aluminate was the principal phase over the catalyst with the lowest

loading (10Co/Al). When increasing the metal content up to 20%wt. the amount of both species was larger. It therefore seemed that the previously formed $CoAl_2O_4$ layer grew. However, above this Co concentration (30Co/Al, 35Co/Al and 40Co/Al samples) the quantity of metal as $CoAl_2O_4$ remained constant around 13-14%wt., irrespective of the cobalt loading. It could be then reasonably believed that the formed Co_3O_4 crystallites were located on top of this aluminate layer, and in principle, did not further converted into aluminate. This assumption was coherent with the larger H_2 uptake required for the reduction of free Co_3O_4 in these samples.

5.2.2. Catalytic performance of the synthesised catalysts

Catalytic activity of alumina supported catalysts was examined under the same conditions as for the bulk catalysts (GHSV = 30,000 h^{-1}). The corresponding light-off curves are included in Figure 5.18. It was noticed that the activity of the alumina supported samples expectedly increased with Co loading, with T_{50} values of 515 and 510 °C over the 35Co/Al and 40Co/Al catalysts, respectively (Table 5.8).

Nevertheless, in no case their efficiency was higher than that of the bulk catalyst, despite exhibiting remarkably better textural properties. This was probably due to two reasons. First, cobalt aluminate, hardly reducible at the selected reaction temperatures, fixed a great amount of the cobalt deposited, thereby decreasing the availability of potentially active cobalt species. Recall that the activity of pure $CoAl_2O_4$ was virtually negligible. Secondly, as shown by the H_2-TPR profiles, the amount of easily reducible, highly active Co^{3+} in the supported catalysts was smaller than that of bulk catalysts, which made free Co_3O_4 within the support intrinsically less active. Similar results were reported by other authors for Co_3O_4/Al_2O_3 catalysts obtained by both wet [216] and incipient wetness impregnation [117].

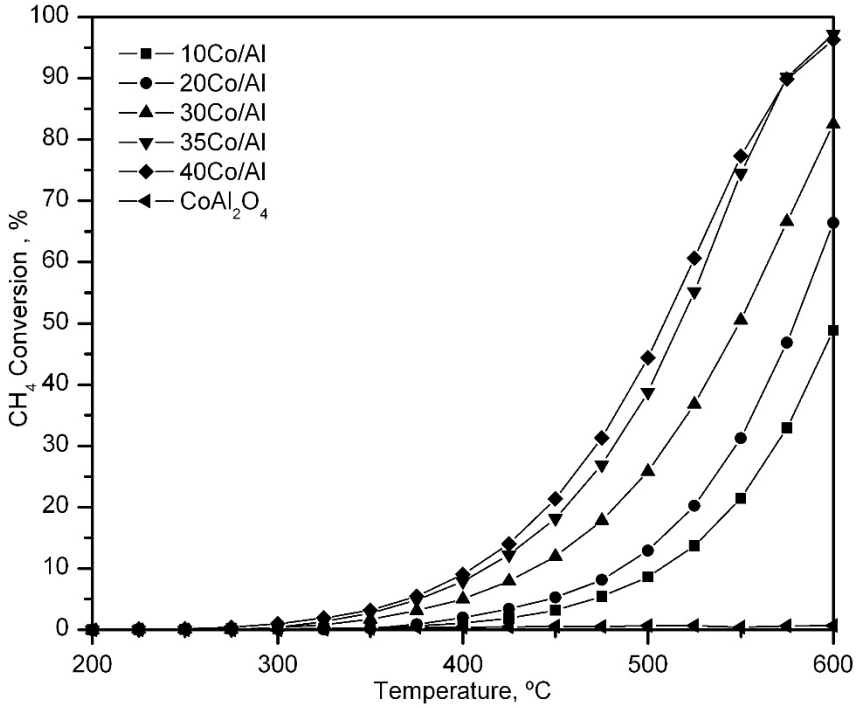

Figure 5.18. Light-off curves of the supported xCo/Al catalysts.

The reaction rates estimated under differential conditions (methane conversions lower than 20% at 425 °C) are listed in Table 5.8. The highest reaction rate was found over the 35Co/Al catalyst (2.2 mmol CH_4 g_{Co}^{-1} h^{-1}) followed by the 40Co/Al and 30Co/Al samples (2.1 and 1.9 mmol CH_4 g_{Co}^{-1} h^{-1}, respectively). Conversely, both 10Co/Al and 20Co/Al samples showed a lower reaction rate, around 1.2 mmol CH_4 g_{Co}^{-1} h^{-1}.

Table 5.8. Kinetic results of the supported xCo/Al catalysts.

Catalyst	T_{10}, °C	T_{50}, °C	T_{90}, °C	Reaction rate, mmol CH_4 g_{Co}^{-1} h^{-1}	E_a, kJ mol^{-1}
10Co/Al	510	›600	›600	1.17	100 ± 2
20Co/Al	485	580	›600	1.17	92 ± 3
30Co/Al	440	550	›600	1.87	82 ± 2
35Co/Al	410	515	575	2.23	78 ± 3
40Co/Al	350	440	520	2.12	79 ± 2

On the other hand, a progressive decrease in the apparent activation energy with Co loading was evident, as seen from the results in Table 5.8. The corresponding linear fits are depicted in Figure 5.19. Over the catalysts with a low Co content, where $CoAl_2O_4$ was the most abundant phase, the activation energy was about 100 kJ mol^{-1}. For higher loadings, and more particularly over the 35Co/Al and 40Co/Al catalysts, the activation energy was close (78-79 kJ mol^{-1}) to that observed for the bulk Co_3O_4 catalyst (74 kJ mol^{-1}). This pointed out that the main active phase present in these samples was the cobalt oxide.

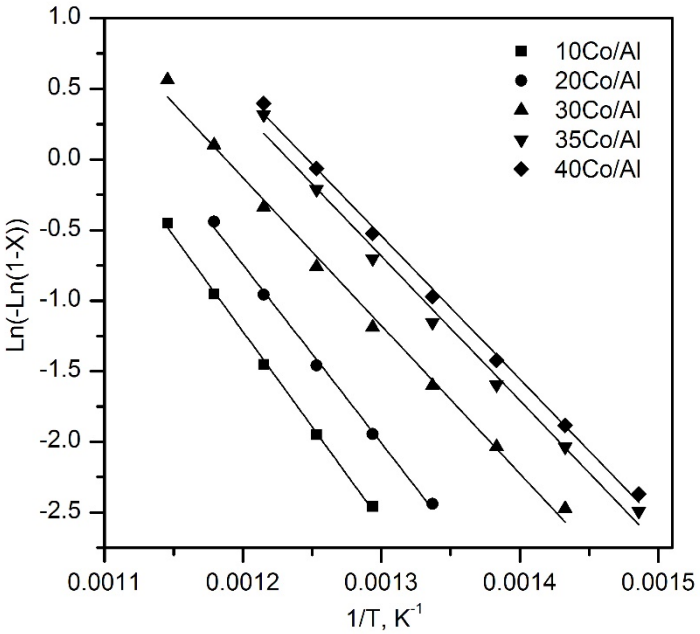

Figure 5.19. Pseudo-first order fit for the experimental data over the supported xCo/Al catalysts.

5.3. GLOBAL VIEW AND CONCLUSIONS

In this chapter, supporting the cobalt oxide over the surface of a porous media was thoroughly investigated as a way to improve the generally poor textural and structural properties that limit the intrinsic activity of bulk Co_3O_4 catalysts. For this purpose, firstly, three different materials were characterised and examined as supports for a cobalt oxide catalyst: a commercial gamma-alumina and as-synthesised magnesia and ceria. These

three materials were chosen based on those the interesting results for the oxidation of methane and other hydrocarbons reported in the available literature.

The physicochemical characterisation of the supports and their corresponding supported catalysts revealed substantially different profiles in view of their properties. Hence, the gamma-alumina exhibited excellent textural properties, as revealed by its noticeably high specific surface area and pore volume, which allowed to obtain a supported catalyst with a relatively high dispersion of the deposited cobalt. However, the strong cobalt-alumina interaction provoked by that high dispersion also entailed an important drawback with the formation of a stable phase of cobalt aluminate that fixed a part of the deposited cobalt as an inactive phase.

Secondly, magnesia presented intermediate textural and structural properties, poorer than those of alumina, but still acceptable enough to make this material applicable as a support. However, similarly to what was observed for the gamma-alumina support, the interaction between the magnesia and the deposited cobalt resulted in the formation of a highly stable Co-Mg solid solution that could not be reduced even at very high temperatures, thus making eventually ineffective an important fraction of the deposited cobalt. Moreover, despite showing somewhat better redox properties than the alumina-supported catalyst, the MgO supported counterpart exhibited a worse behaviour at low temperatures, due to the smaller amount of available cobalt for reaction.

Finally, the ceria synthesised by precipitation route exhibited very poor textural and structural properties, with specific surface areas in the same range as the bulk Co_3O_4 catalysts. Hence, the physicochemical characterisation of the resulting CeO_2 supported sample revealed that a significant part of the deposited cobalt was segregated from the support, thus forming a physical mixture of Co_3O_4 and Co_3O_4/CeO_2. Consequently, the ceria-supported sample presented the best redox properties of the three examined catalysts as they were quite similar to those of bulk Co_3O_4. Correspondingly, the catalytic performance of the Co/Ce sample was considerably better than that shown by its counterparts supported on γ-Al_2O_3 and MgO.

Taking these preliminary results into account, the gamma-alumina was selected as the most suitable material to serve as a support for cobalt oxide, since it provided the larger

improvement of the textural and structural properties of the cobalt oxide, despite its partial transformation into considerably more less active cobalt aluminate.

Once the most suitable support was chosen, it was necessary to optimise the cobalt loading, in order to maximise the amount of cobalt that remained as the active cobalt oxide form. For this purpose, several alumina-supported catalysts with cobalt loading varying between 10 and 40%wt. were prepared, characterised and catalytically tested for the oxidation of lean methane.

Textural characterisation revealed that cobalt could be deposited efficiently over alumina for cobalt loadings up to 30%wt. For higher cobalt loadings, however, some evidence of segregation of cobalt oxide was visible. The characterisation also revealed that the extent of formation of cobalt aluminate on the surface of the alumina increased with the cobalt loading until it reaches the saturation point for a loading of about 30%wt. A further addition of cobalt above this threshold concentration would not significantly increase the amount of cobalt aluminate.

Thus, the catalysts with 35 and 40%wt. Co exhibited a relatively good catalytic activity. However, it was also possible that this behaviour was caused by the presence of segregated Co_3O_4, due to the high cobalt loadings. Among the catalysts in which there was no sign of segregation (those loaded with 10, 20 and 30%wt. Co), the 30Co/Al sample was found to exhibit the best performance.

Nevertheless, despite being the optimal cobalt loading, the use of the deposited cobalt made by the catalyst with a 30%wt. Co loading was clearly sub-optimal, since a relatively large amount ended up in an inactive form. Therefore, in the following chapter, extensive efforts will be focused on several improvement strategies, with the main objective of minimising the ineffective fraction as cobalt aluminate and consequently maximising the intrinsic catalytic activity related to active Co_3O_4.

Chapter 6

COMPARATIVE STUDY OF STRATEGIES FOR ENHANCING THE PERFORMANCE OF ALUMINA-SUPPORTED CATALYSTS

ABSTRACT

The alumina-supported cobalt oxide catalyst obtained in the previous chapter exhibited significantly better textural and structural properties than the bulk catalysts. However, as explained, the strong cobalt-alumina interaction led to the formation of inactive cobalt aluminate, which limited the activity of the resulting catalysts. In this chapter, three different strategies for enhancing the behaviour of alumina-supported catalysts are developed and kinetically evaluated. Firstly, surface protection of the alumina with magnesia prior to the deposition of the cobalt precursor was attempted, with the objective of minimising the cobalt-alumina interaction. Secondly, the co-precipitation of nickel along with cobalt was examined, with the aim of improving the redox properties of the deposited cobalt. Finally, the surface protection of alumina with a redox promoter such as ceria was studied, such that it would eventually provide both a barrier effect, minimising the cobalt-alumina interaction, and a redox promotion effect on the deposited cobalt. From the three investigated approaches, the addition of ceria prior to the deposition of cobalt, resulted in the most active catalysts, and the catalytic testing revealed an optimal composition for a cerium loading of 20%wt.Ce in the modified support.

6. COMPARATIVE STUDY OF STRATEGIES FOR ENHANCING THE PERFORMANCE OF ALUMINA-SUPPORTED CATALYSTS

As widely discussed in previous chapters, spinel-type cobalt oxide (Co_3O_4) is a promising material that can serve as a highly effective alternative to noble metals for catalytic total oxidation due to its good redox properties [111,174,241,254]. However, its generally poor structural and textural properties tend to hinder the potential activity of this material, especially when it is prepared by conventional synthesis methodologies [115,266]. One possible solution to this problem could be to support the cobalt oxide over the surface of a porous media, in order to increase the amount of surface area available for the reaction. Although this option generally enhances the structural properties of the catalyst, it also presents a major drawback related to the fact that the cobalt-support interaction leads to the formation of an inactive cobalt aluminate phase ($CoAl_2O_4$) characterised by a poor reducibility [97,117].

A proposed solution already found in the bibliography is based on the modification of the support with the purpose of altering its stability and affinity for the cobalt oxide supported over it. This can be addressed by introducing some chemical promoters to the alumina support before the incorporation of Co_3O_4, or by adding these promoters to the final Co/Al_2O_3 catalyst. Thus, Liotta et al. [267] found out that adding Ba during the synthesis of Al_2O_3 by a sol-gel method inhibited solid state diffusion of the Co^{2+} ions into the alumina after Co deposition.

On the other hand, Cheng et al. [268] reported that the incorporation of a fourth element during the synthesis of an alumina supported copper-cobalt catalyst improved the reducibility of both metal cations, especially when that fourth element was either Mn or Fe. Also, El-Shobaky et al. [269] found out an increased activity of Co_3O_4/Al_2O_3 catalysts for CO oxidation when these were doped with small amounts of manganese and/or lanthanum. Similarly, using magnesium or cerium as modifiers for this type of catalysts seems to be a good way to improve their performance. For instance, Riad [270] observed that magnesium-modified alumina prepared by coprecipitation exhibited better textural and structural properties than bare alumina, while Genty et al. [271] reported a catalytic activity comparable to that of Pt-Pd catalysts for a hydrotalcite CoAlCe catalyst prepared by precipitation. Both magnesium and cerium oxides can be also used as supports for cobalt catalysts as well, thereby resulting in systems with improved promoted activity

owing to the magnesium-cobalt interaction as reported by Ulla et al. [226] and Ji et al. [255], as well as the cerium-cobalt interaction reported by Liotta et al. [174] and Dou et al. [242].

Alternatively, the promoter can be deposited over the surface of an as-synthesised alumina before the deposition of cobalt. In this sense, Park et al. [272] and Park et al. [273], on different studies, observed that the addition of P to Al_2O_3 resulted in the partial formation of $AlPO_4$, which suppressed the formation of $CoAl_2O_4$. This inhibition effect was also noticed for other metallic promoters such as Mg, Zr or Ce [234,274,275]. In all cases, the deposition of the promoter over the alumina led to the cobalt-alumina interaction switching into a cobalt-promoter interaction.

A third, possible strategy could be the addition of a metallic promoter directly to the cobalt spinel phase. If cobalt and the selected promoter, intimately mixed, are deposited into the alumina simultaneously, then the cobalt-metal interaction should be, in principle, highly favoured, and that would lead to a low formation of cobalt aluminate and an active cobalt phase with improved properties. To ensure this, the promoter should be mainly chosen on account of its ability to insert into the spinel lattice. For this reason, the most appropriate candidates would be those transition metals in the same period as cobalt such as nickel, iron or copper, due to their similar ionic radius, coordination and oxidation states with respect to cobalt.

Taking all these results into consideration, in this chapter, three strategies for improving the performance of alumina-supported Co_3O_4 catalysts are developed and compared for the low-temperature combustion of methane.

6.1. SURFACE PROTECTION OF ALUMINA WITH MAGNESIUM

The first examined approach for enhancing the activity of alumina-supported catalysts consisted of the incorporation of magnesium oxide (MgO) on the surface of the alumina prior to the deposition of the cobalt precursor. The expected effect of magnesium oxide addition was to provide a physical barrier between the alumina and the deposited cobalt in order to minimise the cobalt-alumina interaction, thereby inhibiting the formation of the cobalt aluminate. Magnesium oxide was chosen for this purpose based on the moderately good textural and structural properties that MgO prepared by precipitation exhibited in the previous chapter. This, in turn, would allow modified supports for cobalt deposition with also good textural properties.

To explore this strategy, three MgO-Al_2O_3 modified supports were prepared by precipitation. In each case, 5 g of γ-Al_2O_3 were added to a solution of magnesium nitrate hexahydrate of adjusted concentration, and precipitation was then provoked by addition of sodium carbonate until pH 8.5. The selected magnesium loadings were 7, 12 and 18%wt. Mg. The synthesised supports were denoted as xMg-Al, where x stands for the nominal magnesium content. After calcination of the modified supports at 600 °C, the cobalt precursor was incorporated following the same methodology. The nominal cobalt loading was 30%wt. as previously explained. Each supported catalyst was denoted as Co/xMg-Al, following the aforementioned labelling code. As a comparative reference, two cobalt catalyst supported on MgO (Co/Mg) and γ-Al_2O_3 were also examined. This latter sample was previously named as 30Co/Al catalyst (Chapter 5), but it will be hereafter denominated as Co/Al for the sake of consistency.

6.1.1. Physico-chemical characterisation of the modified xMg-Al supports

The physico-chemical properties of the as-prepared MgO-modified alumina supports were investigated by WDXRF, XRD and N_2 physisorption. The Mg loading as determined by WDXRF varied between 7 and 18%wt. (Table 6.1). The X-ray diffractograms of the supports are shown in Figure 6.1. As a reference the pattern of pure MgO is included as well. Expectedly all the samples displayed signals attributable to a cubic phase of gamma-alumina (2θ = 32.0, 37.7, 45.6 and 67.3°). The samples with a Mg content of 12 and 18%wt. also showed distinct signals assignable to a cubic phase of magnesium oxide (ICDD 00-004-0829) at 2θ = 43.0, 62.3, 74.7 and 78.6°. Note that the signal at 2θ = 37.0° could be ascribed to both Al_2O_3 and MgO phases.

From the XRD peak intensity ratio of the signals of MgO (2θ = 62.3°) and γ-alumina (2θ = 67.3°), which varied from 0.07 for the 7Mg-Al sample to 0.84 for the 18Mg-Al sample, it was verified that the relative amount of crystalline MgO increased with Mg loading. The MgO crystallite size was estimated from the full width half maximum (FWHM) of the characteristic peak located at 2θ = 42.9°, which corresponded to the (2 0 0) plane, by applying the Scherrer equation. Irrespective of the Mg content, the crystallite size was around 10-11 nm, which was half of that of pure magnesia (21 nm), thus evidencing a relatively good dispersion of MgO over the surface of the alumina.

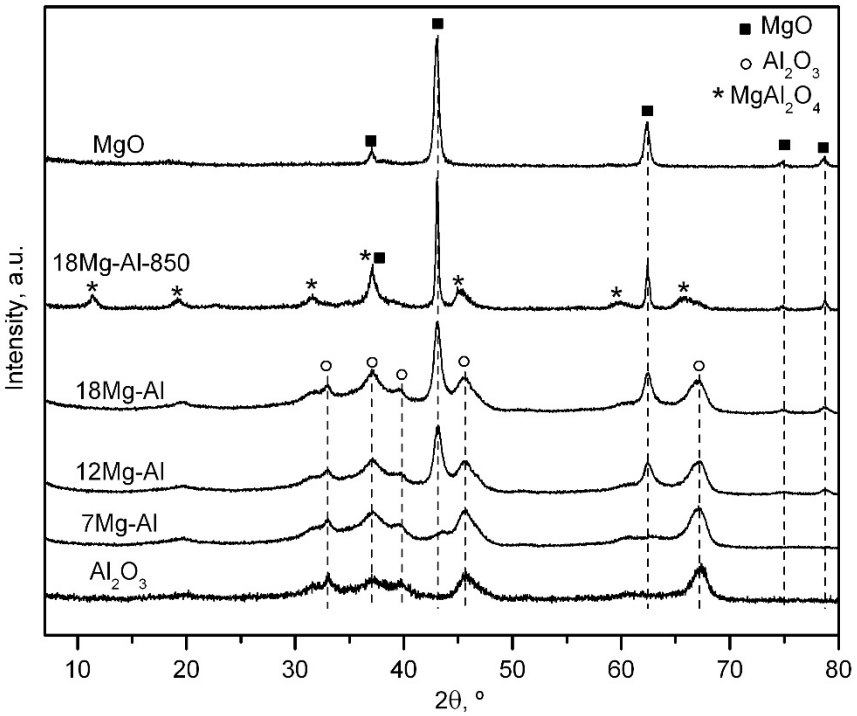

Figure 6.1. Diffraction patterns of the modified xMg-Al supports.

Table 6.1. Physico-chemical properties of the modified xMg-Al supports.

Support	Mg loading, %wt.	BET surface, $m^2 g^{-1}$	Pore volume, $cm^3 g^{-1}$	Pore size distribution maxima, Å
Al_2O_3	-	139	0.56	110, 150
7Mg-Al	6.7	145	0.50	110
12Mg-Al	12.4	142	0.48	110
18Mg-Al	17.8	139	0.44	110
MgO	60.3	80	0.19	35, 45, 110, 150

On the other hand, the absence of segregated MgO in the pattern of the 7Mg-Al support was coherent with the proximity of its Mg loading to that theoretically required to form a MgO monolayer (about 10%wt.). On the other hand, the possible formation of $MgAl_2O_4$ due to the interaction between MgO and Al_2O_3 could be ruled out as the main signals of this spinel (2θ = 31.3, 36.9, 44.8, 59.4 and 65.2°, ICDD 00-005-0672) were not observed. This was reasonably expected since the calcination temperature of the investigated Mg-Al samples

was 600 °C while the formation of the spinel is reported to occur above this temperature [276]. In this sense, the pattern of the 18Mg-Al sample calcined at 850 °C (18Mg-Al-850), on which the formation of $MgAl_2O_4$ was strongly induced, is included in Figure 6.1 for the sake of comparison.

The textural properties of the supports, namely specific surface area, mean pore diameter and pore volume, are listed in Table 6.1. The results corresponding to the blank alumina support are also included. After MgO deposition, the surface area slightly increased up to 139-145 $m^2 g^{-1}$, probably due to the contribution of the noticeable area of pure magnesia (80 $m^2 g^{-1}$) to the resultant support.

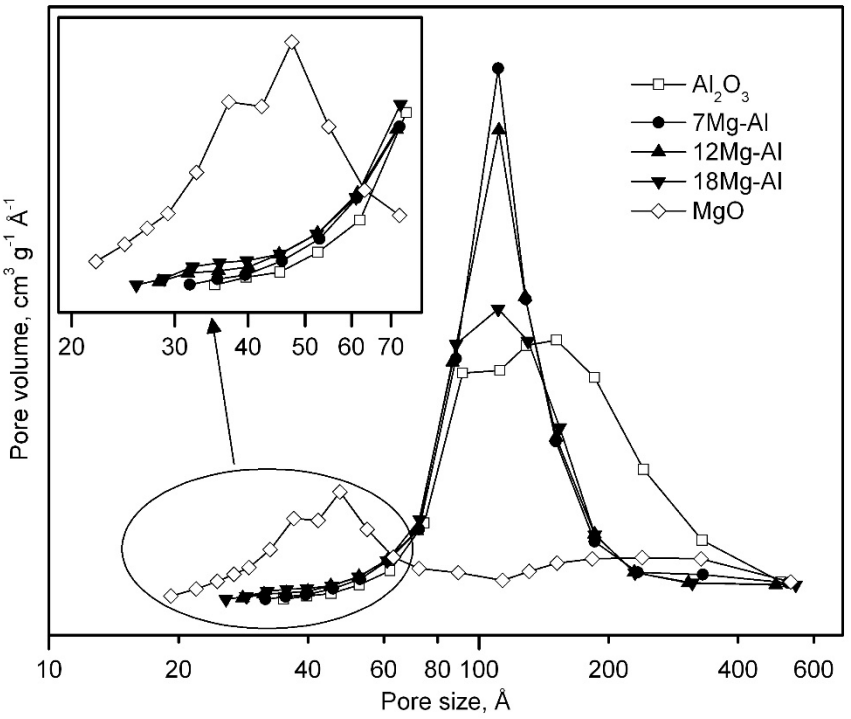

Figure 6.2. Pore size distributions of the modified xMg-Al supports.

In this sense, the pore size distributions of the supports (Figure 6.2) evidenced the appearance of a fraction of small mesopores (with sizes around 30-40 Å) that could be attributed to the high dispersion of magnesia. Recall that pure MgO also exhibited a pore size distribution centred at around that pore size. A similar increase in surface area was found by Caloch et al. [277] when studying $MgO-Al_2O_3$ supports prepared by homogeneous

precipitation. This observation was attributed to the interaction of magnesium and aluminium oxides creating new narrow mesopores that contributed to the total surface area. On the contrary, both pore volume and mean pore size were much more affected with a marked decrease from 0.56 to 0.44 $cm^3\ g^{-1}$ and 123 to 110 Å, respectively.

6.1.2. Physico-chemical characterisation of the Co/xMg-Al catalysts

Table 6.2 includes the composition of the synthesised catalysts as determined by WDXRF. It must be pointed out that the actual Mg loading of the xCo/Mg-Al samples (3-11%wt.) was appreciably lower than that theoretically expected (5-14%wt.) due to a partial leaching of the promoter during the cobalt deposition step. This was verified by the significant presence of Mg in the filtrates after Co precipitation and subsequent washing, as evidenced by ICP-AES analysis.

Table 6.2. Physico-chemical properties of the Co/xMg-Al supported catalysts.

Catalyst	Co loading, %wt.	Mg loading, %wt.	BET surface, $m^2\ g^{-1}$	Pore volume, $cm^3\ g^{-1}$	Pore size distribution maxima, Å
Co/Al	27.9	-	108	0.29	90
Co/7Mg-Al	28.7	3.0	99	0.27	90
Co/12Mg-Al	30.8	4.5	97	0.29	90
Co/18Mg-Al	28.3	7.8	91	0.28	90
Co/Mg	31.9	41.1	47	0.16	320

Figure 6.3 shows the diffractograms of the cobalt catalysts. These patterns were characterised by the presence of γ-alumina (2θ = 67.3°) and a spinel-like cobalt phase (Co_3O_4 and/or $CoAl_2O_4$ at 2θ = 31.3, 37.0, 45.1, 59.4 and 65.3°). Note that it was not possible to differentiate between these two oxides since both phase crystallise in the cubic structure. The MgO phase was only detected (2θ = 43.0 and 62.3°) over the catalysts with the highest content of magnesium, namely Co/18Mg-Al.

Furthermore, a close-up view of the diffraction signals of the Co spinel phase revealed a significant position shift with increasing Mg loading. This shift was noticed for all the signals attributed to this phase. For the sake of clarity only the signal located at around 2θ = 37.0° is shown in Figure 6.4. This signal was noted at 2θ = 37.1° for the catalyst supported on bare alumina (Co/Al) and progressively shifted towards 2θ = 36.9°, being this

diffraction angle virtually coincident with that observed when cobalt was supported on pure magnesia (Co/Mg).

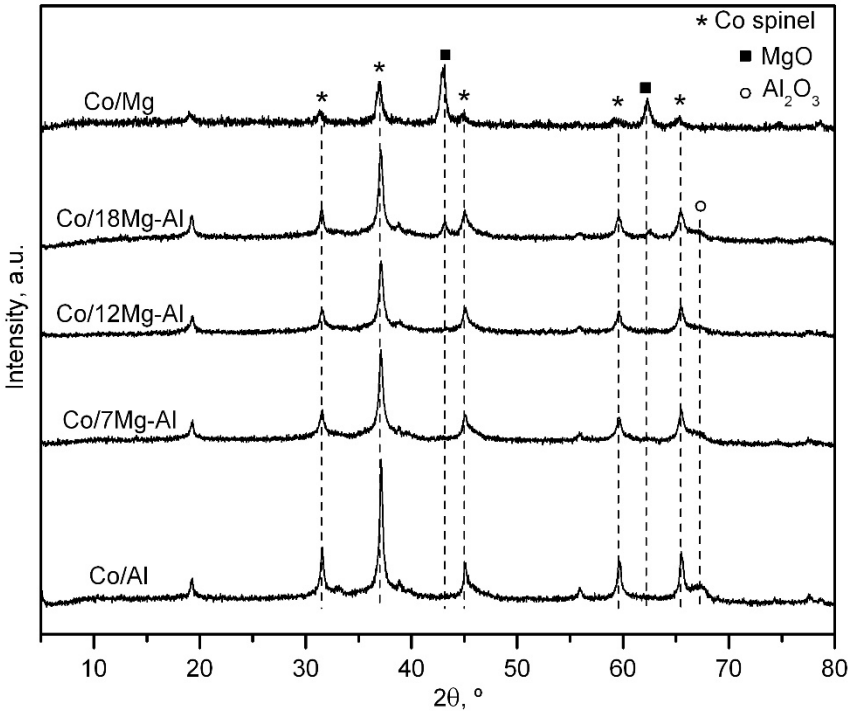

Figure 6.3. Diffraction patterns of the Co/xMg-Al supported catalysts.

This finding suggested that the Co_3O_4 phase switched from a Co-alumina-type interaction (which resulted in the formation of $CoAl_2O_4$) to a Co-magnesia-type interaction (which eventually involved a less favoured formation of $CoAl_2O_4$) with increasing Mg loadings. This shift was also indicative of an enlargement of the unit cell (from 8.097 to 8.127 Å) of the associated Co spinel phase, this being in agreement with some extent of lattice distortion of the cobalt spinel phase due to the interaction with magnesia [183]. Moreover, a progressive widening of these signals was observed, thereby suggesting some inhibition of the crystallisation of the Co-phase [278].

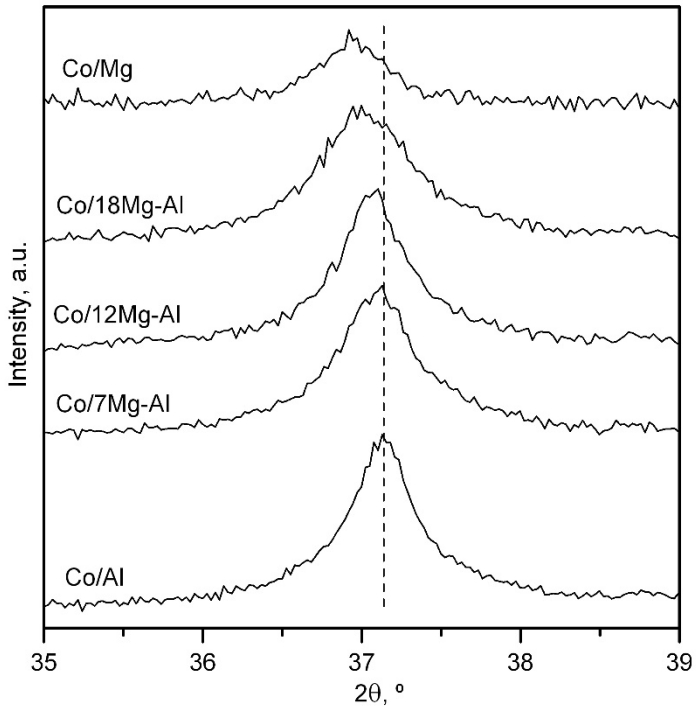

Figure 6.4. Close-up view of the diffraction patterns of the Co/xMg-Al supported catalysts in the 2θ = 35-39 range.

The addition of notable amounts of cobalt oxide (close to 30%wt.Co) led to an appreciable negative impact on the textural properties of the resultant catalyst (Table 6.2). Hence, when compared with the corresponding MgO-modified alumina support, the specific surface area decreased by about 32% for the Co/xMg-Al catalysts. The same trend was found for the mean pore size (36-46%). These results clearly indicated that the cobalt species deposited over the surface of the support gradually blocked its largest pores with increasing metallic loading. On the other hand, when compared with the base unmodified alumina-supported cobalt catalysts (Table 6.2), a noticeable decrease impact was visible (91-99 $m^2 g^{-1}$ versus 108 $m^2 g^{-1}$ over Co/Al).

The Raman spectra of the Co/xMg-Al catalysts are shown in Figure 6.5. For the sake of comparison the spectra of the Co/Al and Co/Mg counterpart catalysts and the bulk Co_3O_4 (CC sample) and $CoAl_2O_4$ ($CoAl_2O_4$ 600) samples are also included. All the supported catalysts displayed the five Raman actives modes associated with Co_3O_4, namely three F_{2g}

modes located at 194, 519 and 617 cm^{-1}, and the E_g and A_{1g} modes at 479 and 687 cm^{-1}, respectively. However, the Mg-containing catalysts showed comparatively weaker and wider signals. In line with the XRD results, this feature suggested a lattice distortion of the Co_3O_4 phase in these samples due to its interaction with magnesium.

On the other hand, a close-up view of the A_{1g} vibration mode (650-725 cm^{-1}) clearly evidenced the presence of additional shoulders attached to this peak at 705 and 725 cm^{-1} in the Co/Al sample (Figure 6.6). These signals (denoted as A_{1g}*) were also visible for the bulk $CoAl_2O_4$ sample, and are usually attributed to some inversion degree in the structure of cobalt aluminate, as already explained in the previous chapter. The absence of these signals over the Co/xMg-Al catalysts pointed out that these samples contained lower amounts of $CoAl_2O_4$, owing to a lesser extent of the cobalt-alumina interaction.

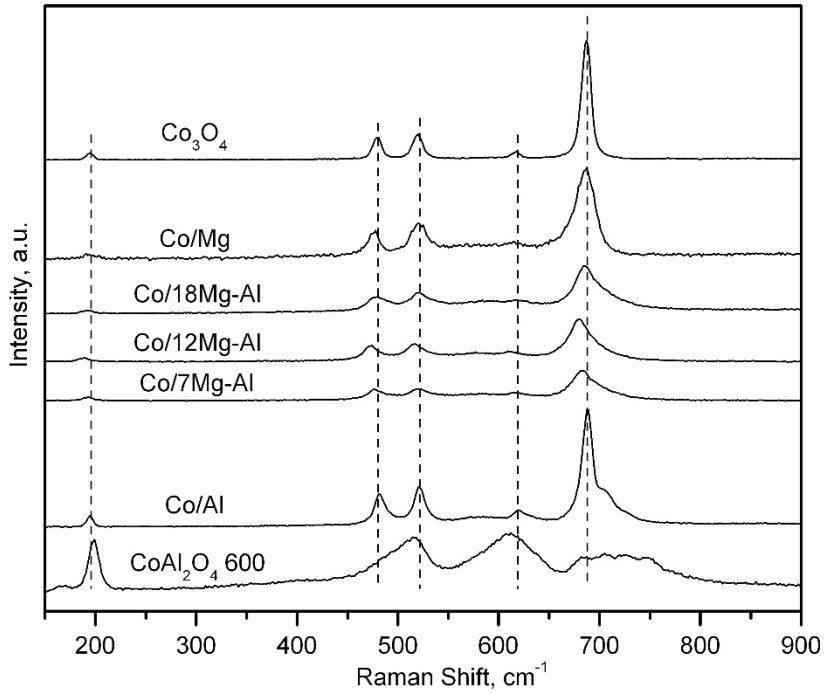

Figure 6.5. Raman spectra of the Co/xMg-Al supported catalysts.

In addition to that, the A_{1g} signal of the Mg-containing catalysts displayed an initial bathochromic shift (7 cm^{-1}) with increasing magnesium loadings up to 5%wt. (Co/12Mg-Al) that could be attributed to a change in the predominant cobalt-support interaction, from

cobalt-alumina to cobalt-magnesia [226]. For higher magnesium loadings (11%wt.Mg, Co/18Mg-Al), the signal returned to a very similar position (683 cm^{-1}) to that of cobalt supported on pure magnesia (684 cm^{-1}). This evidenced a promotion of the interaction between cobalt and magnesium with increasing magnesium concentration at the cost of the interaction between cobalt and aluminium.

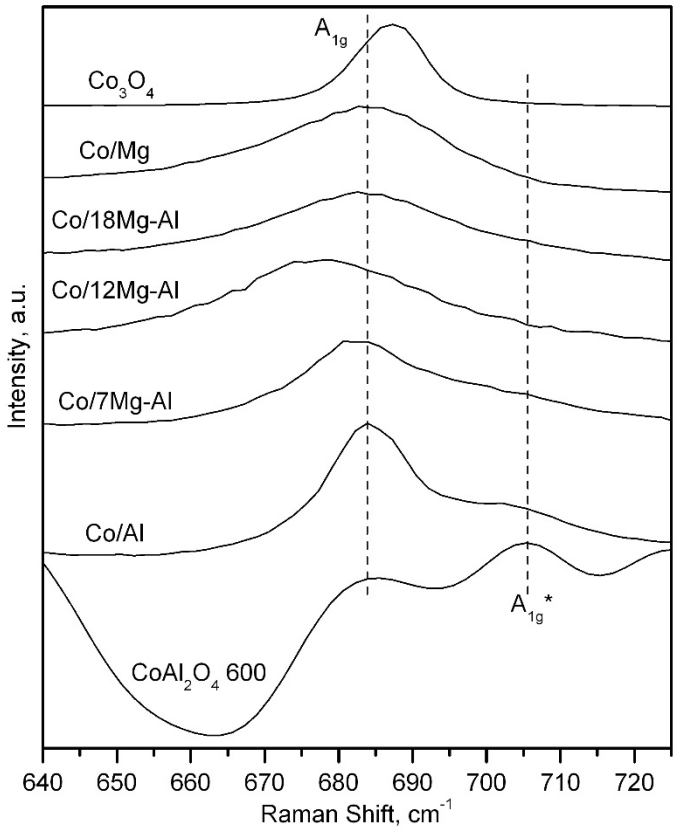

Figure 6.6. Close-up view of the Raman spectra of the Co/xMg-Al supported catalysts in the 650-725 cm^{-1} range.

The redox properties of the samples were investigated by means of H_2-TPR (Figure 6.7 and Table 6.3). Note that the H_2 uptake corresponding to the pure supports (Al_2O_3 and MgO) and MgO-modified alumina supports (xMg-Al) was negligible. For a better understanding of the influence of MgO deposition on the alumina support, the results corresponding to the catalysts supported on blank alumina and magnesia were firstly analysed.

As previously described in Chapter 5, the TPR profile of the 30Co/Al catalyst evidenced two distinct H_2 uptakes. The consumption observed at 250-500 °C was associated with the reduction of free Co_3O_4, while the uptake at markedly higher temperatures (above 550 °C) corresponded to the reduction of $CoAl_2O_4$ [222]. The measured overall H_2 uptake was 20.0 mmol H_2 g_{Co}^{-1}, significantly lower than the theoretical value for the full reduction of cobalt species as Co_3O_4 exclusively (22.6 mmol H_2 g_{Co}^{-1}). Simultaneously, these values were larger than that corresponding to the exclusive presence of $CoAl_2O_4$ in the samples (17.0 mmol H_2 g_{Co}^{-1}). Judging from these findings, it was reasonable to believe that a mixture of both Co_3O_4/$CoAl_2O_4$ was formed on the sample, which presented an overall degree of reduction of 88%.

As for the Co/Mg sample, a distinct H_2 peak centred at 300 °C was noticed, which was related to the reduction of free Co_3O_4. A substantial H_2 consumption was also noticed in the 350-950 °C temperature range. This broad band was assigned to the reduction of a non-stoichiometric Mg-containing spinel phase and/or a CoO-MgO solid solution [275], as also pointed out in Chapter 5. Similarly to the behaviour of the catalyst supported on bare alumina, the total H_2 consumption of the Co/Mg sample was also considerably lower (14.5 mmol H_2 g_{Co}^{-1}) than the theoretical uptake. Consequently, an overall degree of reduction of 64%, was estimated. In view of these results, it could be said that cobalt-magnesia interactions were comparatively much stronger than those created between cobalt species and alumina.

Over the series of catalysts supported on the modified xMg-Al supports, the total reducibility was enhanced with respect to the MgO-free sample (Table 6.3). The largest promotion corresponded to the Co/12Mg-Al sample with an increase in the degree of reduction from 88% (Co/Al) to 93%. Furthermore, the onset of the reduction process of free Co_3O_4 significantly decreased by 20-40 °C. This shift was also more notable for the catalyst supported on 12Mg-Al, as shown in Figure 6.8.

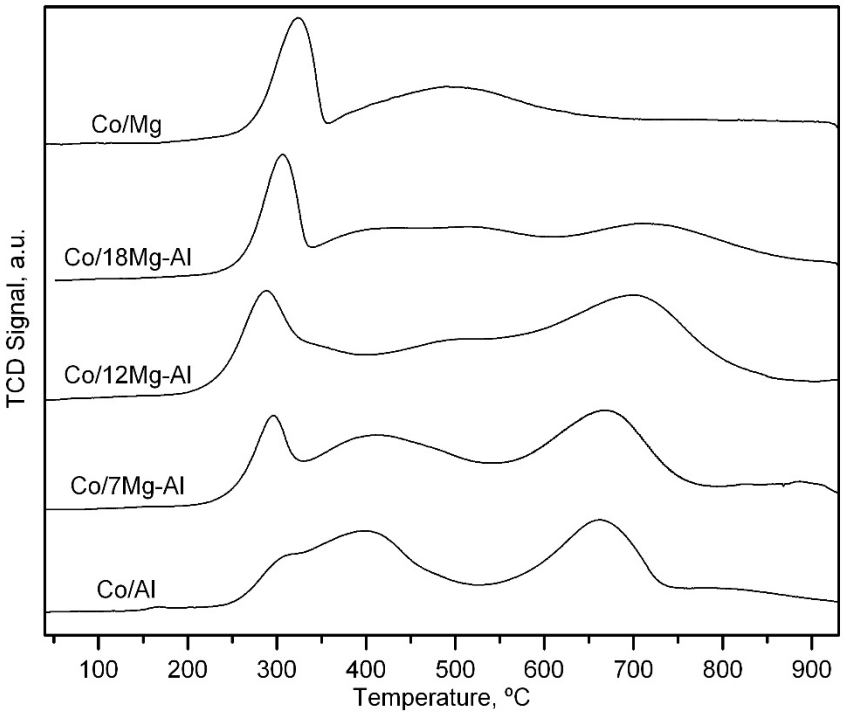

Figure 6.7. H_2-TPR profiles of the Co/xMg-Al supported catalysts.

Likewise, a small shoulder at about 450-500 °C was noticed over the Co/12Mg-Al and Co/18Mg-Al samples. This evidenced that a minor fraction of deposited cobalt species strongly interacted with the promoter. On the other hand, the reduction band occurring at higher temperatures (above 550 °C), which was an evidence of the presence of $CoAl_2O_4$, was still noticed over the MgO-modified alumina supported catalysts, although its relative intensity was somewhat lower with respect to the Co/Al sample.

An attempt was made to estimate the relative amount of each type of Co species present in the various catalysts by deconvolution of the experimental TPR profiles. The threshold temperature of 550 °C was taken as a criterion to distinguish between easily reducible cobalt species (low-temperature uptake) that would include free Co_3O_4 (200-450 °C) and cobalt-MgO species (450-550 °C) and hardly reducible cobalt species (high-temperature uptake) in the form of cobalt aluminate (›550 °C) [279].

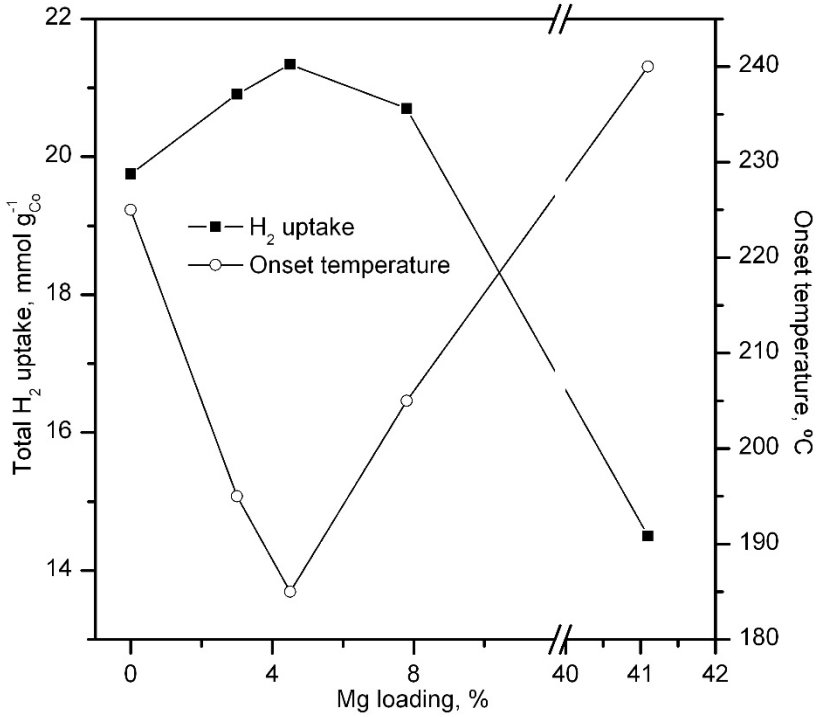

Figure 6.8. Relationship among the total H_2 uptake, reduction onset temperature and the Mg loading of the Co/xMg-Al supported catalysts.

The results are summarised in Table 6.3. It was interesting to note that the amount of the first type of cobalt species increased when MgO was present on the support. This promotion was notable, especially over the Co/12Mg-Al and Co/18Mg-Al samples (11-11.3 mmol H_2 g_{Co}^{-1}), with respect to the unmodified catalyst (9.8 mmol H_2 g_{Co}^{-1}) Simultaneously, increasing amounts of MgO led to a decrease in the fraction of hardly reducible $CoAl_2O_4$, which was about 8% lower for the Co/18Mg samples. Hence, the coverage of alumina with MgO was shown to be efficient for partially inhibiting the strong interaction between Co_3O_4 and Al_2O_3 that could ultimately lead to the formation of cobalt aluminate.

In general, the redox behaviour of free Co_3O_4 present in the Co/Mg-Al catalysts tended to be more similar to that observed over the Co/Mg instead of the Co/Al counterpart. This evidenced a change in the nature of the cobalt-support interaction induced by the addition

of magnesium to the alumina support in agreement with the results from XRD and Raman spectroscopy.

Table 6.3. Results from the H_2-TPR analysis of the Co/xMg-Al supported catalysts.

Catalyst	Low-temperature H_2 uptake, mmol g_{Co}^{-1}	High-temperature H_2 uptake, mmol g_{Co}^{-1}	Onset reduction temperature, °C	Degree of reduction, %
Co/Al	9.8	10.2	225	88
Co/7Mg-Al	10.3	10.4	195	92
Co/12Mg-Al	11.0	10.1	185	93
Co/18Mg-Al	11.3	9.4	205	92
30Co/Mg	9.9	7.6	240	64

6.1.3. Catalytic performance of the Co/xMg-Al catalysts

As detailed in Chapter 2, the criteria for intra-particle and extra-particle mass and energy diffusion, as well as the temperature gradients were checked to be above the limit, to ensure that any diffusional effects did not affect the kinetic results. In this sense, Table 6.4 summarises the calculated values for the various criteria.

Table 6.4. Criteria for accurate analysis of intrinsic reaction rates (as evaluated for the Co/12Mg-Al catalyst at 450 °C).

Criterion number	Recommendation	At 450 °C	Least favourable conditions
1.	Bodenstein parameter $< L_{bed}/d_{particle}$	$21.9 < 79.5$	$55.6 < 79.5$[a]
2.	$d_{tube}/d_{particle} > 10$	31.2	31.2
3.	Carberry number $< 0.05/n$	0.019	0.046[a]
4.	$\gamma\beta_e Ca < 0.05$	0.006	0.041[b]
5.	Wheeler-Weisz modulus < 0.15	$1.7 \cdot 10^{-4}$	$3.3 \cdot 10^{-4}$[c]
6.	Mears parameter < 0.1	$4.4 \cdot 10^{-6}$	$4.4 \cdot 10^{-6}$
7.	Radial gradient < 0.05	0.012	0.020[c]
8.	Bed dilution parameter < 0.05	0.047	0.047
9.	Temperature gradient < 0.3	0.15	0.175[b]

[a]Determined at 500 °C; [b]Determined at 600 °C; [c]Determined at 525 °C.

Figure 6.9 includes the corresponding conversion-temperature profiles of the investigated MgO-modified cobalt catalysts (GHSV = 30,000 h^{-1}). The T_{50} value was used as an index of the relative reactivity of each sample (Table 6.5). It must be noticed that the oxidation of methane to exclusively CO_2 was always observed in the whole temperature range. The reaction started to appreciably occur above 350 °C over the Co/xMg-Al catalysts. Accordingly, at 600 °C conversion values at around 80-95% were noted, respectively.

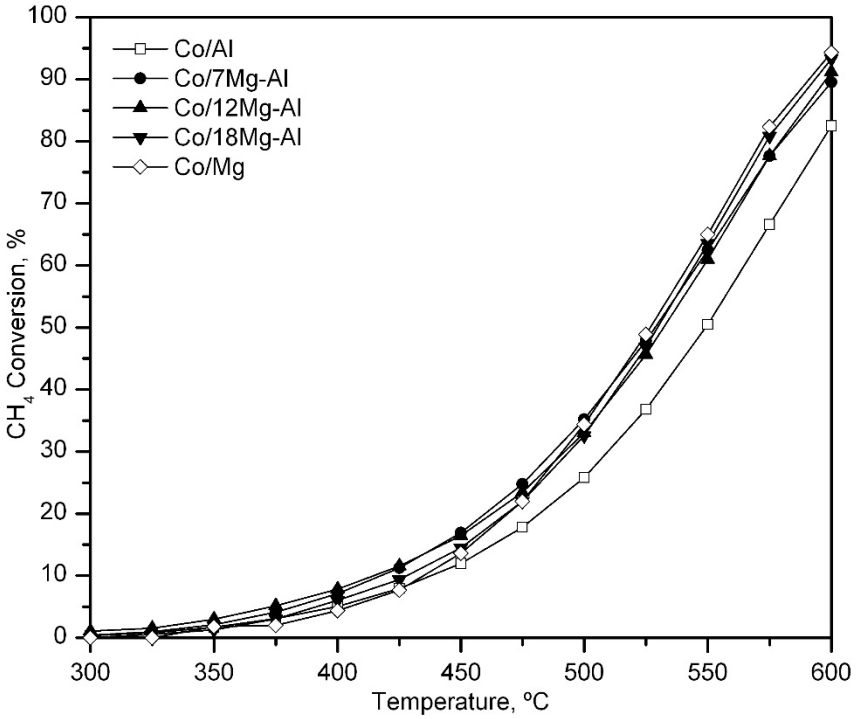

Figure 6.9. Light-off curves of the Co/xMg-Al supported catalysts.

The cobalt catalysts supported on MgO-modified alumina were more efficient than the corresponding alumina-supported counterpart since the T_{50} values were lowered by 25-30 °C. It seems reasonable to assume that the observed improvement in performance could be associated with the substantially enhanced redox properties of the catalysts due to MgO coverage of the alumina surface. Hence, the best results were found over the Co/12Mg-Al sample.

The specific reaction rate of the cobalt catalysts was calculated at 450 °C (Table 6.5) by the differential method. The estimated rates varied between 3.0-3.5 mmol h^{-1} g_{Co}^{-1} over the Co/xMg-Al samples, while these were 2.5 mmol h^{-1} g_{Co}^{-1} (Co/Mg) and 2.7 mmol h^{-1} g_{Co}^{-1} (Co/Al) for the catalysts supported over the pure oxides (Al_2O_3 and MgO). Note that the highest specific activity was found for the sample supported on 12MgAl.

Table 6.5. Kinetic results of the Co/xMg-Al supported catalysts.

Catalyst	T_{50}, °C	Specific rate at 450 °C, mmol CH_4 g_{Co}^{-1} h^{-1}	E_a, kJ mol^{-1}
Co/Al	550	2.7	82 ± 2
Co/7Mg-Al	535	3.3	83 ± 2
Co/12Mg-Al	525	3.5	79 ± 3
Co/18Mg-Al	530	3.0	88 ± 3
Co/Mg	525	2.5	102 ± 2

Taking into consideration that the oxidation of methane over cobalt oxide catalysts involves the participation of highly active oxygen species [172], the observed increase in catalytic activity was proposed to be connected to the amount of easily reducible cobalt species the sample as expressed by the specific hydrogen uptake at low temperatures in the TPR profiles. In this sense, Figure 6.10 shows that there was a reasonable good correlation between the specific reaction rate with the H_2 consumption measured below 550 °C, which corresponded to active oxygen species involved in the reduction of free Co_3O_4 and unstable cobalt-MgO species, and the estimated reaction rate at 450 °C.

These findings would be consistent with the lowest abundance of inactive, hardly reducible cobalt species such as $CoAl_2O_4$ and/or CoO-MgO solid solution on the Co/12Mg-Al catalyst, and the concomitant largest population of highly active cobalt species mainly in the form of Co_3O_4. In this way, it could be established that the presence of $CoAl_2O_4$ would affect the performance of Co/Al and Co/7Mg-Al catalysts while the formation of a stable CoO-MgO solid solution would negatively affect the performance of the Co/18Mg-Al and Co/Mg samples.

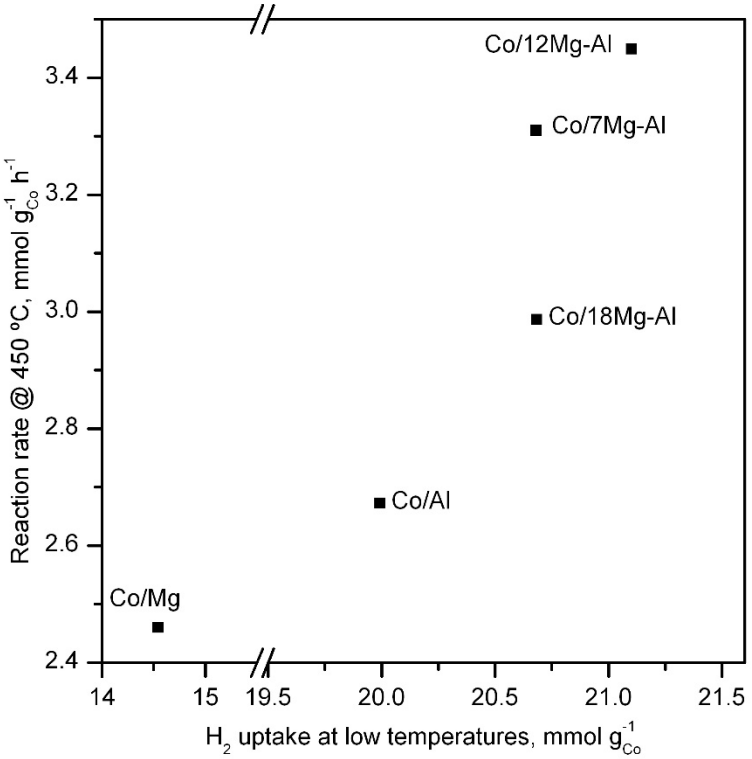

Figure 6.10. Correlation between the specific reaction rate and the H_2 specific uptake at low temperature (‹550 °C) of the Co/xMg-Al supported catalysts.

The apparent activation energy of the reaction was evaluated by applying the integral method. The results are listed in Table 6.5 and the linearised Arrhenius plots are depicted in Figure 6.11. The activation energy for the magnesium-free catalyst (Co/Al) was 82 kJ mol^{-1}. Similarly, with increasing magnesium loadings (7 and 12%wt.), the apparent activation energy remained in similar values (79-83 kJ mol^{-1}). However, the apparent activation energy significantly increased up to 88-102 kJ mol^{-1} over the catalysts with the highest Mg loading and the catalysts supported on pure MgO. This increase was probably due to the lower activity of the Co-Mg solid solution present in these samples.

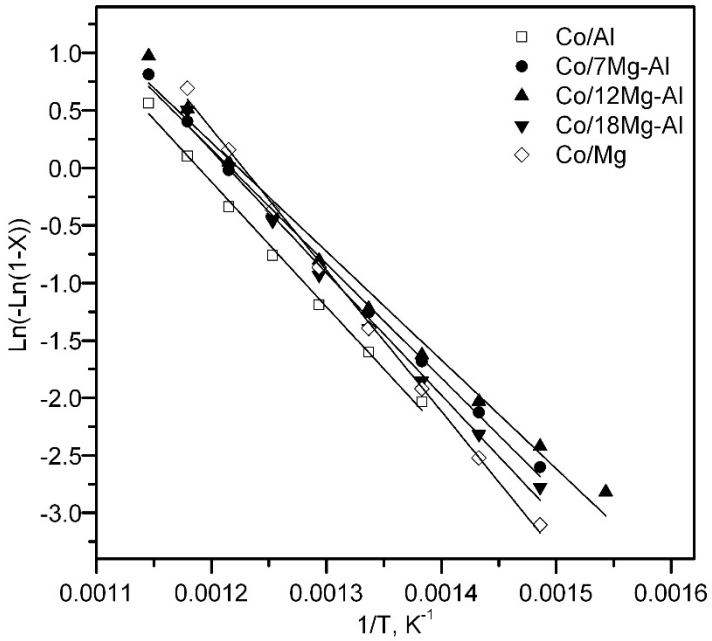

Figure 6.11. Pseudo-first order fit for the experimental data over the supported Co/xMg-Al catalysts.

6.2. REDOX PROMOTION OF Co_3O_4 WITH NICKEL

The second examined strategy focused on the addition of a metallic promoter directly to the cobalt spinel phase, and not to the alumina. If cobalt and the selected promoter, intimately mixed, are deposited onto the alumina simultaneously, then the cobalt-metal interaction should be, in principle, highly favoured. Eventually, this activated metal-metal interaction would lead to a lower formation of cobalt aluminate and an active cobalt phase with improved properties. To facilitate this, the promoter would be mainly chosen in view of its ability to insert into the spinel lattice. For this reason, the most appropriate candidate could be nickel, due to its similar ionic radius (69 pm), coordination (tetrahedral/octahedral) and oxidation states (+2/+3) with respect to cobalt.

To address the effectiveness of this strategy, three bimetallic Co-Ni/Al_2O_3 supported catalysts were synthesised by simultaneously precipitating both cobalt and nickel precursors over the alumina. The selected cobalt loadings were 25, 20 and 15%wt., while the total metallic (Co + Ni) loading was fixed at 30%wt. for all samples.

Accordingly, the nickel content of the samples was 5, 10 and 15%wt., respectively. The obtained samples were denoted as xCo-(30-x)Ni/Al where x stands for the nominal cobalt loading. A monometallic nickel catalyst supported on alumina with a 30%wt. loading (30Ni/Al) and bulk NiO and $NiCo_2O_4$ samples were also synthesised by the same route. The 30Co/Al sample was also included in this set of these reference samples.

6.2.1. Physico-chemical characterisation of the bimetallic Co-Ni/Al catalysts

The composition and textural and structural properties of the nickel-cobalt catalysts were characterised by WDXRF, N_2 physisorption, XRD and Raman spectroscopy. The textural properties of the samples, along with their actual cobalt and nickel loadings, are summarised in Table 6.6. The chemical analysis revealed that the amount of each metal deposited (cobalt and nickel) was relatively close to the corresponding nominal loading.

Table 6.6. Physico-chemical properties of the bimetallic Co-Ni/Al catalysts.

Catalyst	Co loading, %wt.	Ni loading, %wt.	BET surface, $m^2\ g^{-1}$	Pore volume, $cm^3\ g^{-1}$	Pore size distribution maxima, Å	Crystallite size, nm
Al_2O_3	-	-	139	0.56	90, 150	-
30Co/Al	27.0	-	108	0.29	90	29
25Co-5Ni/Al	23.2	4.8	113	0.35	90	21
20Co-10Ni/Al	18.1	9.4	123	0.38	90	22
15Co-15Ni/Al	13.3	14.0	117	0.40	90, 125, 340	23
30Ni/Al	-	27.1	128	0.37	90	14[a]
$NiCo_2O_4$	49.0	24.4	11	0.06	320	17

[a]Crystallite size of NiO.

The coprecipitated samples revealed a slightly lower surface with respect to the bare alumina, in the 113-123 $m^2\ g^{-1}$ range, with a concomitant decrease in pore volume by around 30-40%. The samples showed type IV isotherms with H2 hysteresis loops, commonly related to pore blocking over a wide pore size distribution (Figure 6.12). No significant change in the hysteresis loops was found after the metallic deposition.

Pore size distribution was determined by the BJH method. The bare alumina support showed a bimodal pore size distribution centred at 110 and 150 Å. This changed into a unimodal distribution peaking at about 90 Å for the Co-Ni catalysts, irrespective of their composition, probably due to the narrowing of the largest pores (150 Å) caused by the addition of the active phases. As for the pore volume, the lowest value (0.29 $cm^3 g^{-1}$) was seen for the 30Co/Al sample. When Ni was present, it tended to appreciably increase up to 0.35-0.40 $cm^3 g^{-1}$.

It is well known that the characterisation by XRD of gamma-alumina supported Co- or Ni-containing catalysts is frequently not helpful in providing useful information on the nature of the eventually present phases since both Co_3O_4, $CoAl_2O_4$, $NiAl_2O_4$ (ICDD 00-078-1601) and $NiCo_2O_4$ (ICDD 00-002-1074) spinel oxides crystallise in the same cubic (Fd-3m) structure.

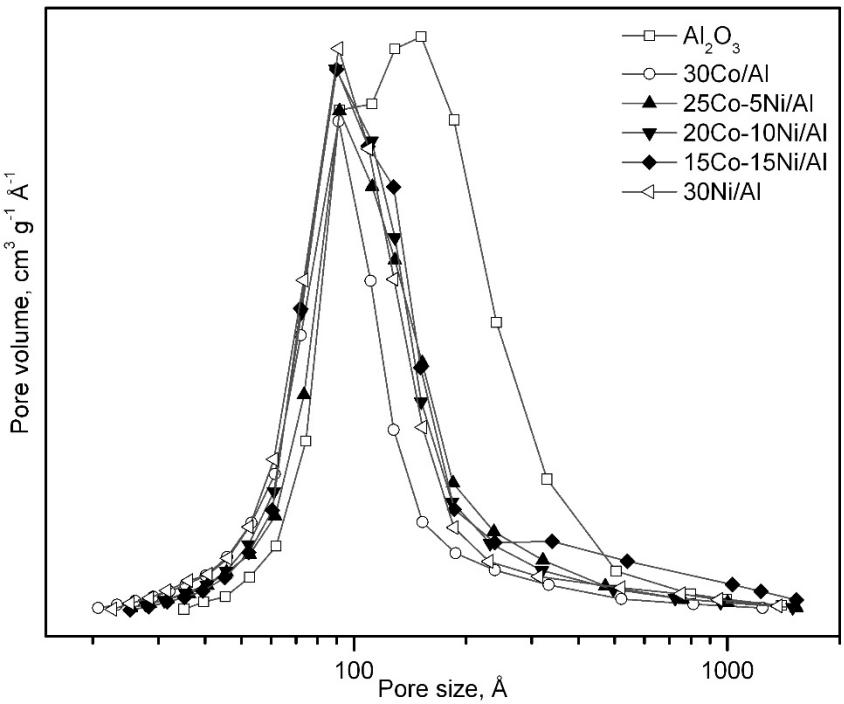

Figure 6.12. Pore size distribution of the bimetallic Co-Ni/Al catalysts.

Note that the formation of notable amounts of both amorphous cobalt aluminate and nickel aluminate was plausible due to the interaction of Co_3O_4 and NiO with the γ-Al_2O_3 at relatively moderate temperatures (›450 °C) [279,280]. Therefore, the patterns of the Co-Ni catalysts, shown in Figure 6.13, exhibited signals at 2θ = 31.3, 37.0, 45.1, 59.4 and 65.3°, which was coherent with the expected presence of one or several crystalline spinelic phases.

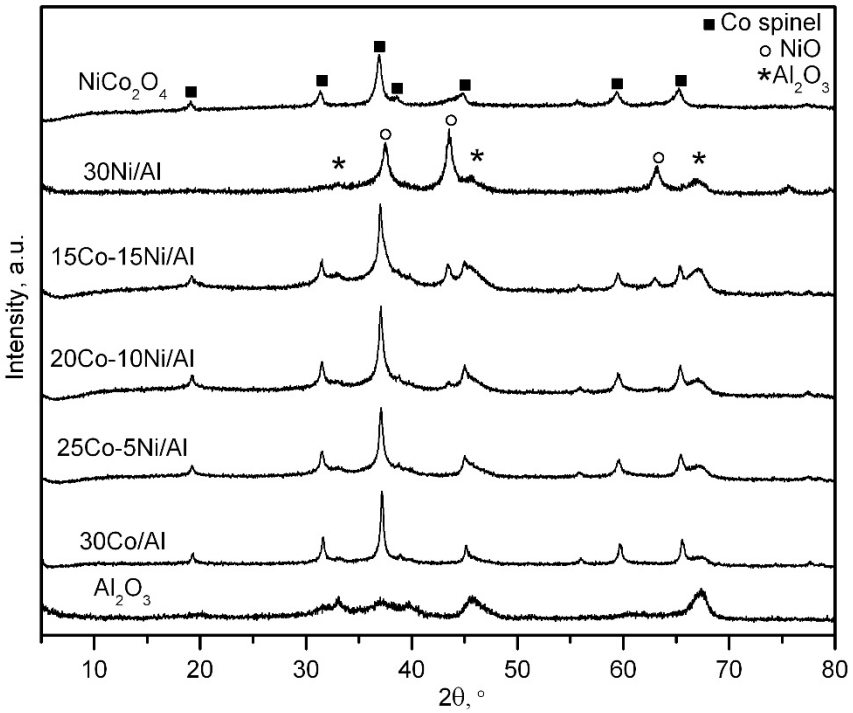

Figure 6.13. Diffraction patterns of the bimetallic Co-Ni/Al catalysts.

In addition, the bimetallic catalysts with a high Ni loading (20Co-10Ni/Al and 15Co-15Ni/Al) along with the 30Ni/Al sample also revealed signals located at 2θ = 43.9 and 62.9 assignable to the presence of segregated NiO (ICDD 00-089-7131). In relation to the 30Ni/Al sample, it should be remarked that, although the presence of nickel aluminate was highly probable, its diffraction pattern did not show distinct signals attributable to a crystalline spinel phase.

As aforementioned, a clear definition of the cobalt species present (Co_3O_4 and/or $CoAl_2O_4$) in the Co/Al sample was not possible. However, since it is known that the $CoAl_2O_4$ phase formed below 600 °C possesses a low degree of crystallinity [224,281], its signals are normally weaker compared with those of more crystalline Co_3O_4. For these reasons, the eventual presence of the different spinels in the coprecipitated samples could not be a priori discerned owing to their similar diffraction patterns. Nevertheless, it could be reasonably assumed that the high-intensity spinel signals observed in the bimetallic catalysts should be preferentially attributed to either Co_3O_4 or $NiCo_2O_4$ phases.

Besides, the analysis of the relative intensity and position of various selected diffraction signals could provide some insights into the prevailing oxide phases in each sample. Hence, it was noticed that the signal located at $2\theta = 67.2°$, attributed to the γ-Al_2O_3, changed its relative intensity with respect to the signals of the spinel when the nickel loading was varied. More precisely, the intensity ratio between the characteristic signal of the spinel located at $2\theta = 65.3°$ and the aforementioned characteristic signal of the alumina monotonously decreased from 2.0 for the 30Co/Al sample to 0.6 for the 15Co-15Ni/Al sample.

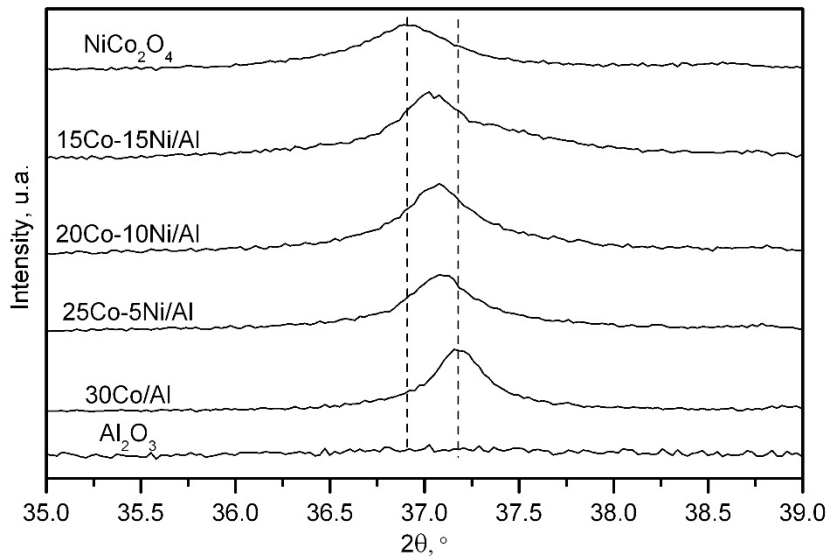

Figure 6.14. Close-up view of the diffraction patterns of the bimetallic Co-Ni/Al catalysts in the 2θ = 35-39 range.

On the other hand, a close-up view of the main spinel signal at $2\theta = 37.1°$ of the coprecipitated catalysts (Figure 6.14) revealed a continuous shift towards a lower angle value, that tended to be similar to that showed by the bulk $NiCo_2O_4$ sample ($2\theta = 36.7°$), with increasing Ni loadings. These findings suggested that the addition of nickel resulted in a favoured formation of the nickel cobaltite spinel, which in turn inhibited the formation of alumina-derived spinels (such as $CoAl_2O_4$ and $NiAl_2O_4$), hence making the signals of the alumina support relatively more intense. The introduction of nickel also led to a decrease in the crystallite size (Table 6.5) of the spinel-like phase, from 29 nm for the 30Co/Al catalyst, to 21-23 nm for the Co-Ni coprecipitated samples.

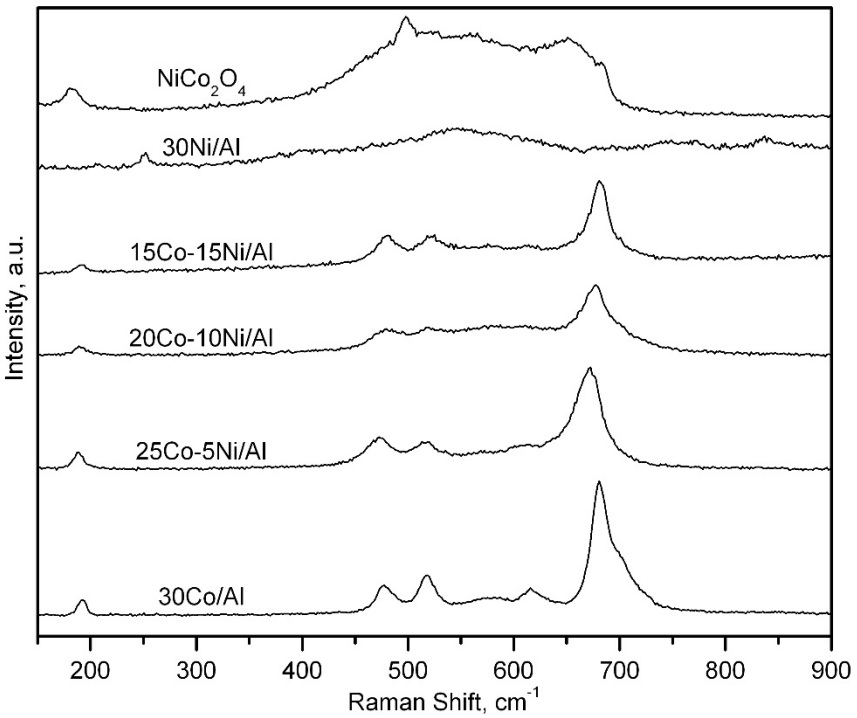

Figure 6.15. Raman spectra of the bimetallic Co-Ni/Al catalysts.

The structure of the samples was further investigated by Raman spectroscopy. As a reminder, the Raman spectra (Figure 6.15) of the 30Co/Al sample showed the five vibration modes expected from the presence of Co_3O_4 and the two shoulders at 705 and 725 cm^{-1}, both associated with an A_{1g} vibration mode derived from the partial inversion of the $CoAl_2O_4$ spinel. On the other hand, the 30Ni/Al sample suggested the presence of both NiO

and $NiAl_2O_4$ phases, although the latter was not directly observed by XRD, probably due to its amorphous character. Hence, the main signal for this sample was located at 545 cm^{-1}, between the main signals from the first order phonon of NiO at 510 cm^{-1} and the main signal of $NiAl_2O_4$ at 574 cm^{-1} [282,283], which evidenced a significant presence of both nickel phases. Likewise, some weaker signals from $NiAl_2O_4$ 250, 746 and 835 cm^{-1} were detected as well [284].

As for the bimetallic catalysts, these only showed four (196, 480, 520 and 687 cm^{-1}) out of the five signals assigned to the Co_3O_4 spinel. The signal at 619 cm^{-1} was not visible due to the appearance of a wide vibration band in the 540-650 cm^{-1} range, similar to that displayed by the as-synthesised bulk $NiCo_2O_4$. Furthermore, these signals were found to be significantly shifted towards lower values, especially for the 25Co-5Ni/Al (9 cm^{-1}) and 20Co-10Ni/Al (6 cm^{-1}) samples. This alteration accordingly indicated some degree of distortion of the spinel Co_3O_4 lattice owing to the partial insertion of Ni^{2+} cations [285], as also revealed by XRD. Finally, the aforementioned shoulders at 705 and 725 cm^{-1} noted for the 30Co/Al catalyst were not detected, thereby suggesting a concomitant decreased formation of the $CoAl_2O_4$ phase in these samples.

The surface structure of the bi- and monometallic catalysts was investigated by X-Ray photoelectronic spectroscopy (XPS). For the sake of comparison, the as-synthesised $NiCo_2O_4$ sample was also examined. The surface composition and the distribution of nickel, cobalt and oxygen species was determined by deconvolution and integration of the $Ni2p_{3/2}$ (850-870 eV), $Co2p_{3/2}$ (777-792 eV) and O1s (526-536 eV) spectra, respectively, as shown in Figure 6.16.

Firstly, the $Co2p_{3/2}$ spectra of the samples was deconvoluted into three main and two satellite contributions as previously described elsewhere [252,286]. Likewise, the $Ni2p_{3/2}$ was deconvoluted following a similar procedure. Hence, three main contributions located at 853.9, 855.4 and 856.9 eV were detected. These features were related to the presence of Ni^{2+} as NiO species, the existence of Ni^{2+} belonging to a spinel lattice and the formation of Ni^{3+} species, respectively [287,288]. The satellite contribution of the nickel spectra was dominated by an intense signal centred at 861.0 eV, characteristic of the major presence of nickel in the +2 oxidation state, with a small shoulder located at around 865.3 eV coherent with a relatively small amount of Ni^{3+} species in the samples.

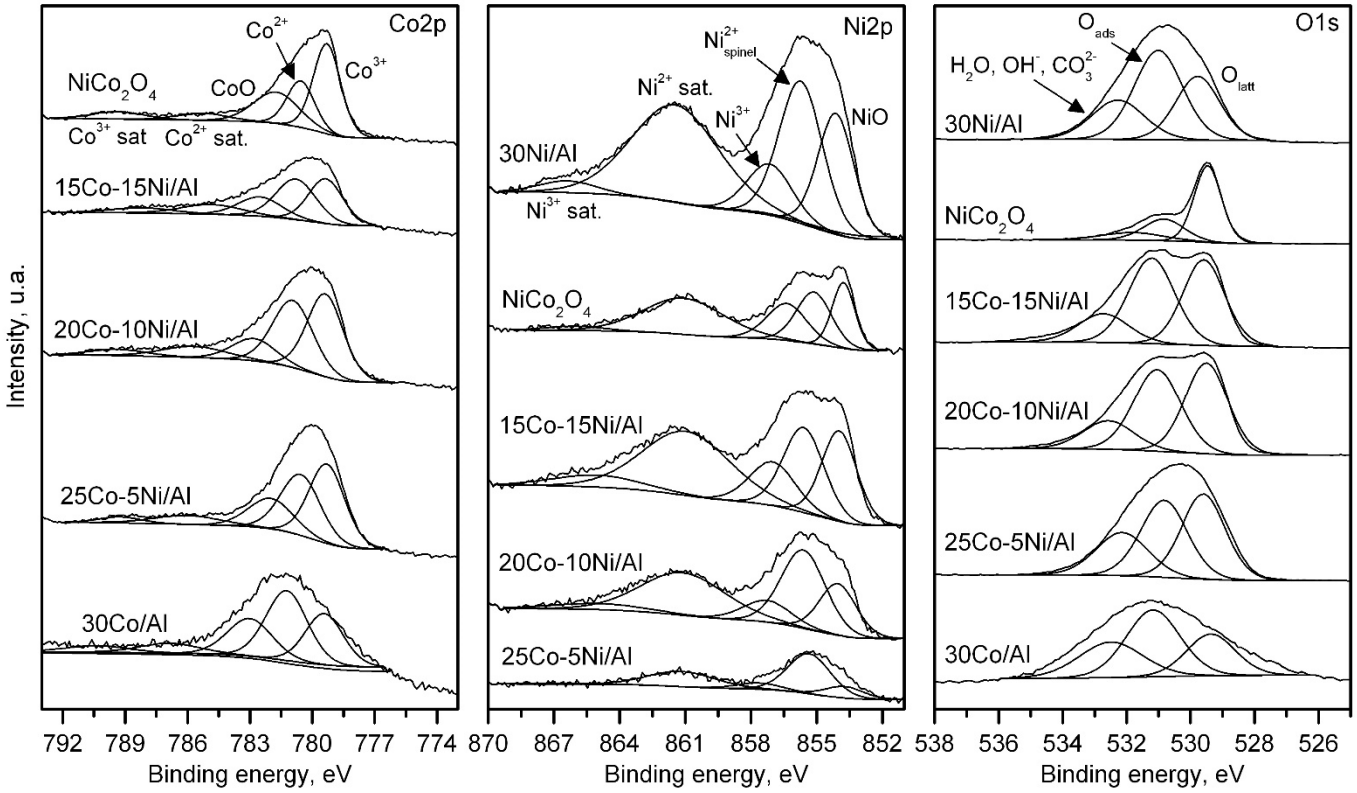

Figure 6.16. XPS spectra of the bimetallic Co-Ni/Al catalysts.

Finally, the O1s spectra were deconvoluted into three peaks located at 529.3, 531.3 and 532.6 eV. The first two were attributed to the lattice and adsorbed oxygen species, respectively, while the last one was assigned to oxygen from water molecules, hydroxyl and carbonate groups on the surface of the samples [190,191]. The surface composition estimated from these spectra is included in Table 6.7, along with the bulk composition determined by WDXRF for comparative purposes.

Expectedly the aluminium concentration on the surface was appreciably lower. On the other hand, no marked differences in Co concentration were noticed between the surface and the bulk. By contrast, a favoured accumulation of nickel at the surface level was evident for all the samples, with remarkably higher Ni concentrations (almost twice) when compared with the loading estimated by WDXRF.

The main band of the $Co2p_{3/2}$ spectra of the Co/Al catalyst was located at 781.2 eV. This position was influenced by the notable presence of Co^{2+} species as $CoAl_2O_4$, in line with the results from Raman spectroscopy. In fact, the Co^{3+}/Co^{2+} molar ratio was as low as 0.67. With the addition of small amounts nickel (5%wt.) the binding energy of this band significantly decreased down to 779.8 eV. This shift was assigned to a lower abundance of Co^{2+} species as cobalt aluminate.

As shown in Figure 6.17, a further increase in Ni loading did not lead to remarkable changes in the position of the band (779.9 eV for both 20Co-10Ni/Al and 15Co-15Ni/Al samples). More importantly, irrespective of the Ni content of the catalyst, the position was close to that observed for both bulk Co_3O_4 and $NiCo_2O_4$ (779.5 eV), which in addition are characterised by quite high Co^{3+}/Co^{2+} molar ratios (1.96 and 2.10, respectively). In view of the results included in Table 6.7 the presence of Co^{3+} species is most favoured for the lowest Ni content (25Ni-5Co/Al sample, with a Co^{3+}/Co^{2+} molar ratio of 1.21). However, the origin of this considerable relative increase in the presence of Co^{3+} species (Co_3O_4 or $NiCo_2O_4$) cannot be clearly known.

Table 6.7. Physico-chemical properties of the bimetallic Co-Ni/Al catalysts.

Catalyst	Ni content, %wt.	Co content, %wt.	Al content, %wt.	Co^{3+}/Co^{2+} molar ratio	O_{ads}/O_{latt} molar ratio	Ni^{2+}(NiO)/Ni^{2+}(spinel) molar ratio	Ni^{3+}/Ni^{2+} molar ratio
30Co/Al	-	22.6 (27.9)	32.1 (37.0)	0.67	1.41	-	-
25Co-5Ni/Al	8.2 (4.8)	25.4 (23.2)	22.7 (33.0)	1.20	0.94	0.26	0.13
20Co-10Ni/Al	18.6 (9.4)	22.7 (18.1)	22.5 (33.6)	1.11	1.04	0.55	0.24
15Co-15Ni/Al	27.9 (14.0)	14.8 (13.3)	21.7 (33.7)	0.95	1.10	0.93	0.29
30Ni/Al	40.6 (27.1)	-	22.1 (34.7)	-	1.54	0.71	0.30
$NiCo_2O_4$	31.5 (24.4)	38.8 (49.0)	-	2.10	0.43	0.82	0.39

Values in brackets correspond to the metallic loading as determined by WDXRF.

In order to gain some insights on this question, the Ni2p$_{3/2}$ spectra were analysed in detail. As stated earlier, the predominant nickel phases were Ni^{2+} as NiO or in the form of either $NiAl_2O_4$ or $NiCo_2O_4$. As reflected in Table 6.7, the presence of NiO was promoted by high Ni loadings with the Ni^{2+}(NiO)/Ni^{2+}(spinel) molar ratio increasing from 0.21 over the 25Co-5Ni/Al sample to 0.89 over the 15Co-15Ni/Al sample. On the other hand, while no remarkable changes were observed in the position of the Ni^{2+}(NiO) band, some significant alterations were evident for the band associated with Ni^{2+} species belonging to a spinelic lattice (Figure 6.16). It is noteworthy that this band was located at 855.7 eV for the Ni/Al catalyst, which only contained $NiAl_2O_4$ along with NiO. Conversely, this band was positioned at 855.1 eV for the bulk $NiCo_2O_4$ sample. Therefore, the position with respect to these two reference values may be helpful in at least qualitatively defining the nature of the spinel that was preferably formed on the catalysts as a function of its nickel content.

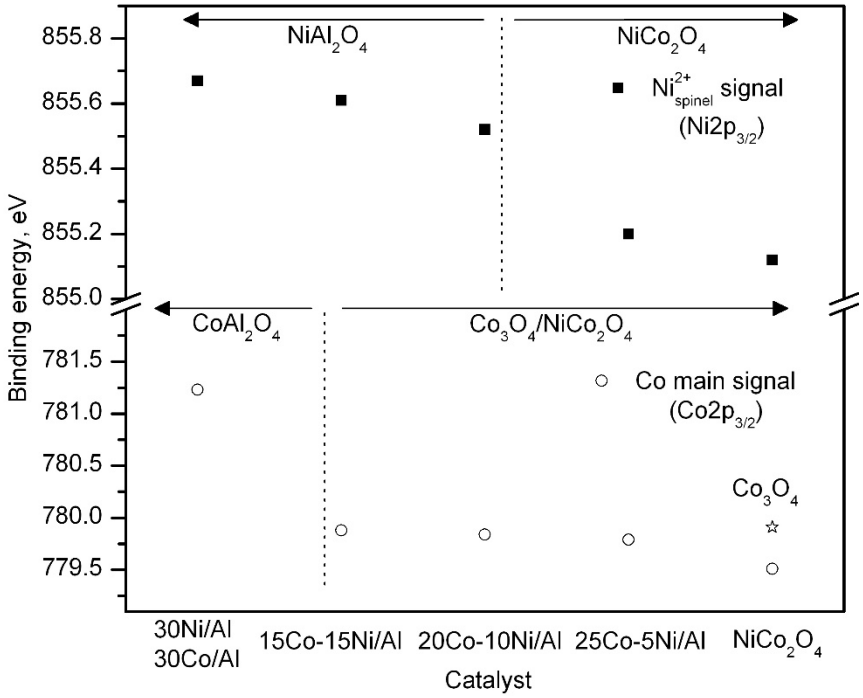

Figure 6.17. Evolution of the Co2p$_{3/2}$ main signal and the Ni^{2+} signal from a spinel lattice for the bimetallic Co-Ni/Al catalysts.

The trend visualised in Figure 6.17 pointed to a favoured formation of nickel cobaltite with small amounts of nickel while the Ni-rich samples were more prone to the generation of nickel aluminate. Moreover, these findings confirmed that the high Co^{3+}/Co^{2+} molar ratio of the 25Co-5Ni/Al sample was due to the formation of $NiCo_2O_4$ at the cost of Co_3O_4. Finally, data collected in Table 6.7 revealed that this increase in the amount of Co^{3+} species was in turn accompanied by a marked presence of lattice oxygen species. These have been regarded as the active oxygen species in the oxidation of methane following a Mars-van Krevelen mechanism. As shown in Figure 6.18, the presence of this type of species was optimised for the 25Co-5Ni/Al catalyst. Also note that, regardless the Ni content, lattice oxygen species were more abundant, with O_{ads}/O_{latt} molar ratios in the 0.94-1.10 range, than in the monometallic counterparts (1.41 and 1.54 for the Co/Al and Ni/Al samples, respectively).

All the examined catalysts including the supported mono- and bimetallic catalysts and the bulk $NiCo_2O_4$ and NiO oxides contained a significant fraction of Ni^{3+} species. The corresponding Ni^{3+}/Ni^{2+} molar ratios are included in Table 6.7. The assessment of the origin of this signal is complex since Ni^{3+} may be related to the mixed Co-Ni spinel but also to Ni_2O_3 derived from the surface oxidation of NiO. It was found that Ni^{3+} species are more abundant with the Ni loading of the supported catalysts, from 0.13 over the 25Co-5Ni/Al sample to 0.30 over the 30Ni sample. This trend was consistent with the increasing NiO content of the catalysts, as dictated by XRD and Raman spectroscopy. Note that the pure bulk NiO sample exhibited a molar ratio as high as 0.50. On the other hand, the presence of Ni^{3+} species in the 25Co-5Ni/Al sample could be attributed to nickel cobaltite in view of its reduced amount of NiO.

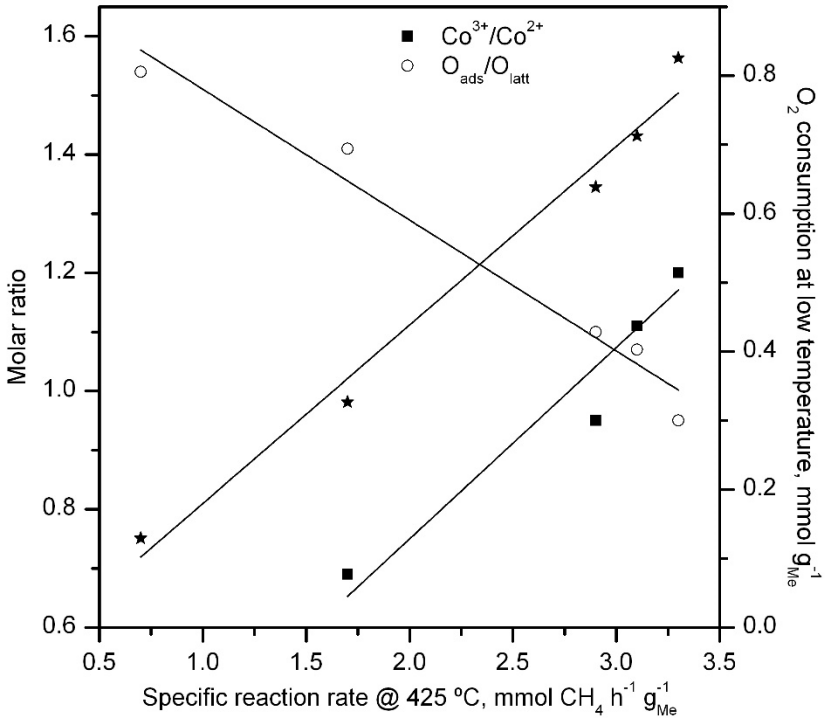

Figure 6.18. Relationship between the surface composition (XPS) and O_2 consumption at low temperature (CH_4-TPRe) with the activity of the bimetallic Co-Ni/Al catalysts.

In order to get a more precise insight on the surface chemical structure of the cobalt-nickel catalysts, a study on the elemental composition was carried out. The bimetallic catalysts along with the monometallic 30Co and 30 Ni samples were thus characterised by scanning transmission electron microscopy–high-angle annular dark field (STEM–HAADF). Additionally, 2D EELS elemental maps (Figure 6.19) were generated for certain areas in each sample to allow studying the spatial distribution of cobalt and nickel in the bimetallic catalysts. These were generated by selectively choosing the signals of the absorption edges Co L (779 eV) and Ni L (854 eV) after background subtraction.

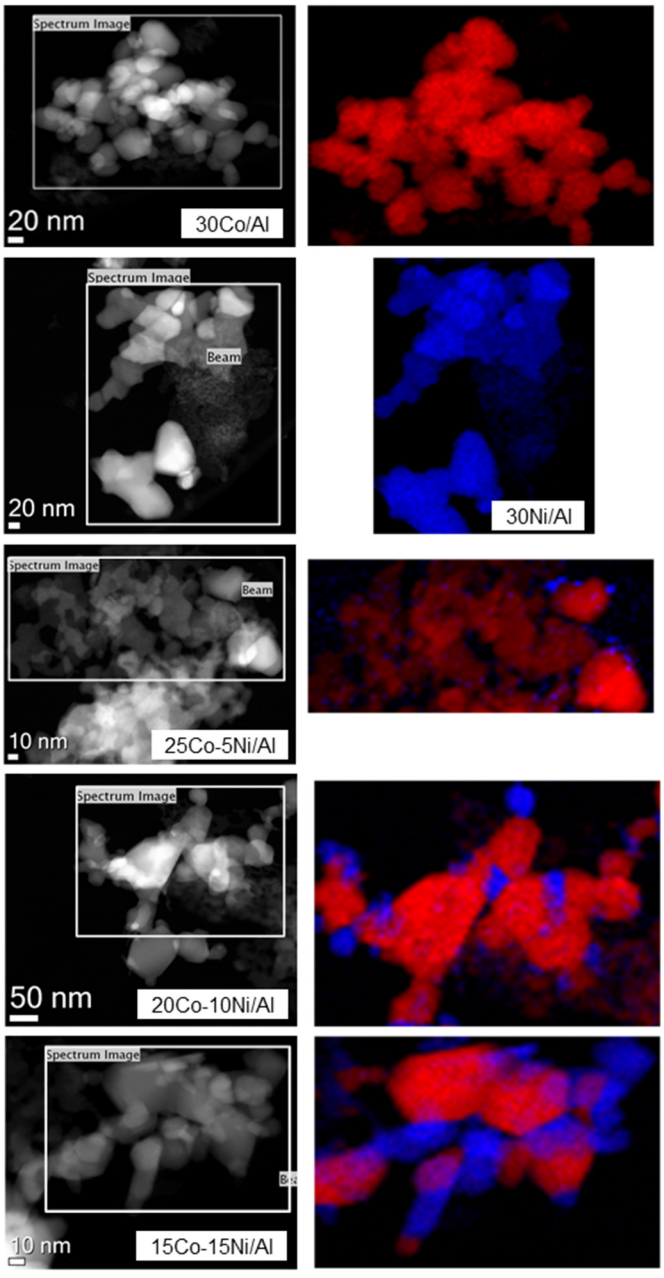

Figure 6.19. STEM-HAADF images and EELS maps of the bimetallic Co-Ni/Al catalysts. (Red) cobalt and (blue) nickel.

The 30Co and 30Ni catalysts were characterised by the presence of Co_3O_4 and NiO polycrystallites with sizes ranging from 20-40 and 10-30 nm, respectively (in some cases formed by the apparent attachment of smaller crystallites). On both samples, the abundance of relatively large regions of less crystalline aluminates was also evidenced. As far as the bimetallic Co-Ni catalysts was concerned, it was found that nickel was homogeneously present and well mixed with cobalt when the Ni content was low (5%wt.), thus expectedly favouring the formation of $NiCo_2O_4$-like species. Small Ni-containing patches assigned to isolated NiO with a size of 10-20 nm were observed as well. For increased Ni loadings (20Co-10Ni/Al and 15Co-15Ni/Al samples), noticeably larger areas (› 50 nm) of Ni-rich phases (NiO and $NiAl_2O_4$) were noticed.

Complementary EDX micro-analysis was useful for giving information on the elemental composition/concentration of selected spots of each sample. K(Co), L(Co), K(Ni), K(Al) and K(O) X-ray emission peaks were used for quantification, which was conducted after a previous removal of the spectral background using the *ESVision/TIA* software. About 17 spot EDX analyses were obtained of each sample, except for the 30Ni sample (4 spot measurements). A sample of the corresponding results for the 30Co catalyst is shown in Figure 6.20.

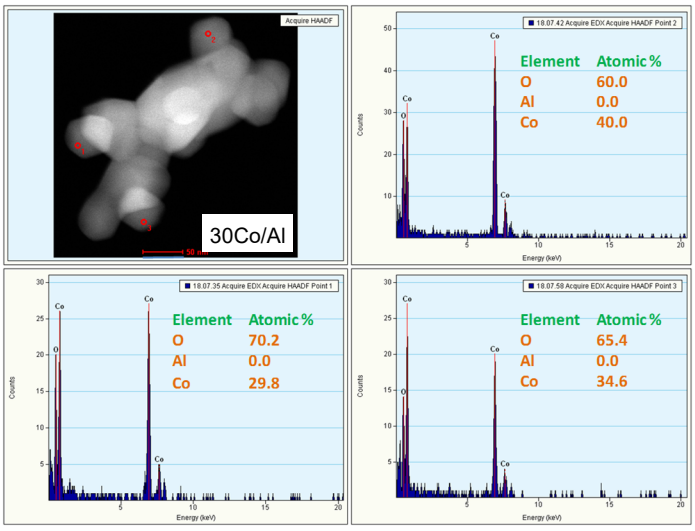

Figure 6.20. HAADF-STEM images and EDX spectra of the bimetallic Co-Ni/Al catalysts.

These data provided a semiquantitative distribution of the various species that were present on the samples as a function of the catalyst formulation, which included alumina, Co_3O_4, NiO, Ni-Al, Co-Al, Ni-Co and Ni-Co-Al species. This assignment was tentatively carried out as function of the relative abundance of Co, Ni, Al and O elements. Results corresponding to the oxide phase distribution over the monometallic and bimetallic catalysts as estimated from EDX measurements are included in Figure 6.21.

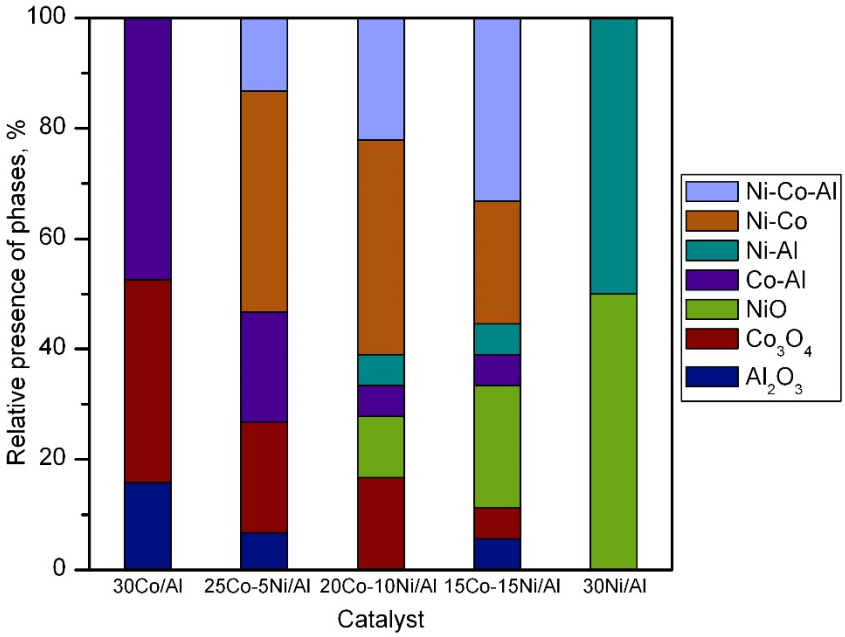

Figure 6.21. Oxide phase distribution over the bimetallic Co-Ni/Al catalysts as determined by STEM-HAADF coupled to EDX.

In line with the EELS maps, the 30Co catalyst consisted of a mixture of Co_3O_4 polycrystallites and Co-Al entities attributable to cobalt aluminate-like species. In addition, some areas of uncovered alumina support could be identified. Analogously, the pure nickel sample (30Ni) presented relatively well-defined NiO crystallites and regions with nickel and aluminium intimately in contact forming amorphous $NiAl_2O_4$-like species.

The analysis of the three bimetallic catalysts evidenced the presence of species with a greater compositional variety including up to seven different oxide phases. Moreover, remarkable changes in the relative abundance as a function of their composition were noticed. Hence, the cobalt contained in the 25Co-5Ni/Al catalyst was mainly in the form of

Ni-Co (40%), Co_3O_4 (20%), Co-Al (20%), and Ni-Co-Al(13%) entities. The Ni-Co species, which showed a Ni/Co molar ratio ranging between 0.1 and 0.2, were ascribed to substoichiometric nickel cobaltite. As the cobalt loading decreased, it was observed that the relative amounts of Co_3O_4 species decreased to 17% and 6% over the 20Co-10Ni/Al and 15Co-15Ni/Al samples. Likewise, Ni-Co species gradually tended to be less abundant, particularly over the 15Co-15Ni/Al catalyst (22%). Accordingly, Ni-rich entities such as NiO (with a Ni/Co molar ratio higher than 3) and Ni-Co-Al were favoured with higher Ni content in the sample, up to 22% and 33%, respectively. It is worth pointing out that results from EDX analysis were in agreement with the conclusions derived from the spectroscopic techniques (Raman spectroscopy and XPS) and XRD, which suggested the favoured formation of $NiCo_2O_4$-like species over the bimetallic catalysts over the 25Co-5Ni/Al catalyst, and the generation of increasing amounts NiO over the 20Co-10Ni/Al and 15Co-15Ni/Al samples.

The samples were examined by HRTEM as well. Figure 6.22 shows some selected HRTEM images for the 30Co and the bimetallic catalysts. Over the four samples the characteristic lattice fringes with interplanar spacing of 0.244 and 0.286 nm assignable to the {311} and the {220} planes of a spinel crystalline phase could be observed. As stated earlier, since the crystallographic parameters of Co_3O_4, $CoAl_2O_4$ and $NiCo_2O_4$ are virtually identical, it is rather difficult to distinguish them by electronic microscopy. Conversely, the lattice-resolved HRTEM images of the 30Ni sample did not reveal the existence of the crystalline $NiAl_2O_4$ spinel.

On the other hand, when analysing the results corresponding to the 20Co-10Ni/Al and 15Co-15Ni/Al samples (Figure 6.23) individual crystallites presenting interlayer distances of 0.209 nm attributable to the spacing of the {200} plane of NiO were also clearly observed. Thus, the presence of segregated nickel oxide along with crystalline spinellic phases was corroborated over the Ni-rich bimetallic catalysts, in line with XRD, XPS and chemical mapping analysis.

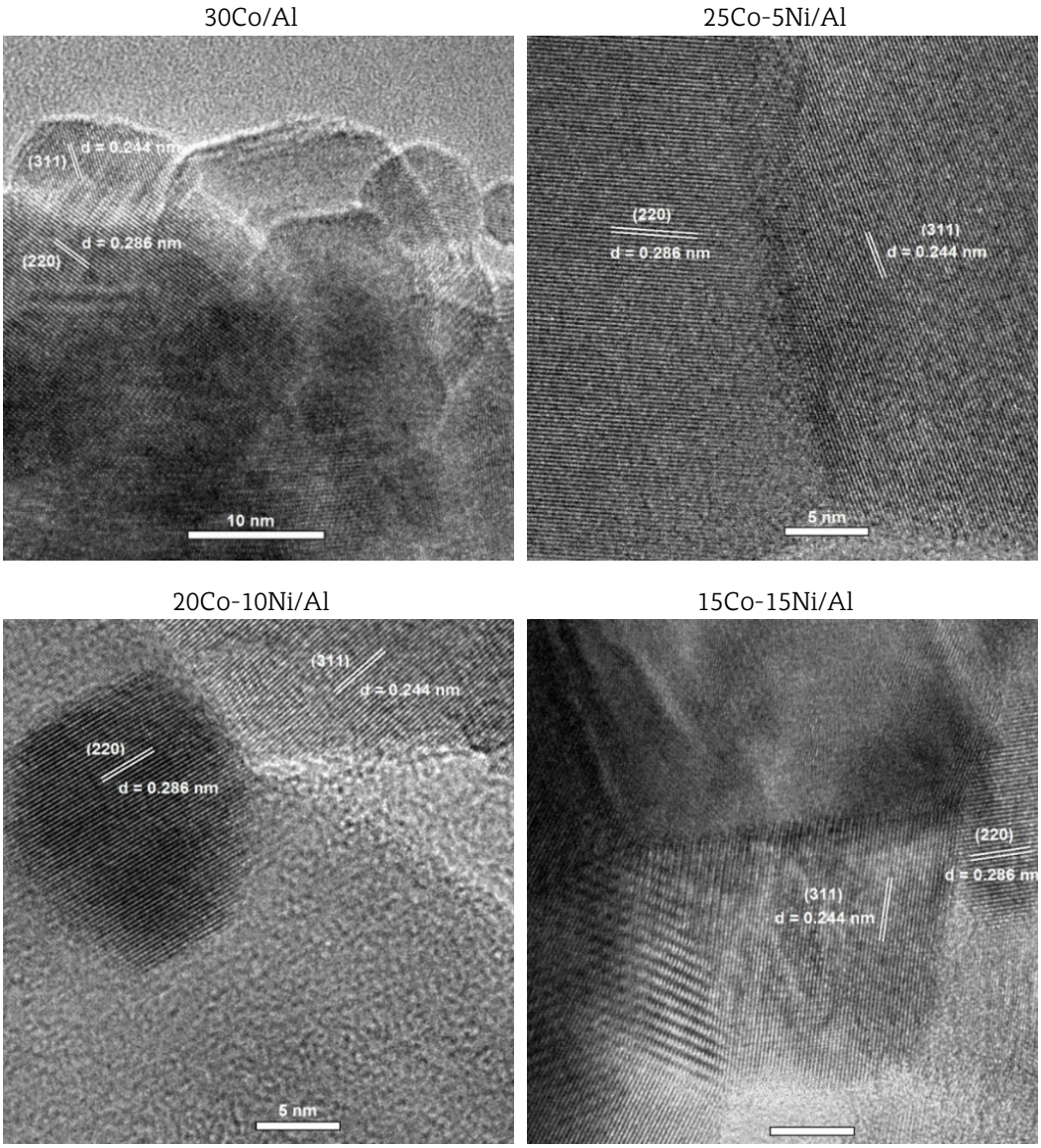

Figure 6.22. HRTEM images of the 30Co/Al, 30Ni/Al and $NiCo_2O_4$ samples.

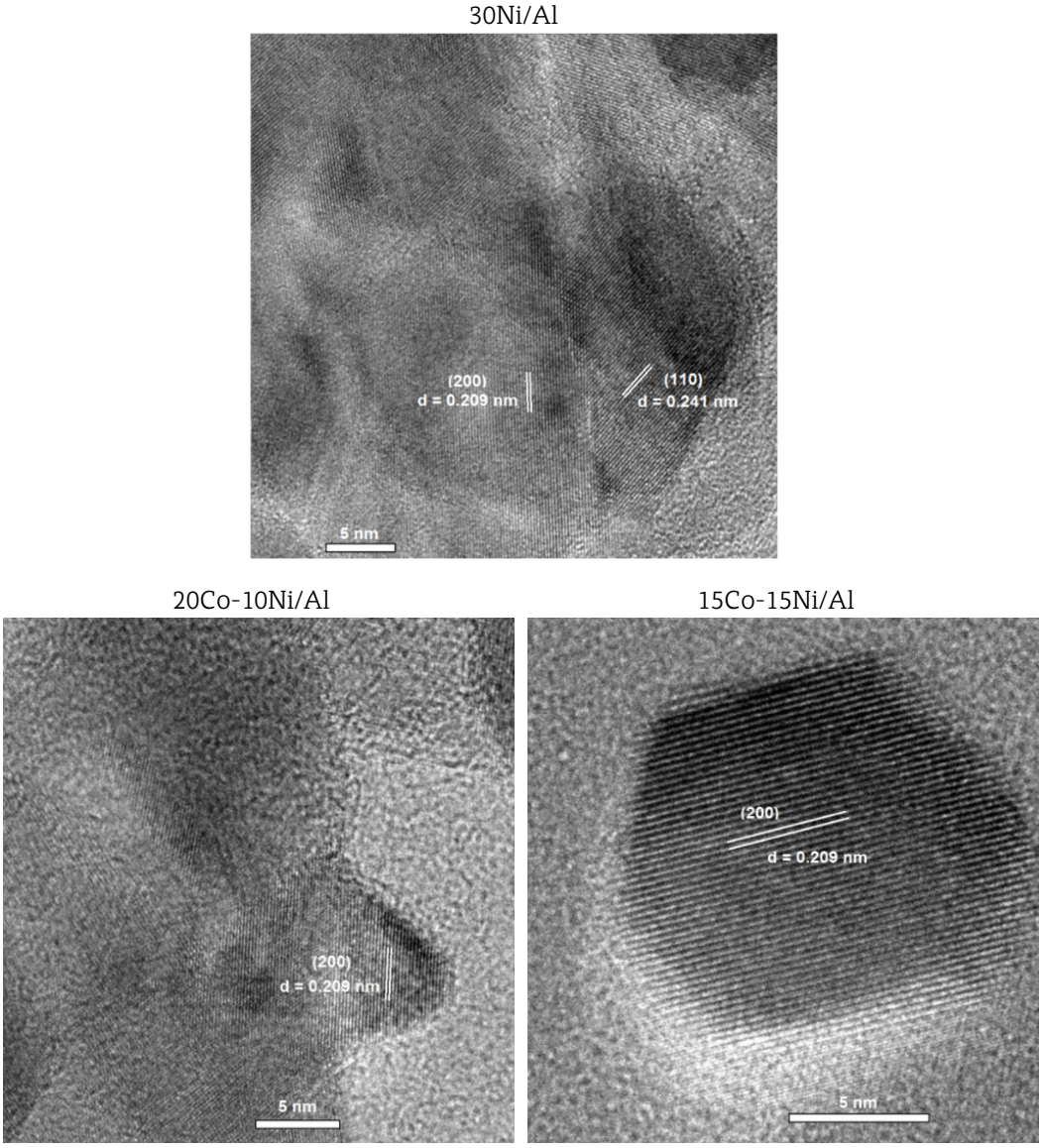

Figure 6.23. HRTEM images of NiO crystallites in the 30Ni/Al, 20Co-10Ni/Al and 15Co-15Ni/Al samples.

The analysis of the samples by H_2-TPR was useful for determining their redox behaviour but also for further corroborating the nature of the oxides phases present in the bimetallic catalysts, as tentatively established by XRD, Raman spectroscopy, XPS and electronic

microcopy coupled to elemental analysis. Firstly, the redox behaviour of the bulk pure oxides (NiO and Co_3O_4) were examined (Figure 6.24).

Briefly, bulk nickel oxide showed a broad profile with a peak reduction temperature at around 420 °C with a shoulder at 525 °C, which was coherent with the redox behaviour of NiO crystallites with a relatively large size (›40 nm). The profile of bulk Co_3O_4 was in concordance with the already described two-step reduction process. The shape of the reduction trace of bulk $NiCo_2O_4$ was similar to that of Co_3O_4 although the former seemed to be more easily reduced. Thus, its H_2 consumption started at significantly lower temperatures, around 180 °C (about 210 °C for Co_3O_4). The reduction process involved the reduction of Co^{3+} to Co^{2+} (260 °C) followed by the simultaneous reduction of Co^{2+} and Ni^{2+} (at 340 °C) to the metallic states [194].

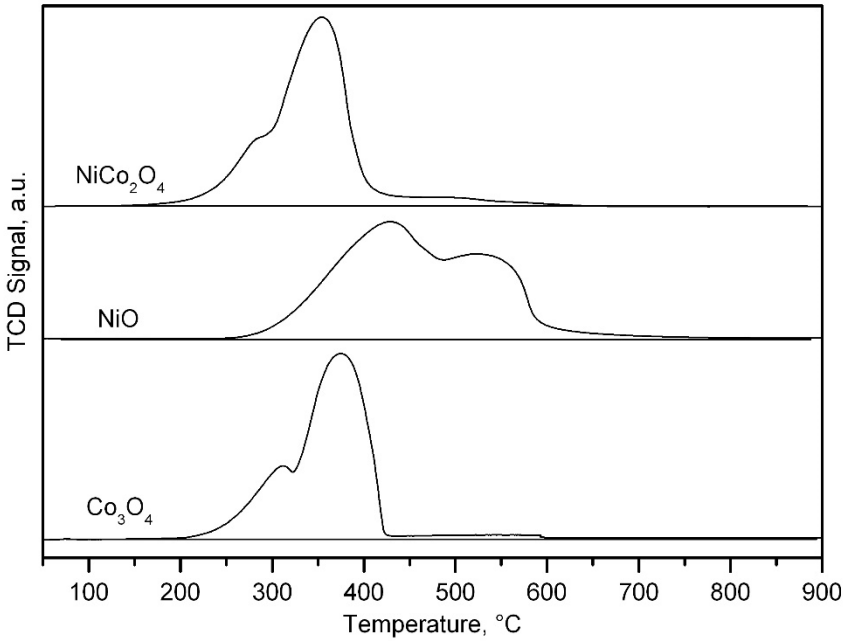

Figure 6.24. H_2-TPR profiles of base bulk samples.

The profiles of the supported samples, including that of bulk nickel cobaltite, are included in Figure 6.25. The 30Ni/Al sample revealed an H_2 uptake at 425 °C that was assigned to the reduction of nickel oxide, in agreement with the profile of the bulk NiO [289]. A second noticeable consumption was noticed at 700 °C, thereby revealing that this catalyst

contained a significant amount of hardly reducible $NiAl_2O_4$ species [290]. The overall H_2 uptake of the sample was 4.5 mmol H_2 g^{-1}, very close to the theoretical value (4.6 mmol H_2 g^{-1}). Note that the H_2:Ni reduction stoichiometry was 1:1 for both NiO and $NiAl_2O_4$. As for the 30Co/Al sample, the two reduction features previously described were observed as well.

Accordingly, the total H_2 consumption (5.2 mmol H_2 g^{-1}) was lower than that expected for the exclusive presence of Co_3O_4 in the sample (6.8 mmol H_2 g^{-1}). Recall that the H_2:Co reduction stoichiometry is 4:3 for Co_3O_4 and 1:1 for $CoAl_2O4$. Therefore, the high affinity of both nickel and cobalt for alumina unavoidably induced the formation of highly stable aluminate species that ultimately negatively influenced the amount of low-temperature active oxygen species.

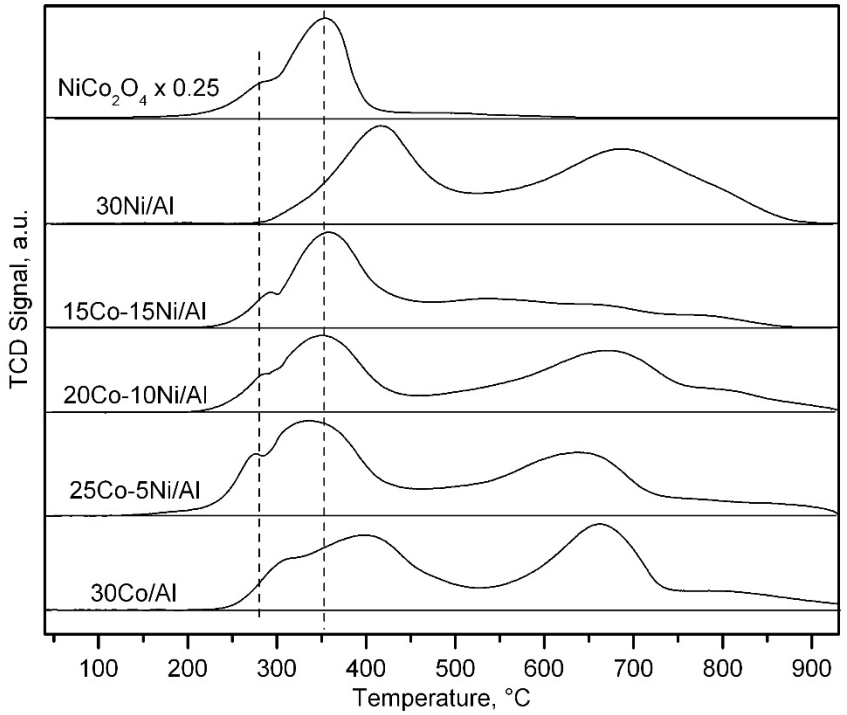

Figure 6.25. H_2-TPR profiles of the bimetallic Co-Ni/Al catalysts.

The H_2-TPR profiles of the alumina supported Co-Ni samples are included in Figure 6.25 as well. Similarly to the 30Co/Al sample, the bimetallic catalysts exhibited two reduction

processes at distinctly different temperature windows located at 175-500 °C and 500-900 °C. The H_2 consumption detected at the high temperature range revealed that the samples still contained a significant fraction of metallic oxides in the form of aluminates with a high resistance to reduction.

Another relevant finding was that the reduction process was significantly accelerated with the presence of relatively low amounts of nickel, namely 5 and 10%wt. Thus, it started at about 175 °C over the 25Co-5Ni/Al sample and 200 °C over the 20Co-10Ni/Al catalyst. However, no marked differences were noted between the 15Co-15Ni/Al and 30Co/Al samples since the reduction took place at 240 °C in both cases.

As proposed earlier, the simultaneous deposition of cobalt and nickel active phases on the surface of the alumina support resulted in the partial insertion of Ni^{2+} cations into the lattice of Co_3O_4. This nickel doping led to the formation of Co-Ni mixed oxides with a structural configuration that tended to be close to that of nickel cobaltite. In this sense, the similarity between the reduction traces, in terms of onset reduction temperature (175-200 °C), peak reduction temperatures at 280 and 380 °C and narrowing of the window of the reduction process at low temperatures, of the bimetallic catalysts and that of the as-synthesised $NiCo_2O_4$ bulk sample implied that this new Co-Ni mixed oxide phase could be partially formed.

The overall H_2 uptake of the bimetallic catalysts, which was divided into two contributions depending on the reduction temperature window, namely 175-500 °C and 500-950 °C, are listed in Table 6.8. The total consumption was found to be considerably higher (5.8 and 5.7 mmol g^{-1} for 25Co-5Ni/Al and 20Co-10Ni/Al, respectively) with respect to that of the 30Co/Al catalyst (5.2 mmol g^{-1}). In the case of the 15Co-15Ni/Al sample, its uptake (5.2 mmol g^{-1}) was close to that of the monometallic 30Co/Al sample.

Interestingly, the H_2 uptake ratio at low and high temperatures increased from 0.6 over the monometallic 30Co/Al catalyst to 0.8-1.0 over the bimetallic catalysts. Thus, the largest reducibility at low temperatures was found for the 25Co-5Ni sample (2.9 mmol H_2 g^{-1}) with the other two Co-Ni samples having a comparable behaviour around 2.6 mmol H_2 g^{-1}. On one hand, the observed promotion of reducibility could be attributed to the lower formation of cobalt and/or nickel aluminate. EDX analysis showed that the relative amount of aluminate-like species decreased from 47% over the 30Co/Al catalyst to 33%

over the 25Co-5Ni/Al and 20Co-10Ni/Al catalysts but only to 44% over the 15Co-15Ni sample. On the other hand, in view of the notable advance in the reduction at low temperatures, the favoured formation of easily reducible $NiCo_2O_4$, as also evidenced by EDX, over the 25Co-5Ni/Al and 20Co-10Ni/Al samples was responsible for the increased H_2 consumption as well.

The observed promotion of reducibility could be attributed to the lower formation of cobalt and/or nickel aluminate and, in view of the notable advance in the reduction at low temperatures, to the formation of easily reducible $NiCo_2O_4$ as well. In this regard, it is worth highlighting that the specific H_2 uptake of $NiCo_2O_4$ is 33.9 mmol H_2 g_{Co}^{-1} was markedly higher than that of Co_3O_4 (22.6 mmol H_2 g_{Co}^{-1}). In sum, and more importantly, the H_2 uptake at low temperatures, which is indicative of the amount of easily reducible oxygen species related to $NiCo_2O_4$-like species, Co_3O_4, and NiO, increased from 2.0 mmol H_2 g^{-1} over the 30Co sample to 2.6-2.9 mmol H_2 g^{-1} over the bimetallic catalysts. The contribution of each species varied as a function of the Ni content. Thus, $NiCo_2O_4$-like species promoted the reducibility of the 25Co-5Ni/Al catalyst while the redox behaviour of the 15Co-15Ni/Al sample was controlled by its larger presence of NiO.

Table 6.8. Results from the H_2-TPR and CH_4-TPRe analysis of the bimetallic Co-Ni/Al catalysts.

	H_2-TPR			CH_4-TPRe
Catalyst	Low temperature H_2 uptake, mmol g^{-1}	High temperature H_2 uptake, mmol g^{-1}	Total H_2 uptake, mmol g^{-1}	Low temperature O_2 consumption, mmol g_{Me}^{-1}
30Co/Al	2.0	3.2	5.2	0.3
25Co-5Ni/Al	2.9	3.0	5.9	0.8
20Co-10Ni/Al	2.6	3.1	5.7	0.7
15Co-15Ni/Al	2.6	2.5	5.1	0.6
30Ni/Al	1.4	3.0	4.4	0.1
$NiCo_2O_4$	16.4	0.3	16.7	1.7

As a complement of the H_2-TPR analysis, the reactivity of oxygen species present in the nickel-cobalt catalysts was also analysed by temperature-programmed reaction with methane in the absence of oxygen (CH_4-TPRe). The evolution of evolved CO_2, CO and H_2 was monitored by mass spectrometry. In general, the CO_2 profiles evidenced a two-step reaction process, as depicted in Figure 6.26. Unfortunately, the comparatively larger

formation of CO_2 and CO (and H_2, not shown) above 500 °C made the proper analysis of the obtained results in the low-temperature range rather difficult.

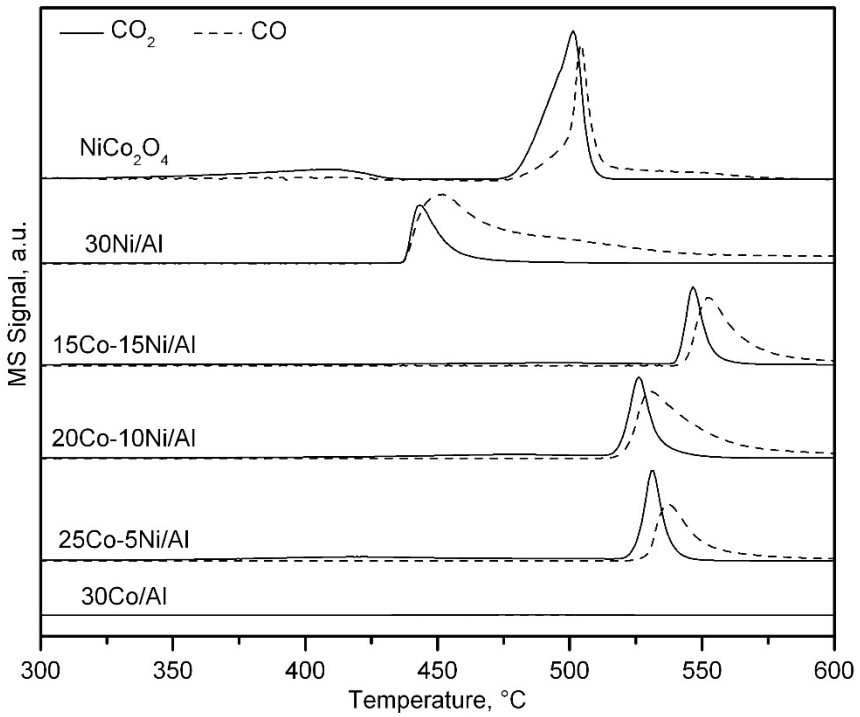

Figure 6.26. CH_4-TPRe profiles of the bimetallic Co-Ni/Al catalysts.

The comparatively larger formation of CO_2 above 500 °C made the proper analysis of the obtained results in the low-temperature range rather difficult. Accordingly, Figure 6.27 only includes the evolution of the CO_2 yield between 200 and 550 °C. This low-temperature reaction step was attributed to the complete oxidation of methane by lattice oxygen species associated with Co^{3+} ions, from either $NiCo_2O_4$ and/or Co_3O_4 species, as determined by XPS analysis. No CO or H_2 was detected during this process. The amount of CO_2 evolved from the complete oxidation reaction was barely perceptible over the 30Ni/Al sample. This low activity was connected to the reduced presence of highly dispersed Ni^{2+} cations.

Secondly, the methane partial oxidation occurred above around 525-550 °C (450 °C for the 30Ni/Al sample), where methane reacted with low-mobility oxygen species associated with Co^{2+} and Ni^{2+} ions from Co_3O_4 and NiO, yielding significant amounts of CO and H_2

along with CO_2 [115]. It must be noted that this second process was not observed over the 30Co/Al catalyst, thus suggesting that it could only occur at temperatures higher than 600 °C.

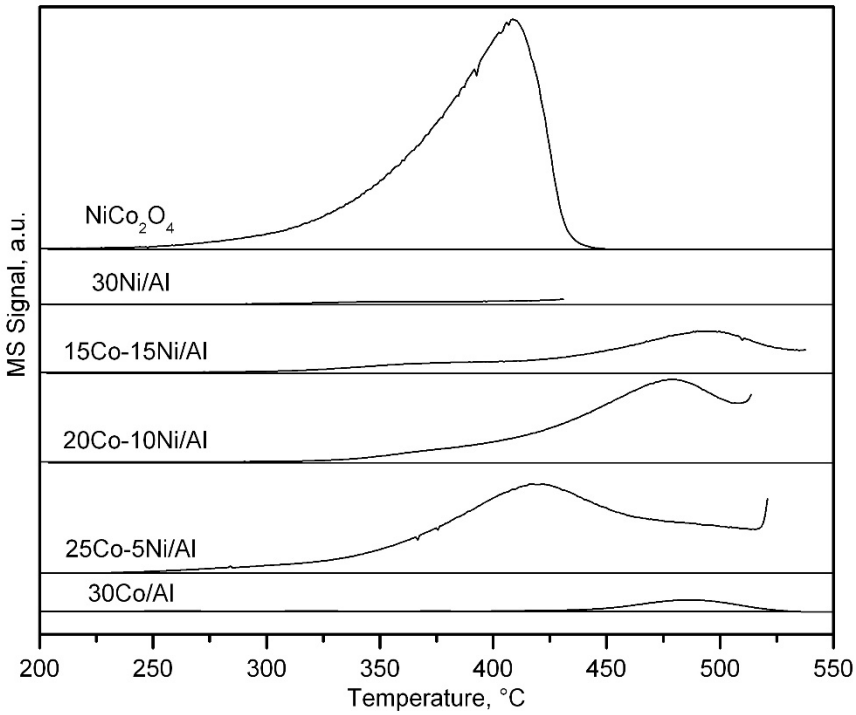

Figure 6.27. CH_4-TPRe profiles of the bimetallic Co-Ni/Al catalysts.

Therefore, when comparing the profiles of the 30Co/Al sample and those of the coprecipitated samples, it was clear that the addition of nickel greatly improved the reactivity of the Co^{3+} cations. This led to not only an increase in the amount of evolved CO_2, and consequently in the amount of highly active oxygen species from 0.33 mmol O_2 g_{Me}^{-1} for the Co/Al sample to 0.83 mmol O_2 g_{Me}^{-1} for the 25Co-5Ni/Al sample (Table 6.8), but also a notable decrease in the temperature needed for the occurrence of the complete oxidation reaction, from around 490 °C for the 30Co/Al sample down to 420 °C for the 25Co-5Ni/Al sample (Figure 6.27).

6.2.2. Catalytic performance of the bimetallic Co-Ni/Al catalysts

The corresponding light-off curves in the 200-600 °C temperature range are shown in Figure 6.28 (GHSV = 30,000 h^{-1}). All studied Co-based catalysts showed a 100% CO_2 selectivity in the whole temperature range. Only over the 30Ni/Al sample, however, notable amounts of carbon monoxide were detected. This resulted in CO_2 selectivity values of only around 90% in the whole 450-600 °C temperature range.

The criteria for intra-particle and extra-particle mass and heat transport, as well as the temperature gradients were checked to be above the limit, as explained in Chapter 2, to ensure that any diffusional effects did not affect the kinetic results. In this sense, Table 6.9 lists the estimated values for the various evaluated criteria.

Both monometallic catalysts (30Co/Al and 30Ni/Al) resulted efficient for deep methane oxidation. The cobalt sample showed a better performance at lower temperatures (below 500 °C). However, above 550 °C, temperature at which the two catalysts attained 50% conversion to CO_2 (Table 6.10), their behaviour was virtually identical with an 82% conversion at 600 °C.

Table 6.9. Criteria for accurate analysis of intrinsic reaction rates (as evaluated for the 25Co-5Ni/Al catalyst at 425 °C).

Criterion number	Recommendation	At 425 °C	Least favourable conditions
1.	Bodenstein parameter $< L_{bed}/d_{particle}$	3.6 < 79.5	49.4 < 79.5[c]
2.	$d_{tube}/d_{particle} > 10$	31.2	31.2
3.	Carberry number $< 0.05/n$	0.002	0.033[b]
4.	$\gamma\beta_e Ca < 0.05$	0.001	0.015[b]
5.	Wheeler-Weisz modulus < 0.15	$2.1 \cdot 10^{-4}$	$4.9 \cdot 10^{-4}$[a]
6.	Mears parameter < 0.1	$6.7 \cdot 10^{-7}$	$1.4 \cdot 10^{-6}$[a]
7.	Radial gradient < 0.05	0.002	0.003[a]
8.	Bed dilution parameter < 0.05	0.047	0.047
9.	Temperature gradient < 0.3	0.15	0.175[b]

[a]Determined at 500 °C; [b]Determined at 600 °C; [c]Determined at 550 °C.

On the other hand, the three bimetallic Co-Ni catalysts evidenced a substantially better performance than their monometallic counterparts in the whole temperature range with

an advance in the combustion temperatures of about 50 °C. It was therefore found that, for a total metal loading of 30%wt., the co-addition of cobalt and nickel was suitable for producing highly active catalysts.

The best results were obtained when the nickel content was limited to 5-10%wt. These two samples, namely 25Co-5Ni/Al and 20Co-10Ni/Al, exhibited very close T_{50} values (495 and 500 °C, respectively). Slight differences in behaviour were noticed as the 25Co-5Ni/Al was more efficient at lower temperatures while the opposite occurred at high temperatures. A higher Ni loading (15%wt.) led to somewhat lower conversion values, with a T_{50} value of 510 °C.

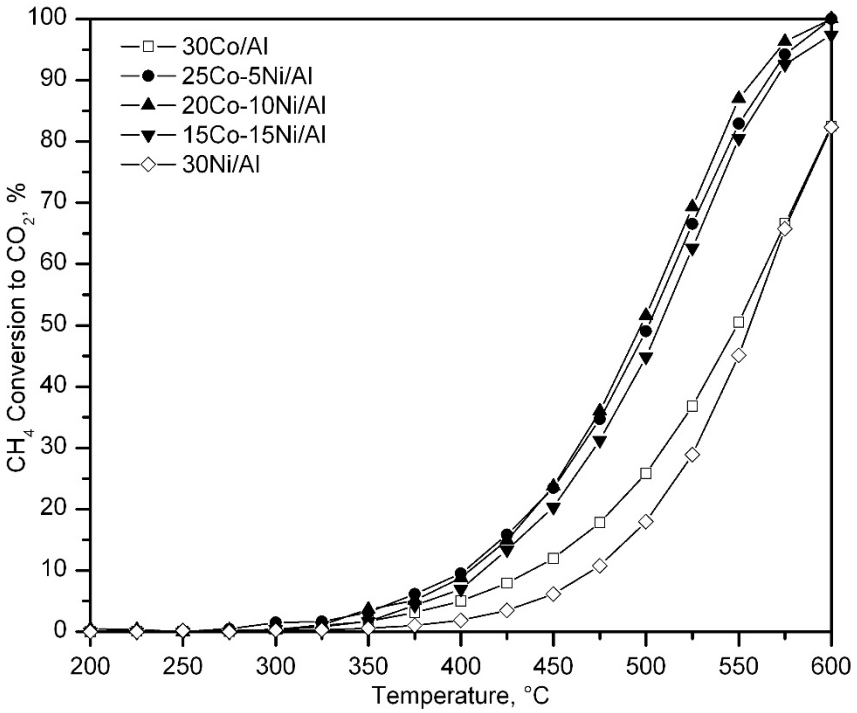

Figure 6.28. Light-off curves of the bimetallic Co-Ni/Al catalysts.

Table 6.10. Kinetic results of the bimetallic Co-Ni/Al catalysts.

Catalyst	T_{50}, °C	Specific reaction rate at 425 °C, mmol CH_4 g_{Me}^{-1} h^{-1}	E_a, kJ mol^{-1}
30Co/Al	550	1.7	82 ± 2
25Co-5Ni/Al	500	3.3	84 ± 2
20Co-10Ni/Al	500	3.1	89 ± 1
15Co-15Ni/Al	510	2.9	91 ± 2
30Ni/Al	555	0.7	128 ± 3

In order to provide further insights on the kinetic behaviour of the investigated catalysts, the reaction rate was estimated using the differential method at 425 °C, where conversion was below 20%. The corresponding results expressed in terms of the total amount of metal are summarised in Table 6.10. Based on the values of the specific reaction rate, the activity decreased in the following order: 25Co-5Ni/Al (3.3 mmol CH_4 g_{Me}^{-1} h^{-1}) › 20Co-10Ni/Al (3.1 mmol CH_4 g_{Me}^{-1} h^{-1}) › 15Co-15Ni/Al (2.9 mmol CH_4 g_{Me}^{-1} h^{-1}) › 30Co/Al (1.7 mmol CH_4 g_{Me}^{-1} h^{-1}) › 30Ni/Al (0.7 mmol CH_4 g_{Me}^{-1} h^{-1}). These values evidenced that the introduction of a relatively low amount of nickel was suitable for the design of improved alumina-supported cobalt catalysts.

The apparent activation energies, estimated by the integral method, of the monometallic catalysts were 82 (30Co/Al) and 128 kJ mol^{-1} (30Ni/Al), thus showing that cobalt oxide is much more active for methane oxidation than nickel oxide. On the other hand, the activation energies of the bimetallic Co-Ni catalysts, increased monotonically with the nickel loading in the 84-91 kJ mol^{-1} range. This was probably related to the increase in the presence of NiO with the nickel loading in these samples. The corresponding Arrhenius plots are shown in Figure 6.29.

The superior activity of the bimetallic catalysts was connected with their better reducibility and higher oxygen mobility. This became clearer when the specific reaction rate was compared with the surface composition (Co^{3+}/Co^{2+} and O_{ads}/O_{latt} molar ratios) determined by XPS and the specific O_2 consumption at low temperatures derived from the CH_4-TPRe runs. As shown in Figure 6.17, a strong correlation was found, thus revealing that the most active catalysts (the bimetallic Co-Ni samples) showed larger O_2 consumption values with respect to the less active monometallic catalysts. Note that these catalysts also exhibited higher H_2 uptakes, as shown in Figure 6.30. Moreover, the influence of the O_{ads}/O_{latt} molar

ratio on the specific activity evidenced that the origin of the active oxygen species was the spinel lattice, and that a higher Co^{3+}/Co^{2+} molar ratio favoured their presence.

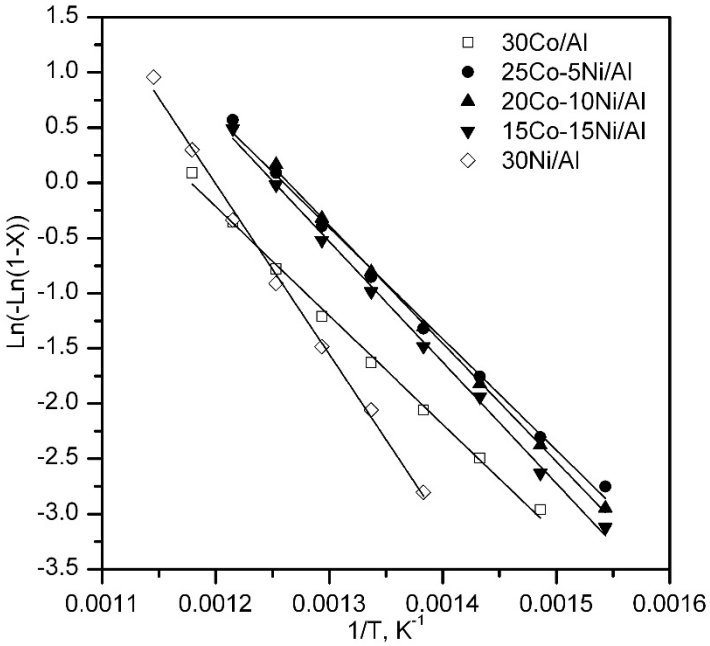

Figure 6.29. Pseudo-first order fit for the experimental data over the bimetallic Co-Ni/Al catalysts.

In this sense, the previously identified optimal catalyst composition (25Co-5Ni/Al) was characterised by the highest values of both O_2 consumption and Co^{3+}/Co^{2+} molar ratio, thereby revealing that its superior reducibility and enhanced oxygen mobility were responsible for its better catalytic behaviour. In addition to the amount of active sites, which was considered to be proportional to measure O_2 uptake, also important was its reactivity at low temperature as expressed as the onset temperature in the CH_4-TPRe run (Figure 6.27). The main reason behind this improved activity seemed to be the insertion of Ni^{2+} ions in the Co_3O_4 lattice and the subsequent formation of a $NiCo_2O_4$-like spinel to some extent combined with a notable presence of Co_3O_4 and a minimal contribution of NiO and metal aluminates. The high efficiency of $NiCo_2O_4$ as an active phase for the oxidation of CO [206], soot [291] and light hydrocarbons [292] has been already reported elsewhere.

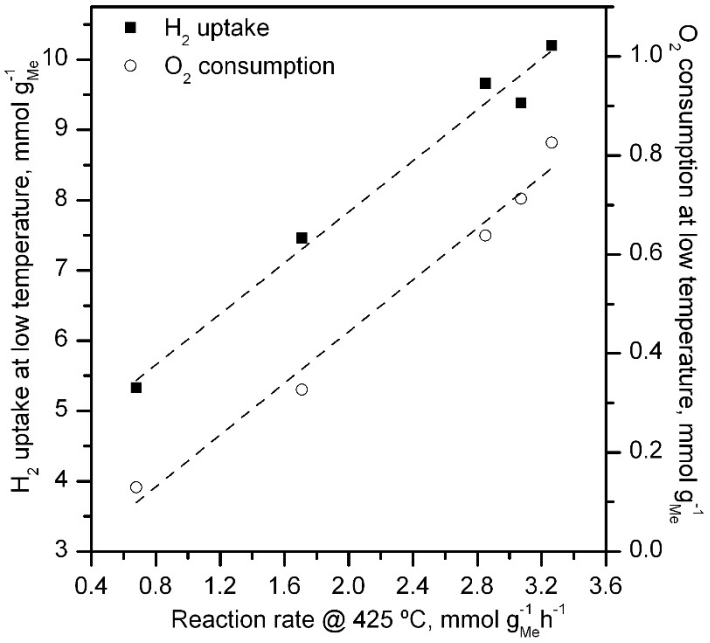

Figure 6.30. Relationship between the specific reaction rate at 425 °C and the H_2 uptake and O_2 consumption derived from the H_2-TPR and CH_4-TPRe analysis of the Co-Ni/Al catalysts.

On the other hand, the apparent activation energies for the 30Co/Al and 25Co-5Ni/Al catalysts were relatively similar (82-84 kJ mol^{-1}) and close to those shown by both bulk Co_3O_4 and $NiCo_2O_4$ (74 and 76 kJ mol^{-1}, respectively). Over the bimetallic samples with a higher Ni content (20Co-10Ni/Al and 15Co-15Ni/Al) the values were significantly higher (89-91 kJ mol^{-1}). This result was coherent with the contribution of less active NiO species, which were more abundant on these catalysts. In fact, the apparent activation energy of the 30Ni/Al sample, with only NiO as active species, was remarkably higher (128 kJ mol^{-1}). To sum up, the kinetic analysis of the behaviour was in agreement with the nature and intrinsic activity of each oxide phase present in the metallic sample, which in turn strongly depended on the catalyst composition.

6.3. DUAL EFFECT OF THE ADDITION OF CERIUM TO ALUMINA

After evaluating the positive effects of adding a surface protector to the alumina and adding a redox promoter to the Co_3O_4, the alternative and logical strategy would be the addition of a surface protector to the alumina that could also activate the reducibility of cobalt oxide, thus making use of the two eventual beneficial effects at the same time. Considering these assumptions, and in view of our previous results on the examination of the most suitable doping metal for Co_3O_4 bulk catalysts (see Chapter 3), the third and last approach will focus on the incorporation of ceria onto the alumina support prior to cobalt deposition. The premise supporting this strategy is that the deposited CeO_2 could have a twofold function as a physical barrier between cobalt and alumina, thus inhibiting the formation of $CoAl_2O_4$, and as a redox promoter for Co_3O_4, thereby enhancing the intrinsic activity of the resulting catalyst.

This feasibility study initially implied the preparation of five CeO_2/Al_2O_3 modified supports by precipitation following the previously optimised methodology. The selected cerium loadings were 5, 10, 15, 20 and 30%wt. These modified supports were denoted as xCe-Al where x stands for the nominal cerium loading. Cobalt catalysts supported on xCe-Al were prepared by following the same synthesis route as for the supports. All catalysts were prepared with a cobalt loading of 30%wt. and denoted as Co/xCe-Al.

6.3.1. Physico-chemical characterisation of the modified xCe-Al supports

The composition and textural and structural properties of the ceria-modified alumina supports were characterised by WDXRF, N_2 physisorption, XRD and Raman spectroscopy. Firstly, it should be pointed out that the chemical analysis revealed that the amount of cerium species deposited on the alumina support was very close to the nominal loading, namely 5, 10, 15, 20 and 30%wt.Ce (Table 6.11).

The specific surface area, total pore volume and pore size distribution maxima are summarised in Table 6.11. The textural properties of the pure oxides (γ-Al_2O_3 and CeO_2) are included for comparative purposes. A roughly linear decrease in surface area was noticed with increasing Ce content. Thus, this loss was around 25% (with respect to the bare alumina) for the sample with 30%wt. Ce (139 vs 105 $m^2\ g^{-1}$). Judging from these results the impact of ceria coating was considered moderate. Accordingly, the pore volume of the samples steadily decreased from 0.56 to 0.32 $cm^3\ g^{-1}$.

Table 6.11. Physico-chemical properties of the modified xCe-Al supports.

Support	Ce loading, %wt.	BET surface, $m^2\ g^{-1}$	Pore volume, $cm^3\ g^{-1}$	Pore size distribution maxima, Å	Crystallite size, nm	Total H_2 uptake, mmol g_{Ce}^{-1}
Al_2O_3	-	139	0.56	110, 150	-	-
5Ce-Al	5.2	128	0.51	110, 150	10	1.9
10Ce-Al	9.8	126	0.51	110, 150	9	2.1
15Ce-Al	15.3	122	0.49	110, 150	10	2.6
20Ce-Al	20.6	117	0.42	110	12	3.3
30Ce-Al	30.3	105	0.32	35, 110	12	3.1
CeO_2	81.4	8	0.03	230	32	1.8

The samples showed type IV isotherms with H2 hysteresis loops, commonly associated with pore blocking over a wide pore size distribution (Figure 6.31). No significant change in the hysteresis loops was apparently detected with the Ce loading. The supports with low Ce loadings (5-15%wt.) displayed a bimodal pore size distribution peaking at around 110 and 150 Å, similar to that exhibited by the bare alumina. This anticipated a fairly good dispersion of the deposited Ce over the surface of the support. For the 20Ce-Al sample, however, the pore size switched to a unimodal distribution centred at 110 Å, probably due to the narrowing of the largest pores (150 Å) caused by an increased cerium deposition. Finally, the 30Ce-Al sample exhibited the same maximum at 110 Å but with a lower pore volume (0.25 $cm^3\ g^{-1}$) compared with the 20Ce-Al sample (0.30 $cm^3\ g^{-1}$). Besides, this sample presented a fraction of small pores with a maximum around 35 Å derived from a marked pore narrowing of the existing 110 Å pores because of the massive cerium incorporation.

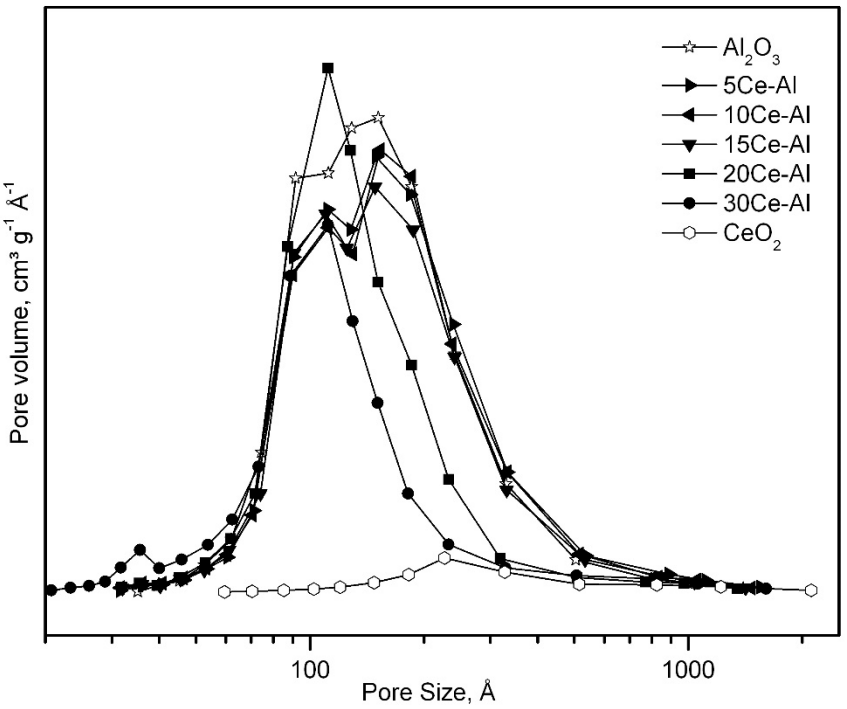

Figure 6.31. Pore size distributions of the xCe-Al supports.

XRD patterns of the xCe-Al supports are shown in Figure 6.32. This graph also includes the diffractograms of the bare alumina and bulk ceria. In all cases the diffraction signals could be indexed as gamma-alumina (2θ = 37.7, 45.8 and 67.3°) and cerium oxide (2θ = 28.5, 33.3, 47.5, 56.4 and 76.7°). Note that no peaks attributable to other possible crystalline phases such as cerium aluminate were noticed.

As an additional evidence of the deposition of ceria on the surface of the alumina support, it was checked that the intensity ratio of the characteristic signals of CeO_2 (2θ = 47.5°) and Al_2O_3 (2θ = 45.8°) increased with cerium loading. Somewhat wide CeO_2 peaks were visible, thereby suggesting that ceria was present in the form of finely divided particles. An attempt was made to estimate the mean crystallite size of ceria from the peak broadening of the most intense reflection ((111) plane) using the Scherrer equation. This size was close to 10 nm for the 5Ce-Al, 10Ce-Al and 15Ce-Al samples and slightly larger (12 nm) for the supports with a higher Ce content (20Ce-Al and 30Ce-Al samples). These values were in

contrast with that found for the as-prepared bulk ceria (32 nm), thus evidencing the achieved high dispersion of ceria.

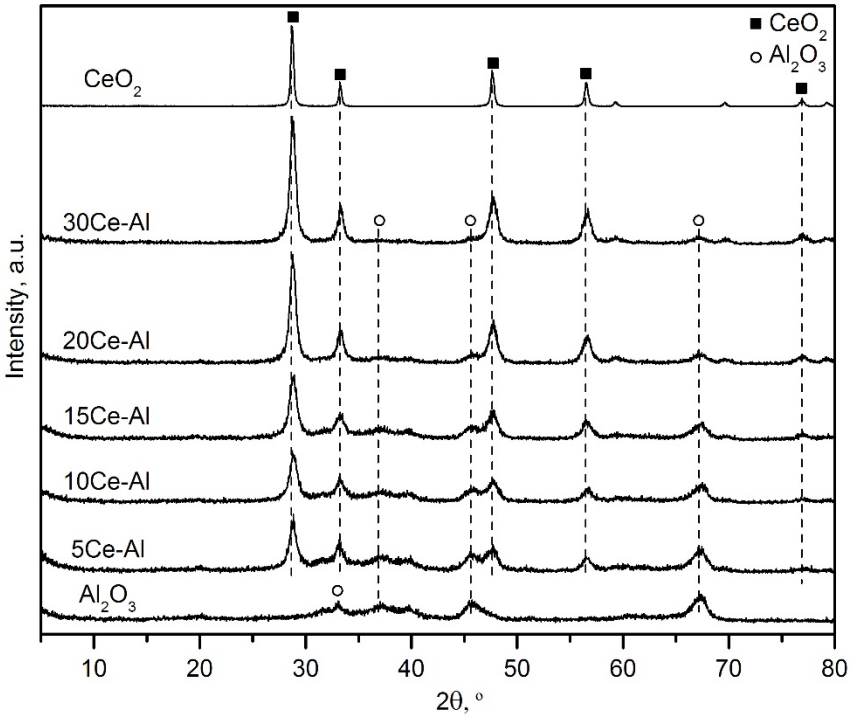

Figure 6.32. Diffraction patterns of the xCe-Al supports.

The presence of segregated ceria was further corroborated by Raman spectroscopy. Thus, all coated alumina supports showed a strong peak assigned to the F_{2g} Raman-active mode characteristic of the fluorite-like lattice of CeO_2 (Figure 6.33). When compared with the Raman spectra of bulk ceria (464 cm^{-1}), the signals were slightly broader and shifted to lower values (462 cm^{-1}) due to the alumina-ceria interaction [293]. Moreover, two additional weak signals at 260 and 595 cm^{-1} were observed. These bands corresponded to nondegenerate longitudinal optical modes of CeO_2, which were linked to with oxygen vacancies from partially reduced CeO_{2-x} species [294].

In view of the higher intensity of these features in the 5Ce-Al and 10Ce-Al supports, the formation of Ce^{3+} species, probably in the form of stable $CeAlO_3$-like species, was favoured with low Ce loadings. As aforementioned these species were not detected by XRD due to its amorphous character and/or its reduced crystallite size.

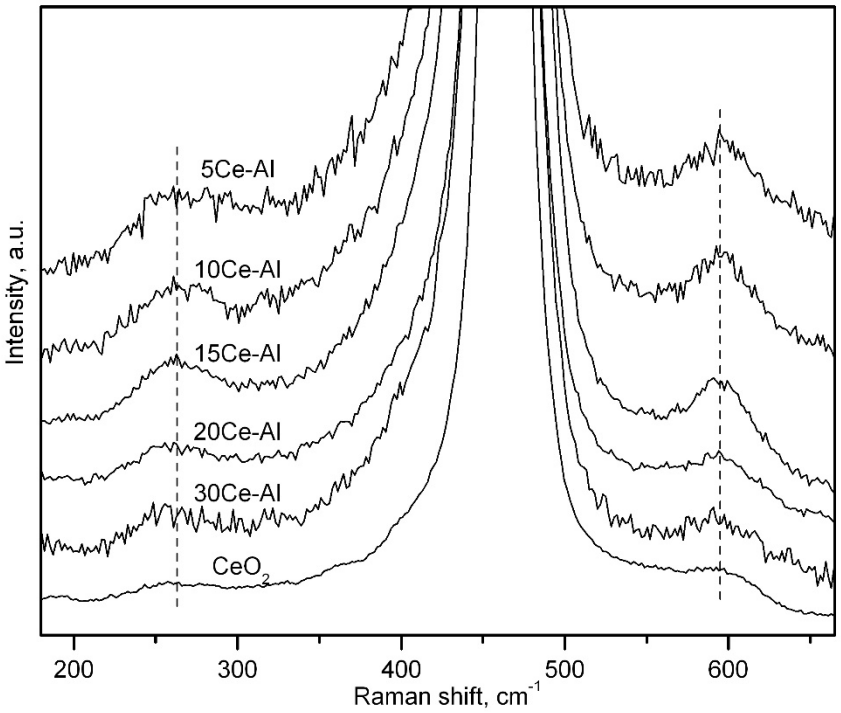

Figure 6.33. Raman spectra of the xCe-Al supports.

It seems clear that this varying abundance of Ce^{3+} and Ce^{4+} as a function of the cerium content should be consistent with the specific hydrogen uptake of the supports estimated by H_2-TPR. In this way, Figure 6.34 includes the reduction profiles of bulk ceria and the various Ce-coated alumina supports. The CeO_2 sample exhibited a weak signal at 450-500 °C that corresponded to the surface reduction of the oxide whereas the intense H_2 uptake peaking at about 800 °C was related to the reduction of the bulk [256].

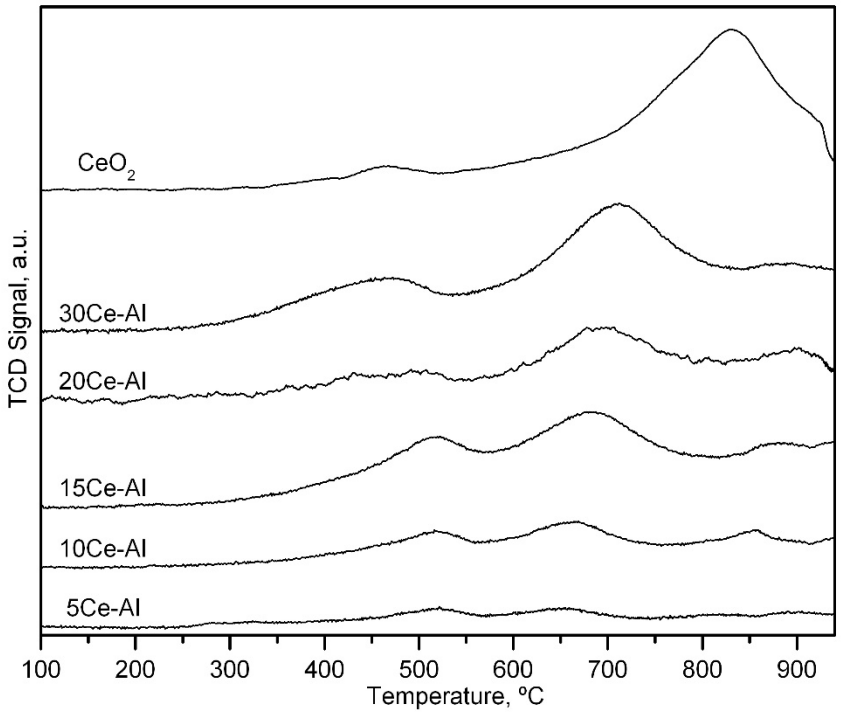

Figure 6.34. H_2-TPR profiles of the xCe-Al supports.

For the xCe-Al supports, these two reduction events were also visible. However, while the surface reduction occurred at 450-500 °C as well, the bulk reduction only required 650-700 °C, probably due to the relatively small crystallite size of deposited ceria (10-12 nm). In addition, a small shoulder above 850 °C related to the formation of $CeAlO_3$ as a result of the interaction of CeO_2 and Al_2O_3 ($2CeO_2 + Al_2O_3 + H_2 \rightarrow 2CeAlO_3 + H_2O$) was noted [295].

The generation of this perovskite phase during the reduction process was further confirmed by subsequent XRD analysis of the samples after the H_2-TPR run. Hence, weak diffraction signals assignable to $CeAlO_3$ were visible on all xCe-Al supports (2θ at 23.6, 33.5, 41.4 and 60.1°, ICDD 00-048-0051) (Figure 6.35). In view of the similar shape of all H_2-TPR traces, it could be assumed the redox characteristics of deposited cerium species, with no marked shift in the reduction temperatures, remained invariant although the degree of reduction substantially varied as a function of the cerium loading.

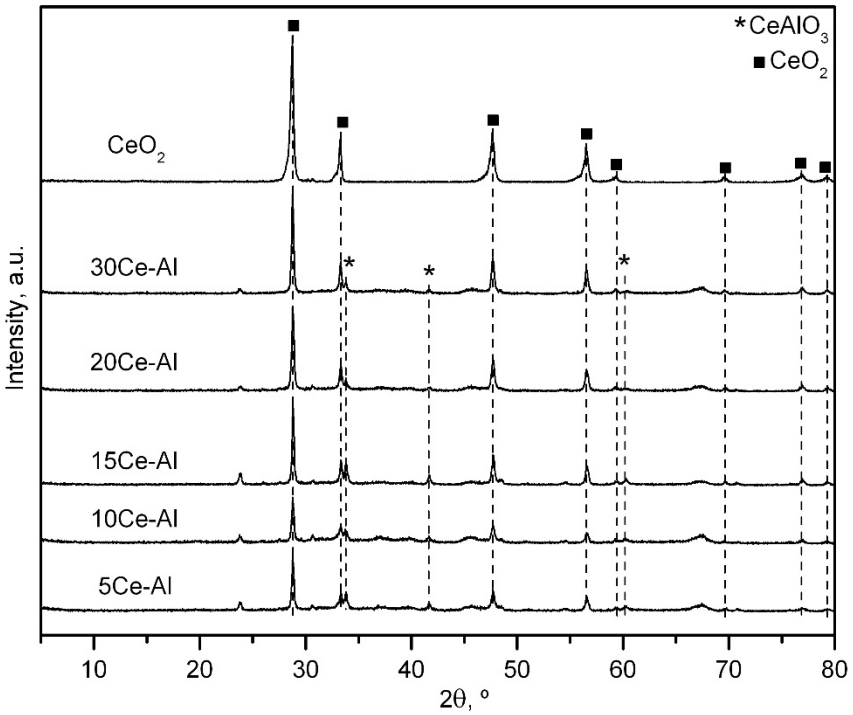

Figure 6.35. Diffraction patterns of the xCe-Al supports after the H_2-TPR analysis.

The overall H_2 consumption of the samples expectedly increased with the cerium content, from 0.09 mmol H_2 g^{-1} over the 5Ce-Al sample to 0.94 mmol H_2 g^{-1} over the 30Ce-Al sample (Table 6.9). However, more notable differences in reducibility were noticed when the specific uptake was examined. Hence, this intrinsic consumption largely depended on the Ce content of the support (Figure 6.36). It progressively increased from 1.9 mmol H_2 g_{Ce}^{-1} (5Ce-Al) to 3.2-3.5 mmol H_2 g_{Ce}^{-1} over the 20Ce-Al and 30Ce-Al samples.

The low H_2 consumption observed for the 5Ce-Al and 10Ce-Al supports was coherent with a favoured presence of Ce^{3+} species on these samples, in the form of CeO_{2-x} species with a strong interaction with the alumina, as evidenced by Raman spectroscopy. For higher Ce concentrations, the predominant cerium species was segregated CeO_2.

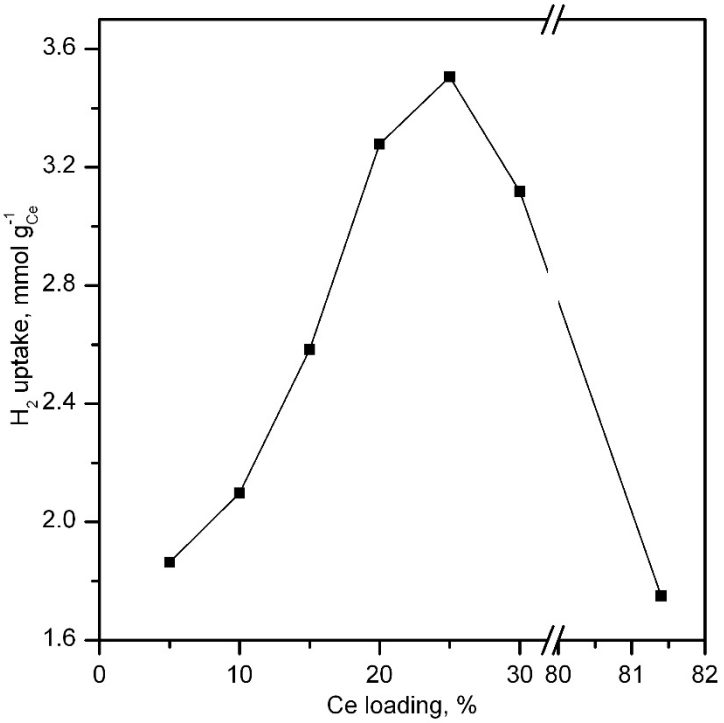

Figure 6.36. Relationship of the specific H_2 uptake with the Ce loading of the xCe-Al supports.

6.3.2. Physico-chemical characterisation of the supported Co/xCe-Al catalysts

The addition of cobalt oxide (in the 27.2-29.5%wt. range as determined by WDXRF) to the ceria-modified alumina supports (the actual Ce loading of the catalysts were in the 3.1-18.2%wt. range as determined by WDXRF as well) resulted in a notable, almost linear loss of surface area of the resulting catalysts (73-102 $m^2 g^{-1}$) (Table 6.12). With respect to the corresponding support (105-139 $m^2 g^{-1}$), this accounted for a decline by 20-30%. This negative effect on surface area was comparable to that noticed for the Co/Al catalyst (22%). As for the pore volume, the Co/30Ce-Al sample presented the lowest value (0.25 $cm^3 g^{-1}$) while no significant differences were found among the other samples (0.30-0.32 $cm^3 g^{-1}$).

Table 6.12. Physico-chemical properties of the Co/xCe-Al catalysts.

Catalyst	Ce loading, %wt.	Co loading, %wt.	BET surface, $m^2 g^{-1}$	Pore volume, $cm^3 g^{-1}$	Pore size distribution maxima, Å	Co spinel crystallite size, nm
Co/Al	-	27.9	108	0.29	90	29
Co/5Ce-Al	3.1	28.8	102	0.32	110	24 (8)
Co/10Ce-Al	5.9	28.9	96	0.30	110	24 (9)
Co/15Ce-Al	9.2	28.0	90	0.32	110	23 (10)
Co/20Ce-Al	12.4	29.5	93	0.30	90	23 (11)
Co/30Ce-Al	18.2	27.2	73	0.25	35, 110	31 (14)
Co/Ce	48.8	28.9	18	0.07	225	44 (33)

Values in brackets correspond to the CeO_2 crystallite size.

Figure 6.37 shows the diffractograms of the Co/xCe-Al catalysts. For comparative purposes, the patterns of the Co/Al and Co/Ce samples were included as well. Along with the presence of the characteristic features of the ceria phase (2θ = 28.5, 33.3, 47.5, 56.4 and 76.7°), a set of signals at 2θ = 31.3, 37.0, 45.1, 59.4 and 65.3° were clearly distinguished. These were related to a spinel-like cobalt phase, namely Co_3O_4 and/or $CoAl_2O_4$.

Obviously, the formation of $CoAl_2O_4$ was only ruled out in the case of the Co/Ce sample. After the addition of cobalt the crystallite size of CeO_2, which was in 9-14 nm range, was not appreciably modified when compared with the corresponding xCe/Al support (10-12 nm). As for the size of the spinel-like cobalt phase estimated from the peak broadening of the signal at 37.1°, it remained almost constant (23-24 nm) irrespective of the composition of the support. Only for the Co/30Ce-Al catalyst the size was slightly larger (31 nm).

The Raman spectra of the cobalt catalysts supported on pure alumina (Co/Al), pure ceria (Co/Ce) and ceria/alumina (Co/xCe-Al) are included in Figure 6.38. Apart from a relatively weak band at 462 cm^{-1} (F_{2g} mode of CeO_2), all supported catalysts displayed the five Raman actives modes associated with Co_3O_4 [130,296].

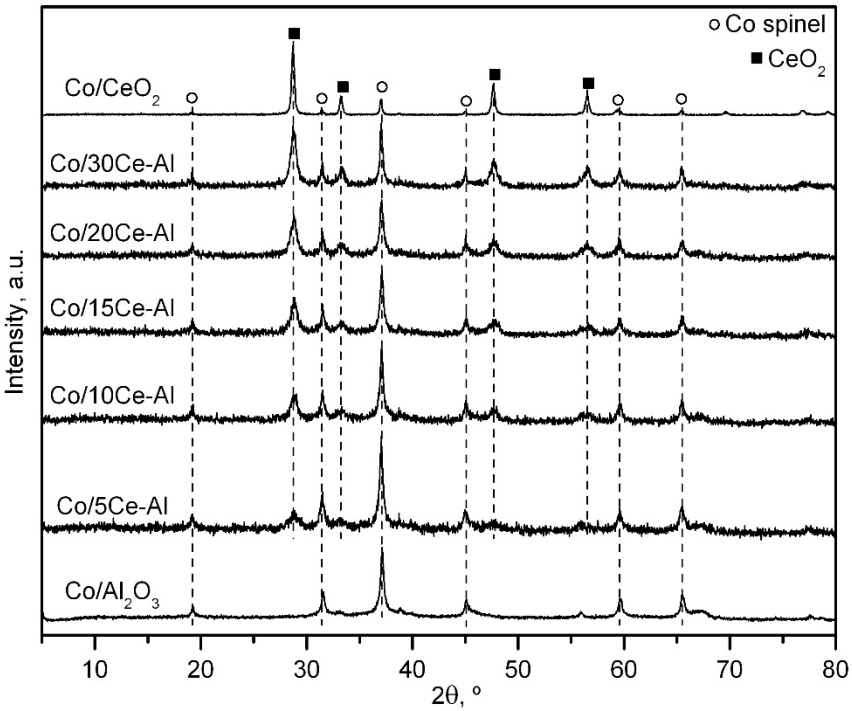

Figure 6.37. Diffraction patterns of the Co/xCe-Al catalysts.

Except from the Co/Ce catalyst, the two shoulders at 705 and 725 cm^{-1} attached to the A_{1g} vibration suggesting the presence of cobalt aluminate were visible. It was found out that the intensity of these features was more notable over the Co/Al and Co/5Ce-Al samples, and tended to decrease when ceria was deposited with a higher loading (›10%wt. Ce, more significantly for 30%wt.Ce). Although the formation of this undesired cobalt phase was not completely inhibited, it seemed that incorporated ceria acted as an efficient physical barrier to prevent the reaction between Co_3O_4 and Al_2O_3 to some extent. From a catalytic point of view, the ceria coating of the alumina support would favour an increase in the amount of highly active Co_3O_4 at the cost of $CoAl_2O_4$.

A closer inspection of the dependence of the A_{1g} mode with the Ce content of the catalysts could be helpful in determining a possible distortion of the Co_3O_4 lattice due to the partial insertion of cerium cations. This effect was analysed in terms of the shift and the full width at half maximum (FWHM) of this signal (Figure 6.39). On one hand, it was observed that the location of the band varied from 689 cm^{-1} in the Co/Al and bulk Co_3O_4 samples to 681 cm^{-1}

in the Co/Ce sample, thus pointing out that the lattice of Co_3O_4 was much more affected by the presence of CeO_2.

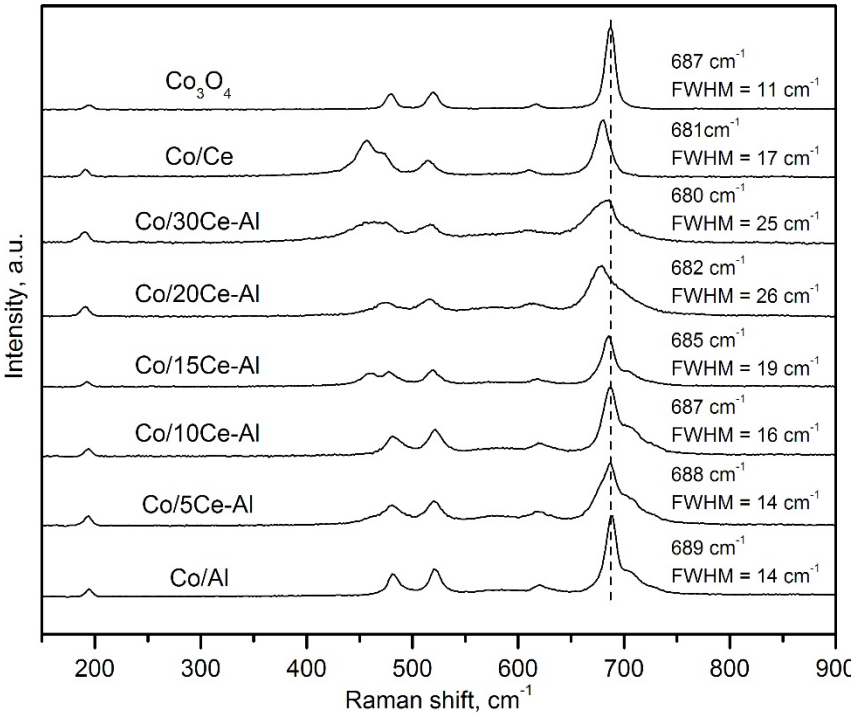

Figure 6.38. Raman spectra of the Co/xCe-Al catalysts.

As the Ce/Co molar ratio of the Co/xCe-Al catalysts increased the band progressively shifted to lower values, from 689 cm^{-1} for Co/Al to 688-685 cm^{-1} for Co/5Ce-Al, Co/10Ce-Al and Co/15Ce-Al, and to 682-680 cm^{-1} for Co/20Ce-Al, Co/30Ce-Al and Co/Ce. It should be noticed that the other Raman active modes (F_{2g} and E_g) shifted as well. This redshift of the Co_3O_4 signals could be attributed to the distortion of the spinel lattice, probably due to insertion of Ce ions [297]. Consistently, the FWHM values of this band were higher for the Ce-rich cobalt catalysts (25-26 cm^{-1} compared with 14-19 cm^{-1} for Co/5Ce-Al, Co/10Ce-Al and Co/15Ce-Al).

The structural change of the Co_3O_4 lattice was further confirmed by the estimation of the cell parameter of the Co spinel from XRD patterns. As aforementioned, the detected diffraction signals could be assigned to both Co_3O_4 and $CoAl_2O_4$. Consequently, the position shifts that denote the change in the cell size could be initially attributed to distortion of

both phases. However, since only the Raman vibration modes of Co_3O_4 phase (and not those of $CoAl_2O_4$ phase) evidenced changes with the addition of Ce, the shift of the diffraction signals was assumed to occur only as a consequence to the distortion of the cobalt oxide phase.

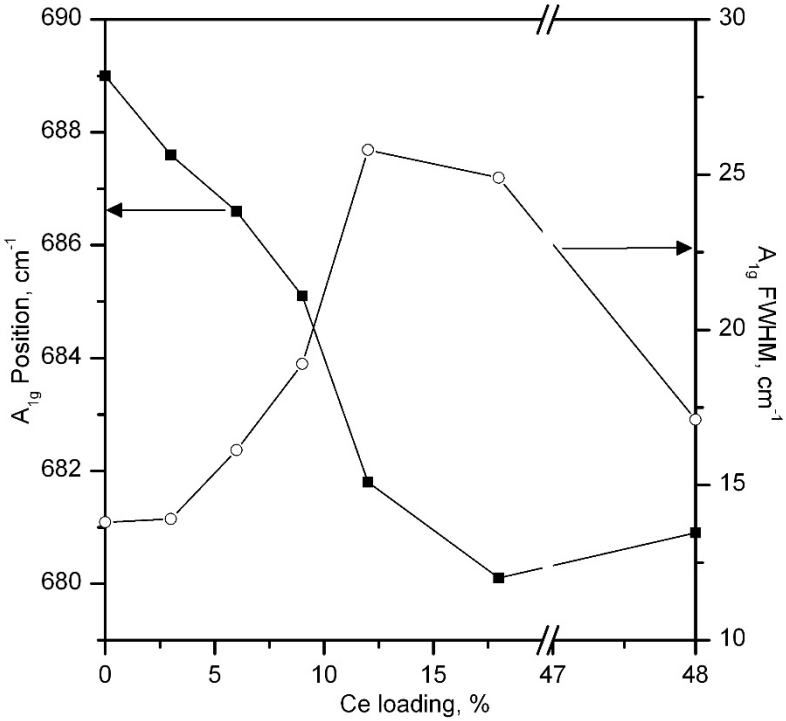

Figure 6.39. Relationship of the position and FWHM of the A_{1g} mode with the Ce loading of the Co/xCe-Al catalysts.

Thus, the cell size of Co_3O_4 in the Co/xCe-Al catalysts was found to be larger than that of the catalyst supported over bare alumina (8.096 Å), as shown in Figure 6.40. More importantly, for the Co/20Ce-Al and Co/30Ce-Al samples, the cell size displayed a maximum value (8.112 Å), which evidenced the largest lattice distortion, in accord with the results obtained from Raman spectroscopy. Note that this eventual insertion of Ce^{4+} ions into the spinel lattice would be accompanied by an increase in the amount of Co^{3+} so as to maintain the charge balance [298].

HAADF-STEM images along with the corresponding EDX maps of the Co/xCe-Al catalysts are shown in Figure 6.41. This analysis evidenced that cobalt species were indeed located

on the surface of the ceria-modified alumina with a low presence of segregated entities. In addition, it was noteworthy that some regions of the support were not massively covered by cobalt. The spinel active phase was present as crystallites with average sizes around 20-25 nm, which was in good agreement with XRD results (Table 6.12), that tended to aggregate into larger patches of 100-150 nm.

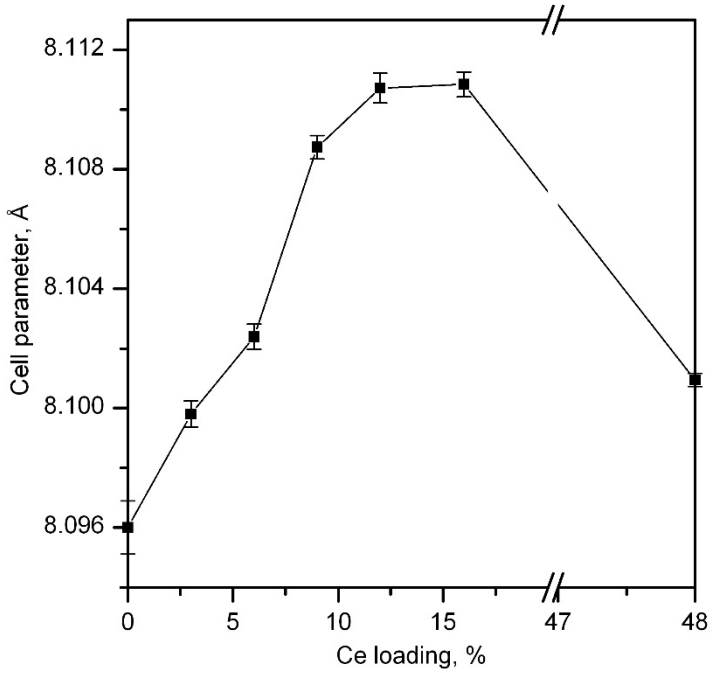

Figure 6.40. Evolution of cell size of Co_3O_4 with the Ce loading of the Co/xCe-Al catalysts.

Only for the Co/30Ce-Al sample, segregated Co_3O_4 crystallites with sizes up to 50-60 nm were marginally observed. As for the cerium, it was homogeneously distributed on the support in the form of quite small crystallites (smaller than 5 nm). Additionally, CeO_2 clusters of about 10 nm were also detected, in line with XRD results (Table 6.12). For the Co/30Ce-Al sample, the size of the clusters increased up to 20 nm, as also evidenced by XRD analysis.

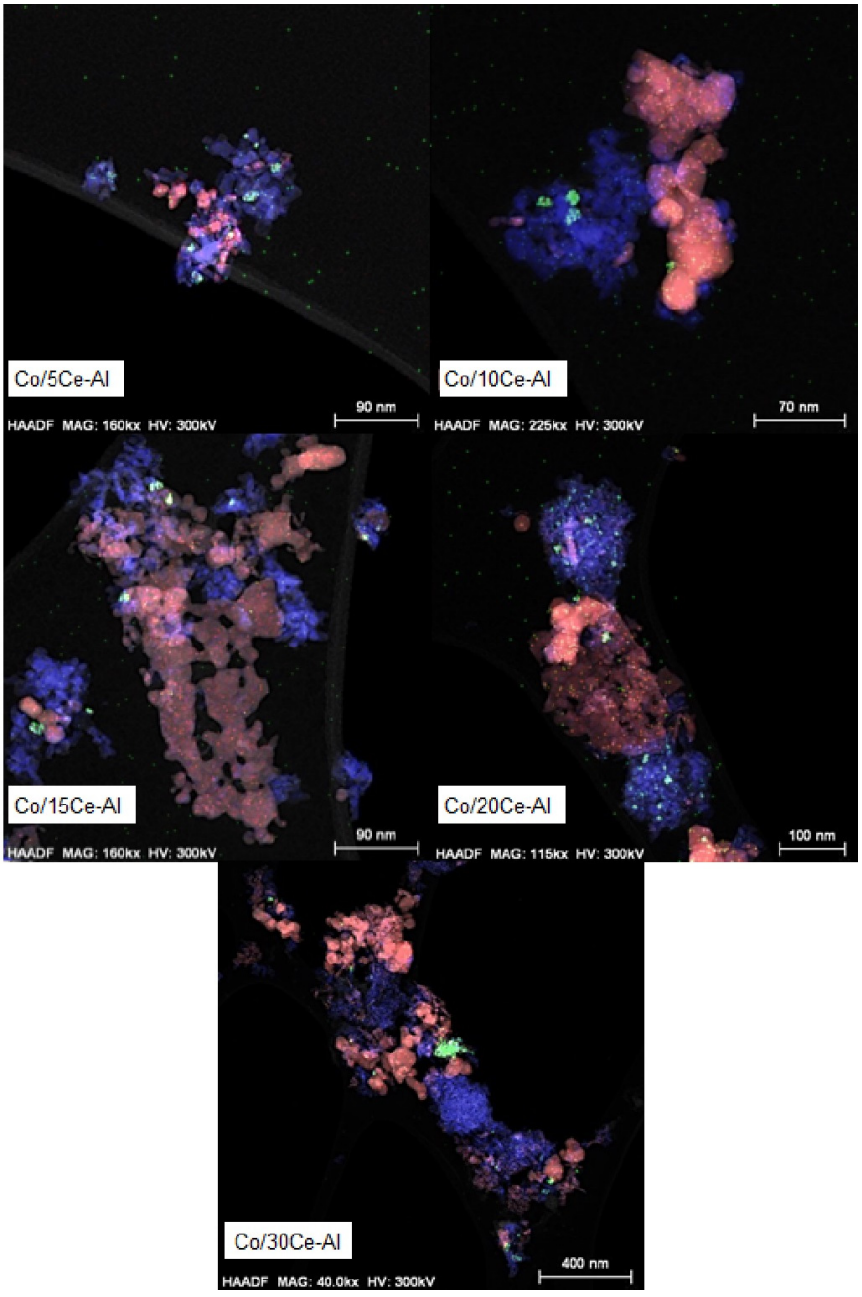

Figure 6.41. HAADF-STEM images of the Co/xCe-Al catalysts coupled with EDX elemental distribution of Co (red), Ce (green) and Al (blue).

Finally, Figure 6.42 shows some selected HRTEM images, where the lattice fringes of Co_3O_4 and CeO_2 could be resolved, along with their corresponding Fast Fourier Transform (FFT) spot patterns. For the cobalt spinel, two lattice spaces, namely 0.29 and 0.24 nm, were identified, which corresponded to the {220} and the {311} planes, respectively. On the other hand, for the ceria two lattice spaces of 0.31 and 0.27 nm were observed, which corresponded to the {111} and {200} planes, respectively.

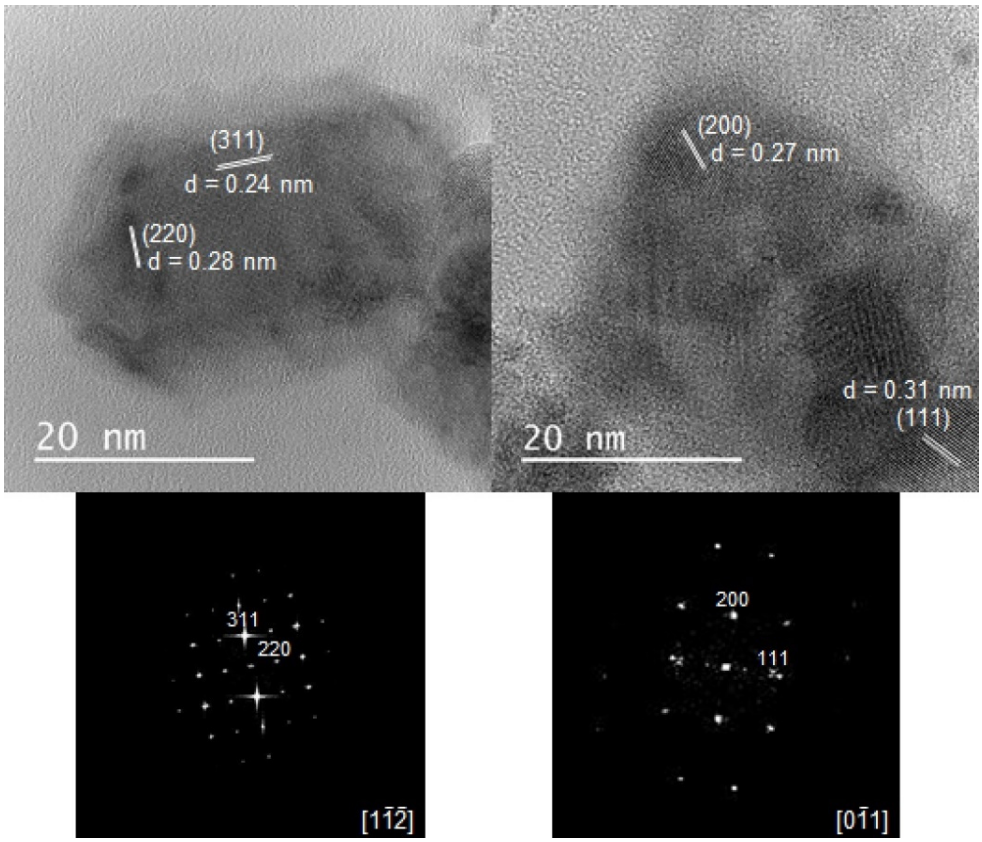

Figure 6.42. HRTEM images and FFT spot patterns of the Co_3O_4 (left) and CeO_2 (right) phases.

The surface structure and composition was investigated by XPS. The distribution of cobalt and oxygen species was determined from the Co2p and O1s spectra of the samples, respectively (Figure 6.43). In particular, the Co $2p_{3/2}$ signal could be deconvoluted in five different contributions, following the formerly described scheme [217]. On the other hand, the O 1s spectra showed three different signals located at 529.8, 530.8 and 532.4 eV, respectively. The first signal was assigned to oxygen species from the spinel lattice (O_{latt}), the second one was related to weakly adsorbed oxygen species on the surface (O_{ads}) and the last feature was attributed to the presence of hydroxyl groups from adsorbed water [190].

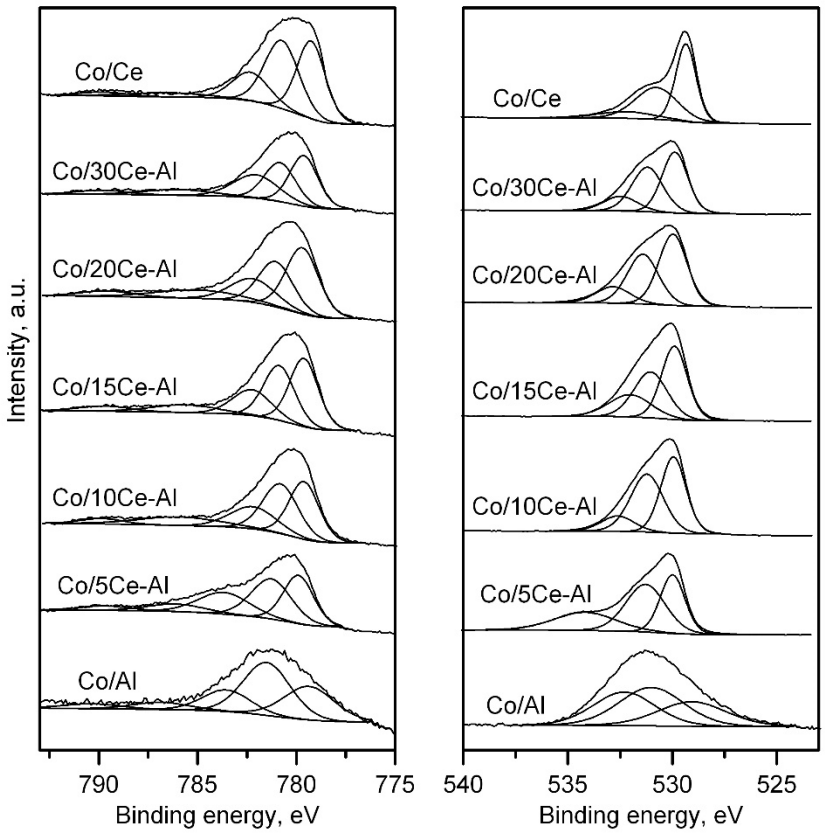

Figure 6.43. XPS Co2p (left) and O1s (right) profiles of the Co/xCe-Al catalysts.

Table 6.13 includes the surface molar composition of the investigated catalysts. The bulk composition as determined by WDXRF is also included for comparative purposes. The Co/Al sample showed a surface Co^{3+}/Co^{2+} molar ratio of 0.67, which was noticeably lower compared with that of the Co/Ce catalyst (0.95). Taking the latter value as representative of the supported Co_3O_4 oxide phase, the low value of the alumina-supported catalyst was in agreement with the significant presence of $CoAl_2O_4$, where cobalt cations are in the +2 oxidation state, as suggested by Raman spectroscopy.

Since the formation of cobalt aluminate involves a gradual diffusion of Co cations into the alumina structure, this necessarily resulted in a lower presence of cobalt on the surface, with a Co/Al molar ratio of 0.32. Furthermore, the relative abundance of surface cobalt increased for the Ce-containing samples as revealed by their higher Co/(Ce+Al) molar ratios (up to 0.84 for the Co/20Ce-Al sample). This finding was coherent with a less favoured formation of cobalt aluminate due to the barrier effect of ceria, in line with the results derived from Raman spectroscopy.

On the other hand, the Co^{3+}/Co^{2+} molar ratio of the Co/xCe-Al catalysts, except for the Co/5Ce-Al sample), was higher (0.99-1.38) than that of the Co/Ce catalyst. This fact revealed that some cerium cations were likely incorporated into the Co_3O_4 lattice, as previously suggested by XRD. This partial insertion necessarily implied an increase in the abundance of Co^{3+} cations at the cost of Co^{2+} cations to maintain the charge balance. This higher abundance of Co^{3+} species on the surface of the samples with increasing Ce loading was accompanied by a concomitant more notable presence of lattice oxygen species in the Co/xCe-Al catalysts (Table 6.13). This type of oxygen species is usually involved in the oxidation of methane by a Mars–van Krevelen mechanism. As shown in Figure 6.44, the relative presence of both species increased with cerium loading and was optimised for the Co/20Ce-Al catalyst.

Table 6.13. Surface composition of the Co/xCe-Al catalysts as determined by XPS.

Catalyst	Co, %wt.	Ce, %wt.	Al, %wt.	Co/(Ce+Al) molar ratio	Co^{3+}/Co^{2+} molar ratio	O_{ads}/O_{latt} molar ratio
Co/Al	22.6 (27.9)	0 (0)	32.1 (37.0)	0.32	0.67	1.41
Co/5Ce-Al	26.7 (28.8)	1.3 (3.1)	23.6 (32.1)	0.51	0.91	1.30
Co/10Ce-Al	30.4 (28.9)	2.4 (5.9)	20.1 (30.0)	0.68	0.99	0.98
Co/15Ce-Al	30.1 (28.0)	3.0 (9.2)	19.4 (29.1)	0.69	1.15	0.82
Co/20Ce-Al	32.9 (29.5)	3.8 (12.4)	17.2 (26.1)	0.84	1.38	0.77
Co/30Ce-Al	29.7 (27.2)	5.3 (18.2)	18.4 (20.1)	0.70	1.17	0.88
Co/Ce	35.6 (28.9)	26.8 (48.8)	0 (0)	3.26	0.95	1.07

The values in brackets correspond to the bulk composition as determined by WDXRF.

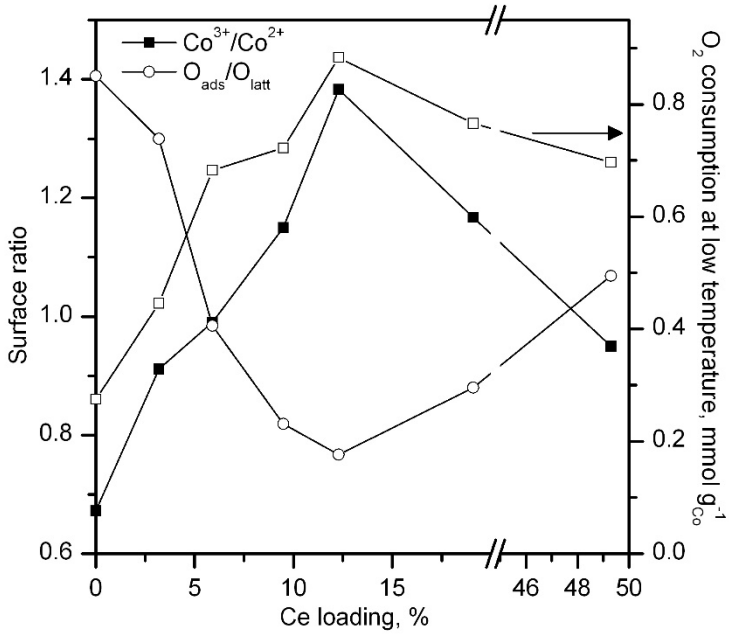

Figure 6.44. Evolution of the surface molar composition (XPS) and O_2 consumption (CH_4-TPRe) with the Ce loading of the Co/xCe-Al catalysts.

The nature of deposited cobalt species and their interaction with underlying ceria-coated alumina was examined by H_2-TPR analysis (Table 6.14). Both Co/Al and Co/Ce catalysts displayed a notable H_2 uptake between 200-600 °C that was related to the reduction of precipitated Co_3O_4, as explained in Chapter 5. Except for a small band observed at 800 °C (this peak corresponded to the reduction of ceria support), the Co/Ce catalyst did not consume hydrogen between 600-800 °C. A quantitative analysis of the amount of consumed H_2 revealed that the overall uptake (7.6 mmol H_2 g^{-1}) reasonably matched with that theoretically expected for the total reduction of Co_3O_4 (22.6 mmol H_2 g_{Co}^{-1}) along with the reduction of ceria (1.8 mmol H_2 g_{Ce}^{-1}).

In the case of Co/Al, an additional peak between 550-750 °C was clearly ascertained. This was assigned to the presence of significant quantities of $CoAl_2O_4$ as also evidenced by Raman spectroscopy. In fact, the total measured amount of H_2 (5.6 mmol H_2 g^{-1}) was rather far from the stoichiometric uptake (6.8 mmol H_2 g^{-1}) when assuming that the cobalt phase was exclusively Co_3O_4.

Table 6.14. Results from the H_2-TPR and CH_4-TPRe analysis of the Co/xCe-Al catalysts.

Catalyst	H_2-TPR			CH_4-TPRe
	H_2 uptake related to Co_3O_4, mmol g^{-1}	H_2 uptake related to $CoAl_2O_4$, mmol g^{-1}	H_2 uptake related to CeO_2, mmol g^{-1}	Low temperature-O_2 consumption, mmol g_{Co}^{-1}
Co/Al	2.7	2.8	-	0.28
Co/5Ce-Al	2.01	3.8	0.1	0.45
Co/10Ce-Al	2.8	3.1	0.2	0.68
Co/15Ce-Al	3.0	2.8	0.4	0.72
Co/20Ce-Al	3.3	2.5	0.7	0.88
Co/30Ce-Al	3.7	1.7	0.9	0.77
Co/Ce	6.8	-	0.8	0.70

The H_2-TPR profiles of the cobalt catalysts supported on ceria-alumina also consisted of two H_2 uptakes at 200-550 °C (reduction of free Co_3O_4) and 550-800 °C (reduction of $CoAl_2O_4$), in a similar fashion to the sample supported on bare alumina (Figure 6.45). It was reasonably inferred that the eventual H_2 consumption related to the reduction of the cerium species deposited on alumina occurred in the high-temperature window.

The total H_2 consumption of the samples is given in Table 6.14. In all cases the H_2 uptake was larger than that shown by the Co/Al sample. A significant increase by 5-16% was found with the amount of cerium in the support. Above 15%wt. Ce the consumption was reasonably similar (6.5-6.7 mmol H_2 g^{-1}). While no significant changes in the reduction onset temperature (about 250 °C) were observed, the relative contribution of these reduction events seemed to be shifted in favour of the low-temperature band with the Ce loading.

Based on the assumption that the amount of H_2 required for ceria reduction was constant for a given Co/xCe-Al catalysts and its corresponding xCe-Al support, an estimation of the uptake related to each reducible species (Co_3O_4, $CoAl_2O_4$ and CeO_2) could be made for each sample (Table 6.14). This revealed a progressive increase in the abundance of free Co_3O_4 accompanied by a concomitant reduced presence of cobalt aluminate. In this sense, the relative abundance of cobalt as $CoAl_2O_4$ decreased from 58% for the Co/Al catalyst to 51%

for the Co/20Ce-Al and Co/30Ce-Al catalysts. In contrast, no noticeable effect was observed for the samples with a lower Ce loading.

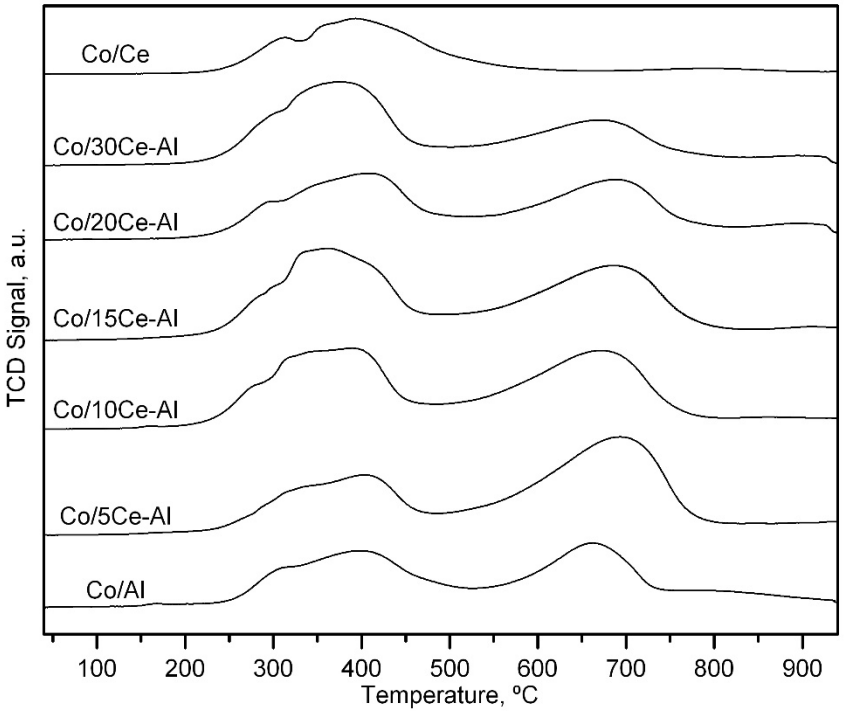

Figure 6.45. H_2-TPR profiles of the Co/xCe-Al catalysts.

This finding was coherent with the results given by Raman spectroscopy that pointed out that the interaction between Co_3O_4 and Al_2O_3 to give $CoAl_2O_4$ was somewhat inhibited by cerium deposition. The insertion of a fraction of cerium atoms into the lattice of Co_3O_4, which was also suggested by Raman spectroscopy and further confirmed by XRD and XPS analysis, could also explain the observed increase in the H_2 uptake at low temperatures.

In sum, the ceria deposited on alumina could play a dual synergetic role by inhibiting the formation of $CoAl_2O_4$ and/or distorting the Co_3O_4 crystalline lattice. Both effects eventually may lead to a larger abundance of highly active oxygen, in the form of lattice oxygen species as evidenced by XPS analysis, over the Co/xCe-Al catalysts in comparison with the Co/Al counterpart.

More useful insights on the influence of the catalyst composition on the reactivity of available oxygen species for methane oxidation were obtained by CH_4-TPRe analysis coupled to mass spectrometry. The evolution of CO_2 (m/z = 44) and CO (m/z = 28) was monitored (Figure 6.46). CO_2 formation occurred at two clearly distinct temperature windows, namely 425-500 °C (only CO_2 was detected) and above 580 °C (both CO and CO_2 were detected accompanied by H_2 as well, not shown in Figure 6.46).

In the low temperature range (Figure 6.47) both Co/Al and Co/Ce catalysts led to the generation of CO_2 at about 485 °C, which was attributed to the oxidation of methane by oxygen species associated with Co^{3+} ions. Table 6.14 includes the O_2 consumption corresponding to this generation of CO_2 for all examined catalysts. Note that the lowest value (0.28 mmol O_2 g_{Co}^{-1}) corresponded to the Co/Al sample in agreement with the marked presence of $CoAl_2O_4$.

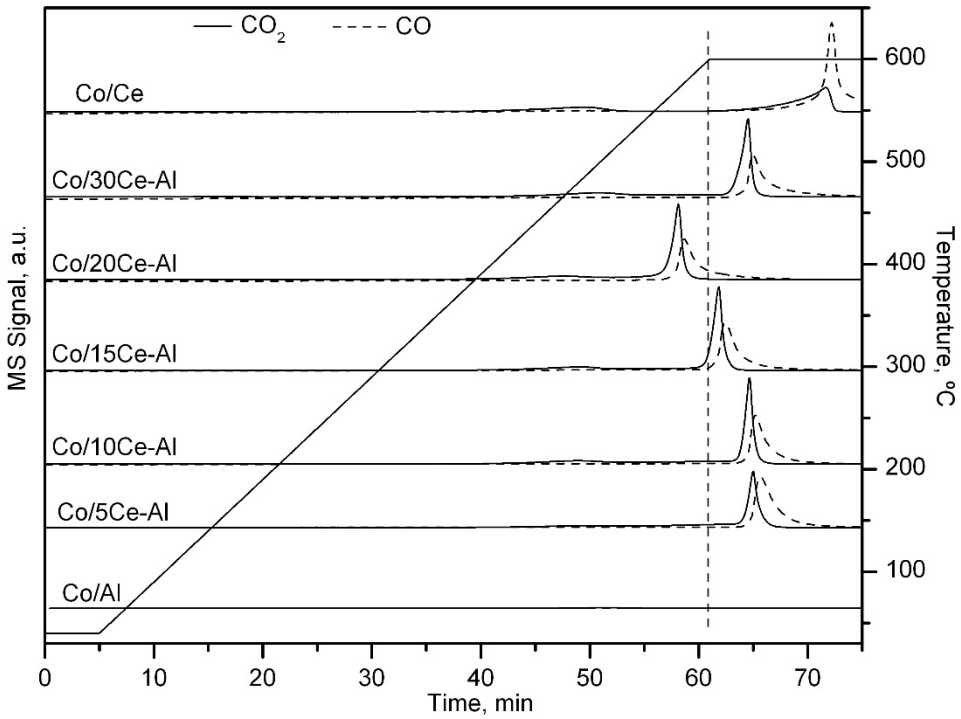

Figure 6.46. CH_4-TPRe profiles of the Co/xCe-Al catalysts.

When -cerium was added to the alumina support, the CO_2 formation was more evident ant took place at significantly lower temperatures. Figure 6.44 revealed that the extent of CH_4 oxidation was noticeably favoured with the presence of lattice oxygen species. On the other hand, the reduction process interestingly occurred at 465 °C over the Co/20Ce-Al sample, and this catalyst consumed the largest amount of oxygen (0.88 mmol O_2 g_{Co}^{-1}). Moreover, the temperature of the onset of reduction (marked by arrows in Figure 6.47) was significantly lower for the Co/20Ce-Al and Co/30Ce-Al samples (around 350 °C) in comparison with the rest of the samples (around 400 °C).

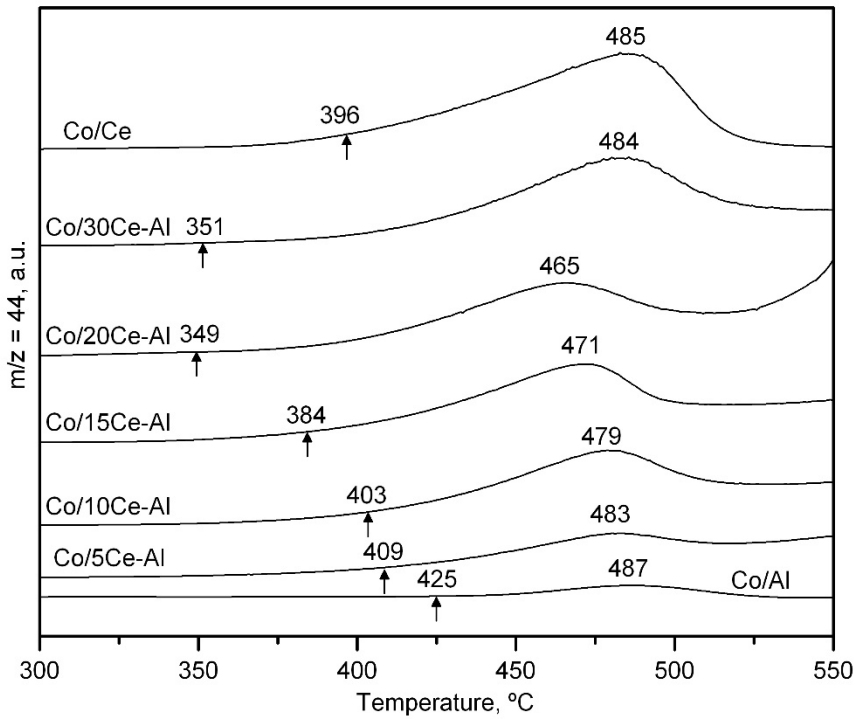

Figure 6.47. Close-up view of the CH_4-TPRe profiles in the 300-550 °C temperature range of the Co/xCe-Al catalysts.

As stated above, the generation of CO_2 was also visible at higher temperatures owing to the oxidation of methane by oxygen species associated with Co^{2+} ions [133]. This mass signal was detected at 600 °C during the isothermal period. Exceptionally, CO_2 was detected at 580 °C over the Co/20Ce-Al catalyst, thereby suggesting a higher mobility of the oxygen species in this sample. In all cases, the high-temperature oxidation was accompanied by

the generation of CO and H_2 to some extent that could be due to partial oxidation or cracking of methane in the presence of metallic or oxygen-deficient cobalt species [213]. In fact, the diffraction pattern of the Co/xCe-Al samples after the CH_4-TPRe run (Figure 6.48) evidenced the formation of graphitic carbon (signal at 2θ = 26.6°) due to the occurrence of these two reactions [280].

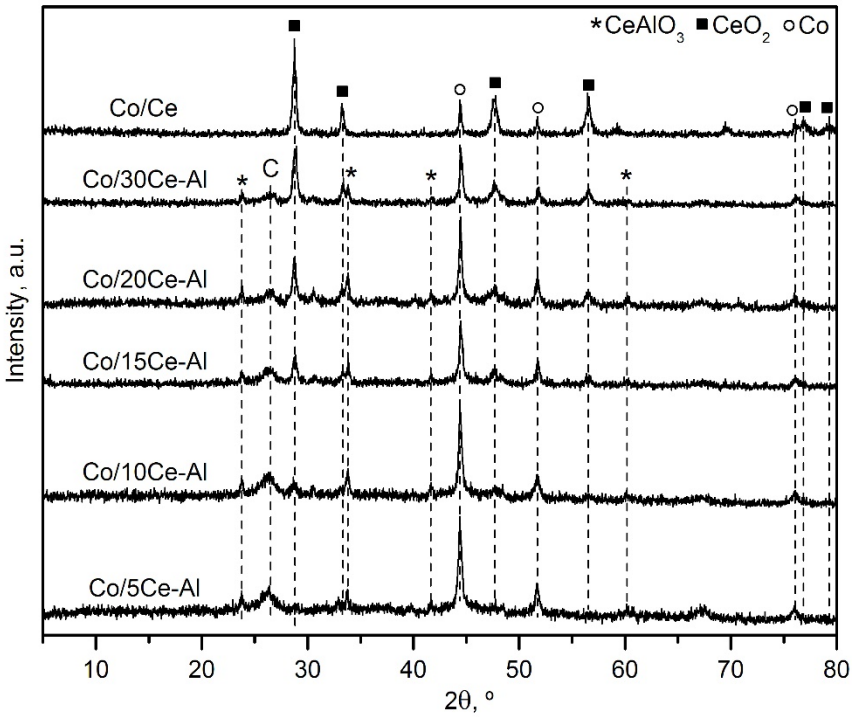

Figure 6.48. XRD patterns of the Co/xCe-Al catalysts after the CH_4-TPRe runs.

6.3.3. Catalytic performance of the supported Co/xCe-Al catalysts

The corresponding light-off curves in the 200-600 °C temperature range are included in Figure 6.49 (GHSV = 30,000 h^{-1}). For the sake of comparison the conversion-temperature profiles of the Co/Al, Co/Ce and bulk CeO_2 catalysts are also included. It must be noticed that all catalysts exhibited a 100% selectivity towards CO_2, irrespective of their cerium loading. However, a negligible activity in the whole temperature range was noticed for bare ceria.

To ensure that any diffusional effects did not affect the kinetic results, the criteria for intra-particle and extra-particle mass and energy diffusion, as well as the temperature gradients were checked to be above the limit, as explained in Chapter 2. Regarding this, Table 6.15 includes the calculated values for the various evaluated criteria.

Table 6.15. Criteria for accurate analysis of intrinsic reaction rates (as evaluated for the Co/20Ce-Al catalyst at 400 °C).

Criterion number	Recommendation	At 400 °C	Least favourable conditions
1.	Bodenstein parameter $< L_{bed}/d_{particle}$	7.9 < 79.5	55.6 < 79.5[a]
2.	$d_{tube}/d_{particle} > 10$	31.2	31.2
3.	Carberry number $< 0.05/n$	0.007	0.046[a]
4.	$\gamma\beta_e Ca < 0.05$	0.003	0.028[b]
5.	Wheeler-Weisz modulus < 0.15	$7.5 \cdot 10^{-4}$	$1.7 \cdot 10^{-3}$[a]
6.	Mears parameter < 0.1	$2.9 \cdot 10^{-6}$	$4.2 \cdot 10^{-6}$[c]
7.	Radial gradient < 0.05	0.005	0.010[c]
8.	Bed dilution parameter < 0.05	0.047	0.047
9.	Temperature gradient < 0.3	0.15	0.175[b]

[a]Determined at 500 °C; [b]Determined at 600 °C; [c]Determined at 450 °C.

Interestingly, all Co/xCe-Al catalysts evidenced a better behaviour than the non-modified catalyst irrespectively the ceria loading, with T_{50} values in the 480-540 °C (Table 6.16) temperature range and a conversion higher than 95% at 600 °C. On the other hand, the observed higher efficiency of the Co/Ce sample (T_{50} of 500 °C) with respect to its counterpart supported on pure alumina indicated that a cobalt-ceria interaction was catalytically more preferable. The following overall trend was found: Co/20Ce-Al (480 °C) > Co/15Ce-Al (490 °C) > Co/30Ce-Al (495 °C) > Co/Ce ~ Co/10Ce-Al (505 °C) > Co/5Ce-Al (525 °C) > Co/Al (550 °C). Thus, an optimum cerium loading (20%wt.) deposited on alumina was defined.

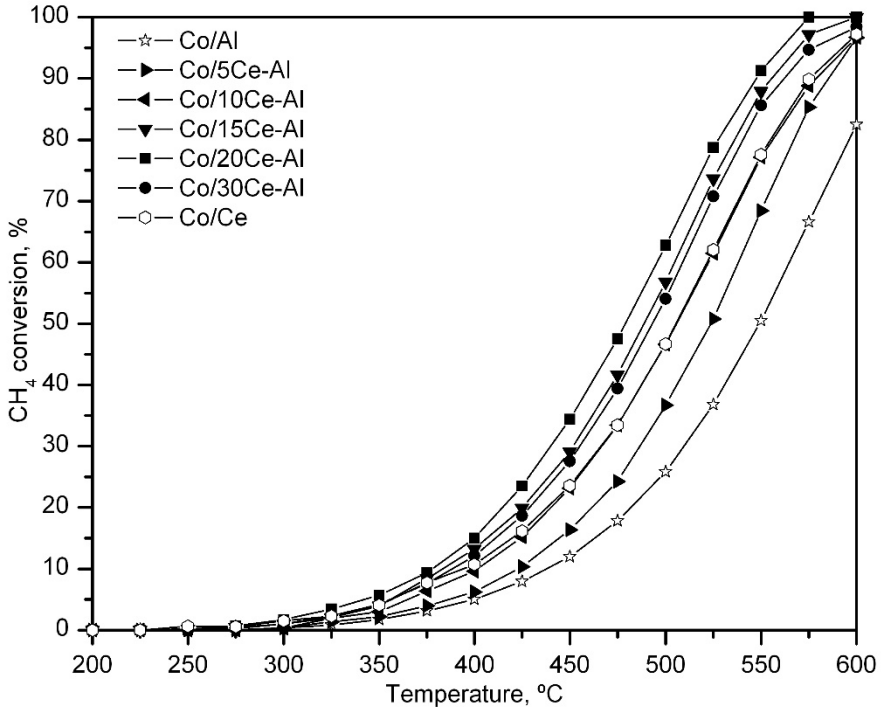

Figure 6.49. Light-off curves of the Co/xCe-Al catalysts.

Table 6.16. Kinetic results of the Co/xCe-Al catalysts.

Catalyst	T_{50}, °C	Specific reaction rate at 400 °C, mmol CH_4 g_{Me}^{-1} h^{-1}	E_a, kJ mol^{-1}
Co/Al	550	1.1	82 ± 2
Co/5Ce-Al	525	1.2	83 ± 2
Co/10Ce-Al	505	1.9	83 ± 2
Co/15Ce-Al	490	2.5	83 ± 1
Co/20Ce-Al	480	3.2	80 ± 2
Co/30Ce-Al	495	2.6	83 ± 2
Co/Ce	505	2.1	82 ± 2

A clearer evidence of the superior performance of the Co/20Ce-Al catalyst was given by the analysis of the specific reaction rate shown by each Co/xCe-Al sample (Figure 6.50). This reaction rate was calculated under differential conditions (conversion ‹20%) at 400 °C. A volcano-type relationship was distinctly seen, given that the reaction rate progressively

increased with Ce loading between 0 and 20%wt. (as referred to the alumina support) from 1.2 to 3.3 mmol CH_4 g_{Co}^{-1} h^{-1}, to then decrease significantly for the samples with a higher Ce concentration (2.9 mmol CH_4 g_{Co}^{-1} h^{-1}). This trend was also consistent with the intrinsic activity shown by the cobalt catalyst supported on pure ceria (2.1 mmol CH_4 g_{Co}^{-1} h^{-1}).

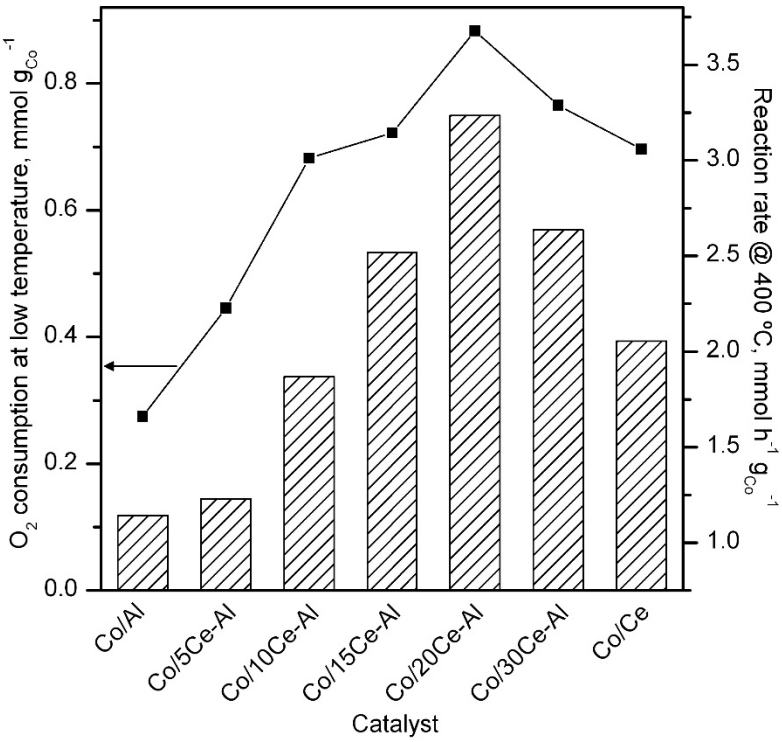

Figure 6.50. Specific reaction rate at 400 °C and O_2 consumption at low temperatures (CH_4-TPRe) of the Co/xCe-Al catalysts.

The results evidenced a promoted activity of Co_3O_4 when supported on ceria-coated alumina. The positive effect of ceria coating was mainly ascribed to the enhanced reactivity of the oxygen species of Co_3O_4, as also shown in Figure 6.50. Hence, a marked dependence of the intrinsic activity with the amount of O_2 consumed at low temperatures (‹500 °C) in the CH_4-TPRe runs was evidenced.

As aforementioned, ceria addition was useful for partially reducing the amount of inactive $CoAl_2O_4$ and simultaneously inducing a distortion of the structure of Co_3O_4. Both phenomena ultimately led to catalysts with an enhanced oxidation ability. The apparent

activation energy of the reaction over the investigated cobalt catalysts was evaluated by applying the integral method and the corresponding linearised plots are shown in Figure 6.51. The values for the apparent activation energy were in the 80-83 kJ mol^{-1} range for all catalysts, which were coherent with the value obtained with the bulk Co_3O_4 catalyst (74 kJ mol^{-1}).

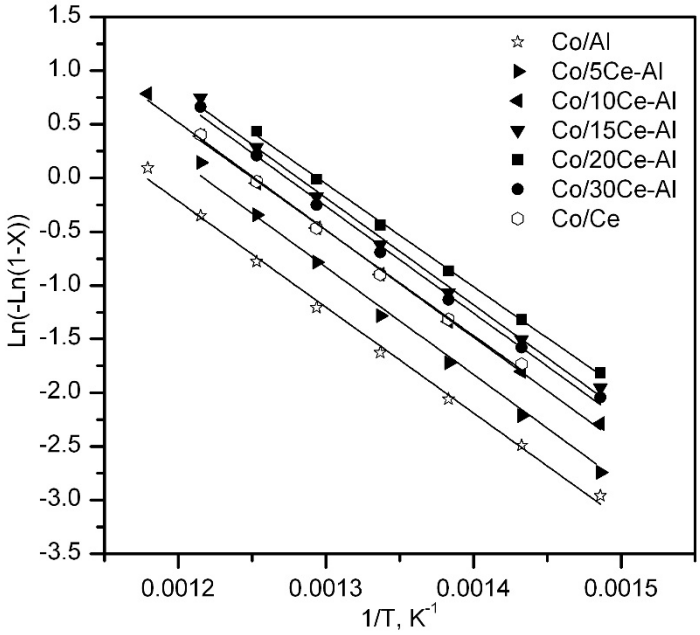

Figure 6.51. Pseudo-first order fit for the experimental data over the bimetallic Co-Ni/Al catalysts.

6.4. COMPARATIVE ANALYSIS OF THE THREE STRATEGIES

Once the efficiency of each strategy has been evaluated individually, next an attempt will be made to compare the optimal catalyst derived from the three examined improving approaches. Such comparison can be found in Figure 6.52 in the form of the light-off curves of each of the optimal catalysts, namely Co/12Mg-Al, 25Co-5Ni/Al and Co/20Ce-Al. The light-off curve of the Co/Al catalyst was also included as reference. Recall that the total metal loading of these samples was 30%wt.

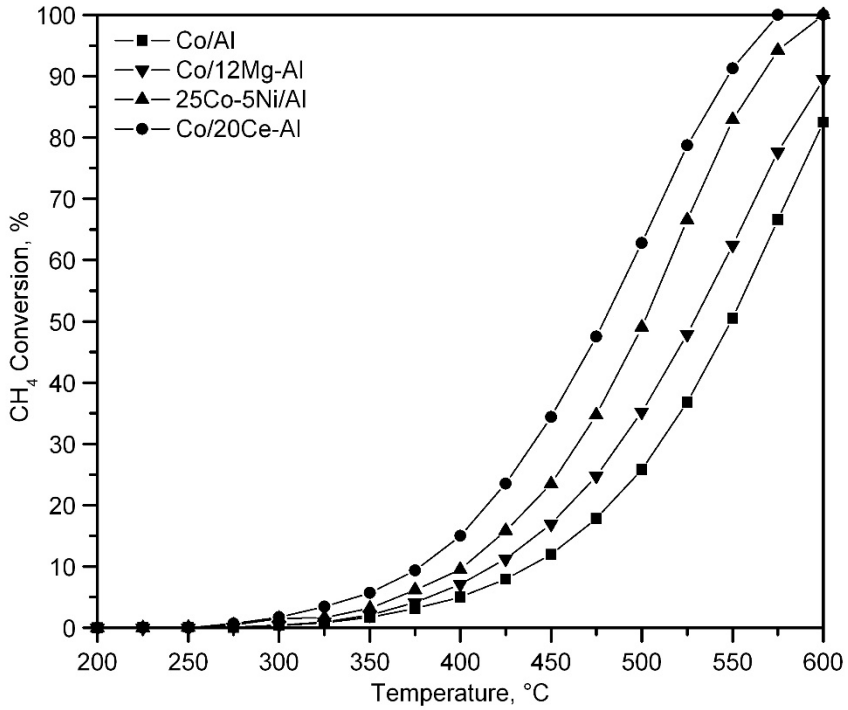

Figure 6.52. Light-off curves of the optimal catalysts from each of the tested strategies.

It was clear that the investigated proposals resulted remarkably efficient for enhancing the performance of the reference supported Co_3O_4/Al_2O_3 catalyst, since the three optimal catalysts exhibited a better behaviour than the reference Co/Al sample at both low and high temperatures. In this sense, these alternative catalysts lowered the corresponding T_{50} value by 25 (Co/12Mg-Al), 50 (25Co-5Ni/Al) and 70 °C (Co/20Ce-Al).

Table 6.17. Kinetic results of the optimal catalysts from each of the examined strategies.

Catalyst	T_{50}, °C	Specific reaction rate at 400 °C, mmol CH_4 g_{Co}^{-1} h^{-1}	E_a, kJ mol^{-1}
Co/Al	550	1.2	82 ± 2
Co/12Mg-Al	525	1.6	79 ± 3
25Co-5Ni/Al	500	2.5	84 ± 2
Co/20Ce-Al	480	3.2	80 ± 2

The specific reaction rates obtained over the various catalysts were previously estimated at different temperatures. In this analysis, for the sake of proper comparison, the specific activity of the optimal catalysts were calculated at the same temperature (400 °C) and normalised per gram of cobalt. The results are shown in Table 6.17. All three catalysts achieved higher reaction rates (1.6-3.2 mmol CH_4 g_{Co}^{-1} h^{-1}) than the unmodified counterpart (1.2 mmol CH_4 g_{Co}^{-1} h^{-1}). The catalyst modified with ceria (Co/20Ce-Al) in particular presented the highest specific activity among the studied strategies that was almost three times higher than that of the catalyst supported over bare alumina. In view of these results, modifying the alumina with ceria prior to the deposition of cobalt would be suitable a quite promising strategy to be applied for improving the activity of the alumina-supported cobalt catalysts.

Briefly, when cobalt was deposited over a Ce-modified gamma alumina support, a dual beneficial effect was evidenced. On one hand, ceria was found to act as a physical barrier between alumina and deposited cobalt, reducing the cobalt-alumina interaction and the subsequent cobalt aluminate formation. On the other hand, the interaction between cobalt and ceria led to a partial incorporation of cerium ions into the structure of the cobalt oxide. Both results eventually led to a larger abundance of Co^{3+} and therefore to a promoted mobility of the lattice oxygen species with ceria loading.

Finally, the thermal and hydrothermal stability of the three selected catalysts was evaluated. For this purpose, each catalyst was subjected to a stability test with prolonged time on stream at a constant temperature of 550 °C for a total reaction time of 150 hours. In each case, the reaction atmosphere was switched every 25 hours between dry ($1\%CH_4/10\%O_2/89\%N_2$) and humid ($1\%CH_4/10\%O_2/10\%H_2O/79\%N_2$) conditions to allow the additional analysis of the influence of hydrothermal ageing. The results of the evolution of methane conversion with time are depicted in Figure 6.53.

Table 6.18. Methane conversion loss over each of the optimal catalysts in the stability tests.

Catalyst	Initial conversion, %	Conversion loss after 25 hours (dry conditions), %	Conversion loss after water admission, %
Co/12Mg-Al	65	17	44
25Co-5Ni/Al	70	9	36
Co/20Ce-Al	79	17	33

All three catalysts underwent an initial thermal deactivation where the conversion appreciably dropped from an initial value of around 65-79% (Table 6.18), and then it stabilised after 15 hours on stream. The conversion loss in the first 25-hour period (under dry conditions) was 17% for the catalysts modified with magnesium and cerium, while it was only 9% for the sample modified with nickel. This suggested that the presence of nickel somewhat improved the thermal resistance of the resulting catalyst.

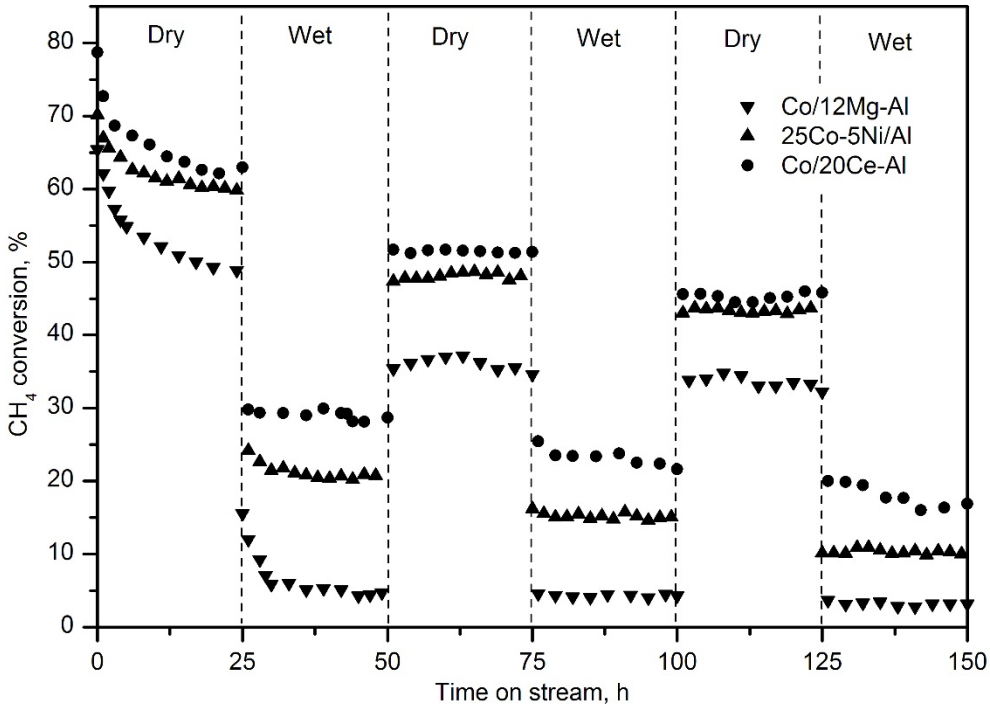

Figure 6.53. Evolution of methane conversion with time on stream over the three optimal catalyst under cycled dry/humid conditions.

The addition of water to the feedstream drastically affected the conversion for all three catalysts. Thus, the observed decrease when water was admitted to the feedstream varied between 33 and 44%. The catalyst modified with cerium exhibited the least appreciable conversion loss, thereby evidencing that the presence of ceria improved the resistance to deactivation by the presence of water vapour. This behaviour could be due to the relatively high hydrophobicity of ceria [299].

The subsequent cut-off of steam after 50 hours on stream enabled a partial recovery of the conversion, thus showing that water also induced some irreversible deactivation over the catalysts. This trend was also observed at longer reaction time intervals, with the conversion continuously decreasing after each of the successive humid cycles.

Table 6.19. Physico-chemical properties of the optimal catalysts after the stability tests.

Catalyst	BET surface, $m^2 g^{-1}$	Pore volume, $cm^3 g^{-1}$	Crystallite size, nm	Low-temperature O_2 consumption, mmol g_{Co}^{-1}
Co/12Mg-Al	87	0.23	18	10.8[a]
25Co-5Ni/Al	97	0.31	32	0.83
Co/20Ce-Al	79	0.22	26	0.85

[a]Low-temperature H_2 uptake from H_2-TPR analysis

Physico-chemical characterisation of the catalysts after the stability tests (Table 6.19) revealed that the used catalysts suffered a notable loss of specific surface area (10-16 $m^2 g^{-1}$) and pore volume (0.04-0.08 $cm^3 g^{-1}$) with respect to the fresh samples, which was also accompanied by a slight sintering of the cobalt spinel phase (3-11 nm), as revealed by XRD measurements. However, the redox properties of the used catalysts, evaluated by H_2-TPR and CH_4-TPRe analysis, remained intact, except for a small increase in the reaction temperatures (from 185 to 210 °C for the Co/12Mg-Al sample, from 420 to 470 °C for the 25Co-5Ni/Al sample and from 465 to 480 °C for the Co/20Ce-Al sample) due to the loss of surface area/sintering phenomenon. These results evidenced that the inhibiting effect of water was mainly due to competition effects with methane for surface adsorption, although a significant impact on the physico-chemical properties of the catalyst was also evidenced [300,301].

6.5. GLOBAL OVERVIEW AND CONCLUSSIONS

Three strategies for enhancing the performance of alumina-supported Co_3O_4 catalysts in the oxidation of lean methane were developed and compared. The three approaches focused on two main objectives: minimising the formation of inactive cobalt aluminate and promoting the activity of the deposited cobalt oxide. Thus, the three proposed strategies were the surface protection of alumina with magnesia, the redox promotion of

Co_3O_4 with nickel oxide and the surface protection of alumina with ceria, which eventually may also act as a redox promoter for Co_3O_4.

Firstly, for the evaluation of the effect of MgO addition on the catalytic behaviour of alumina supported catalysts, magnesia was deposited onto the alumina support prior to Co_3O_4 incorporation. From the textural point of view no marked effect was noticed after incorporating varying amounts of MgO (7-18%wt. Mg), due to the intrinsic properties of this promoter. When cobalt was deposited over these modified supports, magnesium oxide acted as a barrier limiting the interaction between cobalt and alumina, and consequently reducing the formation of inactive cobalt aluminate.

In addition to that, the cobalt-magnesium interaction was found to be more beneficial to the redox properties of free Co_3O_4 than the cobalt-alumina interaction. Hence, the onset temperature for reduction was lowered by about 40 °C and the overall hydrogen uptake of the catalysts increased (5-6%). As a result, the catalysts supported on the MgO-modified supports exhibited a higher activity than those supported on bare alumina. The highest reaction rate was achieved by the Co/12Mg-Al catalyst.

Secondly, a series of bimetallic cobalt-nickel catalysts (with a total metallic content of 30%wt) supported over alumina were synthesised in order to examine the effect of co-precipitating nickel (5-15%wt) along with the cobalt precursor. The resulting Co-Ni catalysts exhibited good textural properties, with only a slight loss of specific surface (12-19%) with respect to the bare alumina. Combined results from XRD and Raman spectroscopy evidenced that the presence of nickel was efficient for inhibiting the formation of $CoAl_2O_4$. In addition to Co_3O_4, the formation of $NiCo_2O_4$, as a result of the partial insertion of Ni^{2+} cation into the lattice of Co_3O_4, was favoured when relatively low amounts of nickel were incorporated. In contrast, segregated NiO was observed for Ni loadings between 10-15%wt.

XPS and electronic microscopy coupled to elemental analysis confirmed all these findings since an marked increase in the Co^{3+}/Co^{2+} molar ratio was noticed for the 25Co-5Ni/Al catalyst, which was coherent with the presence of nickel cobaltite, where major cobalt species were as Co^{3+}, and the preferential abundance of Ni^{2+} species belonging to $NiCo_2O_4$ at the cost of NiO and $NiAl_2O_4$. The high Co^{3+} concentration at the surface level was in turn correlated to an increased presence of lattice oxygen species.

The strong cobalt-nickel interaction that resulted in the formation of $NiCo_2O_4$, instead of Co_3O_4 and mainly $CoAl_2O_4$, promoted the redox properties of the resulting Co-Ni samples. Thus, when compared with the base monometallic catalyst, the reduction onset temperature was noticeably shifted (around 50 °C) to lower temperatures and the specific H_2 uptake in the low temperature range increased to a considerable extent. Furthermore, the higher mobility of active oxygen species for the Co-Ni catalysts, and particularly for the 25Co-5Ni/Al sample, was also evidenced by temperature-programmed reaction analysis with methane in the absence of gaseous oxygen.

A noticeable higher efficiency for lean methane combustion in terms of both specific reaction rate and reaction temperatures needed for full methane conversion to CO_2 was found over the bimetallic catalysts in comparison with their monometallic counterparts (Co/Al and Ni/Al). In line with the characterisation results, its superior activity was associated with their better reducibility and higher mobility of oxygen species. The optimal catalyst composition was that given by the 25Co-5Ni/Al catalyst, which suitably combined the co-presence of highly active $NiCo_2O_4$ and Co_3O_4 at the expense of NiO, $CoAl_2O_4$ and $NiAl_2O_4$.

Finally, the effect of cerium deposition on alumina-supported cobalt oxide catalysts was studied. The addition of cerium (5-30%wt.) to the alumina was carried out prior to the deposition of cobalt (30%wt.). The textural properties of the modified supports were hardly modified with respect to those of bare alumina, due to the good dispersion of ceria over the surface of the alumina. This dispersion also was responsible for a relatively strong interaction between alumina and deposited ceria that resulted in an increased Ce^{3+} content, especially at low Ce loadings (5-15%wt.). At higher Ce loadings, the good dispersion was maintained, but the interaction was less noticeable, thus resulting in the deposited ceria possessing a better reducibility with respect to pure bulk ceria.

When cobalt was deposited over the modified supports, a dual effect of ceria was evidenced. On one hand, ceria was found to act as a physical barrier between alumina and deposited cobalt, reducing the cobalt-alumina interaction and the subsequent cobalt aluminate formation, more remarkably with higher Ce loadings (20-30%wt.). On the other hand, the interaction between cobalt and ceria led to a partial incorporation of cerium ions into the structure of the cobalt oxide. Both findings ultimately led to a larger abundance of Co^{3+} and therefore to a promoted mobility of the lattice oxygen species with ceria loading.

Consequently, cobalt catalysts supported over ceria-alumina were significantly more active than that supported over bare alumina. The best behaviour was found for the Co/20Ce-Al sample.

The comparison of the best catalysts prepared by each strategy revealed that the most suitable option was the addition of cerium to the alumina, prior to the deposition of the cobalt precursor. The resulting optimal catalyst reduced its T_{50} value by 70 °C with respect to the reference catalyst supported over bare alumina, and exhibited a specific reaction rate around three times higher.

Finally, the study of the thermal and hydrothermal stability of these optimised catalysts revealed that the synthesised catalysts were relatively resistant to thermal deactivation, and that the presence of nickel in the cobalt catalyst could improve that resistance. Conversely, the presence of water vapour in the reaction stream was proven to be detrimental to the efficiency of the cobalt catalysts with a marked reversible inhibition effect due to competitive adsorption between methane and water molecules. In this sense, the presence of ceria, due to its high hydrophobicity, proved to induce a positive effect on the hydrothermal resistance of the cobalt catalysts.

Chapter 7

DESIGN OF Co-Ce-BASED CATALYSTS SUPPORTED ON OPEN CELL ALUMINA FOAMS

ABSTRACT

In this last chapter, the viability of the incorporation of the optimal catalyst formulation obtained in Chapter 6 onto structured supports is evaluated. The selected structured support were alpha-alumina open cell foams, owing to the lower interaction potential with cobalt of this material. However, due to the low specific surface area of this substrate, first, the Ce/Co ratio and the Co_3O_4 loading needed to be optimised again. The optimisation was carried out over powdered alpha-alumina, and as a result a suitable formulation was defined (10% Co_3O_4 loading and Ce/Co = 0.05). The structured catalysts were synthesised by solution combustion synthesis. Prior to the incorporation of the active phase into the open cell foams, the parameters of the synthesis methodology were also adjusted properly. Thus, glycine was identified as a better option than urea as fuel, and the optimal fuel/oxidiser ratio was the stoichiometric one. The resulting structured catalysts were found to be active for methane combustion, thereby confirming the viability of open cell foams as structured supports for cobalt oxide-based catalysts.

7. DESIGN OF Co-Ce-BASED CATALYSTS SUPPORTED ON OPEN CELL ALUMINA FOAMS

The development and comparison of strategies for enhancing the performance of cobalt-based catalysts carried out in Chapter 6 gave as a result an optimised formulation in the form of Co_3O_4 catalysts supported over CeO_2-Al_2O_3. As previously demonstrated, the notable activity of this catalyst stemmed from the synergistic effect of ceria, which partially inhibited the formation of cobalt aluminate while simultaneously promoting the redox properties of the supported cobalt oxide. This highly efficient catalyst also exhibited a relatively good stability and improved resistance to inhibition by water vapour with respect to the unmodified Co_3O_4/Al_2O_3 catalyst.

The next step of the advanced design of this promising catalytic system catalyst would be to evaluate the viability of its incorporation onto a structured support, since that would be the configuration in which it would be implemented in a real application. The most common structured supports for automotive applications are cordierite monoliths due to their good thermal and mechanical resistance, and their micro-channel structure that allows for an extremely good contact between the solid catalyst and the gas phase [302,303].

However, an alternative to the traditional monoliths has lately appeared in the form of open cell foams made of ceramic or metallic materials. These foams are generally manufactured by impregnation of a polymeric sponge with a ceramic suspension, or by pumping an inert gas into a ceramic suspension or molten metal before solidification [304]. The result is a cellular structure made of a ceramic or metal substrate with interconnected and often non-ordered pores with a large volume. Typically, only 5-25% of the total volume of the foam is the base material. The alleged advantage of open cell foams when compared with traditional monoliths lies on the high surface/volume ratio, low pressure drop, and the random disposition of the void volume, which can aid in the mass and heat transfer between the gas and the solid phase. The use of foam-supported catalysts is currently focused on both pollution abatement processes (catalytic converters) [129,231,305,306] or conventional catalytic processes such as methane steam reforming or CO_2 methanation [307-310].

The incorporation of a powdered catalyst onto a structured support can be mainly carried out by two methodologies. The most commonly applied procedure on an industrial scale is to prepare a washcoating slurry with the powdered catalyst and a fluid phase such as water or a water/glycerine mixture. The structured support is then dipped into the slurry until it is thoroughly coated, and then dried and calcined to stabilise the deposited material [311]. A second approach involves applying impregnation-based routes to deposit the catalyst formulation directly onto the surface of the structured catalyst. The most frequently used methods in this case are wet impregnation (often in the presence of some surfactants) and solution combustion synthesis.

Once prepared, the evaluation of the synthesised structured samples is often limited to the determination of their catalytic efficiency, since there are few characterisation techniques, namely some electronic microscopies, which are applicable for the relatively large pieces of the structured catalyst. For the rest of the conventional characterisation techniques, it is necessary to destroy the structured support to a powdered catalyst, rendering the structuring process useless.

7.1. OPTIMISATION OF THE Co_3O_4/CeO_2 SYSTEM SUPPORTED OVER ALPHA-ALUMINA

As described in previous chapters, when γ-Al_2O_3 is employed as a support, the strong cobalt-alumina interaction that frequently occurs worsens the redox properties of the cobalt oxide due to the formation of an inactive phase of cobalt aluminate. In Chapter 6, several approaches were proposed to minimise this detrimental effect, but in all cases, the formation of cobalt aluminate was only partially inhibited and never completely avoided. Despite this fact, not using a support for the cobalt oxide is not an option since the majority of the structured supports, especially cordierite monoliths, can also interact with cobalt, with inhibiting results on the catalytic performance [312].

For this reason, another approach for preparing structured catalysts could be the substitution of porous gamma-alumina by more chemically stable, non-porous alpha-alumina, thereby minimising the fixation of the active Co_3O_4 phase as $CoAl_2O_4$. The main drawback of this strategy is that the amount of cobalt oxide that can be deposited on the surface of alpha-alumina is much more limited when compared with gamma-alumina, owing to its low surface area. This means that the cobalt loading needs to be optimised over

this alternative support and cannot be directly extrapolated from that obtained over some other porous media.

Therefore, the first main objective of this last part of the thesis was the design of an efficient Co_3O_4 catalyst, promoted with CeO_2 and supported over α-Al_2O_3, for its subsequent deposition onto an open cell foam structured support. The optimisation strategy involved the determination of the optimal Co_3O_4 loading as well as the Ce/Co ratio and the key parameters of the solution combustion synthesis (SCS) route chosen to incorporate the optimised formulation into the structured supports. The selection of the SCS route instead of other simple synthesis routes such as wet impregnation was made based on the superior properties of this methodology reported by several authors [95,313]. Furthermore, in Chapter 3 it was found that bulk oxides prepared by SCS exhibited a promising behaviour.

The preparation of a cobalt oxide-based structured catalyst by SCS can be described by the flow chart depicted in Figure 7.1. The process starts with the impregnation of a solution containing cobalt nitrate and the fuel on the support, generally by dipping the structured support into the solution. Then, the impregnated support is left to dry (generally in ambient air), and afterwards it is placed in a furnace for the combustion process. Recall that the formation of the Co_3O_4 active component by SCS can be considered as a two-step process, where the first step is the endothermic reaction of the metal-oxide starting from the metal nitrate precursor, and the second step is exothermic and accounts for the reaction between oxygen derived from nitrate decomposition and organic fuel (urea, glycine or citric acid among others) [122].

For the optimisation of the Co_3O_4 loading and the Ce/Co molar ratio, several Co_3O_4-CeO_2 catalysts supported over powdered α-Al_2O_3 were synthesised by incipient wetness impregnation. The water capacity of α-Al_2O_3 was previously determined to be about 1 $cm^3\ g^{-1}$, from which the pore volume was only a 1%, as measured by a N_2 physisorption analysis. Therefore, for each catalyst, 2 g of α-Al_2O_3 were successively co-impregnated with 2 cm^3 of a cobalt nitrate/cerium nitrate solution with adjusted concentrations (3.8M/0.2M). The α-Al_2O_3 was obtained by calcination of boehmite (*Versal*) at 1300 °C for 6 hours. On one hand, the study of the effect of the Ce/Co ratio was performed by varying the Ce/Co molar ratio between 0 and 0.20, with a fixed loading of 10%wt.Co_3O_4. On the other hand, for analysing the influence of the Co_3O_4 loading, the selected cobalt loadings were 2.5, 5, 10, 15 and 20%wt. Co_3O_4, fixing the optimal Ce/Co ratio from the previous step. After

impregnation, all precursors were dried at 110 °C for at least 16 hours and then calcined at 600 °C for 4 hours in static air. The samples were denoted as xCo-yCe, where x and y stand for the Co_3O_4 and CeO_2 loadings, respectively.

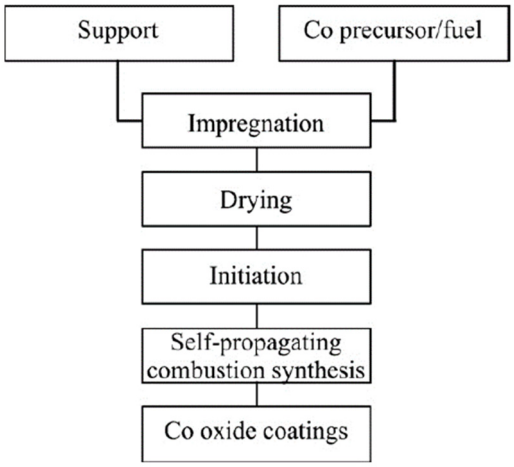

Figure 7.1. Flow chart for the preparation of a supported catalyst by SCS [122].

The activity of these powdered catalysts for the complete oxidation of methane was examined in a fixed bed quartz tubular reactor in the 200-600 °C temperature range. The composition of the feed stream was 1%CH_4/10%O_2/89%Ar with a total flow of 100 cm^3 min^{-1}. Instead of gas chromatography, the composition of the reaction gases was monitored by a *SRS RGA200* quadrupole mass spectrometer following the m/z = 44 (CO_2), 32 (O_2), 28 (CO) and 16 (CH_4) signals. The runs were carried out with 300 mg of catalyst (sieve fraction of 0.2-0.3 mm), which accounted for a GHSV of around 15,000 h^{-1} (20,000 cm^3 g^{-1} h^{-1}).

7.1.1. Optimisation of the Ce/Co ratio for powdered Co-Ce catalysts supported over α-Al_2O_3

The proposed approach to determine the optimal composition of the Ce-Co catalytic system supported on alpha-alumina firstly involved the examination of a series of samples with a reference constant Co_3O_4 loading (10%wt.) and a varying Ce/Co molar ratio, between 0 and 0.2 (0, 0.01, 0.03, 0.05, 0.1 and 0.2; 5 samples). Next, once the suitable Ce/Co molar ratio was selected, a second set of samples were prepared with a Co_3O_4 loading varying in the 2.5-20%wt. (2.5, 5, 10, 15 and 20; 5 samples). The performance of the synthesised samples

was kinetically compared on account of their specific activity at relatively low temperatures (450 °C).

Our attention was then first focused on the determination of the optimum concentration of the ceria promoter, while the nominal cobalt concentration was fixed at 10%wtCo_3O_4. Thus, a set of samples were prepared by incipient wetness impregnation with a Ce/Co molar ratio varying from 0 to 0.2, that was equivalent to a maximum nominal ceria content of 4.3%wt. The samples were designated as 10Co-xCe/Al(α), where x stands form the CeO_2 mass content.

Table 7.1 summarises the actual cobalt loading and ceria content as expressed in terms of the amount of Co_3O_4 and CeO_2, respectively. The composition of the samples, which was determined by EDXRF, was in a fairly good agreement with the nominal loading for each metallic phase. The analysis of the textural properties by N_2 physisorption expectedly revealed a low surface area (4-7 $m^2\ g^{-1}$). No significant differences were found among the various samples. Accordingly, reduced pore volumes were measured (0.008-0.013 $cm^3\ g^{-1}$). Note that the surface area of the bare alpha-alumina support was 5 $m^2\ g^{-1}$. All samples exhibited type III isotherms, characteristic of nonporous or macroporous solids, in agreement with their reduced specific surface areas and pore volumes.

Table 7.1. Physicochemical properties of the 10Co-xCe/Al(α) catalysts.

Sample	Ce/Co molar ratio	BET surface, $m^2\ g^{-1}$	Pore volume, $cm^3\ g^{-1}$	Crystallite size, nm	Total H_2 uptake, mmol g^{-1}
α-Al_2O_3	--	4.8	0.007	--	-
10Co-0Ce/Al(α)	0	4.0	0.007	40	16.6
10Co-0.2Ce/Al(α)	0.01	4.4	0.008	38	17.1
10Co-0.7Ce/Al(α)	0.03	5.2	0.009	37	17.4
10Co-1.1Ce/Al(α)	0.05	5.7	0.013	35	17.4
10Co-2.1Ce/Al(α)	0.10	5.7	0.010	35	17.7
10Co-4.3Ce/Al(α)	0.20	6.6	0.010	34	17.9

The structural properties of the catalysts were evaluated by XRD. The corresponding patterns are included in Figure 7.2. As a reference, the pattern of the bare alpha-alumina and a bulk Co_3O_4 sample prepared by direct calcination of cobalt nitrate at 600 °C are shown

as well (this oxide is the so-called DC sample included in Chapter 3). Recall that, unlike the rest of previously prepared bulk oxides, the DC sample was best preferred for comparison purposes with impregnated catalysts. All samples exhibited intense signals associated with a highly crystalline trigonal phase, indexed as alpha-alumina (ICDD 01-081-1667), at 2θ = 25.3, 34.8, 37.4, 43.0, 52.1, 57.0, 60.7, 65.9, 67.5 and 76.1°, and low intensity signals from a cubic phase, indexed as cobalt spinel oxide Co_3O_4, at 2θ = 19.0, 31.3, 36.8, 38.5, 44.8, 59.4 and 65.2° (ICDD 00-042-1467).

Moreover, the samples with the largest amounts of cerium, namely 10Co-1.1Ce/Al(α), 10Co-2.1Ce/Al(α) and 10Co-4.3Ce/Al(α) catalysts also displayed a very weak signal at 2θ = 28.6°, attributable to a cubic phase of CeO_2 (ICDD 00-004-0593). This was coherent with the relatively large presence of ceria over these samples (1.1. 2.1 and 4.3%wt, respectively). The mean crystallite size of Co_3O_4 included in Table 7.1 was estimated by applying the Scherrer equation to all the identifiable signals assigned to this oxide phase. No marked differences were noticed among the various samples, since the crystallite size was around 36 nm, particularly in the 34-40 nm range.

It was interestingly noticed that diffraction signals of cobalt oxide in the Co-Ce catalysts slightly shifted from their positions with respect to the Ce-free cobalt sample. Hence, Figure 7.3 includes an enlarged view of the diffraction peak at 37.1° for the various Co-Ce catalysts. This finding suggested that that the addition of Ce may cause a significant distortion in the spinel structure. In this sense, results included in Figure 7.4 evidenced a progressive increase in the unit cell size with Ce/Co molar ratio, which was consistent with the larger ionic radius of Ce^{4+} (101 pm), Ce^{3+} (115 pm) in comparison with Co^{2+} (79 pm) and Co^{3+} (69 pm). Apparently, the upper limit for cerium atoms that could be inserted into the lattice of Co_3O_4 seemed to be close to a Ce/Co molar ratio of 0.05 as the largest cell size was noticed for the 10Co-1.1Ce/Al(α) catalyst. Above this loading, excess of cerium led to the formation of segregated CeO_2.

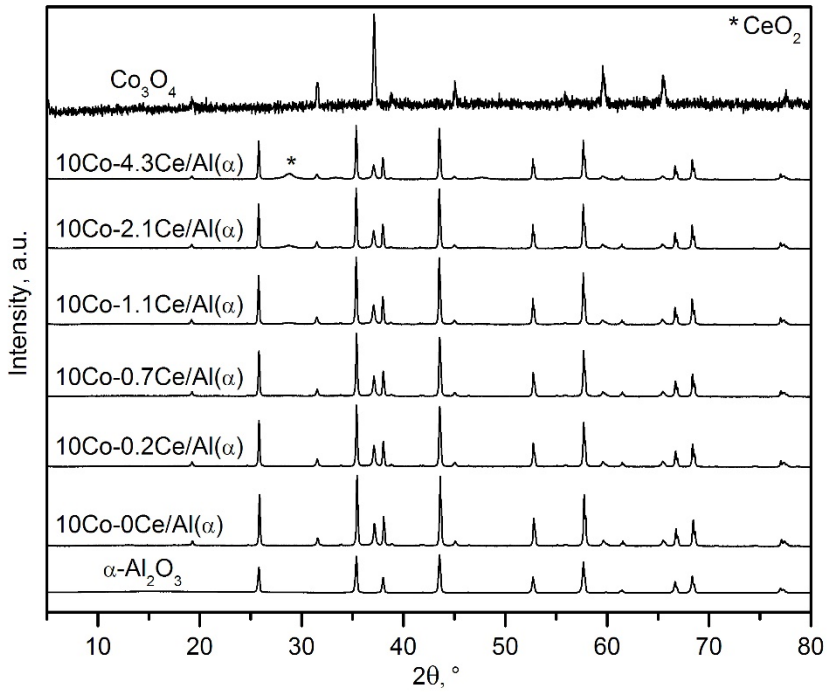

Figure 7.2. Diffraction patterns of the 10Co-xCe/Al(α) catalysts.

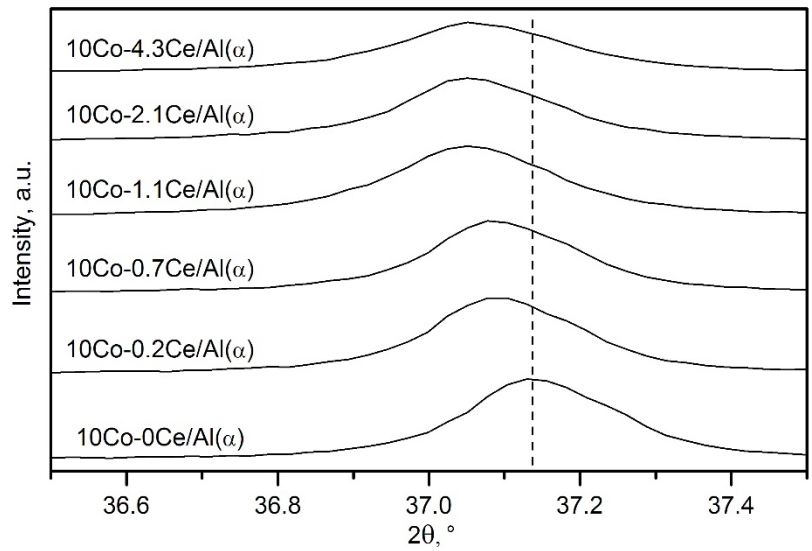

Figure 7.3. Close up view of the diffraction patterns of the 10Co-xCe/Al(α) catalysts in the 2θ = 35-39° range.

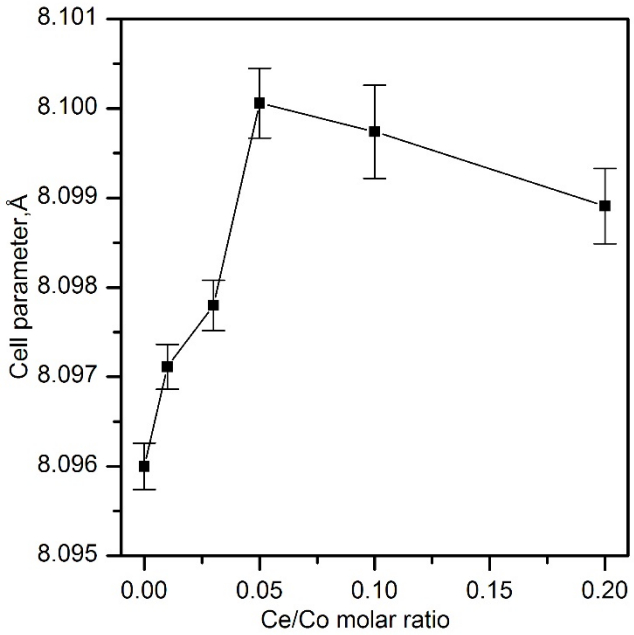

Figure 7.4. Evolution of the cobalt oxide cell size of the 10Co-xCe/Al(α) catalysts.

In an attempt to further confirm the distortion of the spinel lattice, the Co-Ce samples were analysed by Raman spectrometry as well. The resulting spectra are included in Figure 7.5. The spectra of the 10Co-0Ce/Al(α) was that typical of Co_3O_4 with several bands assignable to the F_{2g} mode (194, 519 and 617 cm^{-1}), and two bands which could be attributable to the E_g and A_{1g} modes (479 and 687 cm^{-1}), respectively. It is worth pointing out that the shoulders at 705 and 725 cm^{-1} attributable to the presence of $CoAl_2O_4$ were not observed. In contrast, the spectrum of a sample with a comparable Co_3O_4 content supported on gamma-alumina (10Co/Al catalyst) clearly exhibited these two features, thereby suggesting the formation of this undesired cobalt phase. The cobalt samples with Ce also showed these same five Raman bands, but appreciably shifted from their original positions and with broader shapes. Thus, in line with the XRD results, the Co_3O_4 lattice certainly seemed to be distorted by cerium addition. The intense A_{1g} band therefore shifted from 683 cm^{-1} over the 10Co-0Ce/Al(α) sample to 676 cm^{-1} over the 10Co-1.1Ce sample/Al(α).

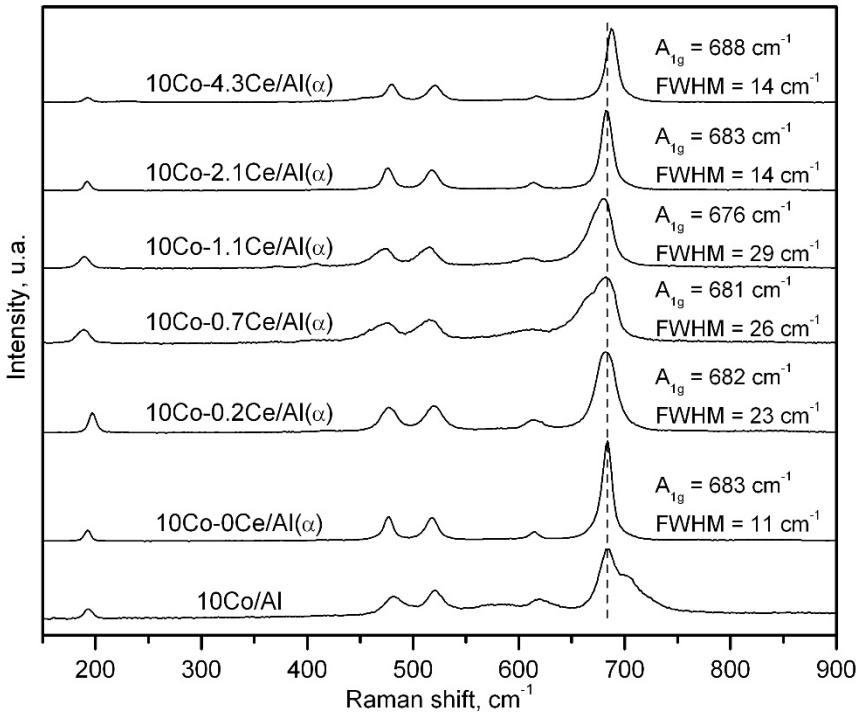

Figure 7.5. Raman spectra of the 10Co-xCe/Al(α) catalysts.

More remarkably, relatively higher FWHM (Full Width Half Maximum) values, between 14 and 29 cm^{-1}, were consistently found in comparison with that of the Ce-free catalyst (11 cm^{-1}). The highest value was noted over the 10Co-1.1Ce/Al(α) sample, thereby pointing out that the largest extent of lattice distortion occurred over this catalyst. Accordingly, this sample presented the largest cell size. A higher Ce/Co molar ratio (0.1 and 0.2) did not lead to appreciable structural changes of the spinel lattice as revealed by the same position of the A_{1g} band and FWHM value, when compared with the unpromoted cobalt catalyst.

XPS measurements could also be useful for gaining insights into the relative abundance of the reducible species on the surface of the spinel. The Co2p spectra (Figure 7.6) displayed broad signals, thereby revealing the presence of various cobalt species with different oxidation state. In particular, the Co $2p_{3/2}$ signal could be deconvoluted into at least five contributions, following the same assignment described in previous chapters. Briefly, the two main contributions centred around 779.5 and 780.7 eV were attributed to Co^{3+} and Co^{2+} ions respectively, whose satellite signals were located at 789.3 and 785.7 eV, respectively.

Finally, the signal centred at 782.2 eV was associated with the presence of CoO species. On the other hand, the O1s spectra exhibited two signals at 529.8 and 530.8 eV, respectively. The former was related to oxygen ions from the lattice (O_{latt}) whereas the latter was associated with adsorbed oxygen species on the surface (O_{ads}). By quantifying the areas of the corresponding signals, both Co^{3+}/Co^{2+} and O_{ads}/O_{latt} molar ratios (Table 7.2) could be estimated. As shown earlier, a direct correlation was found between the presence of Co^{3+} species and the abundance of lattice oxygen species [172,314].

Due to the relative low Ce concentration of the samples, the deconvolution of the Ce 3d spectra (880-916 eV) was not possible and therefore the relative abundance of Ce^{4+} and Ce^{3+} species could not reliably estimated. However, from the Ce3d spectra ($3d_{5/2}$ and $3d_{3/2}$ spin-orbit components) it was possible to quantify the total amount of Ce at the surface and thus examine its eventual influence on the valence changes of cobalt species.

Thus, XPS analysis evidenced a noticeable variation of the relative abundance of cobalt and cerium at the surface level with respect to the bulk composition. Hence, while surface cobalt content gradually decreased from 10%wt. (10Co-0Ce/Al(α)) to around 6%wt. (10Co-4.3Ce/Al(α)), a substantial Ce enrichment varying between 3 and 8.6%wt. was simultaneously noticed. Recall that the corresponding cerium bulk concentration was in the 0.3-4.3%wt. range. As a result, the Ce/Co molar ratio was increased by 10-20 times in relation to the nominal value (0.05).

By quantifying the areas of the corresponding signals, both Co^{3+}/Co^{2+} and O_{ads}/O_{latt} molar ratios (Table 7.2) could be estimated. A direct correlation was found between the presence of Co^{3+} species and the abundance of lattice oxygen species. The addition of cerium resulted in a favoured presence of Co^{3+} at the cost of Co^{2+} as revealed by the significantly high Co^{3+}/Co^{2+} molar ratios, which ranged from 0.91 for the Ce-free sample to about 1.2 over the 10Co-1.1Ce/Al(α) catalyst. Above this Ce loading the relative abundance of Co species did not markedly vary in line with the fact that Ce insertion into the Co_3O_4 lattice was not further activated with higher Ce loadings. On the other hand, it should be pointed out that the abundance of Co^{3+} species was directly related to the presence of lattice oxygen species with decreasing O_{ads}/O_{latt} molar ratios from around 0.4 over the 10Co-0Ce/Al(α) catalyst to about 0.1 for the 10Co-1.1Ce/Al(α), 10Co-2.1Ce/Al(α) and 10Co-4.3Ce/Al(α) catalysts.

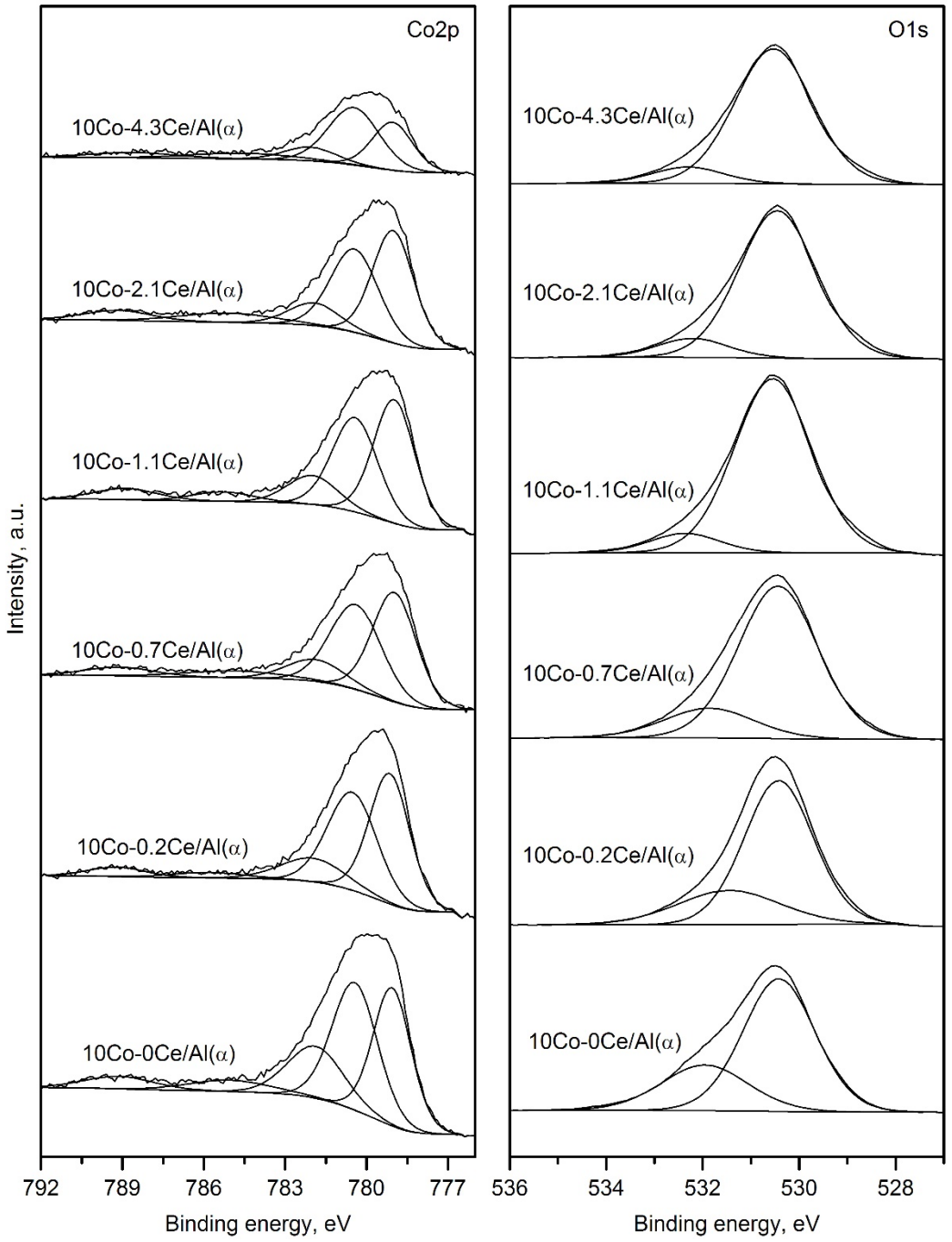

Figure 7.6. Co2p and O1s XPS spectra of the 10Co-xCe/Al(α) catalysts.

Table 7.2. Surface composition of the 10Co-xCe/Al(α) catalysts.

Sample	Co, %wt.	Ce, %wt.	Co^{3+}/Co^{2+} molar ratio	O_{ads}/O_{latt} molar ratio
10Co-0Ce/Al(α)	10.3 (7.4)	0 (0)	0.91	0.41
10Co-0.2Ce/Al(α)	8.1 (7.4)	2.7 (0.2)	1.09	0.35
10Co-0.7Ce/Al(α)	6.7 (7.4)	5.8 (0.6)	1.10	0.22
10Co-1.1Ce/Al(α)	7.0 (7.4)	6.7 (0.9)	1.19	0.10
10Co-2.1Ce/Al(α)	7.4 (7.4)	7.7 (1.7)	1.17	0.12
10Co-4.3Ce/Al(α)	6.4 (7.4)	8.4 (3.5)	1.22	0.11

The values in brackets correspond to the bulk composition as determined by EDXRF.

Finally, the redox properties of the samples were investigated by H_2-TPR. The corresponding profiles are shown in Figure 7.7. For comparative purposes, the traces corresponding to a bulk Co_3O_4 oxide (prepared by direct calcination of cobalt nitrate at 600 °C) and a Co_3O_4 catalyst supported on gamma alumina (12%wt.Co_3O_4) are included (the so-called 10Co/Al sample described in Chapter 5) as well.

Typically, the reduction of the Co_3O_4 phase is a two-step process that involves the consecutive reduction of Co^{3+} to Co^{2+} at low temperatures and the reduction of Co^{2+} to metallic cobalt at high temperatures [96,174]. The profile of the reference Ce-free cobalt catalyst (10Co-0Ce/Al(α)) showed a main reduction band at 375 °C, with a more or less discernible shoulder at lower temperatures (325 °C). No H_2 uptake was detected above 450 °C, which was in agreement with the full reduction of cobalt species as Co_3O_4, since the experimental consumption was 16.6 mmol H_2 g_{Co3O4}^{-1}.

It could be therefore confirmed that this sample supported on alpha alumina did not contain appreciable amounts of highly stable cobalt species such as cobalt aluminate. This was in contrast with the results obtained with an analogous counterpart supported on gamma alumina (12%wt.Co_3O_4/γ-Al_2O_3, i.e 10Co/Al sample), in which a significant fraction of deposited cobalt species (around 90%) were transformed into $CoAl_2O_4$ due to the partial dissolution to Co_3O_4 into the γ-Al_2O_3 lattice, as revealed by its marked H_2 uptake observed at temperatures higher than 500 °C (Figure 7.7). Accordingly, its overall consumption was only 17.7 mmol H_2 g_{Co}^{-1}, significantly lower than the theoretical value (22.6 mmol H_2 g_{Co}^{-1}).

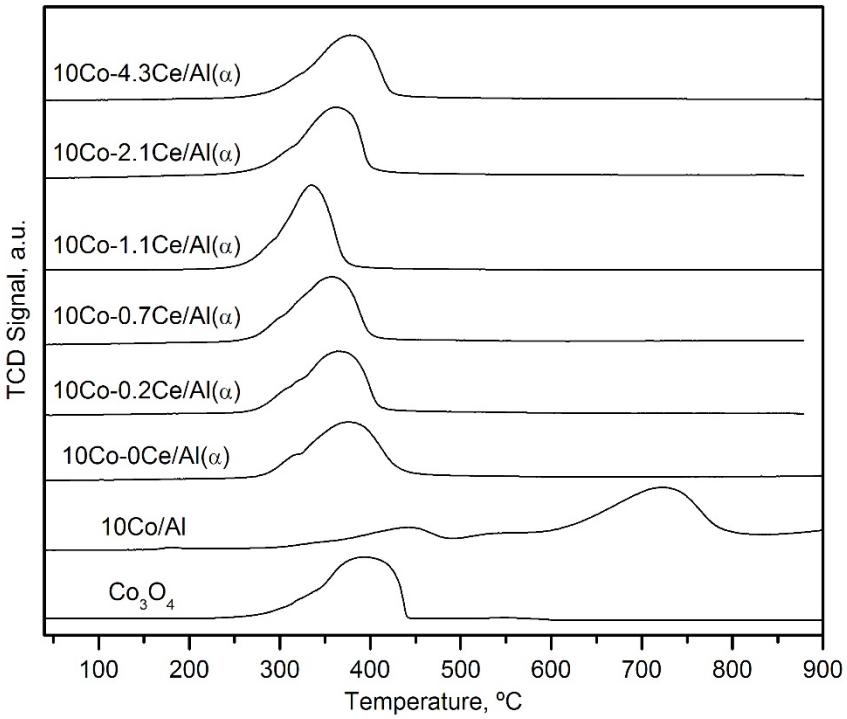

Figure 7.7. H_2-TPR profiles of the 10Co-xCe/Al(α) catalysts.

As the amount of cerium in the catalyst increased, the reducibility of the samples was significantly enhanced since a markedly progressive shift in peak reduction temperatures was visible, from 385 °C (10Co-0Ce/Al(α)) to 335 °C over the sample with a Ce/Co molar ratio of 0.05 (1.1%wt. CeO_2). Above this molar ratio (0.1 and 0.2) the promotion in reducibility was somewhat less evident, with peak reduction temperatures about 360-375 °C. The overall H_2 uptakes increased with the cerium content from 1.6 to 1.8 mmol H_2 g^{-1} (which equated to 17.1 to 17.9 mmol H_2 g_{Co3O4}^{-1}), thereby revealing an increased contribution to the present cerium species to the overall reducibility of the catalysts (Table 7.2).

The observed increase in the H_2 uptake at low temperature could be rationalised in terms of a favoured reduction of Co_3O_4 with a distorted lattice due to cerium doping as revealed by XRD, Raman spectroscopy and XPS analysis. As proposed earlier, another plausible phenomenon that would contribute to a higher reducibility between 200 and 500 °C could be a larger extent of ceria reduction owing to the transfer of hydrogen by metallic cobalt onto the ceria surface [315,316].

The corresponding light-off curves of this series of cobalt catalysts modified with cerium as a promoter are shown in Figure 7.8. Recall that all studied cobalt catalysts exhibited a 100% CO_2 selectivity, following the same behaviour of the previously investigated cobalt catalysts. The observed efficiency could be classified into two groups with a substantially different performance. On one hand, the samples with a Ce/Co molar ratio of 0, 0.01 and 0.03 exhibited a similar value (540-550 °C) of T_{30} (temperature at which 30% conversion was attained) and a conversion as low as 17% at 600 °C.

On the other hand, the 10Co-1.1Ce/Al(α), 10Co-2.1Ce/Al(α) and 10Co-4.3Ce/Al(α) catalysts showed a significantly lower T_{30} value (520-530 °C) with a conversion of 55% at 600 °C. Thus, the efficiency was promoted with the incorporation of cerium but above 1.1%wt. (corresponding to a Ce/Co molar ratio of 0.05) no further improvement was attained. The catalytic benefits of cerium addition were better evidenced when analysing the specific reaction rate at 450 °C (Figure 7.9 and Table 7.3). The specific reaction rate was 2.4 mmol CH_4 h^{-1} g_{Co3O4}^{-1} for the unmodified cobalt catalyst (10Co-0Ce/Al(α)). Nevertheless, this appreciably increased with Ce concentration to a maximum value of 4.1 mmol CH_4 h^{-1} g_{Co3O4}^{-1} for the sample with a Ce/Co molar ratio of 0.05. For higher Ce/Co ratios, the reaction rate somewhat decreased down to around 3.5 mmol CH_4 h^{-1} g_{Co3O4}^{-1}.

The apparent activation energies of the supported Co-Ce catalysts (Table 7.3) were in the 71-79 kJ mol^{-1} range, comparable to those of the pure Co_3O_4 and Ce-Co bulk catalysts described in Chapters 3 and 4. However, for the Ce-free catalyst this value was 93 kJ mol^{-1}, thus showing that the presence of both metals was essential for the activity of the resulting catalysts.

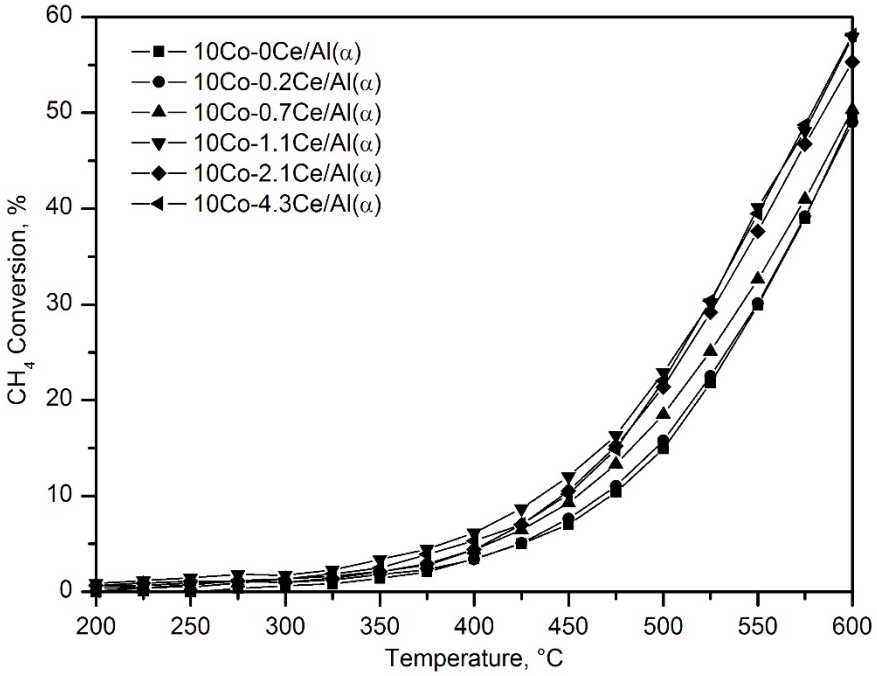

Figure 7.8. Light-off curves of the 10Co-xCe/Al(α) catalysts.

Table 7.3. Kinetic results of the 10Co-xCe/Al(α) catalysts.

Catalyst	T_{30}, °C	Specific reaction rate at 450 °C, mmol CH_4 g_{Co3O4}^{-1} h^{-1}	E_a, kJ mol^{-1}
10Co-0Ce/Al(α)	550	2.4	93
10Co-0.2Ce/Al(α)	550	2.6	79
10Co-0.7Ce/Al(α)	540	3.2	76
10Co-1.1Ce/Al(α)	520	4.1	72
10Co-2.1Ce/Al(α)	530	3.6	71
10Co-4.3Ce/Al(α)	530	3.5	71

As evidenced in Figure 7.9 a clear relationship existed between the activity of the Co-Ce catalyst and the oxygen mobility, which was directly related to the peak reduction temperatures. Given that the interaction between Co_3O_4 and CeO_2 is considered essential for the enhanced activity of these catalysts [230,298], this effect may be due to a saturation of the surface of the catalysts with CeO_2 nanoparticles, with higher Ce/Co molar ratios forcing the ceria to segregate from the surface and not providing any remarkable improvement in the activity. Thus, the optimal Ce/Co molar ratio was defined at 0.05.

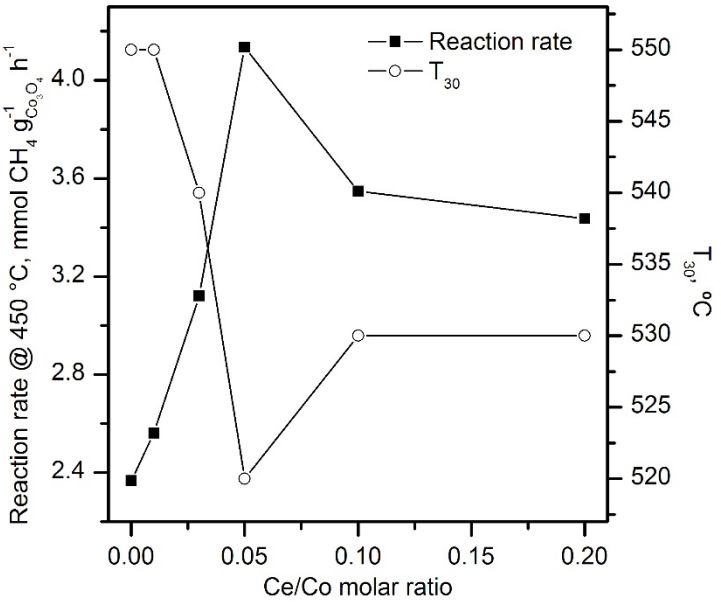

Figure 7.9. Evolution of the specific reaction rate of the 10Co-xCe/Al(α) catalysts.

7.1.2. Optimisation of the Co_3O_4 loading for powdered Co-Ce catalysts supported over α-Al_2O_3

Next, the effect of the Co_3O_4 loading on the physic-chemical properties and performance of the supported Co-Ce catalysts was examined while maintaining constant its Ce/Co molar ratio at the previously defined optimal value (0.05). Hence, a series of samples with a Co_3O_4 loading varying in the 2.5-20wt% range with this fixed Ce/Co molar ratio. The catalysts were named as xCo-yCe/Al(α) where x and y stand for the actual Co_3O_4 and CeO_2 mass content, respectively.

The corresponding composition and textural properties are listed in Table 7.4. The ceria content of the samples accordingly varied between 0.3-2.2%wt. Expectedly, both surface areas and pore volumes were low (5-6 $m^2 g^{-1}$ and 0.008-0.013 $cm^3 g^{-1}$, respectively), with no relevant differences among the various samples.

Table 7.4. Physicochemical properties of the xCo-yCe/Al(α) catalysts.

Sample	Co_3O_4 loading, %wt.	BET surface, $m^2 g^{-1}$	Pore volume, $cm^3 g^{-1}$	Crystallite size, nm	Total H_2 uptake, mmol g_{Co3O4}^{-1}
α-Al_2O_3	--	4.8	0.007	--	-
2.5Co-0.3Ce/Al(α)	2.5	5.1	0.009	25	17.2
5Co-0.5Ce/Al(α)	5.0	5.3	0.011	30	17.2
10Co-1.1Ce/Al(α)	9.9	5.7	0.013	35	17.4
15Co-1.7Ce/Al(α)	15.7	6.0	0.014	39	17.3
20Co-2.2Ce/Al(α)	20.5	5.8	0.012	40	17.5

Analogously to the previous results, the XRD patterns evidenced the signals corresponding to the α-Al_2O_3, Co_3O_4 and CeO_2 phases (Figure 7.10). Segregated ceria was only detected over the 15Co-1.7Ce/Al(α) and 20Co-2.2Ce/Al(α) samples. On the other hand, the relative intensity of the cobalt spinel signals with respect to those of the alumina support consistently increased with Co_3O_4 loading. The mean crystallite size of Co_3O_4, as estimated by applying the Scherrer equation, was found to notably depend on the cobalt content (Table 7.4). Hence, this was 25 nm for the 2.5Co-0.3Ce/Al(α) catalyst and it progressively enlarged with the Co_3O_4 loading up to a reasonably constant value of around 40 nm for the samples with the highest cobalt loadings (15 and 20%wt. Co_3O_4).

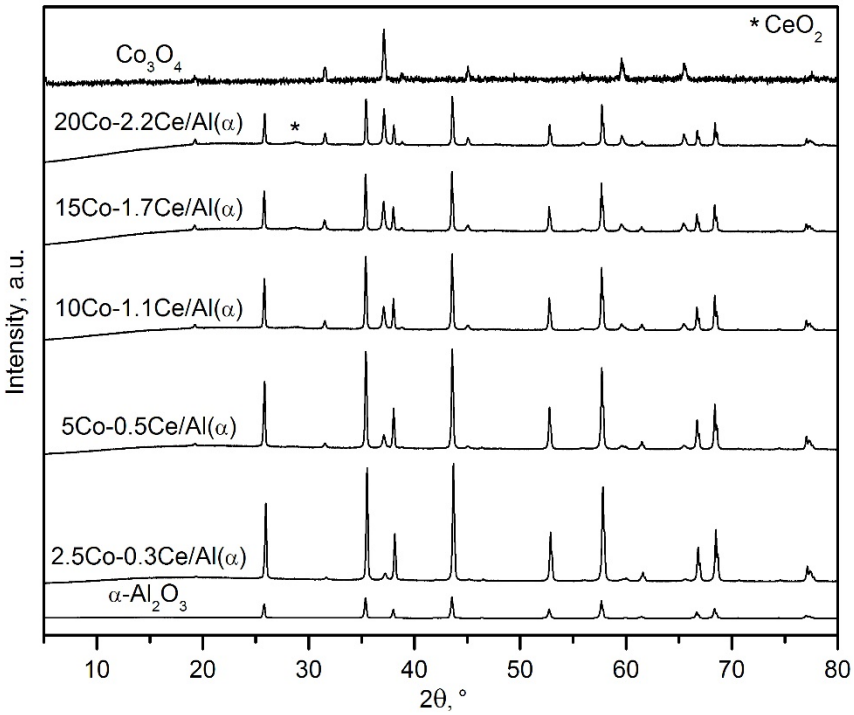

Figure 7.10. Diffraction pattern of the xCo-yCe/Al(α) catalysts.

A certain distortion of the Co_3O_4 lattice was also noted for this set of catalysts as revealed by Raman spectroscopy (Figure 7.11). Thus, the position of the A_{1g} band shifted towards lower values, from 688 cm^{-1} over the 2.5Co-0.3Ce/Al(α) to 675-677 cm^{-1} for the samples with a Co loading between 10-20%wt. Co_3O_4. A similar trend was valid in relation of the FWHM values of this Raman mode, since it increased from 13 cm^{-1} over the catalyst with the lowest Co content to 29 cm^{-1} over the the catalysts with a Co loading of 10-20%wt.Co_3O_4 with a relatively large crystallite size close to 40 nm. However, the crystallites (25-30 nm) of the 2.5Co-0.3Ce and 5Co-0.5Ce samples seemed to be somewhat more resistant to cell distortion by Ce doping judging from their reduced FHWM (13-18 cm^{-1}).

The Co2p XPS spectra of the xCo-yCe/Al(α) catalysts (Figure 7.12) presented the same five contributions previously described for the 10Co-xCe/Al(α) samples. However, in this case, the relative intensity of the spectra varied among the samples, in agreement with their varying cobalt loadings. Besides, the intensity ratio between the two main contributions (centred around 779.5 and 780.7 eV and attributed to Co^{3+} and Co^{2+} ions, respectively)

significantly increased with the cobalt loading, thus evidencing a more predominant presence of Co^{3+} ions in the catalysts with higher cobalt loadings. For the catalysts with lower loadings the Co^{2+} ions were the prevailing species. Likewise, a greater abundance of lattice oxygen species was noticed with increasing Co loading.

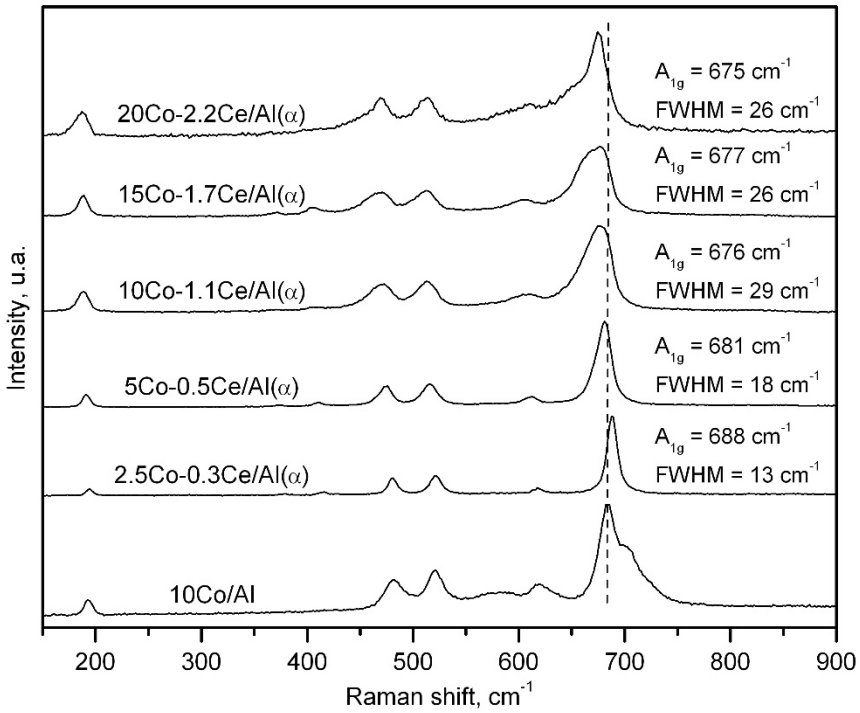

Figure 7.11. Raman spectra of the xCo-yCe/Al(α) catalysts.

The analysis of the surface composition of these samples also revealed important discrepancies with respect to the bulk compositions, similarly to what occurred with the 10Co-xCe/Al(α) catalysts. In this sense, the surface Ce loadings were about 10-20% higher than the nominal bulk loadings for all the examined catalysts. The Co loadings, on the other hand, varied from being 2 times higher than the bulk for the catalysts with lower loadings (2.5Co-0.3Ce/Al(α) and 5Co-0.5Ce/Al(α)), to being slightly lower than the bulk for the catalysts with a higher loading. This could be due to the low dispersion of the cobalt oxide crystallites in the catalysts with higher cobalt loadings.

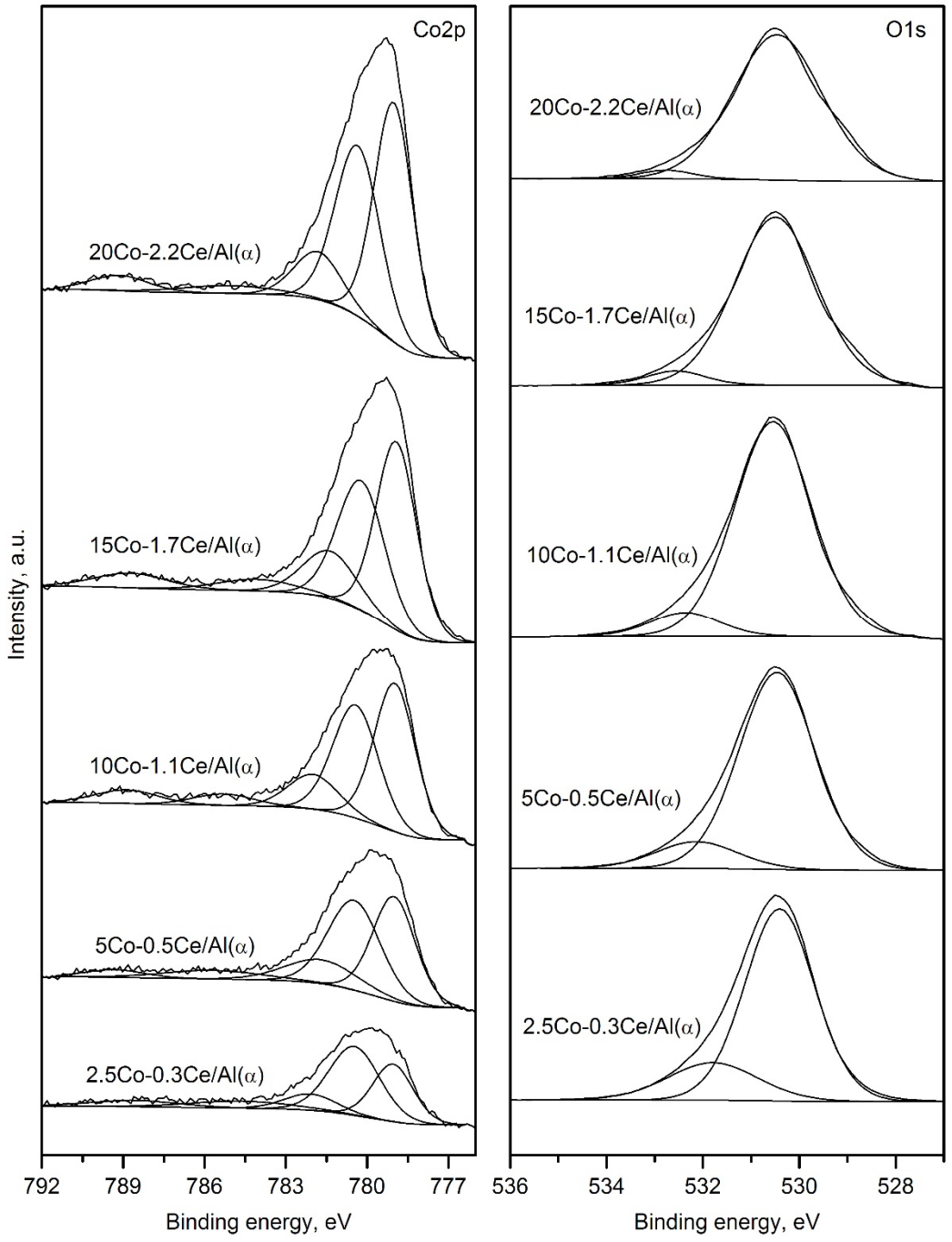

Figure 7.12. Co2p and O1s XPS spectra of the xCo-yCe/Al(α) catalysts.

Table 7.5. Surface composition of the xCo-yCe/Al(α) catalysts.

Sample	Co, %wt.	Ce, %wt.	Co^{3+}/Co^{2+} molar ratio	O_{ads}/O_{latt} molar ratio
2.5Co-0.3Ce/Al(α)	4.2 (1.9)	4.3 (0.2)	0.66	0.25
5Co-0.5Ce/Al(α)	6.1 (3.7)	6.5 (0.4)	0.96	0.15
10Co-1.1Ce/Al(α)	7.0 (7.4)	6.7 (0.9)	1.19	0.10
15Co-1.7Ce/Al(α)	10.3 (11.6)	9.7 (1.4)	1.24	0.06
20Co-2.2Ce/Al(α)	12.9 (15.2)	10.1 (1.8)	1.22	0.04

The values in brackets correspond to the bulk composition as determined by EDXRF.

The cobalt oxide loading also had an effect on the surface species distribution. The catalysts with lower cobalt loadings (2.5Co-0.3Ce/Al(α) and 5Co-0.5Ce/Al(α)) presented lower Co^{3+}/Co^{2+} molar ratios (0.66 and 0.96, respectively) than those with higher loadings, which were between 1.19 and 1.24. Above a cobalt oxide loading of 10%wt., the Co^{3+}/Co^{2+} molar ratio of the catalysts did not vary appreciably. In line with the previous findings, the increase in the abundance of Co^{3+} species was related to decreasing O_{ads}/O_{latt} molar ratios, thus showing a more predominant presence of lattice oxygen species in those catalysts.

The H_2-TPR profiles (Figure 7.13) of the catalysts with the lowest cobalt content, namely the 2.5Co-0.3Ce/Al(α) and 5Co-0.5Ce/Al(α) samples, were characterised by a dominant uptake peaking at 395 and 360 °C, respectively. No clear distinction of the expected of the stepwise reduction process was evident. This was in agreement with other supported cobalt catalysts with this low metal content [317]. For higher metal loadings (10, 15 and 20%wt.) a shoulder located at lower temperatures (290-320 °C) could be ascertained.

The reducibility was promoted for larger crystallite sizes since the H_2 uptake peaked at 335 °C for the 10Co-1.1Ce/Al(α) sample with a mean size of 35 nm. Above this size the reduction temperatures shifted up to 360-375 °C (15Co-1.7Ce/Al(α) and 20Co-2.2Ce/Al(α)), probably due to the fact that a significant fraction of cobalt was present as segregated Co_3O_4 (not deposited on the alumina support). Again, the absence of highly stable cobalt species on the supported catalysts, with expected reduction temperature exceeding 500 °C, was evidenced. On the other hand, the contribution of cerium species to the redox behaviour of the catalysts was also significant with a specific H_2 consumption in the 17.2-17.5 mmol g_{Co3O4}^{-1} range, which was superior to that expected to the exclusive reduction of

Co_3O_4. This excess of H_2 uptake was attributed to the contribution of the reduction of the cerium cations, which in turn can be activated by metallic cobalt [118,258].

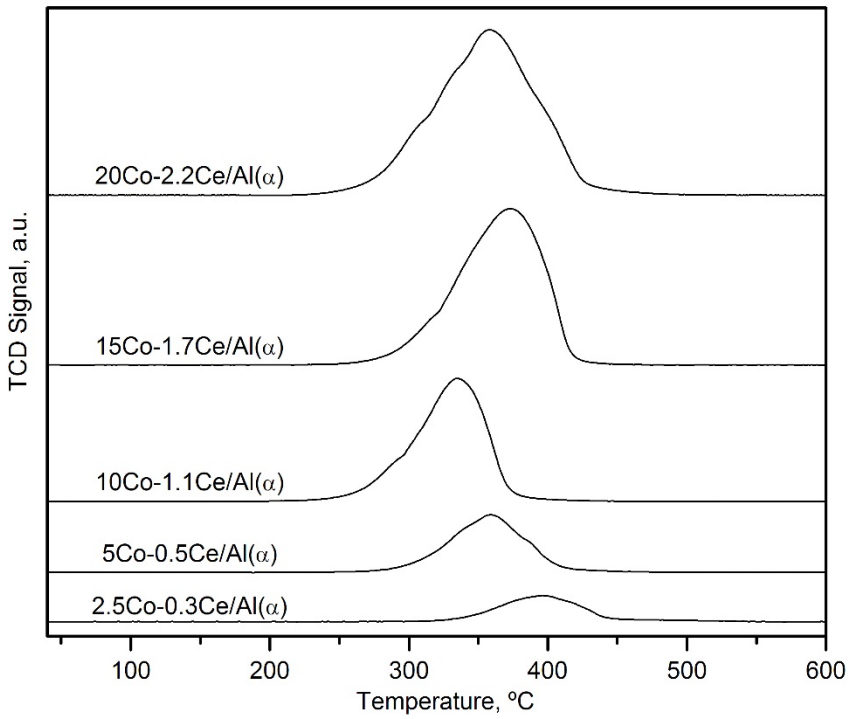

Figure 7.13. H_2-TPR profiles of the xCo-yCe/Al(α) catalysts.

The light-off curves of the combustion of methane are included in Figure 7.14. 100% CO_2 selectivity was always noticed. Clearly, the samples with a relatively low Co loading (2.5Co-0.3Ce/Al(α) and 5Co-0.5Ce/Al(α) samples) evidenced a poorer performance with T_{30} values around 550 °C, and a conversion of 30% and 43% at 600 °C, respectively. A remarkable higher efficiency was observed above this loading (10, 15 and 20%wt.), with no notable differences among these three catalysts. Hence, the T_{30} values were in the 510-520 °C range, while conversion at 600 °C was between 55-61%.

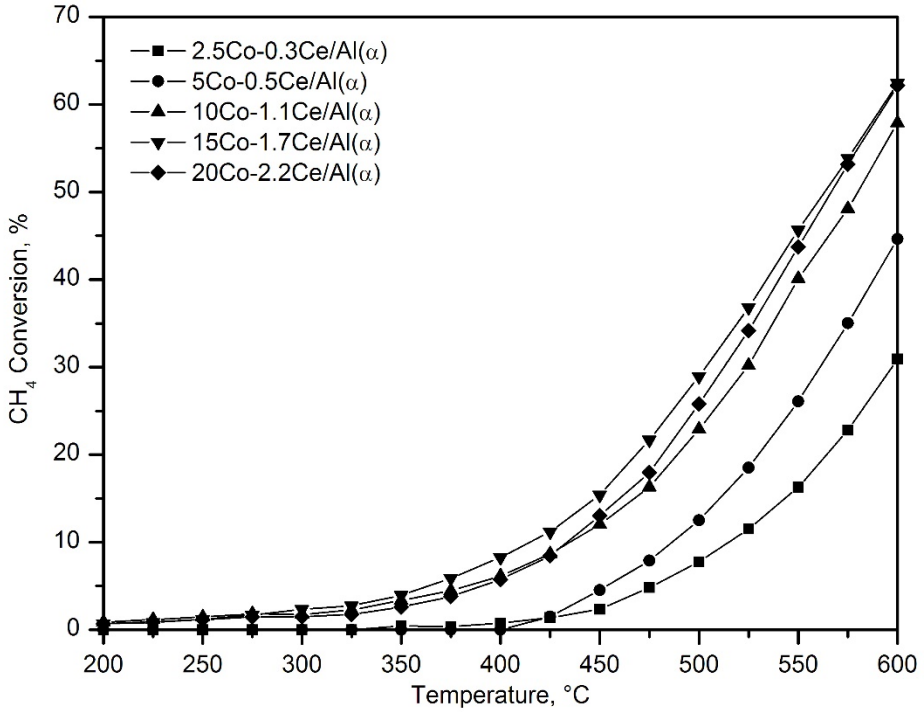

Table 7.14. Light-off curves of the xCo-yCe/Al(α) catalysts.

The activity of the five catalysts was compared in terms of their specific reaction rate estimated under differential conditions (conversion lower than 20%) at a constant temperature (450 °C) (Table 7.6). Results plotted in Figure 7.15 evidenced that the activity was maximised for a Co_3O_4 loading of 10%wt. The better behaviour was connected to its favoured reducibility at lower temperatures which in turn depended on the marked distortion of the Co_3O_4 lattice by cerium for this specific catalyst formulation (10Co-1.1Ce/Al(α)).

Table 7.6. Kinetic results of the xCo-yCe/Al(α) catalysts.

Catalyst	T_{30}, °C	Specific reaction rate at 450 °C, mmol CH_4 g_{Co3O4}^{-1} h^{-1}	E_a, kJ mol^{-1}
2.5Co-0.3Ce/Al(α)	595	2.9	93
5Co-0.5Ce/Al(α)	560	3.3	85
10Co-1.1Ce/Al(α)	520	4.1	72
15Co-1.7Ce/Al(α)	510	3.3	72
20Co-2.2Ce/Al(α)	510	2.2	71

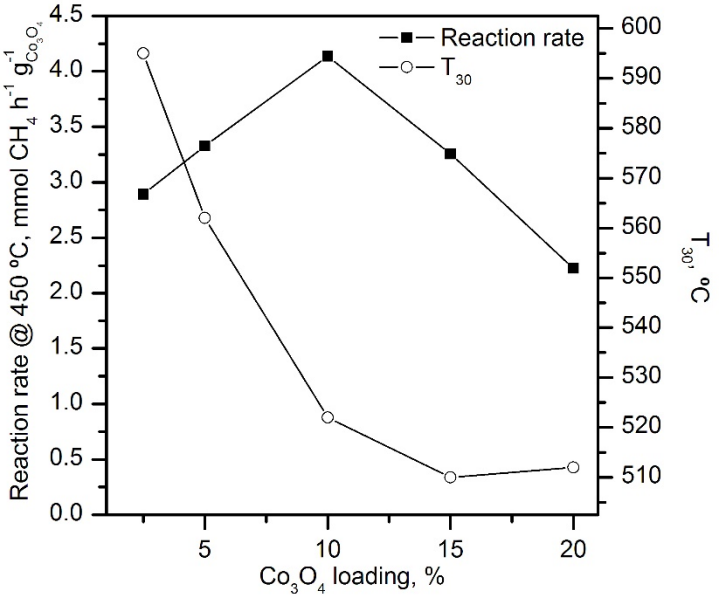

Figure 7.15. Evolution of the specific reaction rate of the xCo-yCe/Al(α) catalysts.

7.1.3. Optimisation of the SCS methodology for Co-Ce catalysts supported over α-Al_2O_3 open cell foams

The last step of our study was focused on designing of a highly efficient structured Co/Ce catalyst for the abatement of lean methane. Hence, once the optimal catalyst composition was defined from the results of the pelleted catalysts, that is, 10%wt.Co_3O_4 and a Ce/Co molar ratio of 0.05, a α-Al_2O_3-based open cell foam (45 ppi) was selected as structured support. Table 7.7 summarises the main geometric properties of the foam substrate.

Table 7.7. Main properties of the open cell foam structured catalysts.

Property	Value
Cell density	45 ppi
Overall dimensions, mm x mm	8 x 30
Overall foam volume, cm^3	1.51
Catalyst mass, mg	≈ 200
Average pore dimension, mm	1.03
Voidage	0.895
Geometric surface area, $m^2\ m^{-3}$	1212
Open frontal area, m^2	$5.03 \cdot 10^{-5}$
Catalyst loading, mg cm^{-2}	11.27

For incorporating the active phase(s) onto the walls of the foam we opted for the solid combustion synthesis (SCS). In addition to avoiding the intermediate and time-consuming steps that other conventional routes would require, this methodology usually leads to well crystallised with nanometric size clusters [313,318,319]. The key operational parameters of the SCS route are basically the selection of the fuel and the corresponding appropriate fuel-to-oxidiser (metallic nitrates) ratio, which is typically denoted as Φ. These two factors strongly influence the mechanism of the combustion process and, in turn, the morphological properties of the active phase. In addition, attention was paid to analysing the use of two different fuels, namely urea and glycine, since these are cheap and readily available commercially, while the Φ ratio was simultaneously varied between 0.25 and 1.0, which corresponded to 25-100% stoichiometric amount of fuel, respectively.

The optimisation of the SCS route was performed by preparing catalysts supported over α-Al_2O_3 open cell foams (*Lanik, s.r.o.*, 45 cpi, length = 30 mm and diameter = 8 mm) with the optimal cobalt loading (10%wt. Co_3O_4) and Ce/Co molar ratio (0.05) as already defined in the previous steps. For the study of the influence of the Φ ratio, four catalysts were synthesised over α-Al_2O_3 cell foams, using urea and glycine as fuels for the combustion. The selected values of Φ were 0.25, 0.50, 0.75 and 1.00. The foams were submerged into the impregnation solutions for 5 minutes, after which the excess was removed with compressed air. The impregnated foams were placed in an oven at 250 °C for 20 minutes to induce the combustion. To prepare foam catalysts with the desired cobalt loadings, several successive

cycles of impregnation-combustion were needed. After the last cycle, the impregnated foams were calcined at 600 °C for 4 hours to form the final catalysts.

For defining the number of cycles required to achieve the desired amount of CeO_2-doped Co_3O_4 (approximately 10%wt.Co_3O_4 and 1%wt.CeO_2), the evolution of the mass oxide concentration as function of the number of cycles is included in Figure 7.16. This graph includes the mean oxide concentration for each cycle, which was calculated from gravimetric measurements of duplicate samples prepared with both fuels and the entire Φ range (0.25-1.0). Thus, data from 16 samples were averaged for each cycle. Hence, the consecutive cycles led to an increase in oxide concentration from about 1% (1st cycle), 2% (2nd cycle), 6% (3rd cycle) to 10% (4th cycle). Particularly, the final oxide content after the fourth cycle varied between 9.3-10.8%wt. Moreover, note that irrespective of the synthesis conditions (type of fuel and Φ ratio) the amount of oxides loaded in each cycle was quite reproducible. In sum, four cycles were required to attain the target concentration.

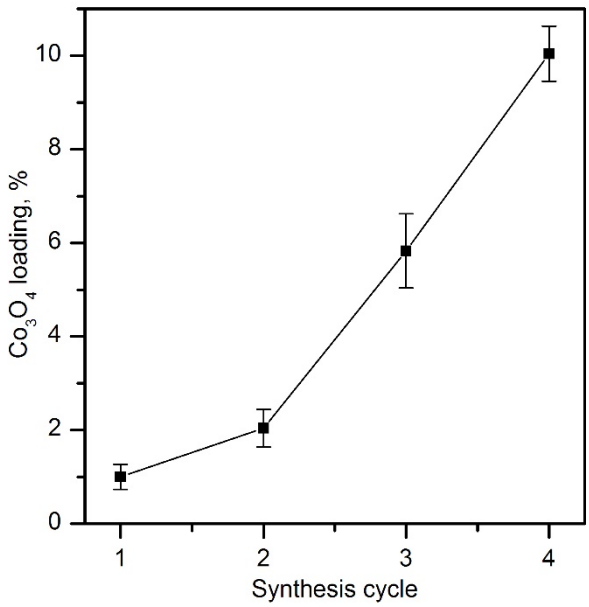

Figure 7.16. Evolution of the Co_3O_4 loading with the number of SCS cycles over α-Al_2O_3 open cell foams.

To allow for the characterisation of the structured catalysts, the foams were crushed and milled to a powder and then investigated by XRD and H_2-TPR, with the aim of studying the effect of the type of fuel and Φ ratio over the structural and redox properties of the deposited cobalt oxide. The X-Ray diffractograms of the structured catalysts prepared with urea and glycine are shown in Figures 7.17 and 7.18, respectively. The diffraction pattern of powdered alpha-alumina is also included for the sake of comparison. All structured catalysts presented intense signals from a trigonal phase (2θ = 25.3, 34.8, 37.4, 43.0, 52.1, 57.0, 60.7, 65.9, 67.5 and 76.1°), comparable to those exhibited by the pure alpha-alumina sample, which evidenced that the structure of the alpha-alumina that formed the open cell foams was identical to that of the previously used alumina support. Also, all samples presented two sets of signals from different phases: a cubic phase, attributed to the presence of the cobalt spinel oxide Co_3O_4, at 2θ = 19.0, 31.3, 36.8, 38.5, 44.8, 59.4 and 65.2°, and a second set of peaks at 2θ = 16.7, 21.9, 26.7, 33.4, 41.2 and 61.5°, characteristic of the presence of graphitic carbon and graphene oxide [320], which could be a residue of the combustion of the organic fuels during the synthesis.

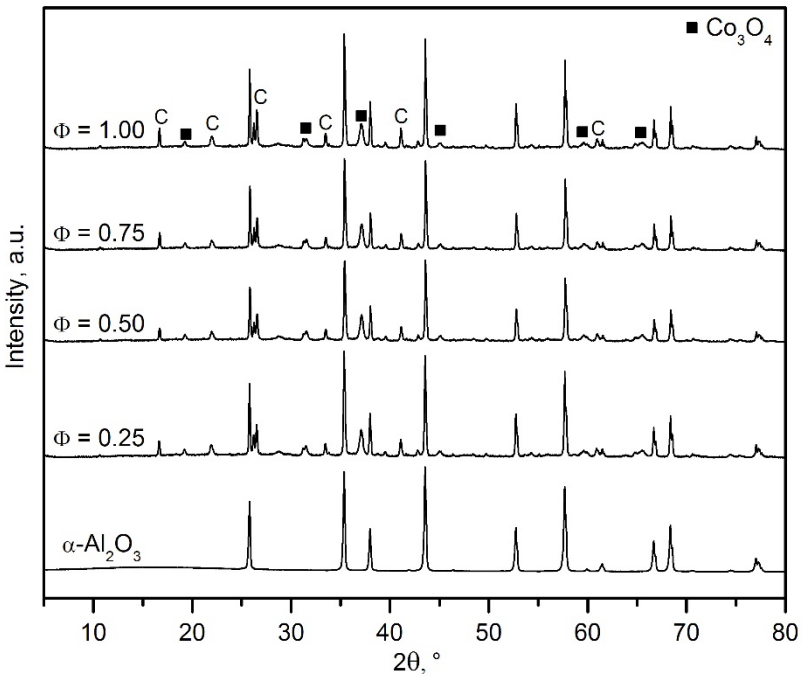

Figure 7.17. X-Ray diffractograms of the structured catalysts prepared with urea.

The mean crystallite size of the Co_3O_4, estimated by the Scherrer equation, was around 50 nm for the catalysts prepared with urea and between 19 and 28 nm for the catalysts prepared with glycine. The amount of urea did not seem to have a very remarkable effect on the crystallite size, while when using glycine the crystallite size slightly decreased with the Φ ratio.

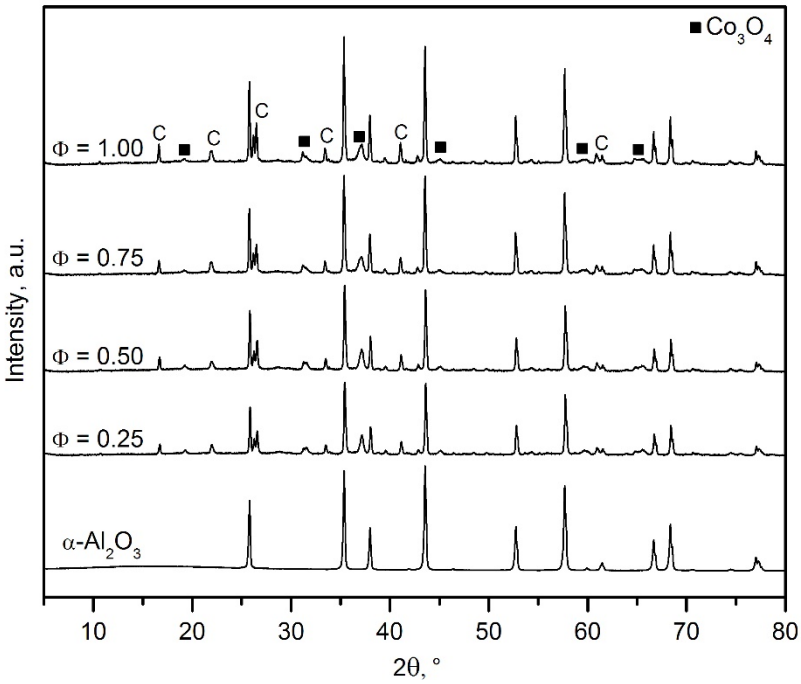

Figure 7.18. X-Ray diffractograms of the structured catalysts prepared with glycine.

Figures 7.19 and 7.20 shows the TPR profiles of the catalysts prepared with the two fuels (urea and glycine), respectively. It must be noticed that no H_2 uptake was observed above 400 °C for any of the samples, which evidenced that the only reducible phase present on them was Co_3O_4. Expectedly, all traces showed a two-step reduction process, although the signal intensity that characterised each of the events varied significantly between the two selected fuels and also strongly depended on the Φ ratio. Thus, for the catalysts synthesised with urea, the low-temperature step (centred at 275-315 °C), generally attributed to the reduction of Co^{3+} ions to Co^{2+}, was barely noticeable irrespective of the Φ ratios, Hence, the observed H_2 uptake of these samples essentially corresponded to the high-temperature reduction step (centred at 350-370 °C).

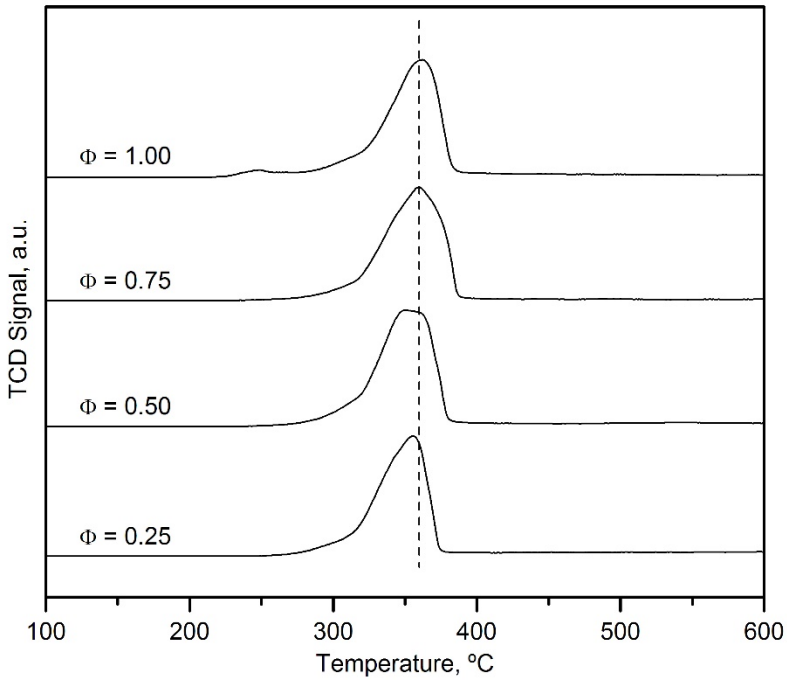

Figure 7.19. H_2-TPR profiles of the structured catalysts prepared with urea.

On the other hand, as for the catalysts prepared with glycine the low-temperature H_2 uptake was almost negligible for the Φ = 0.25 sample, but became more noticeable for increasing Φ ratios, up to the point of being clearly discernible over the samples with a Φ of 0.75 and 1. This result suggested that only high Φ ratios only had a positive effect on the reducibility of Co_3O_4.

The specific H_2 uptakes, obtained by integration of the TPR profiles, are summarised in Table 7.8. The total H_2 uptake of the urea-based samples was comparable among all the samples (around 17. 4 mmol g_{Co3O4}^{-1}), and the low-temperature contribution was identical (1.4 mmol g_{Co3O4}^{-1}) as well, thereby suggesting that the influence of the Φ ratio on the reducibility of the deposited Co_3O_4 was barely perceptible. Conversely, the total H_2 uptake varied between 17.3 and 17.8 mmol g_{Co3O4}^{-1} over the catalysts prepared with glycine, while the contribution at low temperature increased with the Φ ratio, from 1.7 mmol g_{Co3O4}^{-1} for Φ = 0.25 to 3.2 mmol g_{Co3O4}^{-1} for Φ = 1. This evidenced that larger amounts of glycine during synthesis favoured the reducibility of the resulting Co_3O_4 catalyst.

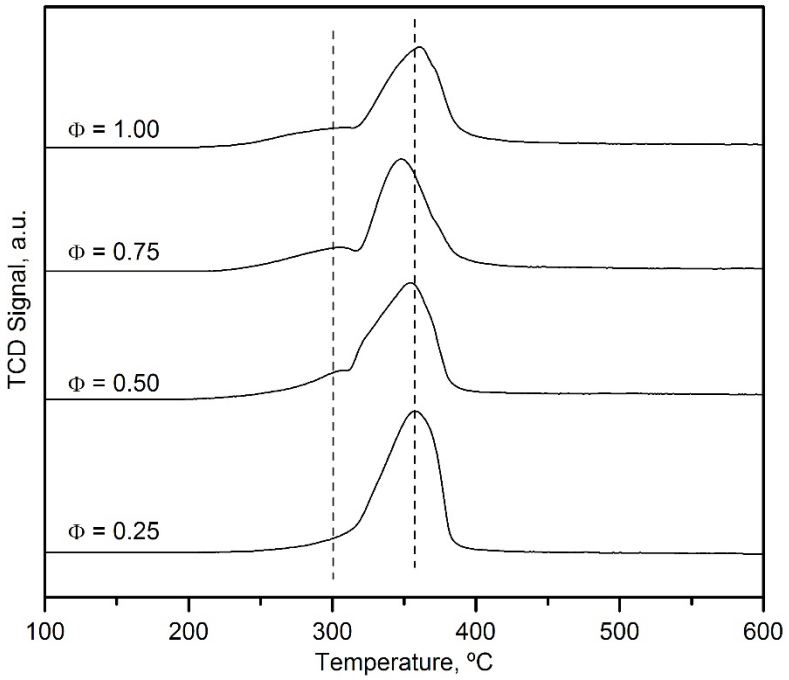

Figure 7.20. H_2-TPR profiles of the structured catalysts prepared with glycine.

Table 7.8. Specific H_2 uptake of the catalysts prepared with urea.

	Urea		Glycine	
F/O ratio	Low-temperature H_2 uptake, mmol g_{Co3O4}^{-1}	High-temperature H_2 uptake, mmol g_{Co3O4}^{-1}	Low-temperature H_2 uptake, mmol g_{Co3O4}^{-1}	High-temperature H_2 uptake, mmol g_{Co3O4}^{-1}
0.25	1.4	16.0	1.7	15.9
0.50	1.4	16.0	2.3	15.0
0.75	1.4	16.1	2.6	14.9
1.00	1.4	15.9	3.2	14.6

Prior to the crushing of the structured catalysts, SEM and TEM pictures were taken in order to ascertain the morphology and size of the deposited Co_3O_4 crystallites, and the effect of using each of the two tested fuels on these properties.

The comparison of the two SEM pictures in Figure 7.21 clearly evidenced the structural differences between using urea and glycine as fuels ($\Phi = 1$). The catalyst prepared with urea presented a surface extensively covered by flat, round patches of cobalt oxide of around 250-300 nm in diameter. Conversely, the surface of the samples prepared with glycine presented much smaller, spherical crystallites of around 25 nm in diameter which were adequately dispersed on the surface of the α-Al_2O_3 substrate. A notable consistency was observed with the results given by XRD (19-28 nm). The crystallites in this catalyst presented such a small size that it was not possible to clearly mark off their contour by SEM analysis.

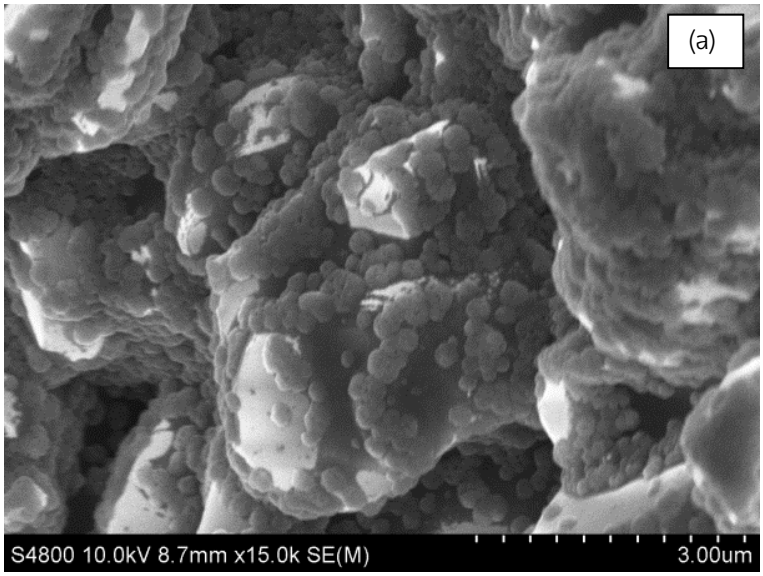

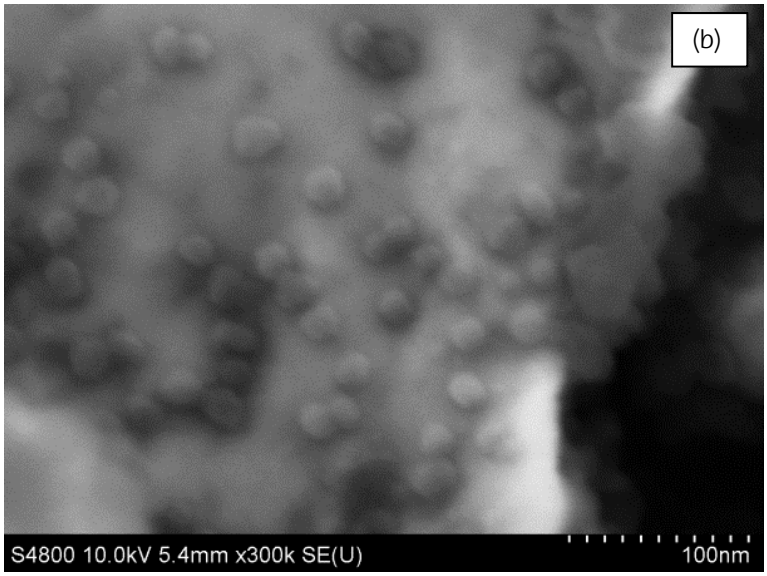

Figure 7.21. SEM pictures of the structured catalysts prepared by SCS ($\Phi = 1$) with urea (a) and glycine (b).

HRTEM analysis of the crushed foam catalysts prepared with both fuels at $\Phi = 1$ (Figure 7.22) offers additional insights into the structure and morphology of the Co_3O_4 crystallites deposited on the structured catalysts. From the low-resolution images the same results given by SEM analysis were corroborated since large metallic clusters were observed for the sample prepared with urea while comparatively smaller crystallites were detected over the counterpart synthesised with glycine.

On the other hand, the differences in morphology of the deposited crystallites became more noticeable in the high-resolution images. In the case of the catalyst prepared with glycine, round crystals of about 20-25 nm were clearly identifiable along the surface of the sample, although in certain areas their accumulation was notable. The urea counterpart, however, only exhibited small crystallites on the edges of the particles, but these were notably less abundant with respect to the catalysts prepared with glycine. In this case, the identification of crystallites in the inner part of the catalytic particles was not possible.

Finally, from the images with a resolution of 5 nm, the individual crystallites could be identified and their respective lattice fringes could be resolved. Interestingly, in both cases

small Co_3O_4 crystallites of about 5-10 nm were observed, irrespective of the fuel type; although its number was significantly higher in the catalyst prepared with glycine. Additionally, CeO_2 crystallites of around 5 nm were identified as well, although their presence was much lower with respect to that of Co_3O_4.

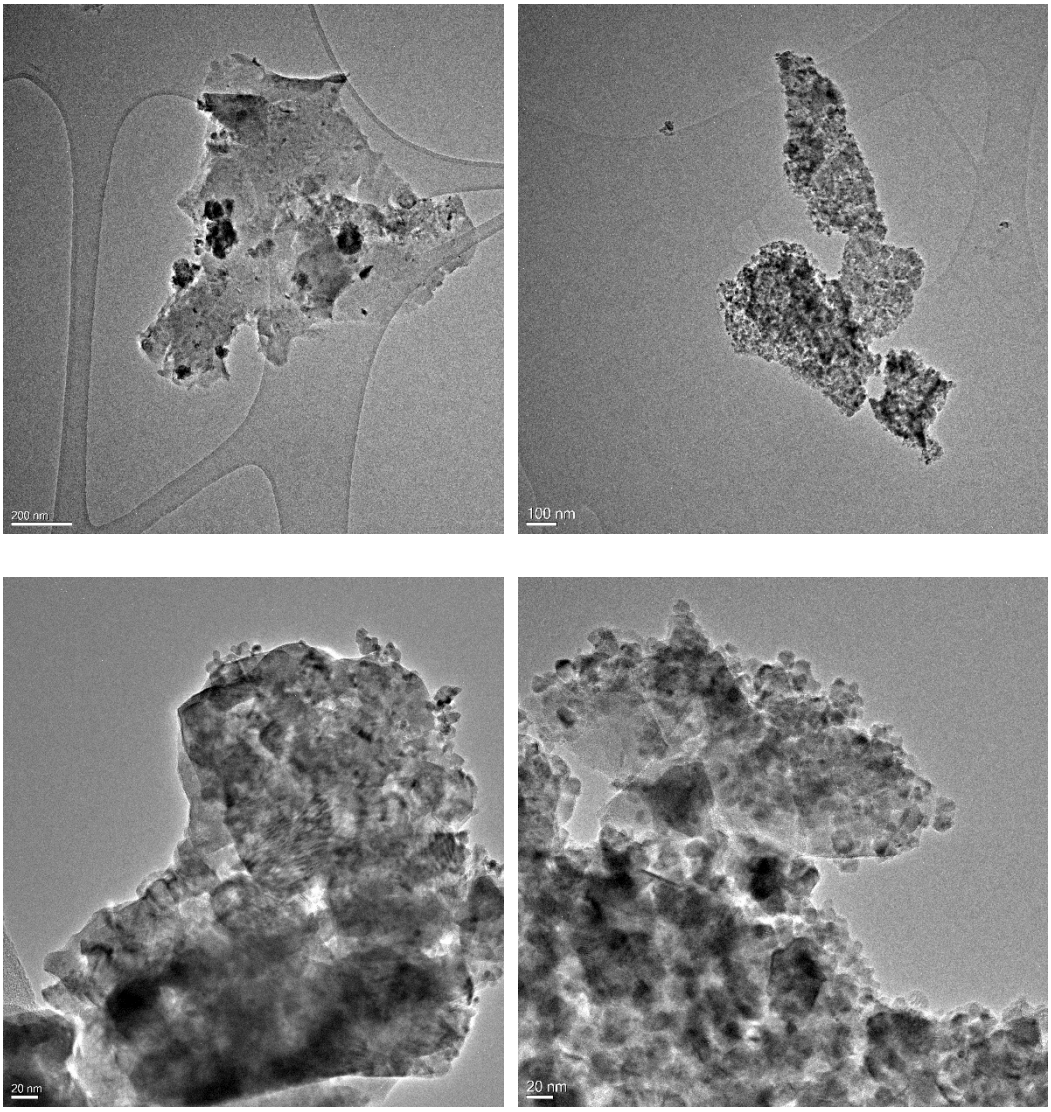

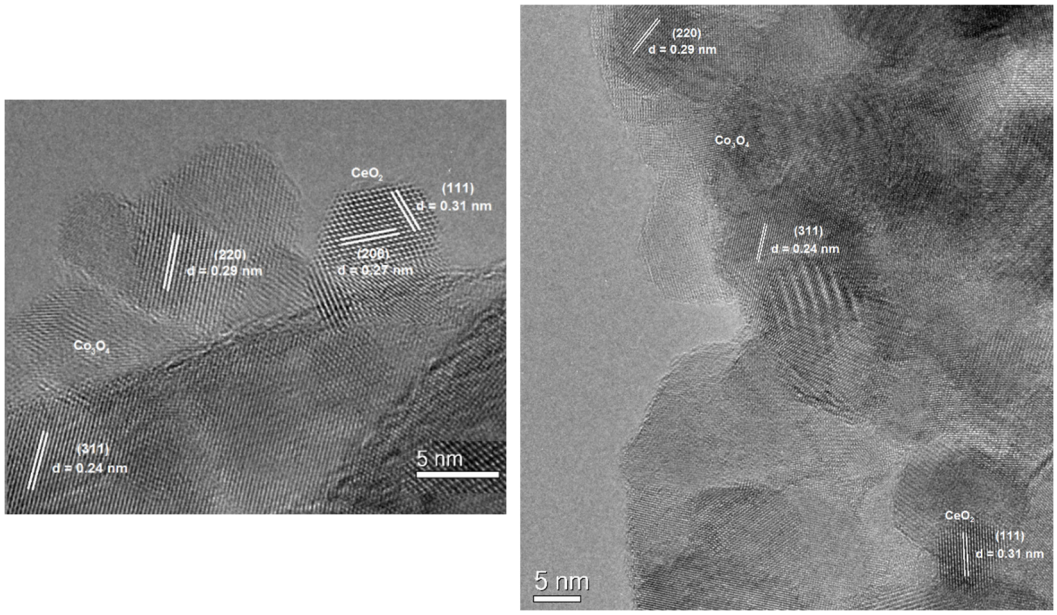

Figure 7.22. HRTEM pictures of the structured catalysts prepared by SCS ($\Phi = 1$) with urea (left) and glycine (right).

HAADF-STEM images along with the corresponding EDX maps of the structured catalysts prepared with both fuels and $\Phi = 1$ are shown in Figure 7.23. These EDX elemental maps were useful to determine the differences in the distribution of cobalt and cerium on the surface of the structured catalysts with the fuel employed in the synthesis. In this sense, the catalyst prepared with urea exhibited clusters of around 100 nm of both metals separately with very low mixing between cobalt and cerium, and the coverage of the surface of alpha-alumina was significantly low. Hence, it was clearly evidenced that the dispersion of both cobalt and cerium was extremely poor when the catalyst was prepared with urea. On the other hand, when the catalyst was prepared with glycine, the surface of alpha-alumina was completely covered with both metals, which also presented a good dispersion and mixing between them, with almost no segregated clusters of ceria. These results pointed out the significantly better structural properties of the supported catalyst prepared with glycine with respect to the urea counterpart.

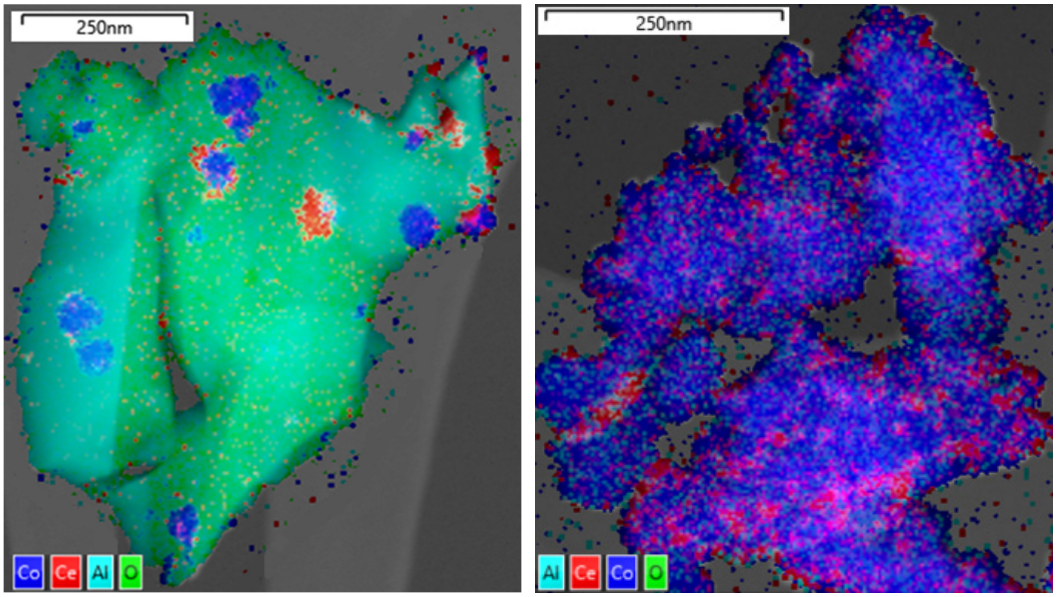

Figure 7.23. HAADF-STEM images of the structured catalysts prepared by SCS (Φ = 1) with urea (left) and glycine (right), coupled with EDX elemental distribution of Co (dark blue), Ce (red), Al (light blue) and O (green).

Figures 7.24 and 7.25 shows the corresponding light-off curves of the oxidation of lean methane over the foam catalysts prepared with each fuel and varying Φ ratio. The GHSV was around 4,000 h^{-1}, calculated on the basis of the total volume of structured foam catalyst (1.5 cm^3).

Previously, the absence of mass and heat transfer limitations within the reactor was checked in order to ensure that the obtained kinetic results were not affected by them. However, since the transfer regimes for a structured catalyst significantly varies with respect to their powdered counterparts, the evaluated criteria needed to be modified. In this case, four different criteria were checked, following the recommendations of Ercolino et al. [129] and Italiano et al. [323]. Unless stated otherwise, the symbol notation applied in these equations corresponds to the one utilised in Chapter 2 (see Table 2.3).

1. External mass transfer: Carberry criterion

For the effects of the external diffusion to be considered negligible, the Carberry number should be lower than 0.05, according to Equation 7.1.

$$Ca = \frac{r_{v,obs}}{k_f \cdot GSA \cdot C_b} < 0.05 \tag{7.1}$$

where GSA is the geometric surface area of the open cell foam per unit of volume.

2. Internal mass transfer: Weisz-Prater criterion

Similarly, if the effects of diffusion inside the pores of the structured catalysts are not affecting the reaction kinetics, then the Weisz-Prater criterion should hold as follows:

$$WP = \frac{r_{obs} \cdot \rho_c \cdot \delta_c^2}{D_e C_i} < 1 \tag{7.2}$$

Where r_{obs} is the reaction rate per mass unit of catalyst, ρ_c is the density of the catalytic layer and δ_c is the thickness of the catalytic layer.

3. External heat transfer: Mears criterion

The absence of heat transfer limitations in the gas-solid interphase can be ensured when the Mears criterion holds, as follows:

$$\frac{E_a(-\Delta H_r) r_{v,obs}}{h \cdot GSA \cdot RT^2} < 0.15 \tag{7.3}$$

4. Internal heat transfer: Anderson criterion

Finally, the temperature gradients inside the catalytic coating can be neglected if the Anderson criterion is met, as follows from Equation 7.4.

$$\frac{E_a(-\Delta H_r) r_{obs} \cdot \rho_c \cdot \delta_c^2}{\lambda_e RT^2} < 0.75 \tag{7.4}$$

As an example, Table 7.9 shows a summary of the values of the four criteria for several temperatures in the whole studied range (200-600°C) for the structured catalyst prepared with glycine and a Φ ratio of 1, which was the one that achieved the closest values to the

aforementioned limits. The analysis of the four criteria revealed that there were not diffusional or heat transfer limitations affecting the obtained kinetic results.

Table 7.9. Criteria for accurate analysis of intrinsic reaction rates of structured catalysts (as evaluated for the catalyst prepared at $\Phi = 1$ with glycine).

Temperature, °C	Carberry	Weisz-Prater	Mears	Anderson
200	$5.6 \cdot 10^{-6}$	$2.9 \cdot 10^{-8}$	$1.2 \cdot 10^{-4}$	$2.0 \cdot 10^{-6}$
250	$2.7 \cdot 10^{-5}$	$1.6 \cdot 10^{-7}$	$5.5 \cdot 10^{-4}$	$9.3 \cdot 10^{-6}$
300	$9.6 \cdot 10^{-5}$	$6.1 \cdot 10^{-7}$	0.0018	$3.1 \cdot 10^{-5}$
350	$2.6 \cdot 10^{-4}$	$1.8 \cdot 10^{-6}$	0.0047	$8.2 \cdot 10^{-5}$
400	$5.5 \cdot 10^{-4}$	$4.0 \cdot 10^{-6}$	0.0093	$1.6 \cdot 10^{-4}$
450	$7.9 \cdot 10^{-4}$	$6.2 \cdot 10^{-6}$	0.0127	$2.2 \cdot 10^{-4}$
500	$6.9 \cdot 10^{-4}$	$5.7 \cdot 10^{-6}$	0.0105	$1.9 \cdot 10^{-4}$
550	$4.3 \cdot 10^{-4}$	$3.8 \cdot 10^{-6}$	0.0062	$1.1 \cdot 10^{-4}$
600	$9.2 \cdot 10^{-7}$	$8.6 \cdot 10^{-9}$	$1.3 \cdot 10^{-5}$	$2.3 \cdot 10^{-7}$

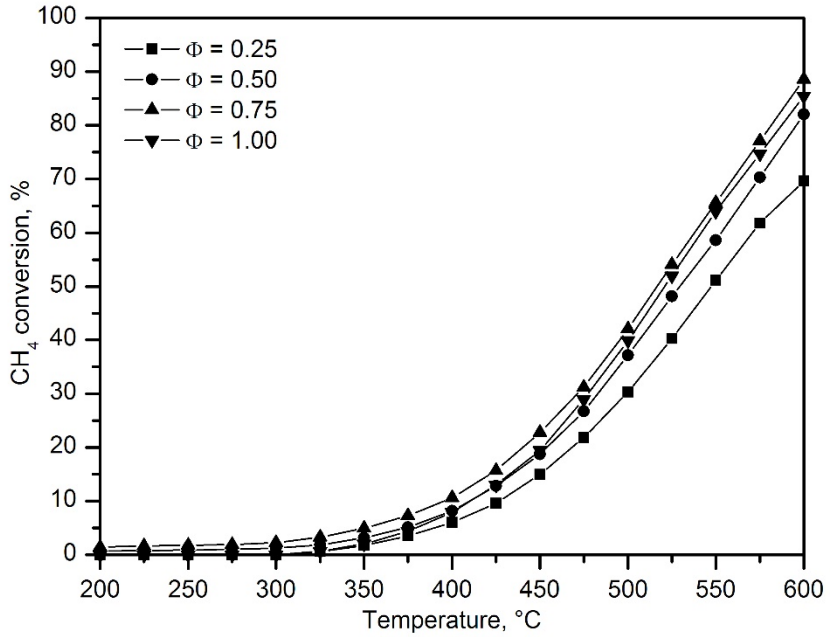

Figure 7.24. Light-off curves of the foam catalysts prepared by SCS with urea.

As for the structured catalysts synthesised with urea an appreciable conversion (10%) was noticed at 400-425 °C. In view of the T_{50} values (Table 7.10) the foam samples with a Φ = 0.75 and Φ = 1.0 showed a similar efficiency with values in the 515-520 °C range, whereas the samples with Φ = 0.5 required 530 °C for this conversion level (50%). Clearly, the poorest performance was shown by the foam catalyst prepared with the lowest amount of urea (Φ = 0.25). Accordingly, the conversion trend at 600 °C followed the same order, that was, 85% conversion (Φ = 0.75-1.0), 80% conversion (Φ = 0.5) and 70% conversion (Φ = 0.25).

Table 7.10. Kinetic results of the foam catalysts prepared by SCS with urea.

Catalyst	T_{50}, °C	Specific reaction rate at 400 °C, mmol CH_4 g_{Co3O4}^{-1} h^{-1}	E_a, kJ mol^{-1}
Φ = 0.25	545	1.2	72 ± 2
Φ = 0.50	530	1.2	73 ± 1
Φ = 0.75	515	1.7	71 ± 2
Φ = 1.00	520	1.4	74 ± 1

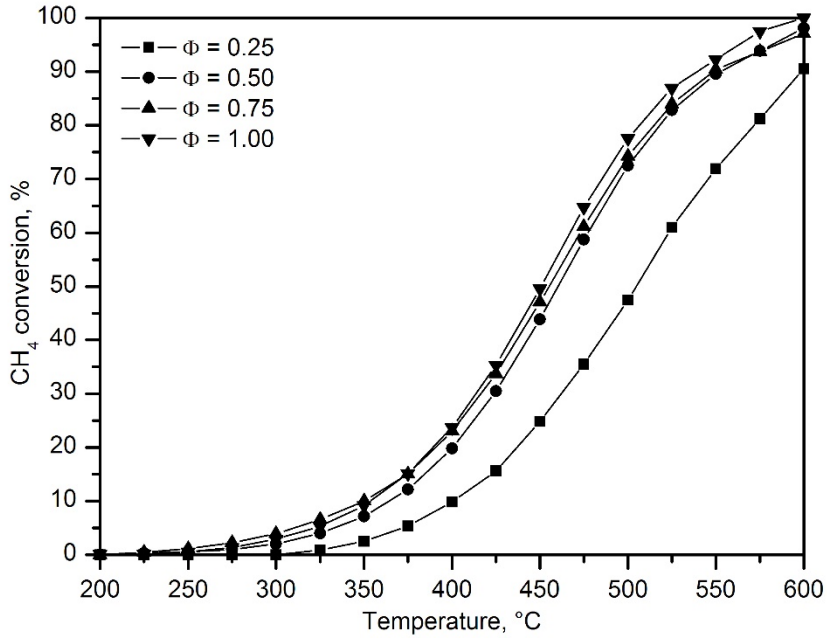

Figure 7.25. Light-off curves of the foam catalysts prepared by SCS with glycine.

In contrast, the use of glycine as fuel comparatively resulted in much more attractive foam catalysts. Hence, at 400-425 °C a conversion as high as 20% was already noticed. No substantial differences were observed among the samples with a Φ ratio of 1.0 (T_{50} = 450 °C), 0.75 (T_{50} = 455 °C) and 0.5 (T_{50} = 460 °C), as shown in Table 7.11. Thus, these three samples achieved at least 95% conversion at 600 °C. Again the catalyst prepared with the lowest Φ ratio exhibited a considerably poorer performance (T_{50} = 500 °C). This could be due to the low amount of fuel not being enough to completely combust the metallic nitrates impregnated on the support, thereby causing a part of that cobalt nitrate to decompose by the thermal route followed by the direct calcination (DC) catalyst. Recall that this route produced a less active catalyst than the route followed by the solution combustion synthesis (SCS) catalyst. Similar results have already been reported in other studies [112,321], being connected to the fact that the lower amount of fuel leads to a reduced development of gaseous products, which in turn translated into lower porosity of the active phase.

Table 7.11. Kinetic results of the foam catalysts prepared by SCS with glycine.

Catalyst	T_{50}, °C	Specific reaction rate at 400 °C, mmol CH_4 g_{Co3O4}^{-1} h^{-1}	E_a, kJ mol^{-1}
Φ = 0.25	505	1.5	76 ± 2
Φ = 0.50	460	2.9	74 ± 1
Φ = 0.75	450	3.5	70 ± 2
Φ = 1.00	450	4.0	71 ± 2

Despite the differences in activity found between the foam catalysts obtained with both fuels, the apparent activation energies of all the tested samples were in the 70-76 kJ mol^{-1} range, which are values comparable to those exhibited by the bulk Co_3O_4 catalysts from chapters 3 and 4. Since the active phase in the open cell foam catalysts was also the Co_3O_4, it could be concluded that the kinetic results obtained over them were not affected by any diffusional limitations, since that would have altered the results and given different values of the activation energies.

Once evidenced that glycine was a more suitable fuel for depositing the active phases over the open cell foams by solid combustion synthesis, the determination of the optimal Φ ratio was made on the basis of the comparison of the specific reaction rate at a selected

temperature of 400 °C. Results included in Tables 7.10 and 7.11 and subsequently compared in Figure 7.26 revealed a notable dependence of the intrinsic activity with increased amounts of fuel. Hence, the reaction rate notably increased from 1.5 ($\Phi = 0.25$) to 3.0 mmol CH_4 g_{Co3O4} h^{-1} ($\Phi = 0.5$). This promotion, although less noticeable, was also evident with larger amounts of fuel. In this way, the foam catalyst prepared with the highest Φ ratio ($\Phi = 1$) exhibited a reaction rate of 4 mmol CH_4 g_{Co3O4} h^{-1}. For comparative purposes, obtained results with urea as fuel were included in Figure 7.26 as well. As dictated by the light-off curves, the intrinsic activity at 400 °C was remarkably lower, in the 1.2-1.5 mmol CH_4 g_{Co3O4} h^{-1} range. Furthermore, the differences in behaviour among the various Φ ratios were rather less significant.

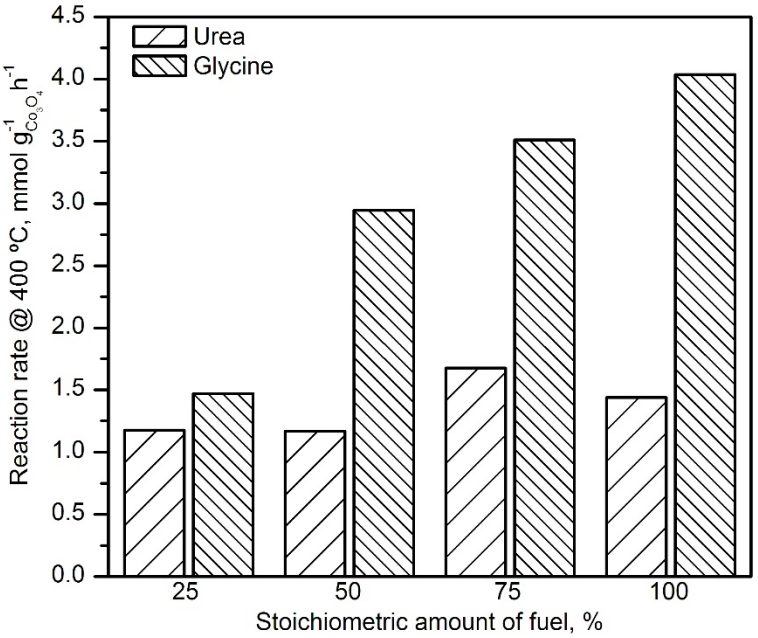

Figure 7.26. Relationship between the specific reaction rate of the catalysts supported over α-Al_2O_3 open cell foams and the Φ ratio.

In addition to that, a significant correlation was found between the low-temperature H_2 uptake of the catalysts prepared with glycine and their specific reaction rate, as shown in Figure 7.27. This trend was presumably also maintained for the catalysts prepared with

urea, taking into account that the specific reaction rates of these samples were almost identical between themselves.

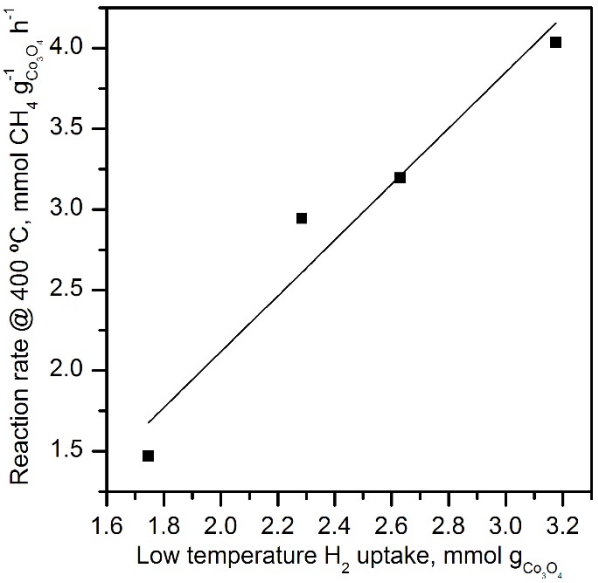

Figure 7.27. Relationship between low-temperature H_2 uptake and the activity of the foam catalysts prepared with glycine.

The superior performance of the catalysts prepared with glycine with respect to the urea counterparts seemed to be associated with their better structural properties of the active phase, as revealed by the SEM photographs. However, the mechanism that leads to those improved properties with one fuel but not the other is not known. The analysed literature is not particularly clear about this point, but a correlation apparently exists between the chemical properties of the fuel-metal precursor complex that is formed in the solution and the properties of the resulting catalyst. More specifically, Mukasyan et al. [322] proposed that the ignition temperature of the fuel-metal complex and the temperature at which the fuel interacts with oxygen in ambient air are the main parameters determining the properties of the final product. In this sense, the carboxylate group present in glycine seems to be key for the formation of a cobalt complex with higher stability than the one formed by the union of urea and cobalt nitrate, although the specific details and mechanisms behind this process are yet to be described [319].

7.2. GLOBAL OVERVIEW AND CONCLUSIONS

In this last chapter, the viability of incorporating the Co_3O_4-CeO_2 formulation into a structured support was investigated. The selected structured supports were α-Al_2O_3 open cell foams. This substrate was chosen on the basis of its low interaction potential with cobalt, which would minimise the problems associated with the formation of cobalt aluminate and the subsequent negative impact on the redox properties. However, due to its extremely low specific surface area, it would also present a limitation related to the metallic loading that it would be capable of supporting effectively. For this reason, the formulation of the Co_3O_4-CeO_2 system needed to be optimised beforehand. The optimisation strategy involved determining the optimal Ce/Co molar ratio and Co_3O_4 loading, as well as the optimal fuel/oxidizer ratio for the solution combustion synthesis.

On one hand, the suitable Ce/Co molar ratio was found to be around 0.05. More specifically, this catalyst exhibited the lowest reduction temperature, which was probably due to an optimal Ce-Co interaction. The catalyst without cerium exhibited a remarkably lower activity with respect to the rest of the Co-Ce catalysts, thus showing that the interaction between Co_3O_4 and CeO_2 was essential for the catalytic behaviour of these systems. For higher Ce/Co ratios, ceria started segregating and a saturation effect was observed. The optimal ratio found in this chapter was comparable to that obtained in Chapter 4 for the cerium-doped bulk Co_3O_4 catalysts.

On the other hand, the optimal Co_3O_4 loading was found to be around 10%wt. Co_3O_4. Again, this catalyst exhibited the lowest reduction temperature of all the investigated catalysts, which allowed it to exhibit the best catalytic performance. The samples with lower loadings were deemed to possess some inhibiting phase, on account of their higher apparent activation energy, while for higher loadings, the poorer dispersion of the Co_3O_4 did not allow for a good reducibility of the active phase.

Regarding the solution-combustion synthesis route, glycine was found to produce catalysts with a considerably better performance than urea when used as fuel, with specific reaction rates being around 3 times higher. The reason behind this behaviour was found in the morphology and size of the cobalt oxide crystallites that were obtained with each fuel. In particular, the catalyst prepared with glycine exhibited relatively small, well dispersed spherical crystallites, while the counterpart synthesised with urea presented large flat

patches of cobalt oxide. The optimal fuel/oxidiser ratio for glycine was found to be the stoichiometric one.

The preliminary results obtained in this final chapter revealed that Co_3O_4-CeO_2 catalytic systems could be successfully implemented into structured supports via solution combustion synthesis, and that the resulting structured catalysts would still show a good catalytic behaviour in the complete oxidation of lean methane. However, open cell foams can be manufactured with many other materials such as zirconia or silicon carbide, and some other structured supports such as cordierite monoliths could be used for the intensification of the previously optimised catalyst. For this reason, further research work is needed on the effect of the structured support material and geometrical configuration, since the random bubble structure of the open cell foams and the channel geometry of the monoliths do not provide the same mass and heat transfer conditions.

Chapter 8

SUMMARY AND CONCLUSIONS

8. SUMMARY AND CONCLUSIONS

8.1. SUMMARY

Climate change is one of the most important environmental challenges that society is facing nowadays. Although its effects are already noticeable, climate change also possesses an immense threat in the medium- and long-term if measures are not put in place to avoid or minimise it. Climate change is a complex phenomenon with multiples causes, effects and feedbacks. However, its main cause is the global warming generated due to the emissions of greenhouse effects gases (CO_2, CH_4, N_2O and tropospheric O_3) associated with the human activity.

The sector with the greatest contribution to the anthropogenic emissions of greenhouse effect gases is the transportation (29%), from which road transport represents the largest contribution (72%). From the road transport emissions, the majority of them are generated by passenger cars. The continued tightening of environmental regulations, coupled with the growing shortage of fossil fuels such as oil, is driving more sustainable forms of transportation. In this sense, regulations such as the National Emission Ceilings directive, or the White paper for transport, are encouraging strategies to reduce the emissions of greenhouse gases. One of such strategies consists of the utilization of alternative fuels for both transportation and energy production. These fuel diversification approaches have a huge potential for emission reduction in transport and indirectly contribute to solve some associated environmental problems, namely oil dependence and urban air quality issues. Hence, sales of vehicles operated with alternative fuels, particularly electricity, are steadily growing each year. However, paying attention solely to current availability and implementation capacity, then the best option for short and medium-term application is natural gas, since it is already widely available and the necessary technology for its processing has already been proven and established.

Natural gas for vehicles possesses the same composition as for domestic use, which means it is composed almost entirely by methane (up to 97%) mixed with small amounts of other gases. This alternative fuel presents numerous environmental and economic advantages in comparison with traditional liquid fuels, even though it is also classified as a fossil fuel. First, natural gas is relatively abundant, and estimates of world reserves are sufficient for at least more than 200 years.

Natural gas is also considered the cleanest available fossil fuel. Vehicles fuelled with NGV produce between 20 and 30% less CO_2 emissions per kilometre than traditional fuels. They also emit less NO_x, achieving reductions of up to 50-80% with respect to conventional fuels without sulphur oxide and practically without particulate matter. Also, maintenance costs of natural gas engines are significantly lower than those of gasoline and diesel engines, and they are actually much safer than those powered by liquid fuels in case of accident. However, despite all the clear advantages over these fuels, implementation of natural gas as an alternative fuel is still reduced. This limitation responds mainly to (i) the public perception of unsafety of natural gas, even though it has been shown to be safer than liquid fuels, (ii) the relatively low amount of refuelling stations that exist nowadays, (iii) the fact that it is necessary the addition of an aftertreatment system to the exhaust pipeline, to allow for removal of residual unburned methane (around 1%vol.) before venting it to the atmosphere.

There are a number of different strategies available for reducing emissions of methane in transport applications. Of these, biofiltration, thermal oxidation and catalytic oxidation are the most efficient. However, biofiltration is only adequate for very low concentrations of methane, around 2 ppm, while thermal oxidation needs compression or the addition of a secondary fuel to achieve the high temperatures needed for complete methane removal. Catalytic oxidation, on the other hand, is considered the most suitable and promising technology to control the methane emissions from natural gas engines.

Nevertheless, the combustion of methane involves the initial activation of the C-H bonds in the methane molecule, which in turn requires high reaction temperatures, owing to the high bond energy of C-H bonds in this molecule. However, the thermal level of the exhaust from a natural gas engine during normal operation does not exceed 500-550 °C, well below the range for the purely thermal activation of these bonds. Therefore, the selected catalysts are required to exhibit a high activity at relatively low temperatures, while maintaining an excellent selectivity towards CO_2 as well. Furthermore, the presence of concentrations of up to 10% of water vapour and CO_2 (and other pollutants in smaller concentrations) may induce an important deactivation effect on the chosen catalyst, thereby limiting both its activity and lifetime.

Traditionally, the most commonly used catalysts for methane oxidation have been based on costly noble metals, namely Pt and Pd. However, several drawbacks reduce their

potential for extensive implementation. Firstly, commercial palladium-based catalysts for methane oxidation contain high metallic loadings around 2-4 %wt. to achieve proper removal of methane. This, coupled with the high price and low availability of palladium, drastically increases the cost of these catalytic systems. Moreover, palladium-based catalysts are sensitive to deactivation by sintering and the presence of sulphur and water vapour in the reaction stream. As a consequence, the lifetime of Pd catalysts operating in the exhaust of natural gas engines is rather limited, which increases the frequency of required maintenance and substitution operations, further increasing the cost of these systems. For this reason, the development of alternative, cheaper materials that can also act as active catalysts for methane oxidation has been a hot topic in the last years.

In this sense, transition metal oxides have many important applications in oxidation catalysis, because they generally possess multiple oxidation states and the capacity to switch between them with relative ease. Among them, spinel oxides show a substantially higher degree of structural flexibility, allowing cations in them to participate in redox cycles. The easiness that cations in spinel structures show for switching between oxidation states gives oxygen species within the crystal lattice extraordinary mobility, which allow them to react at low temperatures. For these reasons, spinel oxides are the most studied among the mixed oxides for oxidation of CO, methane and other hydrocarbons. More specifically, the spinel-type cobalt oxide (Co_3O_4) is considered the most versatile due to its strong Co^{3+}/Co^{2+} redox system.

Nevertheless, the catalytic activity of Co_3O_4 for methane oxidation is relatively limited at low temperatures, and it still requires significant research effort to achieve a reasonable performance for real operation. Hence, the main objective of this thesis project is the design of highly active Co_3O_4-based catalysts for removal of residual methane under conditions similar to those found in the exhaust of natural gas engines.

Thus, in Chapter 3 an initial attempt to prepare this material in bulk form by different synthesis routes was made, with the objective of finding the most suitable methodology, and optimising its main experimental parameters, particularly the calcination temperature. This extensive study revealed that precipitation was the most suitable synthesis route, and that a temperature of 600 °C should be the upper limit for thermal activation by calcination. Higher temperatures greatly favoured sintering and negatively

affected the redox properties. Additionally, a strongly negative effect on the redox properties of Co_3O_4 caused by the presence of residual sodium was also ascertained.

Both reducibility and oxygen mobility were found to be key properties for determining the activity of cobalt oxide catalysts. Hence, the next step of this work focused on improving the redox characteristics by doping the active phase with a secondary metal. Among a wide number of possible dopants, including Mn, Fe, Ni, Cu, Zn and Ce, cerium resulted the most promising additive for enhancing the catalytic behaviour owing to its ability of efficiently inserting and distorting the spinel lattice, thus increasing the mobility of the oxygen species. Hence, an optimal loading of 10%wt. of Ce was needed for maximising the activity of Co_3O_4, while higher loadings did not lead to any further improvement.

Hereafter, a second line of work was started with the objective of improving the generally poor textural and structural properties of bulk Co_3O_4, since even after metal doping it still exhibited very low specific surface areas and large crystallite sizes. The simplest alternative to solve this problem was to use a porous support onto which to deposit and disperse the cobalt oxide in order to lower the crystallite sizes and increase the available surface area. It was evidenced that gamma-alumina instead of ceria or magnesia was the most suitable support for this purpose. However, a negative side effect was observed since the interaction between cobalt and alumina unavoidably led to the formation of a cobalt aluminate spinel with low reducibility, which had a detrimental influence on the redox properties of the resulting Co_3O_4/Al_2O_3 catalyst. The characterisation results and catalytic testing concluded that the optimal Co loading for this catalyst was 30%wt.Co.

For this reason, a series of enhancing strategies were proposed and examined with the sole purpose of reducing the formation of cobalt aluminate, and its impact on the reducibility of the deposited cobalt oxide. Thus, three different approaches for alumina-supported catalysts were evaluated. Firstly, surface protection of the alumina with magnesia prior to the deposition of the cobalt precursor was attempted, with the main objective of minimising the cobalt-alumina interaction and the subsequent formation of cobalt aluminate. Secondly, the co-precipitation of nickel along with cobalt was studied as an efficient way to improve the redox properties of the deposited cobalt. Finally, the surface protection of alumina with a redox promoter such as ceria was analysed, with the aim of providing both a barrier effect, minimising the cobalt-alumina interaction, and a redox promotion effect on the deposited cobalt.

The first approach was found to be efficient for decreasing the formation of cobalt aluminate, by switching the cobalt-alumina interaction into a cobalt-magnesium interaction. Unfortunately, this interaction was also not positive for the activity of the resulting catalyst due to the formation of a Co-Mg solid solution with an even lower reducibility than cobalt aluminate. On the other hand, the addition of nickel greatly increased the redox properties of the deposited cobalt owing to the partial formation of a nickel cobaltite spinel that exhibited even better performance than Co_3O_4 itself. The last approach, which involved the incorporation of ceria prior to the deposition of cobalt, resulted in the most active catalysts, due to the dual effect of deposited ceria decreasing the formation of cobalt aluminate and promoting the redox properties of the deposited cobalt oxide. The catalytic testing revealed an optimal composition for a cerium loading of 20%wt.Ce in the modified support.

Once the optimal formulation for the desired cobalt oxide-based catalysts was obtained, the final research step was to implement this catalytic system into a structured support, since that would be the form in which it would operate under real conditions. In this sense, instead of the conventional cordierite monolith, the attention was focused on the open cell foams made of alpha-alumina, due to the lower interaction potential with cobalt of this material. However, due to the low specific surface area of alpha-alumina, the Ce/Co ratio and the Co_3O_4 loading needed to be optimised again. The preliminary analysis was carried out over powdered alpha-alumina. As a result, an optimal formulation was found (10% Co_3O_4 loading and Ce/Co molar ratio = 0.05). Then, the synthesis of the structured foam catalysts was carried out by solution combustion synthesis. Prior to the incorporation of the active phase into the open cell foams, the critical parameters of the synthesis methodology were also optimised. Thus, glycine was identified as a better option than urea as fuel, and the optimal fuel/oxidiser ratio was the stoichiometric one. The resulting structured catalysts were found to be active for methane combustion, thereby confirming the viability of open cell foams as structured supports for cobalt oxide-based catalysts.

8.2. MAIN CONCLUSIONS

In view of the combined results of the characterisation and catalytic behaviour of the different synthesised catalysts, the most relevant conclusions previously presented at the end of each chapter are summarised:

1. Spinel type cobalt oxide (Co_3O_4) is active for lean methane combustion at moderate and low temperatures (200-600 °C) with 100%CO_2 selectivity and relatively good thermal resistance. However, the presence of water vapour in the reaction stream notably decreases its activity.

2. When preparing bulk Co_3O_4 samples, the precipitation method with sodium carbonate is the methodology that, among the simplest methodologies, results in catalysts with the best behaviour, provided that a proper washing of the precipitated catalytic precursor is conducted and a suitable calcination temperature is selected (600 ºC). In this sense, it is recommended that, at least, 4 litres of water are used in the washing step in order to ensure that no residual sodium ions remain on the surface of the catalytic precursor.

3. The activity of cobalt oxide for the oxidation of methane finds its origin in the Co^{3+}/Co^{2+} redox cycle, as described by the Mars – van Krevelen mechanism. Thus, the oxygen species that actually participate in the oxidation reaction are essentially those from the cobalt oxide spinel lattice. Maintaining that redox cycle at low temperatures is what provides cobalt oxide-based catalysts with the reducibility and oxygen mobility that are key for exhibiting a good performance.

4. When doping Co_3O_4 with a secondary metal, the most important parameters that need to be taken into account are the ability of insertion and distortion of the spinel lattice, and the ability to form highly reducible phases with cobalt. In this sense, Ni and Ce are the two most promising candidates. Its good behaviour was connected to its potential for producing highly active nickel cobaltite in the case of Ni, and to the remarkable redox promotion and oxygen mobility enhancement in the case of Ce.

5. Supporting cobalt oxide on the surface of a porous media could significantly improve its textural and structural properties. However, this almost invariably occurred at the cost of a strong cobalt-support interaction that was usually detrimental for the performance of the resulting catalyst. The strength of the cobalt-support interaction was mainly controlled by the affinity of the support for the cobalt ions and the dispersion of the cobalt oxide on the surface of the support, with higher dispersion leading to stronger interactions.

6. When the chosen support is gamma-alumina, that interaction led to the formation of notable amounts of poorly reducible cobalt aluminate ($CoAl_2O_4$), which dramatically affected the activity of the supported catalyst. All the deposited cobalt that converts into cobalt aluminate was permanently fixed and became inactive.

7. Supporting a secondary promoter over gamma-alumina prior to the deposition of cobalt resulted in a barrier effect that was beneficial for decreasing the extent of the undesired cobalt-alumina interaction and $CoAl_2O_4$ formation. However, when the additive was MgO, the cobalt-magnesia interaction led to the formation of a highly stable Co-Mg solid solution. On the other hand, the addition of nickel was beneficial owing to the partial formation of nickel cobaltite, which exhibited a superior specific activity when compared with Co_3O_4. Interestingly, ceria exhibited the same barrier effect, but also had a redox promotion effect, thus substantially improving the behaviour of the resulting catalyst. In sum, the performance of cobalt catalysts was chiefly controlled by the abundance of Co^{3+} cations which in turn was connected with the preferential existence of oxygen lattice species. Kinetic data obtained over the wide variety of investigated cobalt catalysts were compatible with Mars–van Krevelen kinetics with an excess of oxygen (considering a first pseudo-order for methane and a zero pseudo-order for oxygen).

8. Open cell foams made of alpha-alumina were a suitable alternative to conventional cordierite monoliths to prepare active Co-based structured catalysts. The low affinity of alpha-alumina for cobalt inhibited the formation of inactive cobalt aluminate. When coupled with a suitable synthesis methodology such as solution combustion synthesis, the resulting structured catalysts can exhibit a remarkable performance for lean methane combustion.

Chapter 9

NOMENCLATURE

9. NOMENCLATURE

Abbreviations and acronyms

BET	Brunauer, Emmett and Teller
BJH	Barrett, Joyner and Halenda
CFCs	Chlorofluorocarbons
CNG	Compressed natural gas
EDX	Energy Dispersive X-Ray Spectroscopy
EELS	Electron Energy Loss Spectroscopy
EU	European Union
FFT	Fast Fourier Transform
FWHM	Full Width at Half Maximum
GHSV	Gas Hourly Space Velocity
GWP	Global warming potential
HAADF	High-Angle Annular Dark Field
HFCs	Hydrochlorofluorocarbons
HRTEM	High-Resolution Transmission Electron Microscopy
ICDD	International Centre for Diffraction Data
ICP-AES	Inductively Coupled Plasma – Atomic Emission Spectroscopy
IPCC	Intergovernmental Panel on Climate Change
IUPAC	International Union of Pure and Applied Chemistry
LNG	Liquefied natural gas
MS	Mass Spectroscopy
NGV	Natural gas for vehicles
NO_x	Nitrogen oxides

SCS	Solution Combustion Synthesis
SEM	Scanning Electron Microscopy
STEM	Scanning Transmission Electron Microscopy
TCD	Thermal Conductivity Detector
TEM	Transmission Electron Microscopy
TPO	Temperature-Programmed Oxidation
TPR	Temperature-Programmed Reduction
TPRe	Temperature-Programmed Reaction
UV-vis-NIR DRS	Ultraviolet-visible-Near Infrared Diffuse Reflectance Spectroscopy
VOCs	Volatile Organic Compounds
WDXRF	Wavelength-Dispersive X-Ray Fluorescence
WHSV	Weight Hourly Space Velocity
XPS	X-Ray Photoelectronic Spectroscopy
XRD	X-Ray Diffraction

Variables and physical constants

a_0	Cell parameter
a'	External surface of the catalytic particles
A_m	Cross section area of the adsorbate
b	Instrumental contribution to peak width
B	Experimental peak width
Bi	Biot number
Bo	Bodenstein number
C	BET constant

C_i	Molar concentration of species i
Ca	Carberry number
d	Spacing
d_p	Particle diameter
d_t	Reactor tube diameter
D	Crystallite size
D_e	Effective diffusivity
E_a	Activation energy
F_i	Molar flow of species i
ħ	Planck constant
k_0	Pre-exponential factor
k_f	Mass transfer coefficient
K	Shape factor
L	Characteristic length
L_b	Bed length
m	Mass
n	Reaction order
N_A	Avogadro constant
P	Total pressure
P_0	Saturation pressure
r_p	Pore radius
$r_{v,obs}$	Observed reaction rate per unit volume of catalyst
R	Universal constant of ideal gases
t	Thickness

T	Temperature
T_{10}	Temperature at which 10% methane conversion is attained
T_{50}	Temperature at which 50% methane conversion is attained
T_{90}	Temperature at which 90% methane conversion is attained
V_{ads}	Adsorbed volume
V_m	Adsorbed gas volume in the monolayer
V_{mol}	Molar volume of the adsorbed gas
W	Catalyst weight
X_i	Conversion of species i

Greek letters

β	Full Width at Half Maximum
ε	Porosity
θ	Diffraction angle
λ	Wavelength
λ_e	Effective thermal conductivity
ν	Frequency
σ	Surface tension
υ	Contact angle
ϕ	Work function

Chapter 10

REFERENCES

10. REFERENCES

[1] M.S. Calvo, "Tratado de la contaminación atmosférica: problemas, tratamiento y gestión", Ediciones Mundi-Prensa, Madrid, 2002.

[2] United Nations, "The Sustainable Development Goals Report 2019", United Nations Publications, New York, 2019.

[3] J. Poushter, C. Huang, "Climate Change Still Seen as the Top Global Threat, but Cyberattacks a Rising Concern", Pew Research Center, Washington, 2019.

[4] EU Parliament, "Resolution on the climate and environment emergency", 2019/2930(RSP), 2019.

[5] IPCC "Climate Change 2014: Synthesis Report. Contribution of Working Groups I, II and III to the Fifth Assessment Report of the Intergovernmental Panel on Climate Change", IPCC, Geneva, 2014.

[6] J.R. Petit, J. Jouzel, D. Raynaud, N.I. Barkov, J.-. Barnola, I. Basile, M. Bender, J. Chappellaz, M. Davis, G. Delaygue, M. Delmotte, V.M. Kotiyakov, M. Legrand, V.Y. Lipenkov, C. Lorius, L. Pépin, C. Ritz, E. Saltzman, M. Stievenard, "Climate and atmospheric history of the past 420,000 years from the Vostok ice core, Antarctica", Nature 399 (1999) 429-436.

[7] R.M. DeConto, D. Pollard, "Contribution of Antarctica to past and future sea-level rise", Nature 531 (2016) 591-597.

[8] K. Pistone, I. Eisenman, V. Ramanathan, "Radiative heating of an ice-free Arctic ocean", Geophys. Res. Lett. 46 (2019) 7474-7480.

[9] J.P. Kossin, T. Hall, T. Knutson, K.E. Kunkel, R.J. Trapp, D.E. Waliser, M.F. Wehner, "Extreme storms", in: *Climate Science Special Report: Fourth National Climate Assessment, Volume I,* D.J. Wuebbles, D.W. Fahey, K.A. Hibbard, D.J. Dokken, B.C. Stewart, T.K. Maycock (Eds.), U.S. Global Change Research Program, Washington, DC, USA, 2017, 257-276.

[10] J.A. Francis, S.J. Vavrus, "Evidence linking Arctic amplification to extreme weather in mid-latitudes", Geophys. Res. Lett. 39 (2012) L06801.

[11] P.G. Curtis, C.M. Slay, N.L. Harris, A. Tyukavina, M.C. Hansen, "Classifying drivers of global forest loss", Science 361 (2018) 1108-1111.

[12] IPCC, "Climate Change and Land: an IPCC special report on climate change, desertification, land degradation, sustainable land management, food security, and greenhouse gas fluxes in terrestrial ecosystems", IPCC, Geneva, 2019.

[13] B.H. Samset, M. Sand, C.J. Smith, S.E. Bauer, P.M. Forster, J.S. Fuglestvedt, S. Osprey, C. Schleussner, "Climate impacts from a removal of anthropogenic aerosol emissions", Geophys. Res. Lett. 45 (2018) 1020-1029.

[14] B.A. Albrecht, "Aerosols, cloud microphysics, and fractional cloudiness", Science 245 (1989) 1227-1230.

[15] A.P. Schurer, G.C. Hegerl, M.E. Mann, S.F.B. Tett, S.J. Phipps, "Separating forced from chaotic climate variability over the past millennium", J. Climate 26 (2013) 6954-6973.

[16] G.A. Schmidt, R.A. Ruedy, R.L. Miller, A.A. Lacis, "Attribution of the present-day total greenhouse effect", J. Geophys. Res. Atmos. 115 (2010) D20106.

[17] I.M. Held, B.J. Soden, "Water vapor feedback and global warming", Annu. Rev. Energy Environ. 25 (2000) 441-475.

[18] J.G. Canadell, C. Le Quéré, M.R. Raupach, C.B. Field, E.T. Buitenhuis, P. Ciais, T.J. Conway, N.P. Gillett, R.A. Houghton, G. Marland, "Contributions to accelerating atmospheric CO_2 growth from economic activity, carbon intensity, and efficiency of natural sinks", Proc. Natl. Acad. Sci. U. S. A. 104 (2007) 18866-18870.

[19] K.M. Walter, S.A. Zimov, J.P. Chanton, D. Verbyla, F.S. Chapin III, "Methane bubbling from Siberian thaw lakes as a positive feedback to climate warming", Nature 443 (2006) 71-75.

[20] CAIT Climate Data Explorer. https://cait.wri.org, 2017 (accessed 27 April 2020).

[21] European Environment Agency (EEA), Greenhouse gas emissions by source sector, European Union, Copenhagen, 2019.

[22] Greenhouse gas emissions from transport in Europe. https://www.eea.europa.eu/data-and-maps/indicators/transport-emissions-of-greenhouse-gases/transport-emissions-of-greenhouse-gases-12, 2019 (accessed 28 April 2020).

[23] European Commission, "The implementation of the 2011 White Paper on Transport "Roadmap to a Single European Transport Area – towards a competitive and resource-efficient transport system" five years after its publication: achievements and challenges", SWD 226, European Commission, Brussels, 2016.

[24] OECD, "Strategies to Reduce Greenhouse Gas Emissions from Road Transport: Analytical Methods", OECD, Paris, 2002.

[25] Current Natural Gas Vehicle Statistics. http://www.iangv.org/current-ngv-stats, 2019 (accessed 28 April 2020).

[26] M.I. Jahirul, H.H. Masjuki, R. Saidur, M.A. Kalam, M.H. Jayed, M.A. Wazed, "Comparative engine performance and emission analysis of CNG and gasoline in a retrofitted car engine", Appl. Therm. Eng. 30 (2010) 2219-2226.

[27] A. Raj, "Methane emission control", Johns. Matthey Technol. Rev. 60 (2016) 228-235.

[28] M.I. Khan, T. Yasmin, A. Shakoor, "Technical overview of compressed natural gas (CNG) as a transportation fuel", Renew. Sust. Energ. Rev. 51 (2015) 785-797.

[29] T. Korakianitis, A.M. Namasivayam, R.J. Crookes, "Natural-gas fueled spark-ignition (SI) and compression-ignition (CI) engine performance and emissions", Prog. Energ. Combust. 37 (2011) 89-112.

[30] H. Engerer, M. Horn, "Natural gas vehicles: An option for Europe", Energ. Policy 38 (2010) 1017-1029.

[31] D. Zhang, "8 - Direct injection natural gas engines", in: *Advanced Direct Injection Combustion Engine Technologies and Development,* H. Zhao (Ed.), Woodhead Publishing, Cambridge, 2010, 199-228.

[32] D. Yadav, P. Singh, R. Prasad, "Advanced thermally stable, self-sustaining $NiCo_2O_4$ catalyst for CNG emissions in lean burn environment", Int. J. Hydrogen Energy 44 (2019) 29057-29065.

[33] L. Zhou, Y. Liu, L. Sun, H. Hou, K. Zeng, Z. Huang, "Effect of hot exhaust gas recirculation on the combustion characteristics and particles emissions of a pilot-ignited natural gas engine," SAE Int. J. Engines 6 (2013)1116-1125.

[34] R.W. Melse, A.W. Van Der Werf, "Biofiltration for mitigation of methane emission from animal husbandry", Environ. Sci. Technol. 39 (2005) 5460-5468.

[35] J.K. Stolaroff, S. Bhattacharyya, C.A. Smith, W.L. Bourcier, P.J. Cameron-Smith, R.D. Aines, "Review of methane mitigation technologies with application to rapid release of methane from the arctic", Environ. Sci. Technol. 46 (2012) 6455-6469.

[36] B. Lan, Y. Li, X. Zhao, J. Kang, "Industrial-scale experimental study on the thermal oxidation of ventilation air methane and the heat recovery in a multibed thermal flow-reversal reactor", Energies 11 (2018) 1578.

[37] T. Maunula, K. Kallinen, N. Kinnunen, M. Keenan, T. Wolff, "Methane abatement and catalyst durability in heterogeneous lean-rich and dual-fuel conditions", Top. Catal. 62 (2019) 315-323.

[38] N.M. Kinnunen, J.T. Hirvi, K. Kallinen, T. Maunula, M. Keenan, M. Suvanto, "Case study of a modern lean-burn methane combustion catalyst for automotive applications: What are the deactivation and regeneration mechanisms?", Appl. Catal. B Environ. 207 (2017) 114-119.

[39] N. Kinnunen, T. Kinnunen, K. Kallinen, "Improved sulfur resistance of noble metal catalyst for lean-burn natural gas applications", SAE Tech. Pap. 6 (2013) 24-0155.

[40] Z. Li, G.B. Hoflund, "A review on complete oxidation of methane at low temperatures", J. Nat. Gas Chem. 12 (2003) 153-160.

[41] J.H. Lee, D.L. Trimm, "Catalytic combustion of methane", Fuel Process. Technol. 42 (1995) 339-359.

[42] T.V. Choudhary, S. Banerjee, V.R. Choudhary, "Catalysts for combustion of methane and lower alkanes", Appl. Catal. A Gen. 234 (2002) 1-23.

[43] D. Ciuparu, M.R. Lyubovsky, E. Altman, L.D. Pfefferle, A. Datye, "Catalytic combustion of methane over palladium-based catalysts", Catal. Rev. Sci. Eng. 44 (2002) 593-649.

[44] J. Chen, H. Arandiyan, X. Gao, J. Li, "Recent advances in catalysts for methane combustion", Catal. Surv. Asia 19 (2015) 140-171.

[45] M. Rotko, A. Machocki, B. Stasinska, "Studies of catalytic process of complete oxidation of methane by SSITKA method", Appl. Surf. Sci. 256 (2010) 5585-5589.

[46] P. Briot, A. Auroux, D. Jones, M. Primet, "Effect of particle size on the reactivity of oxygen-adsorbed platinum supported on alumina", Appl. Catal. 59 (1990) 141-152.

[47] T.R. Baldwin, R. Burch, "Remarkable activity enhancement in the catalytic combustion of methane on supported palladium catalysts", Catal. Lett. 6 (1990) 131-138.

[48] R.J. Farrauto, M.C. Hobson, T. Kennelly, E.M. Waterman, "Catalytic chemistry of supported palladium for combustion of methane", Appl. Catal. A Gen. 81 (1992) 227-237.

[49] R.F. Hicks, H. Qi, M.L. Young, R.G. Lee, "Structure sensitivity of methane oxidation over platinum and palladium", J. Catal. 122 (1990) 280-294.

[50] S.H. Oh, P.J. Mitchell, "Effects of rhodium addition on methane oxidation behavior of alumina-supported noble metal catalysts", Appl. Catal. B Environ. 5 (1994) 165-179.

[51] R. Burch, F.J. Urbano, "Investigation of the active state of supported palladium catalysts in the combustion of methane", Appl. Catal. A Gen. 124 (1995) 121-138.

[52] M. Lyubovsky, L. Pfefferle, "Methane combustion over the α-alumina supported Pd catalyst: Activity of the mixed Pd/PdO state", Appl. Catal. A Gen. 173 (1998) 107-119.

[53] I.E. Beck, V.I. Bukhtiyarov, I.Y. Pakharukov, V.I. Zaikovsky, V.V. Kriventsov, V.N. Parmon, "Platinum nanoparticles on Al_2O_3: Correlation between the particle size and activity in total methane oxidation", J. Catal. 268 (2009) 60-67.

[54] K. Fujimoto, F.H. Ribeiro, M. Avalos-Borja, E. Iglesia, "Structure and reactivity of PdO_x/ZrO_2 catalysts for methane oxidation at low temperatures", J. Catal. 179 (1998) 431-442.

[55] G. Groppi, "Combustion of CH_4 over a PdO/ZrO_2 catalyst: An example of kinetic study under severe conditions", Catal. Today 77 (2003) 335-346.

[56] O. Demoulin, M. Navez, E.M. Gaigneaux, P. Ruiz, A.-. Mamede, P. Granger, E. Payen, "Operando resonance Raman spectroscopic characterisation of the oxidation state of palladium in $Pd/\gamma\text{-}Al_2O_3$ catalysts during the combustion of methane", Phys. Chem. Chem. Phys. 5 (2003) 4394-4401.

[57] D. Ciuparu, L. Pfefferle, "Contributions of lattice oxygen to the overall oxygen balance during methane combustion over PdO-based catalysts", Catal. Today 77 (2002) 167-179.

[58] R.M. Heck, R.J. Farrauto, S.T. Gulati, "Catalytic Air Pollution Control: Commercial Technology" 3rd ed., John Wiley & Sons, Inc., New Jersey, 2009.

[59] K.C. Taylor, "Automobile Catalytic Converters", 1st ed., Springer-Verlag Berlin Heidelberg, Berling, 1984.

[60] K. Persson, L.D. Pfefferle, W. Schwartz, A. Ersson, S.G. Järås, "Stability of palladium-based catalysts during catalytic combustion of methane: The influence of water", Appl. Catal. B Environ. 74 (2007) 242-250.

[61] D.L. Mowery, R.L. McCormick, "Deactivation of alumina supported and unsupported PdO methane oxidation catalyst: The effect of water on sulfate poisoning", Appl. Catal. B Environ. 34 (2001) 287-297.

[62] P. Velin, M. Ek, M. Skoglundh, A. Schaefer, A. Raj, D. Thompsett, G. Smedler, P. Carlsson, "Water inhibition in methane oxidation over alumina supported palladium catalysts", J. Phys. Chem. C 123 (2019) 25724-25737.

[63] O. Mihai, G. Smedler, U. Nylén, M. Olofsson, L. Olsson, "The effect of water on methane oxidation over Pd/Al_2O_3 under lean, stoichiometric and rich conditions", Catal. Sci. Technol. 7 (2017) 3084-3096.

[64] N. Bion, F. Can, X. Courtois, D. Duprez, "6 - Transition metal oxides for combustion and depollution processes", in: *Metal Oxides in Heterogeneous Catalysis,* J.C. Védrine (Ed.), Elsevier, Amsterdam, 2018, 287-353.

[65] G. Águila, F. Gracia, J. Cortés, P. Araya, "Effect of copper species and the presence of reaction products on the activity of methane oxidation on supported CuO catalysts", Appl. Catal. B Environ. 77 (2008) 325-338.

[66] Y. Feng, P.M. Rao, D.R. Kim, X. Zheng, "Methane oxidation over catalytic copper oxides nanowires", Proc. Combust. Inst. 33 (2011) 3169-3175.

[67] P.W. Park, J.S. Ledford, "The influence of surface structure on the catalytic activity of alumina supported copper oxide catalysts. Oxidation of carbon monoxide and methane", Appl. Catal. B Environ. 15 (1998) 221-231.

[68] Y. Zhang, Z. Qin, G. Wang, H. Zhu, M. Dong, S. Li, Z. Wu, Z. Li, Z. Wu, J. Zhang, T. Hu, W. Fan, J. Wang, "Catalytic performance of MnO_x-NiO composite oxide in lean methane combustion at low temperature", Appl. Catal. B Environ. 129 (2013) 172-181.

[69] Y.-F. Han, L. Chen, K. Ramesh, E. Widjaja, S. Chilukoti, I. Kesumawinata Surjami, J. Chen, "Kinetic and spectroscopic study of methane combustion over α-Mn_2O_3 nanocrystal catalysts", J. Catal. 253 (2008) 261-268.

[70] N. Nabih, R. Schiller, I. Lieberwirth, E. Kockrick, R. Frind, S. Kaskel, C.K. Weiss, K. Landfester, "Mesoporous CeO_2 nanoparticles synthesized by an inverse miniemulsion technique and their catalytic properties in methane oxidation", Nanotechnology 22 (2011) 135606.

[71] W. Shan, M. Luo, P. Ying, W. Shen, C. Li, "Reduction property and catalytic activity of $Ce_{1-x}Ni_xO_2$ mixed oxide catalysts for CH_4 oxidation", Appl. Catal. A Gen. 246 (2003) 1-9.

[72] J.R. Paredes, E. Díaz, F.V. Díez, S. Ordóñez, "Combustion of methane in lean mixtures over bulk transition-metal oxides: Evaluation of the activity and self-deactivation", Energ. Fuel. 23 (2009) 86-93.

[73] M. Misono, "Chapter 3 - Catalysis of Perovskite and Related Mixed Oxides", in: *Heterogeneous Catalysis of Mixed Oxides,* M. Misono (Ed.), Elsevier, Amsterdam, 2013, 67-95.

[74] V. Bashan, Y. Ust, "Perovskite catalysts for methane combustion: applications, design, effects for reactivity and partial oxidation", Int. J. Energy Res. 43 (2019) 7755-7789.

[75] H. Arandiyan, H. Chang, C. Liu, Y. Peng, J. Li, "Dextrose-aided hydrothermal preparation with large surface area on 1D single-crystalline perovskite $La_{0.5}Sr_{0.5}CoO_3$ nanowires without template: Highly catalytic activity for methane combustion", J. Mol. Catal. A Chem. 378 (2013) 299-306.

[76] J. Deng, H. Dai, H. Jiang, L. Zhang, G. Wang, H. He, A.U. Chak Tong, "Hydrothermal fabrication and catalytic properties of $La_{1-x}Sr_xM_{1-y}Fe_yO_3$ (M = Mn, Co) that are highly active for the removal of toluene", Environ. Sci. Technol. 44 (2010) 2618-2623.

[77] L. Giebeler, D. Kießling, G. Wendt, "$LaMnO_3$ perovskite supported noble metal catalysts for the total oxidation of methane", Chem. Eng. Technol. 30 (2007) 889-894.

[78] Y. Wang, H. Arandiyan, J. Scott, M. Akia, H. Dai, J. Deng, K.-. Aguey-Zinsou, R. Amal, "High Performance Au-Pd Supported on 3D Hybrid Strontium-Substituted Lanthanum Manganite Perovskite Catalyst for Methane Combustion", ACS Catal. 6 (2016) 6935-6947.

[79] P. Ciambelli, S. Cimino, L. Lisi, M. Faticanti, G. Minelli, I. Pettiti, P. Porta, "La, Ca and Fe oxide perovskites: Preparation, characterization and catalytic properties for methane combustion", Appl. Catal. B Environ. 33 (2001) 193-203.

[80] A. Musialik-Piotrowska, H. Landmesser, "Noble metal-doped perovskites for the oxidation of organic air pollutants", Catal. Today 137 (2008) 357-361.

[81] L. Fabbrini, A. Kryukov, S. Cappelli, G.L. Chiarello, I. Rossetti, C. Oliva, L. Forni, "$Sr_{1-x}Ag_xTiO_{3\pm\delta}$ (x = 0, 0.1) perovskite-structured catalysts for the flameless combustion of methane", J. Catal. 232 (2005) 247-256.

[82] S. Laassiri, N. Bion, D. Duprez, H. Alamdari, S. Royer, "Role of M^{n+} cations in the redox and oxygen transfer properties of $BaM_xAl_{12-x}O_{19-\delta}$ (M = Mn, Fe, Co) nanomaterials for high temperature methane oxidation", Catal. Sci. Technolog. 3 (2013) 2259-2269.

[83] H.M.J. Kusar, A.G. Ersson, S.G. Järås, "Catalytic combustion of gasified refuse-derived fuel", Appl. Catal. B Environ. 45 (2003) 1-11.

[84] M. Tian, X.D. Wang, T. Zhang, "Hexaaluminates: A review of the structure, synthesis and catalytic performance", Catal. Sci. Technol. 6 (2016) 1984-2004.

[85] Y. Zhu, N. Jin, R. Liu, X. Sun, L. Bai, H. Tian, X. Ma, X. Wang, "Bimetallic $BaFe_2MAl_9O_{19}$ (M=Mn, Ni, and Co) hexaaluminates as oxygen carriers for chemical looping dry reforming of methane", Appl. Energy 258 (2020) 114070.

[86] R. Amrousse, A. Tsutsumi, "Novel Rh-substituted hexaaluminate catalysts for N_2O decomposition", Catal. Sci. Technol. 6 (2016) 438-441.

[87] F. Yin, S. Ji, P. Wu, F. Zhao, C. Li, "Preparation, characterization, and methane total oxidation of $AAl_{12}O_{19}$ and $AMAl_{11}O_{19}$ hexaaluminate catalysts prepared with urea combustion method", J. Mol. Catal. A Chem. 294 (2008) 27-36.

[88] Z. Jiang, Z. Hao, J. Su, T. Xiao, P.P. Edwards, "Water/oil microemulsion for the preparation of robust La-hexaaluminates for methane catalytic combustion", Chem. Commun. (2009) 3225-3227.

[89] S. Wei, S.B. Zhang, "First-principles study of cation distribution in eighteen closed-shell $A^{II}B^{III}_2O_4$ and $A^{IV}B^{II}_2O_4$ spinel oxides", Phys. Rev. B Condens. Matter Mater. Phys. 63 (2001) 045112.

[90] C. Biagioni, M. Pasero, "The systematics of the spinel-type minerals: An overview", Am. Mineral. 99 (2014) 1254-1264.

[91] Q. Zhao, Z. Yan, C. Chen, J. Chen, "Spinels: controlled preparation, oxygen reduction/evolution reaction application, and beyond", Chem. Rev. 117 (2017) 10121-10211.

[92] K. Uusi-Esko, E. Rautama, M. Laitinen, T. Sajavaara, M. Karppinen, "Control of oxygen nonstoichiometry and magnetic property of $MnCo_2O_4$ thin films grown by atomic layer deposition", Chem. Mater. 22 (2010) 6297-6300.

[93] J. Hu, W. Zhao, R. Hu, G. Chang, C. Li, L. Wang, "Catalytic activity of spinel oxides $MgCr_2O_4$ and $CoCr_2O_4$ for methane combustion", Mater. Res. Bull. 57 (2014) 268-273.

[94] Z. Ma, "Cobalt oxide catalysts for environmental remediation", Curr. Catal. 3 (2014) 15-26.

[95] S. Wójcik, G. Ercolino, M. Gajewska, C.W.M. Quintero, S. Specchia, A. Kotarba, "Robust Co_3O_4|α-Al_2O_3|cordierite structured catalyst for N_2O abatement - Validation of the SCS method for active phase synthesis and deposition", Chem. Eng. J. 377 (2019) 120088.

[96] B. De Rivas, R. López-Fonseca, C. Jiménez-González, J.I. Gutiérrez-Ortiz, "Synthesis, characterisation and catalytic performance of nanocrystalline Co_3O_4 for gas-phase chlorinated VOC abatement", J. Catal. 281 (2011) 88-97.

[97] B. Solsona, T.E. Davies, T. Garcia, I. Vázquez, A. Dejoz, S.H. Taylor, "Total oxidation of propane using nanocrystalline cobalt oxide and supported cobalt oxide catalysts", Appl. Catal. B Environ. 84 (2008) 176-184.

[98] S. Wang, J. Cao, W. Cui, L. Fan, X. Li, D. Li, T. Zhang, "One-dimensional porous Co_3O_4 rectangular rods for enhanced acetone gas sensing properties", Sens. Actuators, B Chem. 297 (2019) 126746.

[99] Y. Liu, J. Xie, M. Luo, S. Jian, B. Peng, L. Deng, "The synthesis and characterization of Al/Co_3O_4 magnetic composite pigments with low infrared emissivity and low lightness", Infrared Phys. Technol. 83 (2017) 88-93.

[100] C. Lohaus, J. Morasch, J. Brötz, A. Klein, W. Jaegermann, "Investigations on RF-magnetron sputtered Co_3O_4 thin films regarding the solar energy conversion properties", J. Phys. D 49 (2016) 155306.

[101] A. Setiawan, E.M. Kennedy, B.Z. Dlugogorski, A.A. Adesina, M. Stockenhuber, "The stability of Co_3O_4, Fe_2O_3, Au/Co_3O_4 and Au/Fe_2O_3 catalysts in the catalytic combustion of lean methane mixtures in the presence of water", Catal. Today 258 (2015) 276-283.

[102] X. Wang, W. Tian, T. Zhai, C. Zhi, Y. Bando, D. Golberg, "Cobalt(II,III) oxide hollow structures: Fabrication, properties and applications", J. Mater. Chem. 22 (2012) 23310-23326.

[103] X. Xie, W. Shen, "Morphology control of cobalt oxide nanocrystals for promoting their catalytic performance", Nanoscale 1 (2009) 50-60.

[104] K. Li, D. Xu, K. Liu, H. Ni, F. Shen, T. Chen, B. Guan, R. Zhan, Z. Huang, H. Lin, "catalytic combustion of lean methane assisted by an electric field over Mn_xCo_y catalysts at low temperature", J. Phys. Chem. C 123 (2019) 10377-10388.

[105] S. Nasr, N. Semagina, R.E. Hayes, "Kinetic modelling of Co_3O_4- and Pd/Co_3O_4-catalyzed wet lean methane combustion", Emiss. Control Sci. Technol. 6 (2020) 269-278.

[106] Q. Huang, W. Li, Q. Lin, X. Zheng, H. Pan, D. Pi, C. Shao, C. Hu, H. Zhang, "Catalytic performance of Pd–$NiCo_2O_4$/SiO_2 in lean methane combustion at low temperature", J. Energy Inst. 91 (2018) 733-742.

[107] Y. Zheng, Y. Liu, H. Zhou, W. Huang, Z. Pu, "Complete combustion of methane over Co_3O_4 catalysts: Influence of pH values", J. Alloys Compd. 734 (2018) 112-120.

[108] Z. Feng, C. Du, Y. Chen, Y. Lang, Y. Zhao, K. Cho, R. Chen, B. Shan, "Improved durability of Co_3O_4 particles supported on $SmMn_2O_5$ for methane combustion", Catal. Sci. Technol. 8 (2018) 3785-3794.

[109] M. Zhou, J. Zhang, L. Liao, W. Wu, "Enhanced catalytic methane combustion over Co_3O_4 nanowire arrays by cation substitution", Mater. Res. Express 4 (2017) 125006.

[110] S. Liu, P. Liu, R. Niu, S. Wang, J. Li, "Facile synthesis of mesoporous Co_3O_4 nanoflowers for catalytic combustion of ventilation air methane", Chem. Res. Chin. Univ. 33 (2017) 965-970.

[111] Z. Pu, H. Zhou, Y. Zheng, W. Huang, X. Li, "Enhanced methane combustion over Co_3O_4 catalysts prepared by a facile precipitation method: Effect of aging time", Appl. Surf. Sci. 410 (2017) 14-21.

[112] G. Ercolino, P. Stelmachowski, G. Grzybek, A. Kotarba, S. Specchia, "Optimization of Pd catalysts supported on Co_3O_4 for low-temperature lean combustion of residual methane", Appl. Catal. B Environ. 206 (2017) 712-725.

[113] X. Cao, R. Zhou, N. Rui, Z. Wang, J. Wang, X. Zhou, C.-J. Liu, "Co_3O_4/HZSM-5 catalysts for methane combustion: The effect of preparation methodologies", Catal. Today 297 (2017) 219-227.

[114] B. Wang, X. Lu, K.Y. Wong, Y. Tang, "Facile solvothermal synthesis and superior lithium storage capability of Co_3O_4 nanoflowers with multi-scale dimensions", Mater. Chem. Front. 1 (2017) 468-476.

[115] Z. Chen, S. Wang, W. Liu, X. Gao, D. Gao, M. Wang, S. Wang, "Morphology-dependent performance of Co_3O_4 via facile and controllable synthesis for methane combustion", Appl. Catal. A Gen. 525 (2016) 94-102.

[116] H. Lu, C. Jiang, Z. Ding, W. Wang, W. Chu, Y. Feng, "Effects of ultrasonic impregnation combined with calcination in N_2 atmosphere on the property of Co_3O_4/CeO_2 composites for catalytic methane combustion", J. Energy Chem. 25 (2016) 387-392.

[117] Q. Wang, Y. Peng, J. Fu, G.Z. Kyzas, S.M.R. Billah, S. An, "Synthesis, characterization, and catalytic evaluation of Co_3O_4/γ-Al_2O_3 as methane combustion catalysts: Significance of Co species and the redox cycle", Appl. Catal. B Environ. 168-169 (2015) 42-50.

[118] H. Li, G. Lu, D. Qiao, Y. Wang, Y. Guo, Y. Guo, "Catalytic methane combustion over Co_3O_4/CeO_2 composite oxides prepared by modified citrate sol-gel method", Catal. Lett. 141 (2011) 452-458.

[119] X. Tang, J. Hao, J. Li, "Complete oxidation of methane on Co_3O_4-SnO_2 catalysts", Front. Environ. Sci. Eng. China 3 (2009) 265-270.

[120] G. Laugel, J. Arichi, P. Bernhardt, M. Molière, A. Kiennemann, F. Garin, B. Louis, "Preparation and characterisation of metal oxides supported on SBA-15 as methane combustion catalysts", C. R. Chim. 12 (2009) 731-739.

[121] L.F. Liotta, G. Di Carlo, G. Pantaleo, G. Deganello, "Catalytic performance of Co_3O_4/CeO_2 and Co_3O_4/CeO_2–ZrO_2 composite oxides for methane combustion:

Influence of catalyst pretreatment temperature and oxygen concentration in the reaction mixture", Appl. Catal. B Environ. 70 (2007) 314-322.

[122] U. Zavyalova, P. Scholz, B. Ondruschka, "Influence of cobalt precursor and fuels on the performance of combustion synthesized Co_3O_4/γ-Al_2O_3 catalysts for total oxidation of methane", Appl. Catal. A Gen. 323 (2007) 226-233.

[123] X. Zhang, Z. Liu, Z. Wei, X. Du, M. Gong, Y. Chen, "Preparation of high performance methane combustion catalyst and its application to natural gas catalytic combustion fan-boiler", Chin. J. Catal. 27 (2006) 823-826.

[124] M.J. Tiernan, E.A. Fesenko, P.A. Barnes, G.M.B. Parkes, M. Ronane, "The application of CRTA and linear heating thermoanalytical techniques to the study of supported cobalt oxide methane combustion catalysts", Thermochim. Acta 379 (2001) 163-175.

[125] M. Selim, N. Deraz, M. Ramadan, "Influence of precursor compounds on the structural and catalytic properties of cobalt-based catalysts", Adsorption Sci. Technol. 27 (2009) 883-891.

[126] S.N. Karthick, K.V. Hemalatha, C. Justin Raj, H.J. Kim, M. Yi, "Synthesis of nano-bound microsphere Co_3O_4 by simple polymer-assisted sol-gel technique", J. Nanopart. Res. 15 (2013) 1474.

[127] A. Arango-Diaz, J.A. Cecilia, J. Marrero-Jerez, P. Nuñez, J. Jiménez-Jiménez, E. Rodríguez-Castellón, "Freeze-dried Co_3O_4-CeO_2 catalysts for the preferential oxidation of CO with the presence of CO_2 and H_2O in the feed", Ceram. Int. 42 (2016) 7462-7474.

[128] H. Du, K. Huang, M. Li, Y. Xia, Y. Sun, M. Yu, B. Geng, "Gas template-assisted spray pyrolysis: A facile strategy to produce porous hollow Co_3O_4 with tunable porosity for high-performance lithium-ion battery anode materials", Nano. Res. 11 (2018) 1490-1499.

[129] G. Ercolino, P. Stelmachowski, S. Specchia, "Catalytic performance of Pd/Co_3O_4 on SiC and ZrO_2 open cell foams for process intensification of methane combustion in lean conditions", Ind. Eng. Chem. Res. 56 (2017) 6625-6636.

[130] Q. Liu, L. Wang, M. Chen, Y. Cao, H. He, K. Fan, "Dry citrate-precursor synthesized nanocrystalline cobalt oxide as highly active catalyst for total oxidation of propane", J. Catal. 263 (2009) 104-113.

[131] B. Liu, J. Peng, L. Zhang, R. Wan, S. Guo, L. Zhou, "Optimization of preparation for Co_3O_4 by calcination from cobalt oxalate using response surface methodology", Chem. Eng. Res. Des. 88 (2010) 971-976.

[132] Z. Fei, S. He, L. Li, W. Ji, C.-T. Au, "Morphology-directed synthesis of Co_3O_4 nanotubes based on modified Kirkendall effect and its application in CH_4 combustion", Chem. Commun. 48 (2012) 853-855.

[133] L. Hu, Q. Peng, Y. Li, "Selective synthesis of Co_3O_4 nanocrystal with different shape and crystal plane effect on catalytic property for methane combustion", J. Am. Chem. Soc. 130 (2008) 16136-16137.

[134] B. Beckhoff, B. Kanngiesser, N. Langhoff, R. Wedell, "Handbook of practical X-ray fluorescence analysis", Springer, Berlin, 2006.

[135] Grieken, R. van Markowicz, A., "Handbook of X-ray spectrometry", Marcel Dekker, New York, 2002.

[136] M.S. Faraldos Izquierdo, C.E. Goberna Selma, "Técnicas de análisis y caracterización de materiales", 2ª ed. rev. y aum. ed., CSIC, Madrid, 2019.

[137] J. Todoli, J. Mermet, "8 - Applications", in: *Liquid Sample Introduction in ICP Spectrometry,* J. Todoli, J. Mermet (Eds.), Elsevier, Amsterdam, 2008, 217-232.

[138] G. Leofanti, M. Padovan, G. Tozzola, B. Venturelli, "Surface area and pore texture of catalysts", Catal. Today 41 (1998) 207-219.

[139] S. Brunauer, L.S. Deming, W.E. Deming, E. Teller, "On a theory of the Van der Waals adsorption of gases", J. Am. Chem. Soc. 62 (1940) 1723-1732.

[140] S. Brunauer, P.H. Emmett, E. Teller, "Adsorption of gases in multimolecular layers", J. Am. Chem. Soc. 60 (1938) 309-319.

[141] K.S.W. Sing, R.T. Williams, "Empirical procedures for the analysis of physisorption isotherms", Adsorp. Sci. Technol. 23 (2005) 839-853.

[142] M. Thommes, K. Kaneko, A.V. Neimark, J.P. Olivier, F. Rodriguez-Reinoso, J. Rouquerol, K.S.W. Sing, "Physisorption of gases, with special reference to the evaluation of surface area and pore size distribution (IUPAC Technical Report)", Pure Appl. Chem. 87 (2015) 1051-1069.

[143] P. Schneider, "Adsorption isotherms of microporous-mesoporous solids revisited", Appl. Catal. A Gen. 129 (1995) 157-165.

[144] E.P. Barrett, L.G. Joyner, P.P. Halenda, "The determination of pore volume and area distributions in porous substances. I. Computations from nitrogen isotherms", J. Am. Chem. Soc. 73 (1951) 373-380.

[145] H.P. Klug, L.E. Alexander, "X-ray diffraction procedures: for polycrystalline and amorphous materials", 2nd ed.,Wiley, New York, 1974.

[146] A.K. Singh, "Advanced X-ray techniques in research and industry", IOS Press, 2005.

[147] A. López, M. Mar, "Espectroscopía ultravioleta-visible (UV-vis)", in: *Técnicas de Análisis y Caracterización de Materiales,* M. Faraldos, C. Goberna (Eds.), CSIC, Madrid, 2003, 51-108.

[148] A.B. Murphy, "Modified Kubelka - Munk model for calculation of the reflectance of coatings with optically-rough surfaces", J. Phys. D 39 (2006) 3571-3581.

[149] I.E. Wachs, "In situ Raman spectroscopy studies of catalysts", Top. Catal. 8 (1999) 57-63.

[150] M.A. Bañares-González, R. Ximena-Valenzuela, "Espectroscopia Raman", in: *Técnicas de Análisis y Caracterización de Materiales,* M. Faraldos, C. Goberna (Eds.), CSIC, Madrid, 2003, 173-199.

[151] J.M. Campos-Martín, "Espectroscopia fotoelectrónica de Rayos X (XPS)", in: *Técnicas de Análisis y Caracterización de Materiales,* M. Faraldos, C. Goberna (Eds.), CSIC, Madrid, 2003, 425-463.

[152] D.A. Shirley, "High-resolution X-ray photoemission spectrum of the valence bands of gold", Phys. Rev. B 5 (1972) 4709-4714.

[153] S. Bhatia, J. Beltramini, D.D. Do, "Temperature programmed analysis and its applications in catalytic systems", Catal. Today 7 (1990) 309-438.

[154] N.W. Hurst, S.J. Gentry, A. Jones, "Temperature programmed reduction", Catal. Rev. Sci. Eng. 24 (1982) 233-309.

[155] P.A. Midgley, M. Weyland, H. Stegmann, "Applications of Electron Tomography", in: *Advanced Tomographic Methods in Materials Research and Engineering,* Oxford University Press, Oxford, 2008.

[156] W. Zhou, R. Apkarian, Z.L. Wang, D. Joy, "Fundamentals of Scanning Electron Microscopy (SEM)", in: *Scanning Microscopy for Nanotechnology: Techniques and Applications,* W. Zhou, Z.L. Wang (Eds.), Springer New York, New York, 2007, 1-40.

[157] L. Laffont, M. Weyland, R. Raja, J.M. Thomas, P.A. Midgley, "Electron tomography of heterogeneous catalysts", Inst. Phys. Conf. Ser. 179 (2004) 459-462.

[158] J.M. Thomas, C. Ducati, "Transmission Electron Microscopy", in: *Characterization of Solid Materials and Heterogeneous Catalysts - From Structure to Surface Reactivity,* M. Che, C. Védrine (Eds.), Wiley-VCH, Weinheim, 2012, 655-701.

[159] W. Jennings, "Analytical Gas Chromatography", 2nd ed., Academic Press, San Diego, 1997.

[160] Eurokin. http://eurokin.org/, 2018 (accessed 29 April 2020).

[161] A. Aranzabal, J.A. González-Marcos, J.L. Ayastuy, J.R. González-Velasco, "Kinetics of Pd/alumina catalysed 1,2-dichloroethane gas-phase oxidation", Chem. Eng. Sci. 61 (2006) 3564-3576.

[162] N. Wakao, T. Funazkri, "Effect of fluid dispersion coefficients on particle-to-fluid mass transfer coefficients in packed beds. Correlation of Sherwood numbers", Chem. Eng. Sci. 33 (1978) 1375-1384.

[163] M. Puncochár, J. Draho, "The tortuosity concept in fixed and fluidized bed", Chem. Eng. Sci. 48 (1993) 2173-2175.

[164] E.N. Fuller, P.D. Schettler, J.C. Giddings, "New method for prediction of binary gas-phase diffusion coefficients", Ind. Eng. Chem. 58 (1966) 18-27.

[165] W. Sutherland, "LII. The viscosity of gases and molecular force", Philos. Mag. 36 (1893) 507-531.

[166] C.J. Geankoplis, "Transport Processes and Separation Process Principles: Includes Unit Operations", 4th ed., Prentice Hall Professional Technical Reference, New Jersey, 2003.

[167] F.L. Levy, "A modified Maxwell-Eucken equation for calculating the thermal conductivity of two-component solutions or mixtures", Int. J. Refrig. 4 (1981) 223-225.

[168] A. Biabani-Ravandi, M. Rezaei, "Low temperature CO oxidation over Fe-Co mixed oxide nanocatalysts", Chem. Eng. J. 184 (2012) 141-146.

[169] C. Shi, Y. Wang, A. Zhu, B. Chen, C. Au, "$Mn_xCo_{3-x}O_4$ solid solution as high-efficient catalysts for low-temperature oxidation of formaldehyde", Catal. Commun. 28 (2012) 18-22.

[170] C. Gu, Y. Li, Y. Mo, J. Lan, Y. Jiang, S. Feng, "Rod-like and mushroom-like Co_3O_4–CeO_2 catalysts derived from Ce-1,3,5-benzene tricarboxylic acid for CO preferential oxidation: effects of compositions and morphology", React. Kinet. Mech. Catal. 129 (2020) 135-151.

[171] Y. Zheng, Y. Yu, H. Zhou, W. Huang, Z. Pu, "Combustion of lean methane over Co_3O_4 catalysts prepared with different cobalt precursors", RSC Adv. 10 (2020) 4490-4498.

[172] F. Zasada, J. Janas, W. Piskorz, M. Gorczynska, Z. Sojka, "Total oxidation of lean methane over cobalt spinel nanocubes controlled by the self-adjusted redox state of the catalyst: Experimental and theoretical account for interplay between the Langmuir-Hinshelwood and Mars-Van Krevelen mechanisms", ACS Catal. 7 (2017) 2853-2867.

[173] X. Xu, H. Han, J. Liu, W. Liu, W. Li, X. Wang, "Promotional effects of samarium on Co_3O_4 spinel for CO and CH_4 oxidation", J. Rare Earth. 32 (2014) 159-169.

[174] L.F. Liotta, G. Di Carlo, G. Pantaleo, A.M. Venezia, G. Deganello, "Co_3O_4/CeO_2 composite oxides for methane emissions abatement: Relationship between Co_3O_4-CeO_2 interaction and catalytic activity", Appl. Catal. B Environ. 66 (2006) 217-227.

[175] P. Stefanov, S. Todorova, A. Naydenov, B. Tzaneva, H. Kolev, G. Atanasova, D. Stoyanova, Y. Karakirova, K. Aleksieva, "On the development of active and stable Pd-Co/γ-Al_2O_3 catalyst for complete oxidation of methane", Chem. Eng. J. 266 (2015) 329-338.

[176] N. Bahlawane, "Kinetics of methane combustion over CVD-made cobalt oxide catalysts", Appl. Catal. B Environ. 67 (2006) 168-176.

[177] J.M. Rodrigues, M.F. Ribeiro, E.C. Fernandes, "Catalytic activity of electrodeposited cobalt oxide films for methane combustion in a micro-channel reactor", Fuel 232 (2018) 51-59.

[178] G.I. Golodets, "Chapter V: The Kinetics of Gas-Phase Heterogeneous Catalytic Reactions Involving Molecular Oxygen", in: *Heterogeneous Catalytic Reactions Involving Molecular Oxygen,* G.I. Golodets (Ed.), Elsevier, Amsterdam, 1983, 126-150.

[179] "26 - Cobalt, Rhodium and Iridium", in: *Chemistry of the Elements (Second Edition),* N.N. Greenwood, A. Earnshaw (Eds.), Butterworth-Heinemann, Oxford, 1997, 1113-1143.

[180] G. Maniak, P. Stelmachowski, F. Zasada, W. Piskorz, A. Kotarba, Z. Sojka, "Guidelines for optimization of catalytic activity of 3d transition metal oxide catalysts in N_2O decomposition by potassium promotion", Catal. Today 176 (2011) 369-372.

[181] P. Stelmachowski, G. Maniak, A. Kotarba, Z. Sojka, "Strong electronic promotion of Co_3O_4 towards N_2O decomposition by surface alkali dopants", Catal. Commun. 10 (2009) 1062-1065.

[182] P.W. Park, J.K. Kil, H.H. Kung, M.C. Kung, "NO decomposition over sodium-promoted cobalt oxide", Catal. Today 42 (1998) 51-60.

[183] G. Zou, Y. Xu, S. Wang, M. Chen, W. Shangguan, "The synergistic effect in Co-Ce oxides for catalytic oxidation of diesel soot", Catal. Sci. Technol. 5 (2015) 1084-1092.

[184] J. Chen, X. Zhang, H. Arandiyan, Y. Peng, H. Chang, J. Li, "Low temperature complete combustion of methane over cobalt chromium oxides catalysts", Catal. Today 201 (2013) 12-18.

[185] X. Xu, J. Wang, M. Sun, "Spectral analysis on CoO_x films deposited by atomic layer deposition", Chem. Phys. Lett. 742 (2020) 137159.

[186] K. Jirátová, R. Perekrestov, M. Dvoráková, J. Balabánová, P. Topka, M. Kostejn, J. Olejnícek, M. Cada, Z. Hubicka, F. Kovanda, "Cobalt oxide catalysts in the form of thin films prepared by magnetron sputtering on stainless-steel meshes: Performance in ethanol oxidation", Catalysts 9 (2019) 806.

[187] I. Lopes, N. El Hassan, H. Guerba, G. Wallez, A. Davidson, "Size-induced structural modifications affecting Co_3O_4 nanoparticles patterned in SBA-15 silicas", Chem. Mater. 18 (2006) 5826-5828.

[188] C.F. Windisch Jr., G.J. Exarhos, R.R. Owings, "Vibrational spectroscopic study of the site occupancy distribution of cations in nickel cobalt oxides", J. Appl. Phys. 95 (2004) 5435-5442.

[189] J. González-Prior, R. López-Fonseca, J.I. Gutiérrez-Ortiz, B. de Rivas, "Oxidation of 1,2-dichloroethane over nanocube-shaped Co_3O_4 catalysts", Appl. Catal. B Environ. 199 (2016) 384-393.

[190] M.C. Biesinger, B.P. Payne, A.P. Grosvenor, L.W.M. Lau, A.R. Gerson, R.S.C. Smart, "Resolving surface chemical states in XPS analysis of first row transition metals, oxides and hydroxides: Cr, Mn, Fe, Co and Ni", Appl. Surf. Sci. 257 (2011) 2717-2730.

[191] J. Dupin, D. Gonbeau, P. Vinatier, A. Levasseur, "Systematic XPS studies of metal oxides, hydroxides and peroxides", Phys. Chem. Chem. Phys. 2 (2000) 1319-1324.

[192] K. Asano, C. Ohnishi, S. Iwamoto, Y. Shioya, M. Inoue, "Potassium-doped Co_3O_4 catalyst for direct decomposition of N_2O", Appl. Catal. B Environ. 78 (2008) 242-249.

[193] M. Haneda, Y. Kintaichi, N. Bion, H. Hamada, "Alkali metal-doped cobalt oxide catalysts for NO decomposition", Appl. Catal. B Environ. 46 (2003) 473-482.

[194] T.H. Lim, S.J. Cho, H.S. Yang, M.H. Engelhard, D.H. Kim, "Effect of Co/Ni ratios in cobalt nickel mixed oxide catalysts on methane combustion", Appl. Catal. A Gen. 505 (2015) 62-69.

[195] R. Dumitru, F. Papa, I. Balint, D.C. Culita, C. Munteanu, N. Stanica, A. Ianculescu, L. Diamandescu, O. Carp, "Mesoporous cobalt ferrite: A rival of platinum catalyst in methane combustion reaction", Appl. Catal. A Gen. 467 (2013) 178-186.

[196] J. Li, X. Liang, S. Xu, J. Hao, "Catalytic performance of manganese cobalt oxides on methane combustion at low temperature", Appl. Catal. B Environ. 90 (2009) 307-312.

[197] N.E. Machin, C. Karakaya, A. Celepci, "Catalytic combustion of methane on La-, Ce-, and Co-based mixed oxides", Energ. Fuel. 22 (2008) 2166-2171.

[198] N. M. Deraz, "Surface and catalytic properties of Co_3O_4-doped CuO-Al_2O_3 catalysts", Colloids Surf. A Physicochem. Eng. Asp. 207 (2002) 197-206.

[199] X. Xu, J. Li, Z. Hao, "CeO_2-Co_3O_4 catalysts for CO oxidation", J. Rare Earth. 24 (2006) 172-176.

[200] J. Kaczmarczyk, F. Zasada, J. Janas, P. Indyka, W. Piskorz, A. Kotarba, Z. Sojka, "Thermodynamic stability, redox properties, and reactivity of Mn_3O_4, Fe_3O_4, and Co_3O_4 model catalysts for N_2O decomposition: Resolving the origins of steady turnover", ACS Catal. 6 (2016) 1235-1246.

[201] C. Wang, S. Yang, H. Chang, Y. Peng, J. Li, "Structural effects of iron spinel oxides doped with Mn, Co, Ni and Zn on selective catalytic reduction of NO with NH_3", J. Mol. Catal. A Chem. 376 (2013) 13-21.

[202] E.R. Stobbe, B.A. De Boer, J.W. Geus, "The reduction and oxidation behaviour of manganese oxides", Catal. Today 47 (1999) 161-167.

[203] C. Tang, W. Yu, C. Lin, C. Wang, S. Chien, "Phase transformation in CeO_2-Co_3O_4 binary oxide under reduction and calcination pretreatments", Catal. Lett. 116 (2007) 161-166.

[204] F. Rong, J. Zhao, P. Su, Y. Yao, M. Li, Q. Yang, C. Li, "Zinc-cobalt oxides as efficient water oxidation catalysts: The promotion effect of ZnO", J. Mater. Chem. A 3 (2015) 4010-4017.

[205] A.K. Das, N.H. Kim, S.H. Lee, Y. Sohn, J.H. Lee, "Facile synthesis of $CuCo_2O_4$ composite octahedrons for high performance supercapacitor application", Compos. Part B: Eng. 150 (2018) 269-276.

[206] S. Trivedi, R. Prasad, "Selection of cobaltite and effect of preparation method of $NiCo_2O_4$ for catalytic oxidation of CO–CH_4 mixture", Asia-Pac. J. Chem. Eng. 12 (2017) 440-453.

[207] K.K. Babitha, A. Sreedevi, K.P. Priyanka, B. Sabu, T. Varghese, "Structural characterization and optical studies of CeO_2 nanoparticles synthesized by chemical precipitation", Indian J. Pure Appl. Phys. 53 (2015) 596-603.

[208] M. Romeo, K. Bak, J. El Fallah, F. Le Normand, L. Hilaire, "XPS Study of the reduction of cerium dioxide", Surf. Interface Anal. 20 (1993) 508-512.

[209] J. Chen, C. Li, S. Li, P. Lu, L. Gao, X. Du, Y. Yi, "Simultaneous removal of HCHO and elemental mercury from flue gas over Co-Ce oxides supported on activated coke impregnated by sulfuric acid", Chem. Eng. J. 338 (2018) 358-368.

[210] M. Florea, F. Matei-Rutkovska, G. Postole, A. Urda, F. Neatu, V.I. Pârvulescu, P. Gelin, "Doped ceria prepared by precipitation route for steam reforming of methane", Catal. Today 306 (2018) 166-171.

[211] C.G. Rotaru, G. Postole, M. Florea, F. Matei-Rutkovska, V.I. Pârvulescu, P. Gelin, "Dry reforming of methane on ceria prepared by modified precipitation route", Appl. Catal. A Gen. 494 (2015) 29-40.

[212] L. Wang, H. Liu, Y. Liu, Y. Chen, S. Yang, "Effect of precipitants on Ni-CeO_2 catalysts prepared by a co-precipitation method for the reverse water-gas shift reaction", J. Rare Earth. 31 (2013) 969-974.

[213] A.W. Budiman, S. Song, T. Chang, C. Shin, M. Choi, "Dry reforming of methane over cobalt catalysts: A literature review of catalyst development", Catal. Surv. Asia 16 (2012) 183-197.

[214] D. Qiao, G. Lu, Y. Guo, Y. Wang, Y. Guo, "Effect of water vapor on the CO and CH_4 catalytic oxidation over CeO_2-MO_x (M=Cu, Mn, Fe, Co, and Ni) mixed oxide", J. Rare Earth. 28 (2010) 742-746.

[215] L. He, Y. Fan, J. Bellettre, J. Yue, L. Luo, "A review on catalytic methane combustion at low temperatures: Catalysts, mechanisms, reaction conditions and reactor designs", Renew. Sust. Energ. Rev. 119 (2020) 109589.

[216] T. Xiao, S. Ji, H. Wang, K.S. Coleman, M.L.H. Green, "Methane combustion over supported cobalt catalysts", J. Mol. Catal. A Chem. 175 (2001) 111-123.

[217] J. González-Prior, R. López-Fonseca, J.I. Gutiérrez-Ortiz, B. de Rivas, "Catalytic removal of chlorinated compounds over ordered mesoporous cobalt oxides synthesised by hard-templating", Appl. Catal. B Environ. 222 (2018) 9-17.

[218] Q. Ren, S. Mo, R. Peng, Z. Feng, M. Zhang, L. Chen, M. Fu, J. Wu, D. Ye, "Controllable synthesis of 3D hierarchical Co_3O_4 nanocatalysts with various morphologies for the catalytic oxidation of toluene", J. Mater. Chem. A 6 (2018) 498-509.

[219] G. Salek, P. Alphonse, P. Dufour, S. Guillemet-Fritsch, C. Tenailleau, "Low-temperature carbon monoxide and propane total oxidation by nanocrystalline cobalt oxides", Appl. Catal. B Environ. 147 (2014) 1-7.

[220] G. Laugel, J. Arichi, H. Guerba, M. Molière, A. Kiennemann, F. Garin, B. Louis, "Co_3O_4 and Mn_3O_4 nanoparticles dispersed on SBA-15: Efficient catalysts for methane combustion", Catal. Lett. 125 (2008) 14-21.

[221] V.G. Milt, M.A. Ulla, E.A. Lombardo, "Cobalt-containing catalysts for the high-temperature combustion of methane", Catal. Lett. 65 (2000) 67-73.

[222] Y. Ji, Z. Zhao, A. Duan, G. Jiang, J. Liu, "Comparative study on the formation and reduction of bulk and Al_2O_3-supported cobalt oxides by H_2-TPR technique", J. Phys. Chem. C 113 (2009) 7186-7199.

[223] Y. Li, X. Wang, "MgO modifying Al_2O_3 to load cobalt oxide for catalytic N_2O decomposition", Catal. Lett. 149 (2019) 1856-1863.

[224] I. Zacharaki, C.G. Kontoyannis, S. Boghosian, A. Lycourghiotis, C. Kordulis, "Cobalt oxide supported on alumina catalysts prepared by various methods for use in catalytic afterburner of PEM fuel cell", Catal. Today 143 (2009) 38-44.

[225] Y. Kobayashi, Y. Iwasaki, "Fabrication of macroporous Co_3O_4–MgO composite catalysts for methylene blue degradation using oxone as an oxidant", J. Chem. Eng. Japan 50 (2017) 821-826.

[226] M.A. Ulla, R. Spretz, E. Lombardo, W. Daniell, H. Knözinger, "Catalytic combustion of methane on Co/MgO: Characterisation of active cobalt sites", Appl. Catal. B Environ. 29 (2001) 217-229.

[227] L. Bai, F. Wyrwalski, M. Safariamin, R. Bleta, J. Lamonier, C. Przybylski, E. Monflier, A. Ponchel, "Cyclodextrin-cobalt (II) molecule-ion pairs as precursors to active Co_3O_4/ZrO_2 catalysts for the complete oxidation of formaldehyde: Influence of the cobalt source", J. Catal. 341 (2016) 191-204.

[228] M. Pudukudy, Z. Yaakob, "Methane decomposition over Ni, Co and Fe based monometallic catalysts supported on sol gel derived SiO_2 microflakes", Chem. Eng. J. 262 (2015) 1009-1021.

[229] W.K. Jozwiak, E. Szubiakiewicz, J. Góralski, A. Klonkowski, T. Paryjczak, "Physico-chemical and catalytic study of the Co/SiO_2 catalysts", Kinet. Catal. 45 (2004) 247-255.

[230] G. Grzybek, P. Stelmachowski, S. Gudyka, P. Indyka, Z. Sojka, N. Guillén-Hurtado, V. Rico-Pérez, A. Bueno-López, A. Kotarba, "Strong dispersion effect of cobalt spinel active phase spread over ceria for catalytic N_2O decomposition: The role of the interface periphery", Appl. Catal. B Environ. 180 (2016) 622-629.

[231] A. Klegova, A. Inayat, P. Indyka, J. Grybos, Z. Sojka, K. Pacultová, W. Schwieger, A. Volodarskaja, P. Kustrowski, A. Rokicinska, D. Fridrichová, L. Obalová, "Cobalt mixed oxides deposited on the SiC open-cell foams for nitrous oxide decomposition", Appl. Catal. B Environ. 255 (2019) 117745.

[232] H. Song, Q. Zhao, X. Zhou, Z. Cao, M. Luo, "Selection of highly active and stable Co supported SiC catalyst for Fischer-Tropsch synthesis: Effect of the preparation method", Fuel 229 (2018) 144-150.

[233] Z. Zhu, G. Lu, Z. Zhang, Y. Guo, Y. Guo, Y. Wang, "Highly active and stable Co_3O_4/ZSM-5 catalyst for propane oxidation: Effect of the preparation method", ACS Catal. 3 (2013) 1154-1164.

[234] K. Jirátová, J. Balabánová, F. Kovanda, A. Klegová, L. Obalová, R. Fajgar, "Cobalt oxides supported over ceria–zirconia coated cordierite monoliths as catalysts for deep oxidation of ethanol and N_2O decomposition", Catal. Lett. 147 (2017) 1379-1391.

[235] G. Grzybek, K. Ciura, S. Wójcik, J. Grybos, P. Indyka, M. Inger, K. Antoniak-Jurak, P. Kowalik, A. Kotarba, Z. Sojka, "On the selection of the best polymorph of Al_2O_3 carriers for supported cobalt nano-spinel catalysts for N_2O abatement: an interplay between preferable surface spreading and damaging active phase-support interaction", Catal. Sci. Technol. 7 (2017) 5723-5732.

[236] M.M. Yung, E.M. Holmgreen, U.S. Ozkan, "Cobalt-based catalysts supported on titania and zirconia for the oxidation of nitric oxide to nitrogen dioxide", J. Catal. 247 (2007) 356-367.

[237] D.S. Kim, Y.H. Kim, J.E. Yie, E.D. Park, "NO oxidation over supported cobalt oxide catalysts", Korean J. Chem. Eng. 27 (2010) 49-54.

[238] F. Wyrwalski, J. Giraudon, J. Lamonier, "Synergistic coupling of the redox properties of supports and cobalt oxide Co_3O_4 for the complete oxidation of volatile organic compounds", Catal. Lett. 137 (2010) 141-149.

[239] W. Zhang, H.L. Tay, S.S. Lim, Y. Wang, Z. Zhong, R. Xu, "Supported cobalt oxide on MgO: Highly efficient catalysts for degradation of organic dyes in dilute solutions", Appl. Catal. B Environ. 95 (2010) 93-99.

[240] L. Lukashuk, N. Yigit, R. Rameshan, E. Kolar, D. Teschner, M. Hävecker, A. Knop-Gericke, R. Schlögl, K. Föttinger, G. Rupprechter, "Operando Insights into CO Oxidation on Cobalt Oxide Catalysts by NAP-XPS, FTIR, and XRD", ACS Catal. 8 (2018) 8630-8641.

[241] F. Zasada, W. Piskorz, J. Janas, J. Grybos, P. Indyka, Z. Sojka, "Reactive oxygen species on the (100) facet of cobalt spinel nanocatalyst and their relevance in $^{16}O_2/^{18}O_2$ isotopic exchange, *de*N_2O, and *de*CH_4 processes - A theoretical and experimental account", ACS Catal. 5 (2015) 6879-6892.

[242] J. Dou, Y. Tang, L. Nie, C.M. Andolina, X. Zhang, S. House, Y. Li, J. Yang, F. Tao, "Complete oxidation of methane on Co_3O_4/CeO_2 nanocomposite: A synergic effect", Catal. Today 311 (2018) 48-55.

[243] M. Kumar, G. Rattan, R. Prasad, "Optimisation of cobalt loading on γ-Al_2O_3 for total oxidation of methane", Indian Chem. Eng. 59 (2017) 161-176.

[244] P.J. Jodlowski, J. Kryca, M. Iwaniszyn, R. Jedrzejczyk, J. Thomas, A. Kolodziej, J. Lojewska, "Methane combustion modelling of wire gauze reactor coated with Co_3O_4-CeO_2, Co_3O_4-PdO catalysts", Catal. Today 216 (2013) 276-282.

[245] J. Pérez-Ramírez, G. Mul, F. Kapteijn, J.A. Moulijn, "In situ investigation of the thermal decomposition of Co-Al hydrotalcite in different atmospheres", J. Mater. Chem. 11 (2001) 821-830.

[246] X. Jiang, Y. Ma, Y. Chen, Y. Li, Q. Ma, Z. Zhang, C. Wang, Y. Yang, "Raman analysis of cobalt blue pigment in blue and white porcelain: A reassessment", Spectrochim. Acta Part A Mol. Biomol. Spectrosc. 190 (2018) 61-67.

[247] V. D'Ippolito, G.B. Andreozzi, D. Bersani, P.P. Lottici, "Raman fingerprint of chromate, aluminate and ferrite spinels", J. Raman Spectrosc. 46 (2015) 1255-1264.

[248] M. Wu, Y. Fu, W. Zhan, Y. Guo, Y. Guo, Y. Wang, G. Lu, "Catalytic performance of MgO-supported Co catalyst for the liquid phase oxidation of cyclohexane with molecular oxygen", Catalysts 7 (2017) 155.

[249] L. Wu, D. Jiao, J.-A. Wang, L. Chen, F. Cao, "The role of MgO in the formation of surface active phases of $CoMo/Al_2O_3$-MgO catalysts for hydrodesulfurization of dibenzothiophene", Catal. Commun. 11 (2009) 302-305.

[250] E. Cazzanelli, A. Kuzmin, G. Mariotto, N. Mironova-Ulmane, "Study of vibrational and magnetic excitations in $Ni_cMg_{1-c}O$ solid solutions by Raman spectroscopy", J. Phys. Condens. Matter 15 (2003) 2045-2052.

[251] B. Cui, L. Zhou, K. Li, Y.-. Liu, D. Wang, Y. Ye, S. Li, "Holey Co-Ce oxide nanosheets as a highly efficient catalyst for diesel soot combustion", Appl. Catal. B Environ. 267 (2020) 118670.

[252] J. Yang, H. Liu, W.N. Martens, R.L. Frost, "Synthesis and characterization of cobalt hydroxide, cobalt oxyhydroxide, and cobalt oxide nanodiscs", J. Phys. Chem. C 114 (2010) 111-119.

[253] X. Duan, M. Pan, F. Yu, D. Yuan, "Synthesis, structure and optical properties of $CoAl_2O_4$ spinel nanocrystals", J. Alloy. Compd. 509 (2011) 1079-1083.

[254] L.F. Liotta, H. Wu, G. Pantaleo, A.M. Venezia, "Co_3O_4 nanocrystals and Co_3O_4-MO_x binary oxides for CO, CH_4 and VOC oxidation at low temperatures: A review", Catal. Sci. Technol. 3 (2013) 3085-3102.

[255] S. Ji, S. Ji, H. Wang, E. Flahaut, K.S. Coleman, M.L.H. Green, "Catalytic combustion of methane over cobalt-magnesium oxide solid solution catalysts", Catal. Lett. 75 (2001) 65-71.

[256] B. de Rivas, C. Sampedro, M. García-Real, R. López-Fonseca, J.I. Gutiérrez-Ortiz, "Promoted activity of sulphated Ce/Zr mixed oxides for chlorinated VOC oxidative abatement", Appl. Catal. B Environ. 129 (2013) 225-235.

[257] B. de Rivas, C. Sampedro, E.V. Ramos-Fernández, R. López-Fonseca, J. Gascon, M. Makkee, J.I. Gutiérrez-Ortiz, "Influence of the synthesis route on the catalytic oxidation of 1,2-dichloroethane over CeO_2/H-ZSM5 catalysts", Appl. Catal. A Gen. 456 (2013) 96-104.

[258] S. Zeng, X. Fu, T. Zhou, X. Wang, H. Su, "Influence of pore distribution on catalytic performance over inverse CeO_2/Co_3O_4 catalysts for CH_4/CO_2 reforming", Fuel Process Technol. 114 (2013) 69-74.

[259] F. Zasada, J. Grybos, E. Budiyanto, J. Janas, Z. Sojka, "Oxygen species stabilized on the cobalt spinel nano-octahedra at various reaction conditions and their role in catalytic CO and CH_4 oxidation, N_2O decomposition and oxygen isotopic exchange", J. Catal. 371 (2019) 224-235.

[260] D. Li, Y. Ding, X. Wei, Y. Xiao, L. Jiang, "Cobalt-aluminum mixed oxides prepared from layered double hydroxides for the total oxidation of benzene", Appl. Catal. A Gen. 507 (2015) 130-138.

[261] L. Zhang, L. Dong, W. Yu, L. Liu, Y. Deng, B. Liu, H. Wan, F. Gao, K. Sun, L. Dong, "Effect of cobalt precursors on the dispersion, reduction, and CO oxidation of CoO_x/γ-Al_2O_3 catalysts calcined in N_2", J. Colloid Interface Sci. 355 (2011) 464-471.

[262] L.G.A. van de Water, G.L. Bezemer, J.A. Bergwerff, M. Versluijs-Helder, B.M. Weckhuysen, K.P. de Jong, "Spatially resolved UV-vis microspectroscopy on the preparation of alumina-supported Co Fischer-Tropsch catalysts: Linking activity to Co distribution and speciation", J. Catal. 242 (2006) 287-298.

[263] Y. Brik, M. Kacimi, M. Ziyad, F. Bozon-Verduraz, "Titania-supported Cobalt and cobalt-phosphorus catalysts: Characterization and performances in ethane oxidative dehydrogenation", J. Catal. 202 (2001) 118-128.

[264] T. Das, S. Sengupta, G. Deo, "Effect of calcination temperature during the synthesis of Co/Al_2O_3 catalyst used for the hydrogenation of CO_2", React. Kinet. Mech. Catal. 110 (2013) 147-162.

[265] F. Dumond, E. Marceau, M. Che, "A study of cobalt speciation in Co/Al_2O_3 catalysts prepared from solutions of cobalt-ethylenediamine complexes", J. Phys. Chem. C 111 (2007) 4780-4789.

[266] A.H.A. Monteverde Videla, P. Stelmachowski, G. Ercolino, S. Specchia, "Benchmark comparison of Co_3O_4 spinel-structured oxides with different morphologies for

oxygen evolution reaction under alkaline conditions", J. Appl. Electrochem. 47 (2017) 295-304.

[267] L.F. Liotta, G. Pantaleo, A. Macaluso, G. Di Carlo, G. Deganello, "CoO_x catalysts supported on alumina and alumina-baria: influence of the support on the cobalt species and their activity in NO reduction by C_3H_6 in lean conditions", Appl. Catal. A Gen. 245 (2003) 167-177.

[268] J. Cheng, J. Yu, X. Wang, L. Li, J. Li, Z. Hao, "Novel CH_4 combustion catalysts derived from Cu-Co/X-Al (X = Fe, Mn, La, Ce) hydrotalcite-like compounds", Energ. Fuels 22 (2008) 2131-2137.

[269] H.G. El-Shobaky, M.A. Shouman, A.A. Attia, "Effect of La_2O_3 and Mn_2O_3-doping of Co_3O_4/Al_2O_3 system on its surface and catalytic properties", Colloids Surf. A Physicochem. Eng. Asp. 274 (2006) 62-70.

[270] M. Riad, "Influence of magnesium and chromium oxides on the physicochemical properties of γ-alumina", Appl. Catal. A Gen. 327 (2007) 13-21.

[271] E. Genty, S. Siffert, R. Cousin, "Investigation of reaction mechanism and kinetic modelling for the toluene total oxidation in presence of CoAlCe catalyst", Catal. Today 333 (2019) 28-35.

[272] S. Park, G. Kwak, Y. Lee, K. Jun, Y.T. Kim, "Effect of H_2O on slurry-phase Fischer–Tropsch synthesis over alumina-supported cobalt catalysts", Bull. Korean Chem. Soc. 39 (2018) 540-547

[273] J. Park, S. Yeo, T. Kang, I. Heo, K. Lee, T. Chang, "Enhanced stability of Co catalysts supported on phosphorus-modified Al_2O_3 for dry reforming of CH_4", Fuel 212 (2018) 77-87.

[274] V. Garcilaso, J. Barrientos, L.F. Bobadilla, O.H. Laguna, M. Boutonnet, M.A. Centeno, J.A. Odriozola, "Promoting effect of CeO_2, ZrO_2 and Ce/Zr mixed oxides on Co/γ-Al_2O_3 catalyst for Fischer-Tropsch synthesis", Renew. Energ. 132 (2019) 1141-1150.

[275] Y. Zhang, H. Xiong, K. Liew, J. Li, "Effect of magnesia on alumina-supported cobalt Fischer-Tropsch synthesis catalysts", J. Mol. Catal. A Chem. 237 (2005) 172-181.

[276] G. Ye, G. Oprea, T. Troczynski, "Synthesis of $MgAl_2O_4$ spinel powder by combination of sol-gel and precipitation processes", J. Am. Ceram. Soc. 88 (2005) 3241-3244.

[277] B. Caloch, M.S. Rana, J. Ancheyta, "Improved hydrogenolysis (C–S, C–M) function with basic supported hydrodesulfurization catalysts", Catal. Today 98 (2004) 91-98.

[278] Z. Fattah, M. Rezaei, A. Biabani-Ravandi, A. Irankhah, H.R. Arandiyan, "Synthesis, characterization and application of Co–MgO mixed oxides in oxidation of carbon monoxide", Chem. Eng. Commun. 203 (2016) 200-209.

[279] J.L. Ewbank, L. Kovarik, C.C. Kenvin, C. Sievers, "Effect of preparation methods on the performance of Co/Al_2O_3 catalysts for dry reforming of methane", Green Chem. 16 (2014) 885-896.

[280] M. Gil-Calvo, C. Jiménez-González, B. De Rivas, J.I. Gutiérrez-Ortiz, R. López-Fonseca, "Hydrogen production by reforming of methane over $NiAl_2O_4$/$Ce_xZr_{1-x}O_2$ catalysts", Chem. Eng. Trans. 57 (2017) 901-906.

[281] Y.J. Wong, M.K. Koh, N.F. Khairudin, S. Ichikawa, Y. Morikawa, A.R. Mohamed, "Development of Co supported on Co–Al spinel catalysts from exsolution of amorphous Co–Al oxides for carbon dioxide reforming of methane", ChemCatChem 11 (2019) 5593-5605.

[282] Y. Chan, C. Wu, P. Shen, S. Chen, "Nickel aluminate oxides/hydroxides by pulsed laser ablation of $NiAl_2O_4$ powder in water", Appl. Phys. A 116 (2014) 1065-1073.

[283] G. George, S. Anandhan, "Synthesis and characterisation of nickel oxide nanofibre webs with alcohol sensing characteristics", RSC Adv. 4 (2014) 62009-62020.

[284] R. Benrabaa, A. Barama, H. Boukhlouf, J. Guerrero-Caballero, A. Rubbens, E. Bordes-Richard, A. Löfberg, R. Vannier, "Physico-chemical properties and syngas production via dry reforming of methane over $NiAl_2O_4$ catalyst", Int. J. Hydrogen Energy 42 (2017) 12989-12996.

[285] P. Stelmachowski, A.H.A. Monteverde Videla, K. Ciura, S. Specchia, "Oxygen evolution catalysis in alkaline conditions over hard templated nickel-cobalt based spinel oxides", Int. J. Hydrogen Energy 42 (2017) 27910-27918.

[286] H.A.E. Hagelin-Weaver, G.B. Hoflund, D.M. Minahan, G.N. Salaita, "Electron energy loss spectroscopic investigation of Co metal, CoO, and Co_3O_4 before and after Ar^+ bombardment", Appl. Surf. Sci. 235 (2004) 420-448.

[287] Y. Wan, J. Chen, J. Zhan, Y. Ma, "Facile synthesis of mesoporous $NiCo_2O_4$ fibers with enhanced photocatalytic performance for the degradation of methyl red under visible light irradiation", J. Environ. Chem. Eng. 6 (2018) 6079-6087.

[288] I. Preda, R.J.O. Mossanek, M. Abbate, L. Alvarez, J. Méndez, A. Gutiérrez, L. Soriano, "Surface contributions to the XPS spectra of nanostructured NiO deposited on HOPG", Surf. Sci. 606 (2012) 1426-1430.

[289] D. Delgado, R. Sanchís, J.A. Cecilia, E. Rodríguez-Castellón, A. Caballero, B. Solsona, J.M.L. Nieto, "Support effects on NiO-based catalysts for the oxidative dehydrogenation (ODH) of ethane", Catal. Today 333 (2019) 10-16.

[290] G. Garbarino, C. Wang, I. Valsamakis, S. Chitsazan, P. Riani, E. Finocchio, M. Flytzani-Stephanopoulos, G. Busca, "A study of Ni/Al_2O_3 and Ni-La/Al_2O_3 catalysts for the steam reforming of ethanol and phenol", Appl. Catal. B Environ. 174-175 (2015) 21-34.

[291] M. Zhao, J. Deng, J. Liu, Y. Li, J. Liu, Z. Duan, J. Xiong, Z. Zhao, Y. Wei, W. Song, Y. Sun, "Roles of surface-active oxygen species on 3DOM cobalt-based spinel catalysts

$M_xCo_{3-x}O4$ (M = Zn and Ni) for NO_x-assisted soot oxidation", ACS Catal. 9 (2019) 7548-7567.

[292] Y. Huang, W. Fan, B. Long, H. Li, W. Qiu, F. Zhao, Y. Tong, H. Ji, "Alkali-modified non-precious metal 3D-$NiCo_2O_4$ nanosheets for efficient formaldehyde oxidation at low temperature", J. Mater. Chem. A 4 (2016) 3648-3654.

[293] Q. Yu, X. Wu, C. Tang, L. Qi, B. Liu, F. Gao, K. Sun, L. Dong, Y. Chen, "Textural, structural, and morphological characterizations and catalytic activity of nanosized CeO_2–MO_x ($M = Mg^{2+}$, Al^{3+}, Si^{4+}) mixed oxides for CO oxidation", J. Colloid Interf. Sci. 354 (2011) 341-352.

[294] A. Martínez-Arias, M. Fernández-García, L.N. Salamanca, R.X. Valenzuela, J.C. Conesa, J. Soria, "Structural and redox properties of ceria in alumina-supported ceria catalyst supports", J. Phys. Chem. B 104 (2000) 4038-4046.

[295] M. Gil-Calvo, C. Jiménez-González, B. de Rivas, J.I. Gutiérrez-Ortiz, R. López-Fonseca, "Novel nickel aluminate-derived catalysts supported on ceria and ceria-zirconia for partial oxidation of methane", Ind. Eng. Chem. Res. 56 (2017) 6186-6197.

[296] D.K. Chlebda, R.J. Jedrzejczyk, P.J. Jodlowski, J. Lojewska, "Surface structure of cobalt, palladium, and mixed oxide-based catalysts and their activity in methane combustion studied by means of micro-Raman spectroscopy", J. Raman Spectrosc. 48 (2017) 1871-1880.

[297] Q. Zhang, S. Mo, B. Chen, W. Zhang, C. Huang, D. Ye, "Hierarchical Co_3O_4 nanostructures in-situ grown on 3D nickel foam towards toluene oxidation", Mol. Catal. 454 (2018) 12-20.

[298] R. Dziembaj, A. Chojnacka, Z. Piwowarska, M. Gajewska, M. Swietoslawski, S. Górecka, M. Molenda, "Comparative study of Co-rich and Ce-rich oxide nanocatalysts ($Co_xCe_{1-x}O_y$) for low-temperature total oxidation of methanol", Catal. Today 333 (2019) 196-207.

[299] G. Azimi, R. Dhiman, H. Kwon, A.T. Paxson, K.K. Varanasi, "Hydrophobicity of rare-earth oxide ceramics", Nat. Mater. 12 (2013) 315.

[300] Ø. Borg, Z. Yu, D. Chen, E.A. Blekkan, E. Rytter, A. Holmen, "The effect of water on the activity and selectivity for carbon nanofiber supported cobalt Fischer-Tropsch catalysts", Top. Catal. 57 (2014) 491-499.

[301] A.K. Dalai, B.H. Davis, "Fischer–Tropsch synthesis: A review of water effects on the performances of unsupported and supported Co catalysts", Appl. Catal. A Gen. 348 (2008) 1-15.

[302] X. Guo, K. Nakanishi, K. Kanamori, Y. Zhu, H. Yang, "Preparation of macroporous cordierite monoliths via the sol–gel process accompanied by phase separation", J. Eur. Ceram. Soc. 34 (2014) 817-823.

[303] C. Hung, "Characterization and performance of Pt-Pd-Rh cordierite monolith catalyst for selectivity catalytic oxidation of ammonia", J. Hazard. Mater. 180 (2010) 561-565.

[304] A.R. Studart, U.T. Gonzenbach, E. Tervoort, L.J. Gauckler, "Processing routes to macroporous ceramics: A review", J. Am. Ceram. Soc. 89 (2006) 1771-1789.

[305] G. Ercolino, S. Karimi, P. Stelmachowski, S. Specchia, "Catalytic combustion of residual methane on alumina monoliths and open cell foams coated with Pd/Co_3O_4", Chem. Eng. J. 326 (2017) 339-349.

[306] F.C. Patcas, G.I. Garrido, B. Kraushaar-Czarnetzki, "CO oxidation over structured carriers: A comparison of ceramic foams, honeycombs and beads", Chem. Eng. Sci. 62 (2007) 3984-3990.

[307] N. Gao, Y. Han, C. Quan, "Study on steam reforming of coal tar over NiCo/ceramic foam catalyst for hydrogen production: Effect of Ni/Co ratio", Int. J. Hydrogen Energy 43 (2018) 22170-22186.

[308] K. Urasaki, S. Kado, A. Kiryu, K. Imagawa, K. Tomishige, R. Horn, O. Korup, Y. Suehiro, "Synthesis gas production by catalytic partial oxidation of natural gas using ceramic foam catalyst", Catal. Today 299 (2018) 219-228.

[309] M. Frey, T. Romero, A. Roger, D. Edouard, "Open cell foam catalysts for CO_2 methanation: Presentation of coating procedures and in situ exothermicity reaction study by infrared thermography", Catal. Today 273 (2016) 83-90.

[310] R. Faure, F. Rossignol, T. Chartier, C. Bonhomme, A. Maître, G. Etchegoyen, P. Del Gallo, D. Gary, "Alumina foam catalyst supports for industrial steam reforming processes", J. Eur. Ceram. Soc. 31 (2011) 303-312.

[311] C. Italiano, R. Balzarotti, A. Vita, S. Latorrata, C. Fabiano, L. Pino, C. Cristiani, "Preparation of structured catalysts with Ni and $Ni–Rh/CeO_2$ catalytic layers for syngas production by biogas reforming processes", Catal. Today 273 (2016) 3-11.

[312] P. Stelmachowski, G. Maniak, J. Kaczmarczyk, F. Zasada, W. Piskorz, A. Kotarba, Z. Sojka, "Mg and Al substituted cobalt spinels as catalysts for low temperature deN_2O—Evidence for octahedral cobalt active sites", Appl. Catal. B Environ. 146 (2014) 105-111.

[313] S. Specchia, C. Galletti, V. Specchia, "Solution Combustion Synthesis as intriguing technique to quickly produce performing catalysts for specific applications", Stud. Surf. Sci. Catal. 175 (2010) 59-67.

[314] J. Rosen, G.S. Hutchings, F. Jiao, "Ordered mesoporous cobalt oxide as highly efficient oxygen evolution catalyst", J. Am. Chem. Soc. 135 (2013) 4516-4521.

[315] H. Sohn, G. Celik, S. Gunduz, D. Dogu, S. Zhang, J. Shan, F.F. Tao, U.S. Ozkan, "Oxygen mobility in pre-reduced nano- and macro-ceria with Co loading: An AP-XPS, in-situ DRIFTS and TPR study", Catal. Lett. 147 (2017) 2863-2876.

[316] M. Meng, Y. Zha, J. Luo, T. Hu, Y. Xie, T. Liu, J. Zhang, "A study on the catalytic synergy effect between noble metals and cobalt phases in Ce-Al-O supported catalysts", Appl. Catal. A Gen. 301 (2006) 145-151.

[317] S. Gudyka, G. Grzybek, J. Grybos, P. Indyka, B. Leszczynski, A. Kotarba, Z. Sojka, "Enhancing the deN_2O activity of the supported Co_3O_4|α-Al_2O_3 catalyst by glycerol-assisted shape engineering of the active phase at the nanoscale", Appl. Catal. B Environ. 201 (2017) 339-347.

[318] S. Specchia, G. Ercolino, S. Karimi, C. Italiano, A. Vita, "Solution combustion synthesis for preparation of structured catalysts: A mini-review on process intensification for energy applications and pollution control", Int. J. Self Propag. High Temp. Synth. 26 (2017) 166-186.

[319] A. Varma, A.S. Mukasyan, A.S. Rogachev, K.V. Manukyan, "Solution combustion synthesis of nanoscale materials", Chem. Rev. 116 (2016) 14493-14586.

[320] E. Aliyev, V. Filiz, M.M. Khan, Y.J. Lee, C. Abetz, V. Abetz, "Structural characterization of graphene oxide: surface functional groups and fractionated oxidative debris", Nanomaterials-Basel 9 (2019) 1180.

[321] Y. Wu, L. Luo, W. Liu, "Effect of stoichiometric ratio of organic fuel to oxidizer on performance of $La_{0.8}Sr_{0.2}CoO_3$ catalysts for CH_4 combustion", React. Kinet. Catal. Lett. 97 (2009) 59-67.

[322] A.S. Mukasyan, P. Dinka, "Novel approaches to solution-combustion synthesis of nanomaterials", Int. J. Self Propag. High Temp. Synth. 16 (2007) 23-35.

[323] C. Italiano, M.A. Ashraf, L. Pino, C.W.M. Quintero, S. Specchia, A. Vita, "Rh/CeO_2 thin catalytic layer deposition on alumina foams: Catalytic performance and controlling regimes in biogas reforming processes", Catalysts 8 (2018) 448.

LIST OF PUBLICATIONS

Thesis-derived publications

1. A. Choya, B. de Rivas, J.I. Gutiérrez-Ortiz, J.R. González-Velasco, R. López-Fonseca, "Oxidation of residual methane from VNG vehicles over Co_3O_4-based batalysts: comparison among bulk, Al_2O_3-supported and Ce-doped catalysts", Appl. Catal. B Environ. 237 (2018) 844-854.

2. A. Choya, B. de Rivas, J.I. Gutiérrez-Ortiz, R. López-Fonseca, "Effect of residual Na^+ on the combustion of methane over Co_3O_4 bulk catalysts prepared by precipitation", Catalysts 8 (2018) 427-441

3. A. Choya, B. de Rivas, J.I. Gutiérrez-Ortiz, J.R. González-Velasco, R. López-Fonseca, "On the beneficial effect of MgO promoter on the performance of Co_3O_4/Al_2O_3 catalysts for combustion of dilute methane", Appl. Catal. A Gen. 582 (2019) 117099.

4. A. Choya, B. de Rivas, J.I. Gutiérrez-Ortiz, J.R. González-Velasco, R. López-Fonseca, "Synthesis, characterization and kinetic behavior of supported cobalt catalysts for oxidative after-treatment of methane lean mixtures", Materials 12 (2019) 3174

5. A. Choya, B. de Rivas, J.R. González-Velasco, J.I. Gutiérrez-Ortiz, R. López-Fonseca, "Oxidation of lean methane over cobalt catalysts supported on ceria/alumina", Appl. Catal. A Gen. 591 (2020) 117381

6. A. Choya, B. de Rivas, J.I. Gutiérrez-Ortiz, R. López-Fonseca, "Comparative study of strategies for enhancing the performance of Co_3O_4/Al_2O_3 catalysts for lean methane combustion", Catalysts 10 (2020) 757.

7. A. Choya, B. de Rivas, J.R. González-Velasco, J.I. Gutiérrez-Ortiz, R.López-Fonseca, "Optimisation of bimetallic Co-Ni supported catalysts for oxidation of methane in natural gas vehicles", Appl. Catal B. Environ, article number 119712, 'in press', DOI: 10.1016/j.apcatb.2020.119712

Other publications

1. C.A. Rolph, R. Villa, B. Jefferson, A. Brookes, A. Choya, G. Iceton, F. Hassard, "From full-scale biofilters to bioreactors: Engineering biological metaldehyde removal", Sci. Total Environ. 685 (2019) 410-418.

2. Z. Bouhka, A. Choya, M. Cortés-Reyes, B. de Rivas, L.J. Alemany, J. R. González-Velasco, J.I. Gutiérrez-Ortiz, R. López-Fonseca, "Influence of the calcination temperature on the activity of hydroxyapatite supported palladium catalyst in the methane oxidation reaction", Appl. Catal B. Environ. 277 (2020) 119280.